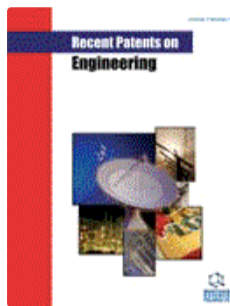




Search here...

Login

Register

Cart 0Search Articles ▼

Recent Patents on Engineering

Editor-in-Chief »

ISSN (Print): 1872-2121

ISSN (Online): 2212-4047

Back

Journal ▼

Subscribe

Research Article

Medical Image Classification Using DL-based Feature Extraction in IoMT

Author(s): [Madhuri Thimmapuram](#), [Shoba Rani Salvadi](#), [Narsimhulu Pallati](#) and [Rajanikanth Aluvalu*](#) ^{id}

Volume 18, Issue 9, 2024

Published on: 31 March, 2023

Article ID: e220223213881

Pages: 12

DOI: [10.2174/1872212117666230222093128](https://doi.org/10.2174/1872212117666230222093128)

Price: \$65





**THE INTERNATIONAL
MEDICINE AND BIOSCIENCES
CONFERENCE 2025**
6th - 8th November, 2025 Dubai, UAE

22nd in the series of Eureka Science
Translational Medicine Conferences

**Call for Papers and
Presentations**

[Submit Now](#)

Early Bird Discount
Register by: January 31, 2025

Abstract

Aim: Recent advances in Artificial Intelligence (AI) and the addition of Deep Learning (DL) have made it possible to analyse both real-time and historical data from the Internet of Things (IoT). Recently, IoT technology has been implemented in healthcare schemes as IoMT to aid in medical diagnoses. Medical image classification is useful for predicting and identifying serious diseases at an early stage, which is crucial in the diagnostic process.

Background: When it comes to managing, treating, and preventing illness, medical photographs are an essential element of a patient's health record. However, it is a difficult issue in computer-based diagnostics to classify images using efficient characteristics.

Objective: The patent study aimed to develop a deep learning-based classification model for feature extraction.

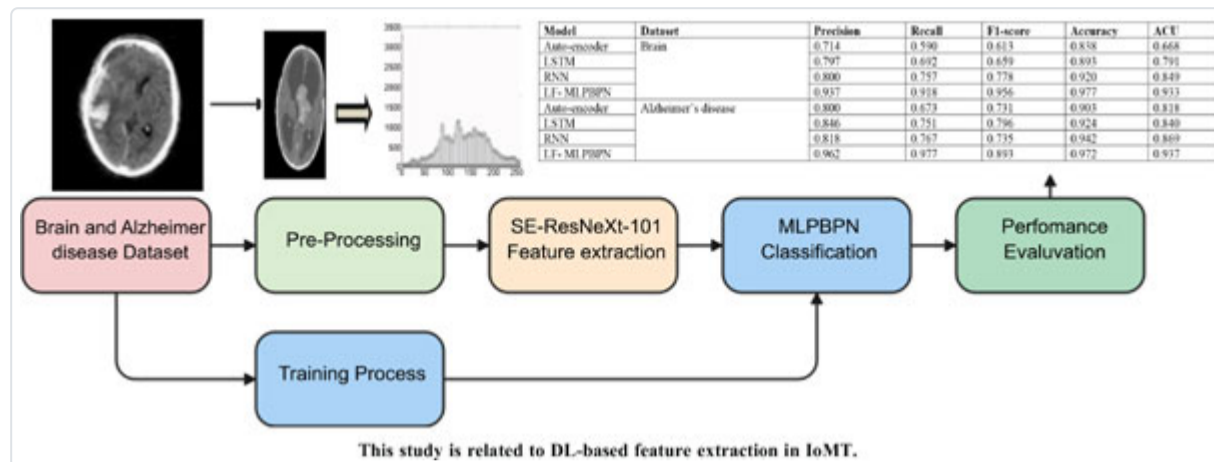
Methods: Levy flight optimization is employed to pick the weight for the classification model optimally. At the end of the day, the optimal weight led to a better classification result and a higher degree of precision when analyzing medical photos for disease.

Results: We tested the proposed results in MATLAB and compared them with conventional methods of classification. The suggested model's best results include 97.71% accuracy on a brain dataset and 97.2% accuracy on an Alzheimer's disease dataset.

Conclusion: The proposed algorithm's high rate of convergence proves that it can successfully balance the exploration and exploitation phases by avoiding capturing in local optimization and classifying thresholds rapidly. In light of the need for improved accuracy, precision, and computational speed in clinical picture classification, a novel approach based on soft sets has been presented.

Keywords: [Artificial intelligence](#), [region-based convolutional neural network](#), [backpropagation network](#), [internet of medical things](#), [medical image classification](#), [levy flight](#).

Graphical Abstract



References

- Mark Item
- Purchase PDF
- Rights & Permissions
- Print
- Cite

Article Metrics



PDF

15



HTML

1

FIND YOUR INSTITUTION

Journal Information

- > About Journal

- > Editorial Board

- > Current Issue

- > Volumes /Issues

For Authors

For Editors

For Reviewers

Explore Articles

Open Access



Measurement: Sensors

Volume 25, February 2023, 100611

Animal image identification and classification using deep neural networks techniques

Thirupathi Battu ^a  , D. Sreenivasa Reddy Lakshmi ^b[Show more](#) [Outline](#) | [Share](#)  [Cite](#) <https://doi.org/10.1016/j.measen.2022.100611> [Get rights and content](#) Under a Creative Commons [license](#) *open access*

Abstract

Animal identification research, there haven't been many effective methods introduced, especially in the area of predator species. In this article, we provide a reliable learning strategy for categorising animals from camera-trap photos captured in naturally inhabited areas with high densities of people and noise. To deal with noisy labels, we offered two distinct network architectures—one with clean samples and the other without. We separate the training data into groups with various properties using k-means clustering. Then, other networks are trained using these groupings. Then, using maximum voting, these more diverse networks are used to jointly forecast or correct sample labels. We test the effectiveness of the suggested method using two publicly accessible camera-trap picture datasets, Snapshot Serengeti and Panama-Netherlands. Our findings show that our method is more accurate and surpasses state-of-the-art techniques for classifying animal species from camera-trap photos with high levels of label noise.



Keywords

Animal detection and classification; Feature learning; Image modalities; Deep neural networks

1. Introduction

According to statistics from 2017, up to five million individuals in the United States are assaulted by animals each year. According to Langley & Morrow, up to two million animal bites occur in the United States each year. Depending on where you live, animal attacks happen more or less often. A term used in slang to describe an animal that uses humans as a form of prey is "man-eater." For instance, tigers are reported to have killed more people than any other animal of their kind [1,2]. They are more likely than any other wild animal to directly attack a person, according to Nowak et al. On the other hand, man-eating lions have been seen invading human settlements both during the day and at night in order to find victims. According to American and Tanzanian specialists, there was a significant increase in man-eating incidents in Tanzania's rural areas between 1990 and 2005. At least 563 locals were attacked at this period, and many victims were eaten. According to Warrel, thousands of humans suffer fatal injuries each year as a result of animal attacks [3]. Though it does not seem that every government does so, they keep records of animal-related deaths. The majority of animals, with the exception of tigers, do not actively seek out humans, while certain species may prey on the unconscious, ill, or dead. Animals may attack humans, livestock, and pets when they get used to people or when they are badly malnourished. Attacks seem to happen more often at night when animals leave their territory in quest of food. There is no predator animal detector mentioned in the literature. In this study, an image processing technology is utilised to propose a way for identifying the species of animals. This method is then tested using a dataset that includes pets and predators. The classification results are then evaluated and debated in terms of accuracy [4].

One of the fundamental notions in computer vision is that the initial goal is to "understand the picture," which leads to a constant increase in the requirement to grasp the high-level meaning of things when it comes to object recognition and image identification. The field has exploded in popularity as a key visual talent required by computer vision systems. As so many individuals and computers extract large quantities of information from photos, images have become ubiquitous in a number of sectors [5].

Automation, schools, self-driving vehicles, tracking, and the construction of 3D model representations all need knowledge that might be crucial. While the above-mentioned applications vary in a variety of ways, they all follow the same procedure of annotating a



Prediction of Seed Germination Quality Utilizing Ensemble-Based Precision Forming

Mukkoti Marathi Venkata Chalapathi¹ A Vijaya Krishna² G Gopichand^{3*}
 Kadiyala Ramana⁴ V C Bharathi¹ Neeraj Sharma⁵

¹School of Computer Science and Engineering, VIT-AP University, Amaravati, India

²Department of Computer Science and Technology, GNITS, Hyderabad, India

³School of Computer Science and Engineering, Vellore Institute of Technology, Vellore, India

⁴Department of Artificial Intelligence & Data Science, Chaitanya Bharathi Institute of Technology, Hyderabad, Telangana, India

⁵Department of Information Technology, VPPCOE & VA, Mumbai, India

* Corresponding author's Email: gopichand.g@vit.ac.in

Abstract: Seed germination is a primary objective of precision agriculture. Precision agriculture, which makes extensive use of machine learning, has been the subject of recent studies on predictive analytics. These machine learning methods typically employ supervised learning models to make predictions about how successfully seeds will germinate. However, a major challenge that modern models face when attempting to make accurate predictions is the curse of dimensionality in the training corpus. The primary contribution of this manuscript is an ensemble-based method for predicting seed germination quality (EL-GQP) in precision agriculture. The accuracy of predictions can be improved using this ensemble method, which combines the positive aspects of a number of different models while minimising the negative aspects of the individual models. The proposed model is significantly superior to the current model, as demonstrated by experimental results of cross-validation on the benchmark dataset. During the simulation, work is done on the corpus dataset contains 4250 negative records and 6230 positive records.

Keywords: Precision farming, Ensemble classification, Germination quality, Machine learning, Predictive analytics.

1. Introduction

[1] Asserts that seed quality is an essential component of agricultural production that directly influences yield. Utilizing high-quality seeds and inbreeding the plant lowers the cost of field experiments while increasing the likelihood of finding the best crop variety. As shown in [2] programmes for ensuring the quality of seeds use a range of methods to validate the traits of seed-like vigour and germination tests. These processes have limitations associated with the consumption of time, destructive nature, and subjectivity of measuring seed quality [3-5]. The work [6] presents that there has been a rapidly increasing demand for effective approaches, which might provide reliable, rapid, objective, and non-destructive identification of the

quality of seed [6].

To a human society, seeds are required as the main source of food and service to be significant crops materials. The yield of a crop is heavily influenced by seed quality and environmental factors. According to [7], measuring seed germination is a necessary task for seed researchers in order to evaluate the various seed lots and enhance the efficiency of the food chain. It is important to note that worldwide crop product needs to be doubled to supply the increasing population by 2050 as in [8]. Traditional measures of seed testing, mainly tests of seed-vigor, have not been utilized extensively because of time-intensive and cumbersome protocols as in [9]. Moreover, many seed tests introduced by ISTA (international seed testing association) have been manually assessed by utilizing a standardized

process, which varies for diversified crops [10]. Concerning to the prologue abovementioned, it is necessary to contribute computer aided models those build on machine learning, artificial intelligence, and deep h platforms. In this context, a novel machine learning model, which is an ensemble learning-based seed germination quality check model has portrayed in this manuscript.

EL-GQP, the proposed precision agriculture method, has several advantages over current methods. First, it uses ensemble-based modelling to improve prediction accuracy. This method reduces model drawbacks, improving predictions. Second, EL-GQP addresses the curse of dimensionality, which plagues machine learning models. Predictions are difficult when the training dataset has many variables. EL-GQP solves this problem by using an ensemble of models to handle more variables and produce more accurate results.

Third, EL-GQP accurately predicts seed germination. Precision agriculture aims to achieve this, and the suggested approach outperforms existing models. Cross-validation on the benchmark dataset shows that EL-GQP performs significantly better than existing models.

The EL-GQP method has several advantages over current precision agriculture methods. Precision agriculture practitioners use it to integrate multiple models, overcome dimensionality, and accurately predict seed germination quality.

This article has been organized into five parts. The first section discusses seed germination and how machine learning (ML) algorithms can be used to predict seed germination quality. The second section contains a comprehensive review of the most recent ML algorithms for predicting seed germination quality. The third section discusses the study's methods and materials, with a focus on an ensemble learning-based seed germination quality check model. Section four presents the results of an experimental study on seed germination quality prediction using the proposed model, as well as performance measures. Finally, the conclusion highlights the study's contribution and summarises the key findings.

2. Related work

Generally, variations in internal anatomical characteristics and chemical composition of seeds have been associated with loss of vigor and viability, as in [11]. However, these variations have been unlikely recognized through visual inspection. Moreover, approaches dependent on X-ray imaging and spectrometric strategies have been utilized successfully to gather data on complex traits

associated with seed quality. In this case, FT-NIR (Fourier transform near-infrared) spectroscopy has demonstrated significant potential for identifying seed compounds by acquiring a large number of spectral details, as shown in [12-18]. FT-NIR spectroscopy can acquire a large amount of spectral data and is effective in identifying seed compounds, according to several studies. As shown in [19], the FT-NIR spectroscopy is dependent on electromagnetic radiation absorption at wavelengths ranging from 780 to 2500 nm. This wide range of wavelengths enables direct and simultaneous measurement of multiple constituents in seed samples. As a result, it is versatile for simultaneous and direct measurements of various constituents in seed samples, as demonstrated in [16, 20-23]. Previous research has found that these characteristics make it an effective method for analysing seed samples. On other dimensions, X-ray imaging has been dependent on X-ray attenuation variances in diversified tissues types [24]. Therefore, it might reveal a physical seed state with an internal morphology as in [11]. Even though these strategies have the maximal possibility for classification of seed quality, integrating the datasets might produce novel information regarding the samples of seed or enhance the performance of the classifier as in [25].

Current advancements of ML algorithms have revolutionized agriculture due to their fundamental for building approaches to categorize products, mainly seeds quality attributes. The robust algorithms might capture non-linear and linear associations, and they might attain maximal accuracy of classification. Various algorithms proved as effective to solve the issues in several researching domains like PLS-DA (partial least squares discriminant analysis), LDA (linear discriminant analysis), NB (naïve Bayes), SVM, and many more, as stated in [12, 15, 17, 25, 26]. Nevertheless, distinct algorithms perform differently, and they might have diversified performances as in [26].

Even though models based on optical might produce accurate data on the quality of seed, combining datasets by ML algorithms might enhance the further performance of classification. Therewere no endeavors in utilizing FT-NIR integrated with X-ray data images for categorizing the qualityof seed. Hence, by utilizing U. Brizantha grass seeds as an approach, we have tested whether combined data from the X-ray imaging and FT-NIR with ML algorithms might enhance the vigor and germination of seed predictions.

In order to cut down on the number of manual steps in the error-prone seed-testing process, several researchers have proposed models for automating

A Comparative Study on Prediction of Endometriosis Causing Infertility Using Machine Learning Techniques: in Detail

Satya Kiranmai Tadepalli¹, Prof. P. V. Lakshmi²

¹Asst. professor, IT Department

CBIT(A)

Hyderabad, India

tadepallikiranmai84@gmail.com

²Department of CSE

GITAM (Deemed to be University)

Visakhapatnam

vpanga@gitam.edu

Abstract— The purpose of this study is to utilize Artificial Intelligence to analyse and predict endometriosis problem in women. All traditional methods are used before to develop or to predict the likelihood of endometriosis based on the symptoms presented. By identifying the symptoms of endometriosis, the machine learning algorithms can determine the type of endometriosis and the appropriate course of action for patients. This technology can be used to educate women globally on the signs and symptoms of endometriosis and help them take preventive measures to avoid this deadly disease. The results of this research demonstrate the potential of advanced technology to revolutionize healthcare by providing early detection and treatment options for endometriosis. In areas with limited access to medical care, this tool can aid in identifying ovarian cancer and reducing mortality rates. By detecting and diagnosing endometriosis at an early stage, this program can play a significant role in promoting women's health and wellbeing. The methodology proposed in this study produces classification results that are on par with cutting-edge deep learning techniques. In addition, the methodology provides visual explanations that offer valuable insights into the inner workings of each model and enhance the accuracy and reliability of the predictions.

Keywords- Artificial Intelligence (AI), Machine Learning Algorithms, Endometriosis, Logistic Regression, Machine Learning, Classification, Feature selection

I. INTRODUCTION

According to Ashfaque [25], endometriosis is the 3rd most common disease among women and the 10th most common disease globally, causing about 400,000 new cases and 50,000 deaths in 2018. The strength of this research lies in its potential to raise awareness of endometriosis among women worldwide, especially in rural areas with low doctor-patient ratios. By predicting the likelihood of endometriosis based on symptoms, the software can help patients identify the type of endometriosis they have and take appropriate steps to reduce mortality rates [1]. Although mortality rates for endometriosis have decreased by more than 20% since the mid-1980s due to improvements in treatment and reduction in rates, less than half of women survive beyond 5 years after diagnosis due to aggressive high-grade serous carcinomas and a lack of early detection techniques and specific early symptoms.

The field of medical science is on the cusp of a technological revolution, with computer science playing a pivotal role [3]. The use of technology will make medical treatment more convenient, effective, and accessible. Artificial intelligence (AI) has the potential to diagnose diseases with greater accuracy than

human expertise, thereby reducing detection errors. This article focuses on the development of an AI model to predict the likelihood of endometriosis. Endometriosis is a major concern among women, as symptoms are not easily detectable at early stages [4,5]. By using the symptoms of endometriosis as variables in any models and techniques of machine learning algorithms to analyse the model prediction and the probability of the disease. All these methods can be compared, and the outcome is analysed based on the result. This prediction can aid in early detection and help women take necessary precautions and receive advanced medical treatment.

Endometriosis is a common disorder observed in women who are of a menstruating age. It occurs when tissues, resembling the endometrium lining, develop on the outside of the uterus and other organs in the pelvic region. Symptoms vary from mild to severe, including pelvic pain, dysmenorrhea, and infertility. While no guaranteed treatment for endometriosis exists, early diagnosis and medical or surgical interventions can reduce the risk of complications and improve patients' quality of life [6]. Predicting the likelihood of endometriosis onset by analysing the medical history of diagnosed patients could aid healthcare

providers in diagnosis and improve patient well-being. To achieve this, the study employed different machine learning algorithms and their comparative studies.

II. BACKGROUND

To start with, this study mainly focuses on different machine learning techniques that can be used for the early detection of endometriosis and comparative evaluation has been made in this study for various datasets used with different proposed algorithms [8].

The main objectives of this article are as follows:

- a. To assess different machine learning models that can accurately predict the probability of endometriosis occurrence based on medical history.
- b. To determine the crucial medical events in a patient's journey that ultimately result in endometriosis diagnosis.
- c. To evaluate and rank the performance of the developed models against various databases and select the best-performing ones.
- d. To use the predicted scores from the models to create patient profiles based on their likelihood of developing endometriosis.

To enable this to happen, here in this article, the datasets of blastocysts containing various time lapse images, patient health claim database of US for the year 2010, PLCO dataset and a Kaggle dataset of endometriosis is considered [7,10]. These databases are tested against different algorithms of machine learning and results and observations are recorded. Various analytical techniques were utilized to analyse the dataset, ranging from rules-based patient qualification criteria to machine learning algorithms, to determine the likelihood of endometriosis [22]. Each method is explained in detail in the subsequent sections of the article.

III. FEATURE REDUCTION

The features used for analysing endometriosis using machine learning techniques can vary depending on the specific study or analysis. However, some common features that have been used in previous studies include age, menstrual history, hormonal medication use, family history of endometriosis, symptoms (such as pelvic pain and dysmenorrhea), and previous surgeries related to endometriosis. Other features that may be considered include comorbidities, medication use, and demographic information [18,14]. Based on the different datasets used and applied, some features are observed and evaluated for reduction. The result of the feature reduction process is furnished below [Table – 1].

TABLE I: FEATURE REDUCTION

Name of the dataset	Number of Initial Parameters	Number of Reduced Parameters	Feature Elimination Ratio (%)
Time-Lapse Embryo	78	11	84.21
Patient Health Claim	75	15	85.52
PLCO	67	08	89.47
Kaggle	77	14	88.15

The result is analysed visually for the feature reduction is given here. [Figure – 1].

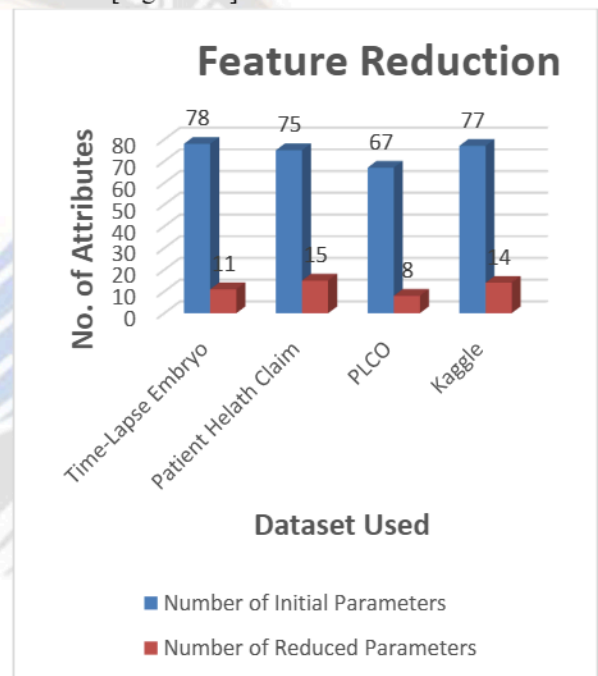


FIGURE I: FEATURE REDUCTION

The number of attributes has been significantly reduced, and the accuracy of the dataset is compared to other standard methods using both the original and reduced sets of attributes.

IV. CLASSIFICATION ACCURACY ANALYSIS

The proposed model generates a subset of features, and when compared to the entire set of features, the classification accuracy is higher [15]. It is recommended to use the smaller set of attributes when training the model for effective prediction and improved accuracy. By using different classification methods, the results of these approaches are analysed. [Table – 2 to 5].

DDoS Attack Detection using Swarm Optimized Random Forest Classification

R. Sarath Babu^{*1}, Dr. K. Radhika²

Submitted: 11/10/2023

Revised: 30/11/2023

Accepted: 11/12/2023

Abstract: With the increasing spread of the Internet, the need for security also increases - both in the private and in the business sector. Corporate networks in particular are often exposed to attempted attacks. In order to avert or limit the damage, these attacks must be recognized and appropriate countermeasures initiated. This task is achieved by an Intruder Detection System (IDS). This paper presents a DDoS attack detection model using swarm optimization-based feature selection and Random Forest (RF) classifier. A modified Grey Wolf Optimization (GWO) algorithm is used to select the features which produce the best accuracy. The fitness function of the conventional GWO algorithm is replaced with Stochastic Gradient Descent (SGD) in order to perform feature selection. The RF classifier is then trained using the chosen subset of features to identify attacks. The proposed model is tested on CICIDS2017 dataset and has been compared with existing machine learning techniques to evaluate the efficiency of the proposed model. GWO earned the highest Accuracy of 99.8. This was accomplished with only 40 out of 75 features. When GWO provided the least number of features, 38, resulting in accuracy of 99.7. Over several experiments, modified GWO with DT had an average classification accuracy of 99.5 percent.

Keywords: DDoS, Grey Wolf Optimization (GWO), Intruder Detection System (IDS), Random Forest (RF), Stochastic Gradient Descent (SGD).

1. Introduction

Intrusion detection is the active monitoring of computer systems and / or networks with the Target of attack and abuse detection identified [1]. The goal of intrusion detection is in filtering out all of the events taking place in the surveillance area. Attacks, attempts to abuse or security breaches indicate, then deepened to investigate. Events should be recognized and reported promptly. Intrusion detection is to be understood as a process and requires suitable organizational integration as well as technical support using suitable tools [2].

IDS are used to detect attacks on the computer network. A distinction is made between IDS on the one hand based on their detection method (anomaly-based vs. signature-based) and on the other hand based on their area of responsibility (host-based vs. network-based). Intrusion detection system is a set of tools that covers the entire intrusion detection process, from event detection to evaluation and escalation. Support and documentation of events. The majority of Intrusion Detection products available on the market have this integrated functionality. However, IDS can also be composed of individual components. The selection and compilation of the IDS are based on this the individual technical and organizational conditions and requirements.

Today, it should come as no surprise that one of the primary goals of an IDS is to ensure the safety of a computer, a network, or both. There is seldom a day that goes by in which one does not hear about fresh attempts to crack business networks or hack into such networks. As a result of attempted burglaries, some credit card data have already been obtained by dishonest persons who are criminals.

In the most recent few years, both the total number of assaults and the expenses that are linked with them have skyrocketed, as indicated by data obtained from the Computer Emergency Response Team (CERT). This tendency could not be fought against at this time; even so-called intrusion prevention technologies frequently failed to accomplish their goal. There are many different ways that danger might present itself. For instance, the attacker may have obtained access to the system or its resources by exploiting flaws in the manner in which the TCP/IP stack was implemented. If a trained expert is able to determine which system is being used based on an analysis of the TCP/IP fingerprint (nmap), they are then able to utilize this knowledge to look for certain vulnerabilities and eventually exploit such vulnerabilities during an attack.

In addition, vulnerabilities may frequently be identified in the software that is installed on the system. These vulnerabilities typically take the form of buffer overflows, which a typical user is able to exploit. You even have the chance to obtain root rights. The DNS daemon BIND, which has been the market leader under Unix and its variants for decades, the FTP server WuFTP, and of course the tried-and-true Microsoft Internet Information Server all

¹Research Scholar, Department of Computer Science and Engineering, University College of Engineering, Osmania University, Hyderabad, Telangana, India.

²Professor and Head, Department of Information Technology, Gandipet, Hyderabad, Telangana, India. Email: kradhika_it@cbit.ac.in

* Corresponding Author Email: sharath.rakki@gmail.com

performed extremely poorly. The first two programs were responsible for introducing worms into the Unix environment. There is currently a worm that exploits many vulnerabilities in the Microsoft Internet Information Services (IIS) and BIND web servers [3].

It is a common misconception that attempts to breach security are exclusively carried out within the context of corporate networks or huge organizations. In point of fact, every single person who uses the private internet is vulnerable to assault. However, an IP address, specifically the one that is known to frequently change behind plug-end computer systems, is not even close to as interesting as a system that maintains permanent contact with the Internet or multiple systems that are connected together in a network, particularly in light of the fact that distributed denial of service attacks used to be possible. A computer that connects to the Internet using flat rate DSL is far more vulnerable to attack than a machine that connects to the Internet using ISDN or an older modem only occasionally.

In the end, a chain is only as strong as its weakest link, which in this case is the individual who is using the system. Passwords that are too easy to guess are frequently the cause of attempted break-ins. Once a criminal has gained access to the system, it is simple for them to obtain even greater levels of privileges, or even absolute root rights, on a computer. In addition to attempts using what are known as brute force, the attacker can, of course, also attempt to steal the user's password by using social engineering. There are always going to be instances in which unscrupulous individuals try to coerce a user into divulging their password under the guise of a pretext or a false identity. This kind of attack (using passwords) can't be stopped by an IDS, of course. One can, at most, observe odd behaviors that come from this login, but by that point, it is sadly frequently too late to take action.

In the absence of an IDS, it becomes difficult to determine how long an intruder was able to operate undetected, how the intruder carried out his attack, or how much damage was caused. In a nutshell, the following points can sum up the objectives that are intended to be achieved through ID systems:

- notifying those responsible (administrator, security officer) or taking active countermeasures in the case of an attack,
- the legal applicability of the information that was gathered;
- The detection of a loss of data,
- Protection from potential future assaults by analyzing the information gathered in the case of a (simulated) break-in

In [4], the authors proposed a network-IDS that reads all of

the packets and investigate them for unusual patterns. In order for IDS to be able to accommodate the large bandwidths of today's networks, it must enable high performance while processing and analyzing data. It is impossible to guarantee that the IDS will do complete monitoring. Hybrid IDS combines host-based and network-based security measures to provide even greater levels of protection.

A comprehensive analysis of the scientific work that has been done on the detection of intrusions using machine learning approaches during the past ten years is presented in [5]. In addition to that, the authors discussed about a few of the unresolved problems that are still outstanding. This survey acted as a supplementary that have been conducted before on the topic of intrusion detection and is designed to support earlier research. Additionally, it will provide researchers who are working on intrusion detection using ML algorithms with a ready reference for their work.

Uhm and Pak [6] presented a fresh approach that makes use of service-aware dataset partitioning, which not only offers high scalability to manage large amounts of data that are expanding at a rapid rate in a flexible manner but also assists the classifier in improving their speed and accuracy. The authors assessed the method using the Kyoto2016 dataset, a dataset for severely unbalanced data.

Zhou et al. [7] presented a framework for the detection of intrusions, based on the approaches of feature selection and ensemble learning. In the first stage of dimensionality reduction, a heuristic approach known as CFS-BA is developed. This algorithm finds the ideal subset by basing its decisions on the association between the features. Then, the authors provide an ensemble method that is a combination of the C4.5 algorithm and Random Forest (RF). In the end, a voting mechanism is utilized to integrate the probability distributions of the several base learners in order to recognize attacks.

Because of the high volume of traffic, an IDS performs analysis on large amounts of data, and it also safeguards data and computer networks from hostile activity. Therefore, in order to differentiate between typical and suspicious activity, a classification method that is both quick and effective is necessary. There are a variety of approaches that make use of the machine learning methodology, and these approaches have recently been available for use in intrusion detection. In [8], a variety of IDS strategies that are based on machine learning are examined, explained, and categorized. IoT is one of the upcoming internet technologies that focuses on the delivery of services and adjusting the way that technologies are implemented across various communication networks [15-17].

Original Article

Combining Super Resolution and EfficientNet Models to Reduce False Positives and False Negatives in Breast Cancer Detection

Vandana Lingampally¹, Radhika Kavuri²

¹Department of CSE, Osmania University, Hyderabad, India

²Department of IT, CBIT, Hyderabad, India

¹Corresponding Author : researchprojectphd9974@gmail.com

Received: 22 January 2023

Revised: 17 April 2023

Accepted: 26 April 2023

Published: 25 May 2023

Abstract - The accurate detection of breast cancer is imperative for optimal therapeutic outcomes, and minimizing false positive and false negative rates is a vital element in this process. Super-resolution images are particularly used in health research due to their ability to provide higher spatial resolution and more detailed information about the appearance of tissues and structures in medical images. These images can enable the model to learn to identify subtle abnormalities and distinguish them from normal tissue, and they are also more resistant to image degradation, such as noise or blur. To obtain high-resolution mammograms, a generator network (SRGAN) was trained and obtained SR images were applied on EfficientNet models, which are highly effective deep learning architectures that exhibit superior performance on a wide range of tasks with a reduced number of parameters and lower computational complexity compared to other models. A combination of three datasets (CBIS-DDSM, Mini-MIAS, and INbreast) with data augmentation was used to train and evaluate the model. The proposed model achieved a false positive and false negative rate of 0.0029, indicating a high level of accuracy in detecting breast cancer. This low rate highlights the efficacy of the approach in minimizing false positive and false negative rates, which is crucial for optimal treatment outcomes.

Keywords - Breast cancer, Deep learning, Efficientnet, SRGAN, Super-resolution.

1. Introduction

False positives and false negatives in breast cancer detection can have significant consequences for patients. False positives, also known as false alarms, occur when a test incorrectly indicates the presence of cancer. This can lead to unnecessary additional testing, such as biopsies, which can be expensive and invasive for the patient. False positives can also cause anxiety and distress for the patient. On the other hand, false negatives, also known as missed diagnoses, occur when a test incorrectly indicates the absence of cancer. This can result in a delay in diagnosis and treatment, which can be particularly harmful in the case of breast cancer, as early detection is often key to successful treatment. False negatives can also lead to a false sense of security for the patient, causing them to forego necessary screenings in the future. It is, therefore, important to strive for high levels of accuracy in breast cancer detection methods in order to minimize both false positives (FP) and false negatives (FN).

1.1. Limitations of Current Breast Mass Classification Models

After analyzing several papers from previous research (presented in section 2), it can be observed that the percentage

of FN and FP results in the classification of breast masses is high, with significant variation between the FN and FP percentages.

Despite the application of robust preprocessing techniques, advanced enhancement methods, and state-of-the-art deep learning models for feature extraction and classification, the classification accuracy of breast masses remains suboptimal. The primary question is why these models cannot accurately diagnose masses with high accuracy. Indeed, it appears that the limited information provided by low-resolution mammograms may be hindering the accuracy of breast mass classification. Therefore, more relevant features are necessary for accurate classification, which may ultimately lead to a reduction in the number of FP and FN results.

To overcome this limitation, high-resolution mammograms can be utilized to extract more detailed and comprehensive features that may be crucial for accurate classification. Incorporating this additional information into the models may enable them to make more accurate decisions, ultimately reducing the number of FP and FN.



1.2. High-Resolution Images

The image is a grid of individual pixels. Pixel density per inch gives the resolution of the image. Low resolution indicates less no. of pixels per inch, and high resolution indicates more pixels per inch. When no. of pixels is more per inch, the image will be of more clarity with much more details.

1.3. High-Resolution Mammograms

A mammogram contains information about the structure and tissue of the breast, which includes fatty tissue, ducts and lobules, and it also shows blood vessels in the breast. There may be the presence of abnormalities in the mammograms, like masses and calcifications, which will be small in size when compared with the full size of the breast. Detailed information on abnormalities is needed to decide whether the abnormalities are benign or malignant, which may not be seen in low-resolution mammograms and especially when the tissue is dense. So there is a need for high-resolution mammograms which give finer details or more detailed information about the abnormalities, which will help in deciding whether the abnormality is benign or malignant.

1.4. Methods to Acquire High-Resolution Mammograms

Interpolation methods: These methods use mathematical algorithms to estimate the values of missing pixels in an image, thereby increasing its resolution. Some frequently used methods for interpolation include the nearest neighbor, bilinear[1], and bicubic interpolation[2]. The bicubic interpolation method calculates the value of each new pixel by taking a weighted average of the 16 pixels that are closest in proximity, using a sophisticated algorithm to derive a precise approximation. This method may be effective at increasing the resolution of an image. Still, it introduces artifacts such as blurriness and ringing, which can reduce the image's level of detail and clarity.

1.4.1. CNNs

These deep learning models can be trained on pairs of LR and HR images, from which they can construct a mapping function to generate HR images from LR images. To construct mapping function 1. SRCNN[3] uses 3 convolutional layers, the initial layer acts as a feature extractor, the subsequent layer serves as a mapping layer, and the last layer acts as a reconstructor. 2. FSRCNN[4] uses feed-forward architecture and a deconvolutional layer. 3. ESPCN[5] uses sub-pixel convolutional layer. 4. VDSR[6] uses very deep network architecture with a residual learning strategy. 5. EDSR [7] uses deep residual network architecture with a high-capacity feature extractor. Many more CNN models have been introduced to generate high-resolution images, but the fact is that CNNs are introduced to recognize and classify images but not to generate images.

1.4.2. GANs

In these models, the generator network generates new images and is paired with a discriminator network that

evaluates the generated images' authenticity. GANs can be used to synthesize HR images from LR ones by training the generator network to produce images that are similar to the original high-resolution ones. Many GAN models have been introduced to generate super-resolution images. Some of the models are SRGAN [8], ESRGAN [9], DCGAN [10], CGAN [11], and WGAN [12]. In this study, SRGAN was initially utilized to obtain the super-resolution mammograms, and other GAN models may be explored in future work.

1.5. Selection of Deep Learning Models

To optimize the performance of the deep learning model for breast cancer(BC) detection using super-resolution mammogram images, a series of experiments were conducted with various architectures. After evaluating the results, it was determined that the EfficientNet model demonstrated superior performance in terms of reducing both FN and FP. As a result, EfficientNet was selected as the most appropriate model for this task.

This paper provides a comprehensive review of relevant previous research in the field in Section 2. The dataset creation and proposed model are presented in detail in Section 3. The implementation procedure is explained, and the study results are analyzed for their significance in Section 4. Lastly, the findings are summarized, and potential avenues for future work are suggested in Section 5.

2. Related Work

Breast cancer has been a rising concern in both rural and urban parts of India, with an alarming estimated count of 224,000 new cases in the year 2021 alone. Over the past decade, the incidence rate of breast cancer in India has been increasing at a yearly pace of 5-6%. Unfortunately, the mortality rate for breast cancer in India remains relatively high, with an estimated 138,000 fatalities in the same year. Early detection is crucial as cancer survival becomes increasingly challenging in advanced stages, and it's disappointing to note that more than half of Indian women are detected with stages 3 and 4 of BC. The best way to curb the mortality rate is by detecting breast cancer in its initial stage to provide better chances of recovery.

Several recent studies have delved into breast cancer research to find ways to address the rising incidence and mortality rates in India. In this section, we present a selection of such literature that sheds light on the current state of breast cancer research.

It has been observed from Table 1. that the percentage of FP and FN is high, with significant variation between the FN and FP percentages. Despite the application of robust preprocessing techniques, advanced enhancement methods, and state-of-the-art deep learning models for feature extraction and classification, the classification accuracy of breast masses remains suboptimal.

Original Article

XGBoost Machine Learning Model-Based DDoS Attack Detection and Mitigation in an SDN Environment

Arvind T¹, K. Radhika²

¹Department of CSE, UCE, OU, Hyderabad, Telangana, India.

²Department of IT, CBIT, Telangana, India.

¹Corresponding Author : mr.arvind@rediffmail.com

Received: 19 November 2022

Revised: 04 February 2023

Accepted: 18 February 2023

Published: 25 February 2023

Abstract - SDN sparked tremendous interest because of its several benefits, such as simple programming, quick scalability, centralized administration, etc. However, security is a significant problem, and Distributed denial of service (DDoS) threats a major challenge for SDN. One way to safeguard a Software-Defined networking infrastructure from DDoS assaults is to use machine learning models. This study presents an XGBoost-based approach for DDoS detection and mitigation. It evaluates it against other Machine Learning techniques, including Logistic Regression, Naive Bayes, Decision Trees, XGBoost, and Multilayer Perceptron. This method will generate, collect, classify, detect, and then mitigate Distributed denial-of-service assaults. The results show that the suggested approach protects SDN from DDoS attacks with high accuracy and a low error level while making good use of network resources. Despite the short training and testing period, the proposed method detects DDoS attacks with greater accuracy.

Keywords - SDN, DDoS, Machine learning, Mininet, Ryu.

1. Introduction

In this dynamic era, conventional networks face a lot of difficulties, such as vendor dependency, lack of support for dynamic policy updates, etc. SDN overcomes these difficulties by transferring all the decision-making capabilities to the control plane and reducing the data plane to the role of a simple packet forwarding unit. This capability of the SDN made it widely spread. However, at the same time, it also made it a primary cause of its failure. One of the popular attacks that can happen on the SDN controller is DDOS, where the controller is overwhelmed with a huge volume of packets from multiple distributed hosts. The switch's flow table also becomes full due to incoming data packets from multiple distributed sources, leading to reduced packet forwarding and dropping of incoming packets. These DDoS attacks can be of various types, such as volume-dependent, protocol-dependent, and application-dependent. Volume-dependent assaults include flooding attacks such as ICMP, UDP, and so on. Protocol-dependent assaults, such as SYN floods, the Ping of Death, Smurf attacks, and so on, target server resources. Active apps in the application plane are the target of application-dependent assaults. Slowloris and zero-day attacks are among them. Several approaches exist for detecting and defending against DDoS assaults; however, Machine learning (ML) techniques offer a promising solution for early detection due to their faster response times compared to manual methods. SDN flow data can be processed using

ML-based DDoS attack detection systems integrated into SDN topologies to create an autonomous, adaptable network. However, the current state of research lacks SDN benchmark datasets and a model that can effectively and accurately predict DDoS attacks using ML techniques. In light of this, there exists a significant research gap in the area of effectively detecting and preventing DDoS attacks in SDN. This study proposes an XGBoost-based DDoS detection and defense system. The procedure includes traffic generation, collection, classification, detection, and mitigation.

The paper includes the following sections: Section 2 explains the effects of DDoS on SDN networks, Section 3 explores the related studies, Section 4 describes the proposed system's experimental settings, Section 5 explores the modules of the proposed approach, and Section 6 discusses the Conclusion and Future Considerations.

2. DDoS attacks in SDN

SDN (Software-Defined Networking) has features that can make it more resilient to DDoS (Distributed denial of service) attacks, as well as features that can be used to victimize others with DDoS attacks.

The features such as centralized management, programmability, traffic engineering, and dynamic flow management make it more resilient to DDoS attacks. While it



can be vulnerable to distributed denial of service (DDoS) attacks as it has features that attackers can exploit, these victimizing features include centralized control, security risks, performance concerns, and a lack of standardization. The DDoS attacks target different layers of SDN.

- Control plane DDoS attacks include flooding, resource exhaustion, poison packet attacks, and so on.
- Data-plane DDoS attacks: can take the form of TCAM exhaustion, Flooding, Data-Control plane link saturation, etc.
- Application-plane DDoS attacks: can take the form of flood attacks, application-layer attacks, command injection attacks, resource exhaustion attacks, and configuration tampering attacks.

3. Related Work

This section of the article focuses on exploring the studies that employ statistical, machine learning, and deep learning techniques.

3.1. Statistical-Based Techniques

Statistical analysis uses statistical methods to look for strange patterns in network traffic that could be signs of a DDoS attack. Methods like mean, median, mode, standard deviation, entropy, and chi-square analysis can be used to find outliers in network data that could be signs of an attack [1,2].

Giotis et al. [4] devised an entropy technique to collect and analyze data to identify network anomalies, thereby reducing the controller's workload. They tested their system on the "National Technical University of Athens" network, where they gathered regular traffic for the anomaly detection module. This module analyses all flow inputs across all time intervals to determine undesirable ones. The mitigation module then specifies a flow rule to block the originating IP. With the assistance of Tcpreplay and Scapy, they were utilized to produce malicious traffic.

Mousavi et al. [5] presented a strategy to identify DDoS assaults using Shannon's entropy. All nodes will experience the same amount of traffic and entropy while the network is running properly.[6] When one or more hosts are exposed to a DDoS attack, they experience a fall in entropy due to an unusually large amount of traffic. After receiving 50 packet-in messages, the controller estimates the entropy using the target IP address. An attack is recognized when the estimated entropy falls below the detection threshold for five consecutive rounds.

The authors, Leu et al. [7], proposed agent-based IDS using the goodness of fit test of the Chi-Square to identify DoS and DDoS assaults. It examines the number of SrcIP variations that send packets to the target and Ipadddr distribution statistics. If an attack is detected, the chi-square value exceeds the threshold.

By integrating entropy-based techniques with machine learning algorithms, Dehkordi et al. [13] were able to identify low and high volumes of DDoS assaults. The method involves determining when detection is optimal in order to maximize efficiency. The suggested solution outperforms previous DDoS protection algorithms in terms of accuracy (99.85%).

Mishra et al. [9] demonstrated an entropy-based DDoS defense system with minimum computing costs. The suggested technique makes use of three different threshold values: entropy, packet flow rate, and a count threshold. Once the predetermined threshold is exceeded, the entropy is computed by a controller using data from the flow table of the associated switches. The count value is increased when the calculated entropy drops below the predetermined threshold. When the overall number of assaults hits a specified threshold, an alert is triggered. As part of the mitigation procedure, a controller will collect the offending IP address, DPID, and switch port information and begin discarding packets from that IP address immediately.

3.2. Machine Learning-Based Techniques

ML algorithms, like Decision Trees, Naive Bayes Random Forest, and Neural Networks, can be trained on normal network traffic patterns and used to detect anomalies that may indicate a DDoS attack. These algorithms can also be used to differentiate between benign and malicious traffic based on characteristics such as source IP address, destination IP address, packet size, and packet rate.

Saurav et al. [32] studied the attack patterns in the network by utilizing ML techniques. The methodology uses 4 different ML algorithms: C4.5, Naive Bayes, Bayes Net, and Decision Table. The models' prediction accuracy was examined, and they concluded that the Bayesian network had the greatest prediction rate.

Santos et al. [18] used a Mininet emulator and POX controller to produce the DDoS dataset with 23 characteristics. The traffic was generated using Scapy. They used different ML models to analyze the dataset, including SVM, MLP, DT, and RF. The findings indicate that the DT has a shorter processing time, and the RF model has the highest accuracy.

Swami et al. [21] presented an ML-based intrusion detection system to identify TCP-SYN flooding assaults. The authors created the traffic as well as classified and analyzed the performance of many models, including DT, LR, RF, MLP, and Adaboost. The experimental research made use of Mininet, the Ryu controller, and the Scapy tool to create traffic, the Tcpdump tool to collect traffic, and the Wireshark tool to analyze packets.

Obaid et al. [17] employed a range of machine learning models, including RF, KNN, J48, and SVM, to detect and mitigate DDoS attacks in an SDN network. Weka was used to train and test the models. Ubuntu served as the platform for



DETECTION OF BATS IN AGRICULTURE FARMS USING MODIFIED RESNET50V2 DEEP LEARNING MODEL

Bharathi Assistant Professor, Department of Informatics, University College of Engineering(A), Osmania University, Hyderabad, Telangana, India: maseed.bharathi@gmail.com,

Dr. Lakshmi Sreenivasa Reddy Associate Professor, Department of Information Technology, Chaitanya Bharathi Institute of Technology(A), Affiliated to Osmania University, Hyderabad, Telangana, India : dlsrinivasareddy_it@cbit.ac.in

Abstract

Farmers are actively exploring ways to enhance crop yield in order to meet the growing global demand for food, and minimizing damage caused by bats is one approach to achieve this goal. Bats can feed on various crops, causing significant economic losses for farmers, especially in orchards and vineyards. They can carry diseases, such as pseudorabies and rabies, that can affect both crops and livestock. This paper presents the use of computer vision and machine learning algorithms to detect bats in images captured in agricultural areas. This technology typically uses cameras equipped visible light sensors to capture images of bats in the farms. The resulting data can provide farmers and other stakeholders with information about bat activity in their fields, including the number of bats, their flight patterns, and the times of day when they are most active. The proposed framework uses a modified ResNet50V2 deep learning model for image classification. The proposed model identifies bats in images by classifying farm images into bat and non-bat images. The proposed model classifies the bat images with an accuracy of 97.8%.

Keywords: bat detection, image classification, Resnet50V2, agriculture, crop yield.

I. Introduction

Agriculture is likely to see a significant productivity boost as a direct result of the rising demand for food. Bats can pose several problems in agriculture:

1. Crop damage: Bats can feed on crops, especially in orchards and vineyards, causing significant economic losses for farmers.
2. Disease transmission: Bats can carry diseases, such as pseudorabies and rabies, that can affect both crops and livestock.
3. Increased pest populations: When bats are disrupted or killed, their natural pest control services are lost, leading to an increase in insect pest populations that can harm crops.
4. Fear and misconceptions: Many people are afraid of bats, and misconceptions about these animals can lead to negative attitudes toward bats and their conservation.

To mitigate these problems, farmers may use exclusion methods, such as netting, to protect their crops, and educate themselves and their communities about the benefits of bats in agriculture. Additionally, promoting sustainable agricultural practices that support bat populations can help to ensure the continued positive impact of bats on agriculture.

Several different methods have been offered as potential ways of determining whether or not bats are inhabiting agriculture farms [4-5]. The detection of acoustic signals is the focus of one strategy, which tries to establish the existence of bats. Bats communicate with their environment by sending out acoustic pulses and listening to the reflections of those pulses [6-7]. Over the course of the last several decades, a lot of research has been done on the subject of monitoring bats using acoustic signals. In spite of the fact that commercial bat detectors are available, getting reliable results from them calls for meticulous gadget setup and operators with plenty of expertise. Due to the high cost associated with these kinds of bat detectors, their use and usage by owners of infrastructure is often restricted. Even when bat detectors are used properly, the findings of bat identification might still be questioned due to inconsistencies between various acoustic signal processing software applications [8].



Visual examination is yet another method that may be used to determine whether or not bats are present on agriculture lands. In the subject of computer visual recognition, image classification is one of the essential problems, and it is also one of the tasks that has established substantial successes over the previous decade. Bats can cause damage to the fruits in horticulture. Some species of bats are known to feed on fruit, and when they do so, they may leave behind marks or wounds that can make the fruit unsuitable for sale or consumption. Additionally, bat droppings can also damage fruit and create food safety concerns.

Image categorization methods may primarily be split up into two distinct categories: those that are based on machine learning (ML) and those that are based on deep learning (DL). In order to classify photos into the categories that are needed, ML-based image classification models depend on features that have been meticulously developed. Deep learning-based models use a huge picture dataset to the construction of deep convolutional neural networks (CNN).

II. Literature

In [9], the authors proposed that a new approach of real-time image processing known as the random bounce algorithm (RBA) be used for the vision-based detection of bats and birds. Extracting flight trajectories requires combining the RBA with object tracking in order to do this. The Bat trajectories are collected in a laboratory flight tunnel. The detection accuracy reported in the paper is 96.3%.

In their study, [10] the authors investigated five types of land cover - irrigated rice, hillside rice, secondary vegetation, forest fragments, and continuous forests. Over the period of November and December 2015, the researchers conducted acoustic research on insectivorous bats in and around Madagascar's Ranomafana National Park. The regional bat assemblage included 19 different species, which resulted in 9569 documented bat passes. Additionally, to identify harmful insect species consumed by bats, the authors collected feces from the six most commonly found bat species and performed DNA metabarcoding.

In the paper [11], the authors presented an algorithm that is suited for counting emerging bats in columns that have relatively consistent trajectories and velocities. This technique is based on statistical analysis. Column density is estimated at intervals of 1/30th of a second, and counts are gathered based upon column velocity. Individual bats are not recognised and tracked in this process; rather, counts are accumulated based upon the velocity of the column.

In [12], the authors examined the diets of two species of bats that are anticipated to offer pest management services across the maize belt of the United States: the large brown bat and the eastern red bat (*Lasiurus borealis*) (*Eptesicus fuscus*). In addition, the authors demonstrate that the selection of primers may have an effect on the variety of taxa found, and that recent developments in primer design can lead to improvements in diet detection investigations. They observed that both species of bats consume a wider variety of food than was previously reported by using novel ANML primers to extract prey DNA from faecal debris.

In [13], the authors highlighted the potential for insectivorous bats to act as natural samplers in order to identify (and maybe manage) pest species that are present in crops. Additional research is necessary to identify the entire scope of the rice water weevil's spread, and it is also necessary to examine integrated pest management strategies, including biological control, in order to reduce the populations of the rice water weevil.

In [14], the authors examined if bats eat insect problem species in macadamia plantations, with the added purpose of encouraging farmers to adopt a more integrated pest management strategy to pest control (IPM). The authors analysed bat pellets using fluorescently labelled and species-specific primers to get insight into the diet of insectivorous bats by using a molecular technique (COI). In the Levubu area of Limpopo, South Africa, between July 2015 and April 2017, faeces pellets were collected either from individuals that had been caught or from trays that had been set below roosts and bathhouses. In order to produce species-specific primers and optimise the test, four of the most common



DETECTION OF PESTS IN AGRICULTURE FARMS USING MODIFIED DENSENET DEEP LEARNING MODEL

B.Venkataratnam Research Scholar, Department of Informatics, University College of Engineering(A), Osmania University, Hyderabad, Telangana, India.

Dr. Lakshmi Sreenivasa Reddy Associate Professor, Department of Information Technology, Chaitanya Bharathi Institute of Technology(A), Affiliated to Osmania University, Hyderabad, Telangana, India. Email: [1venkatarathnam@gmail.com](mailto:venkatarathnam@gmail.com), [2dlsrinivasareddy_it@cbit.ac.in](mailto:dlsrinivasareddy_it@cbit.ac.in)

Abstract

Pests can cause significant damage to crops by feeding on the leaves, stems, roots, and fruits. This can lead to reduced crop yields and financial losses for farmers. Deep learning algorithms can be trained to detect pests in images of crops. This can be done by using supervised learning algorithms to classify images as containing or not containing pests, or by using unsupervised learning algorithms to cluster images based on their similarity. Deep learning based pest control has the potential to improve the efficiency and effectiveness of pest control in agriculture, by providing farmers with more accurate and timely information about pests and diseases. This paper presents a deep learning based model for detection of pests in agriculture. The proposed DenseNet model uses dense connectivity between layers, which allows the network to reuse features learned by the earlier layers. This improves the efficiency of the network and reduce the number of parameters. The dense connectivity in DenseNet helps to alleviate the vanishing gradient problem, which is a common issue in deep networks with many layers. This makes it possible to train deeper networks with DenseNet, which can improve the performance.

Keywords: Pest Detection, Pest Control, Deep Learning, DenseNet, Crop Yield.

1. Introduction

Technology in its current form has a tight relationship to the expansion of farming, which is due in large part to the ongoing success of various agricultural reforms. Understanding and exercising authority over information resources are now also essential to the continued growth of modern agriculture. This indicates that the consumption of environmental assets is no longer the only factor that may contribute to the sustainable growth of contemporary agriculture. Because of the ongoing deterioration of the ecological environment over the last several years [1-2], which makes it more unstable, crop diseases and insect pests often have outbreaks that affect a significant number of acres. The widespread occurrence of crop diseases and insect pests may have a direct impact on the quantity as well as the quality of agricultural goods [3], which can ultimately lead to economic losses. In order to prevent losses that aren't absolutely required, it is essential to do research on the management of crop diseases and insect pests.

Due to the fact that a sizeable amount of the crops is destroyed and their quality is diminished as a result of the pest assault, agricultural bug identification is a difficult job for farmers to do [4]. The traditional method of identifying insects has the limitation that it requires highly-trained taxonomists in order to correctly identify insects based on their physical characteristics. Agriculture is in desperate need of more technologically advanced procedures in order to detect pests at an earlier stage and reduce the need for extensive application of potentially harmful pesticides. By draining the sap from the leaves, and other parts of plants, these insects may spread the illness that is caused by sooty mould [5]. The sickness inhibits photosynthesis and causes tissue infections, both of which lead to the loss of crops and a decline in the market value of the commodities generated from such plants, both in terms of the quality and quantity of such products.

When farmers are faced with an infestation of pests, they depend on their own personal experience and expertise to diagnose the problem. Spraying pesticides is the technique of choice for controlling



pests due to a lack of information; this approach is favored since it is both quick-acting and scalable. However, because of growing worries about the environment and public health, there should be a reduction in the usage of pesticides. Spraying just in areas that need it is one of the most essential things that can be done to decrease the usage of pesticides [6]. Spot spraying is reported to be able to minimize the cost of applying pesticides by as much as 90%. This practice may also limit the amount of pesticides that are released into the environment and help protect important insects like honeybees. Finding the precise location of the insect pest is the first step in the process of spot spraying for it.

In most cases, the detection of pests is accomplished via the use of manual procedures, which require a significant amount of effort and are, as a result, fraught with mistake. Because of recent advancements in computer vision applied to precision agriculture, the identification of insect pests and diseases has become an essential component of the collection of data on the development and health of crops [7,8]. Large farms and orchards require the detection of objects at various stages of agricultural development in order to successfully estimate future yields, activate intelligent spraying systems, and regulate autonomous pesticide spraying robots. All of which need the detection of objects at various phases of agricultural development. However, it can be difficult to detect target objects with reasonable accuracy because of factors such as the similarity of shape, the complexity of the background. Nevertheless, the development of technology has made it feasible to identify insect pests via the use of image processing techniques.

Acquisition of visual information and processing of that information by computer vision are essential components of carrying out insect identification and classification. As a result, deep neural networks, also known as DNNs, are often used in computer vision applications for the purposes of mapping complicated connections and carrying out automated feature extractions. Recent developments in graphics processing units, or GPUs, have made it possible to train artificial neural networks that are deeper, leading to faster and more accurate results. DNN object categorization results are impressive. Regression-based and classification-based object detectors are the two main groups of object recognition algorithms. Two-stage object detectors outperform single-stage detectors in accuracy but are slower in inference speed. In this work, the improved DensNet model has been proposed to accurately detect and classify the pests. Fine-tuning the hyperparameters and the layers of the DenseNet model is done in order to apply the transfer learning method to the pest data set.

2. Literature

In [9] authors developed an anchor-free region convolutional neural network (AF-RCNN) for accurate detection of a total of 24 different types of pests. Deep neural networks have made substantial contributions to object categorization and recognition. There are two primary categories of algorithms that perform object recognition, known as two-stage classification-based detectors and single-stage regression-based detectors. In terms of accuracy, the two-stage detectors tend to perform better, but they also have slower inference times compared to the single-stage detectors. In the end, they combine the anchor-free region perceptron neural network (AFRPN) with the fast region convolutional neural network (Fast R-CNN) to create a single network that they call the anchor-free region convolutional neural network (AF-RCNN). This network is used to detect all 24 classes of pests using an end-to-end method. The authors collected a dataset of pest images including 20k images and 24 classes. The proposed model of AF-RCNN produced a mean Recall of 85.1%.

In [10] authors suggested a diagnostic approach for the diagnosis and identification of pests that is based on transfer learning with CNN. The custom dataset consists of 10 different kinds of pests with 500 images. The technique produced an accuracy of 93.84%. The authors compared the results of the transfer learning technique with those obtained from human experts and a conventional neural network model.

The reference [11] provided a viewpoint on the development and current status of remote sensing technology as well as its applications, in particular the control of insect pests and plant diseases. The measuring, recording, and processing of electromagnetic radiation from the target that is located on

Comparison of Periodic Pattern Mining Algorithms on Temporal Datasets

¹Md. Ghouse Mohiuddin, ²Dr. D. L.Sreenivasa Reddy

¹*Asst.Prof. (C), Dept. of Computer Science, Palamuru University, Mahabubnagar.*

²*Associate Professor, Dept. of Information Technology, CBIT, Hyderabad.*

Abstract: The identification of periodic patterns is of great significance in revealing hidden temporal patterns and regularities across various domains, including finance, healthcare, and social networks. As the availability of large-scale temporal datasets continues to grow, the selection of an appropriate periodic pattern mining algorithm becomes crucial for efficient and accurate analysis. The objective of this research paper is to conduct a comparative evaluation of various periodic pattern mining algorithms applied to temporal datasets. The algorithms under consideration include Apriori-based methods such as Modified-Apriori and LPP-Apriori, as well as Tree-based approaches such as LPP Breadth, and LPP-FP Growth. We have assessed the performance of these algorithms across different datasets, focusing on metrics such as Execution Time, LPP Count, and memory usage.

Keywords: LPP-Apriori, LPP-FP-Growth, Modified-Apriori, Periodic Patterns, Timestamps.

1. Introduction

1.1 Introduction to Periodic Pattern Mining

Periodic pattern mining is a data mining technique that focuses on discovering recurring patterns in temporal datasets. Temporal datasets contain data points associated with timestamps or time intervals, representing events or observations that occur over time. By analyzing these datasets, we can discover hidden regularities and temporal dependencies, providing valuable insights into the underlying dynamics and patterns of various phenomena.

The analysis of temporal data has gained significant importance due to the increasing availability of large-scale datasets in diverse domains such as Retail, finance, healthcare, social networks, transportation, and more. These datasets capture time-varying information, which often exhibits periodic or cyclic behaviour. Examples of periodic patterns include daily stock market fluctuations, Market Basket Analysis, weekly social media trends, seasonal disease outbreaks, and monthly electricity consumption patterns.

The discovery of periodic patterns is crucial for understanding the inherent periodicity in temporal data and extracting meaningful knowledge from it. Periodic pattern mining algorithms are designed to search for recurring patterns that repeat at regular intervals or exhibit cyclical behaviour.

1.2 Motivation for comparing periodic pattern mining algorithms on temporal datasets

Comparing periodic pattern mining algorithms on temporal datasets is essential to identify the best algorithm for extracting recurring patterns from time-dependent data. This comparison is motivated by the need for algorithm selection, performance evaluation, scalability, accuracy, generalization, and advancement of the field. Such comparisons enable researchers and practitioners to make informed decisions, enhance algorithm design, and facilitate effective analysis of temporal data in various domains.

1.3 Research Objectives and Methodology

The research objectives are:

- Compare and evaluate periodic pattern mining algorithms on temporal datasets.
- Assess performance, capabilities, and limitations of selected algorithms.
- Determine algorithm suitability for various temporal data and applications.
- Identify strengths and weaknesses in pattern detection accuracy, scalability, and efficiency.
- Contribute to advancing periodic pattern mining research and algorithm design improvements.

Methodology:

To accomplish the research objectives, the following methodology is employed:

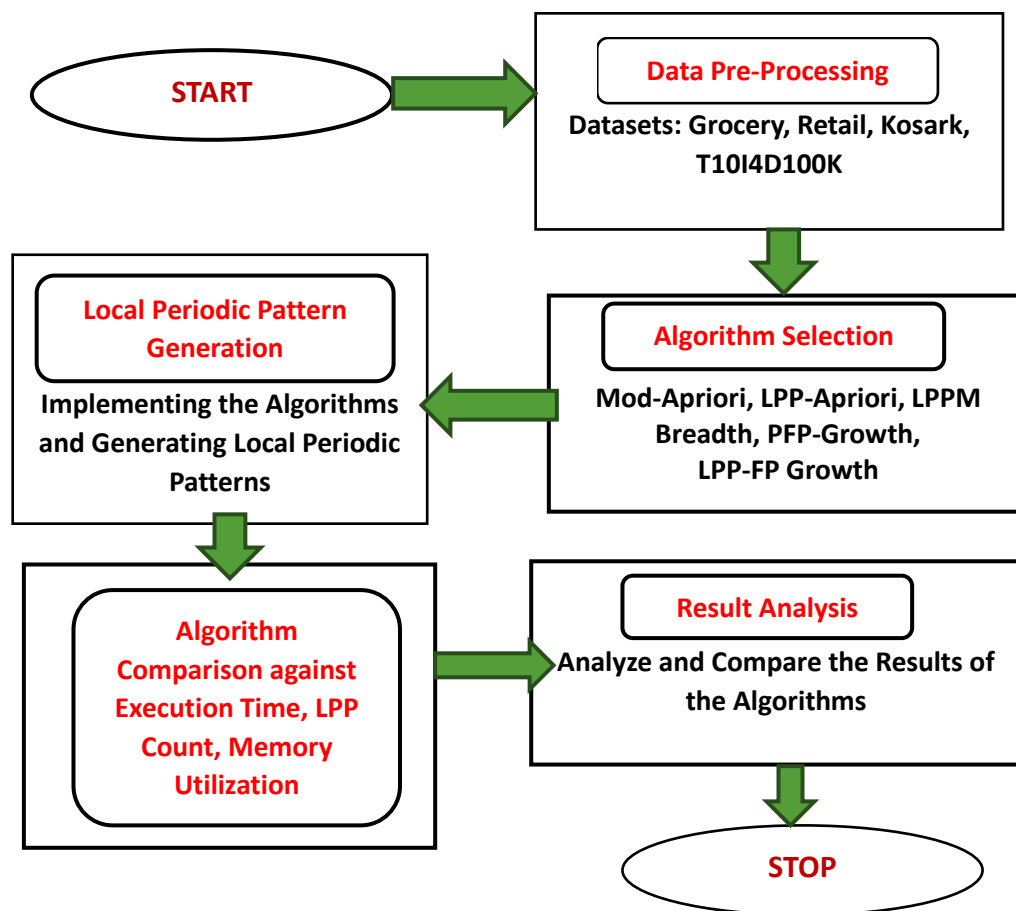


Fig 1.0 Proposed Methodology

By following this methodology, in this research paper we contribute the review of related work in the section 2. In section 3 we present the description of our previously proposed algorithms. Section 4 follows the Results and discussion on comparative analysis of the algorithms. Section 5 concludes the research paper with the scope of future research directions.

2. Related Work

In the field of periodic pattern mining on temporal datasets, several studies have been conducted to compare and evaluate different algorithms. These works have contributed to the understanding of algorithmic performance, scalability, and applicability in various domains. The following is a review of some relevant related works:

Temporal data mining, as explored by Antunes and Oliveira (2001)[1], represents a significant expansion of traditional data mining techniques. By incorporating the temporal aspect, this approach allows for the extraction of more intriguing patterns that are influenced by time. Within temporal data mining, there are two main directions, as highlighted by Roddick and Spilopoulou (1999) [2]. The first direction focuses on uncovering causal relationships among events that are oriented in time. These events are arranged in sequences, where the cause of an event always precedes the event itself. The second direction involves identifying similar patterns within the same time sequence or across different time sequences.

An important expansion of the mining problem involves incorporating a temporal aspect. When a transaction occurs, its timestamp is automatically recorded. In datasets of this nature, certain patterns may exist that are specific to particular time periods rather than spanning the entire dataset's duration. Such patterns can provide valuable insights into customer behaviour. In their work (Ale and Rossi, 2000)[3], Ale and Rossi propose a method for extracting association rules that hold within the lifespan of a given item set, rather than the

A Vision Transformer Approach for Traffic Congestion Prediction in Urban Areas

Publisher: IEEE

[Cite This](#) PDFKadiyala Ramana ; Gautam Srivastava ; Madapuri Rudra Kumar ; Thippa Reddy Gadekallu ; Jerry Chun-Wei Lin ; Mamoun Alazab [All Authors](#)45
Cites in
Papers2626
Full
Text Views

Abstract

Document Sections

- I. Introduction
- II. Related Work
- III. Materials and Methods
- IV. Results and Discussion
- V. Conclusion

[Authors](#)[Figures](#)[References](#)[Citations](#)[Keywords](#)[Metrics](#)[More Like This](#)

Abstract:

Traffic problems continue to deteriorate because of increasing population in urban areas that rely on many modes of transportation, the transportation infrastructure has achieved considerable strides in the last several decades. This has led to an increase in congestion control difficulties, which directly affect citizens through air pollution, fuel consumption, traffic law breaches, noise pollution, accidents, and loss of time. Traffic prediction is an essential aspect of an intelligent transportation system in smart cities because it helps reduce overall traffic congestion. This article aims to design and enforce a traffic prediction scheme that is efficient and accurate in forecasting traffic flow. Available traffic flow prediction methods are still unsuitable for real-world applications. This fact motivated us to work on a traffic flow forecasting issue using Vision Transformers (VTs). In this work, VTs were used in conjunction with Convolutional neural networks (CNN) to predict traffic congestion in urban spaces on a city-wide scale. In our proposed architecture, a traffic image is fed to a CNN, which generates feature maps. These feature maps are then fed to the VT, which employs the dual techniques of tokenization and projection. Tokenization is used to convert features into tokens containing Vision information, which are then sent to projection, where they are transformed into feature maps and ultimately delivered to LSTM. The experimental results demonstrate that the vision transformer prediction method based on Spatio-temporal characteristics is an excellent way of predicting traffic flow, particularly during anomalous traffic situations. The proposed technology surpasses traditional methods in terms of precision, accuracy and recall and aids in energy conservation. Through rerouting, the proposed work will benefit travellers and reduce fuel use.

Published in: [IEEE Transactions on Intelligent Transportation Systems](#) (Volume: 24 , Issue: 4, April 2023)

Page(s): 3922 - 3934

DOI: [10.1109/TITS.2022.3233801](#)

Date of Publication: 09 January 2023 ?

Publisher: IEEE

▼ **ISSN Information:**

[Sign in to Continue Reading](#)

PDF

[Help](#)

Authors	▼
Figures	▼
References	▼
Citations	▼
Keywords	▼
Metrics	▼

IEEE Personal Account

CHANGE USERNAME/PASSWORD

Purchase Details

PAYMENT OPTIONS
VIEW PURCHASED DOCUMENTS

Profile Information

COMMUNICATIONS PREFERENCES
PROFESSION AND EDUCATION
TECHNICAL INTERESTS

Need Help?

US & CANADA: +1 800 678 4333
WORLDWIDE: +1 732 981 0060
CONTACT & SUPPORT

Follow



[About IEEE Xplore](#) | [Contact Us](#) | [Help](#) | [Accessibility](#) | [Terms of Use](#) | [Nondiscrimination Policy](#) | [IEEE Ethics Reporting](#) | [Sitemap](#) | [IEEE Privacy Policy](#)

A public charity, IEEE is the world's largest technical professional organization dedicated to advancing technology for the benefit of humanity.

© Copyright 2025 IEEE - All rights reserved, including rights for text and data mining and training of artificial intelligence and similar technologies.

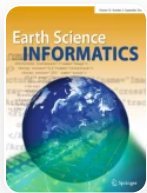
PDF

Help

[Home](#) [Earth Science Informatics](#) [Article](#)

An intelligent optimized cyclone intensity prediction framework using satellite images

RESEARCH Published: 14 March 2023

Volume 16, pages 1537–1549, (2023) [Cite this article](#)[Earth Science Informatics](#)[Aims and scope](#)[Submit manuscript](#)

[C. Kishor Kumar Reddy](#), [P. R. Anisha](#), [Marlia Mohd Hanafiah](#), [Y. V. S. S. Pragathi](#), [B. V. Ramana Murthy](#) & [R. Madana Mohana](#) 

 235 Accesses [Explore all metrics](#) →

Abstract

Weather prediction is the hottest topic in remote sensing to understand natural disasters and their intensity in an early stage. But in many cases, the typical imaging models have resulted in less forecasting rate. Hence, to overcome this problem, a novel buffalo-based Generalized Adversarial Cyclone Intensity Prediction System (BGACIPS) was designed for cyclone intensity prediction using space satellite images. The processed satellite images contained features like rain, snow, Tropical depression (T.Depression), thunderstorms (T.strom), and cyclone. Initially, the noise features were removed in the pre-processing module, and the refined data was entered into the classification layer. Consequently, the analysis of the features was performed, and the intensity of each feature and cyclone stages were identified. Furthermore, the planned design is executed in the python

environment, and the improvement score has been analyzed regarding prediction exactness, mean errors, and error rate. Hence, the proposed novel BGACIPS has a lower error rate and higher prediction accuracy than the compared models.

i This is a preview of subscription content, [log in via an institution](#) to check access.

Access this article

[Log in via an institution](#)

Subscribe and save

Springer+ Basic

€32.70 /Month

Get 10 units per month

Download Article/Chapter or eBook

1 Unit = 1 Article or 1 Chapter

Cancel anytime

[Subscribe now](#) →

Buy Now

[Buy article PDF 39,95 €](#)

Price includes VAT (India)

Instant access to the full article PDF.

Rent this article via [DeepDyve](#)

[Institutional subscriptions](#) →

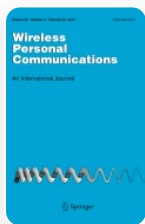
[Home](#) [Wireless Personal Communications](#) [Article](#)

Energy Aware Priority Based Event Routing Protocol Using TDMA Communication for Internet of Things

Published: 06 June 2023


Volume 131, pages 1551–1568, (2023) [Cite this article](#)[Download PDF](#) 

Access provided by CBIT-Library & Information Centre Hyderabad



Wireless Personal Communications

[Aims and scope](#)[Submit manuscript](#)

[Vijaya Krishna Akula](#), [I. Ravi Prakash Reddy](#), [A. Anny Leema](#), [Ramana Kadiyala](#) , [Raman Dugyala](#) & [K. Prasanna](#)

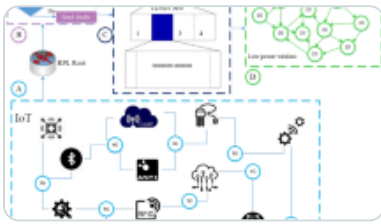
 231 Accesses [Explore all metrics](#) →

Abstract

The Internet of Things (IoT) is a well-known platform for analysing data generated by environmental sensors and instruments. Transporting data from IoT sensor nodes to the cloud is time-consuming due to congestion and energy consumption in IoT networks. As a consequence, in this paper the Priority-Based Event Routing Protocol using TDMA channel to forward the packets in different network traffic constraints. In our proposed work we categorize the normal and priority packet by two properties such as

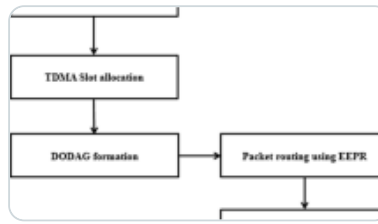
transmission rate and priority then we can use the Time slot based mechanism TDMA protocol to forward the packet in the network based on their time intervals to avoid the congestion and increase the packet forwarding ratio. This approach will increase the network robustness and reduce the congestion. In our work we use the Qualnet Simulator, the experiments showed that the proposed technique performs more and enhances the performance in IoT networks with saving energy consumption by 19.696%, reduces routing overhead by 77%, and reduces end-to-end delay by 50.6% with respect to existing ones.

Similar content being viewed by others



PriNergy: a priority-based energy-efficient routing method for IoT systems

Article | 16 January 2020



Routing Protocol for Low Power and Lossy Network Using Energy Efficient Priority Base...

Article | 24 September 2021



Performance Evaluation of CoAP and MQTT_SN Protocols

Chapter | © 2022

[Use our pre-submission checklist →](#)

Avoid common mistakes on your manuscript.



1 Introduction

The most recent development in communication technology is IoT, where it is a collection of RFID Tags or Sensor nodes [1]. The communication between the sensor nodes is carried through the Wifi, LTE, Wimax and Bluetooth [2,3,4]. The sensor nodes have limited storage, computation and battery power and they can communicate with in shorter distances. IoT devices need to be smart in handling, communicating and transmitting about the occurred event in the environment [5, 6]. The event manager in the IoT environment handles the middleware to publish or subscribe events and it acts as the coordinator between the sensor nodes. Many routing protocols are developed to



Measurement

Volume 211, April 2023, 112636

Sonar glass—Artificial vision: Comprehensive design aspects of a synchronization protocol for vision based sensors

Amutha Balakrishnan ^a✉, Kadiyala Ramana ^b✉, Gokul Ashok ^a✉,
Wattana Viriyasitavat ^c✉, Sultan Ahmad ^d✉, Thippa Reddy Gadekallu ^{e f}✉

Show more ▾

 Share  Cite

<https://doi.org/10.1016/j.measurement.2023.112636> ↗

[Get rights and content](#) ↗

Highlights

- Describes the need for a human-eye-based synchronisation protocol.
- Human visual system is analyzed with the biological aspects of a normal human eye.
- The concepts and technologies of eye tracker development are explained.
- Includes experimental results that attempt to estimate human eye fixation duration.
- Synchronize two sensors to produce artificial vision while human eyes observe an item

Abstract

Supporting visually impaired people during their navigation is a challenging task that involves localization, tracking, navigation, obstacle avoidance, and path guidance. Many researchers have experimented with Sonar, RFID, GPS, NFC, walking sticks, waist-based devices, and even computer vision modules for blind navigation. Using five sonar sensors for obstacle detection with direction and timestamp, we developed Sonar Glass. As humans see in left, right, front, top, and bottom directions based on eye angle and the head pose, the sonar glass is designed to provide obstacle information at the same angle. The head movement of the visually impaired person activates a pair of sensors for each module. Understanding human eye movement mechanisms and developing a synchronization protocol for each pair of visual sensors on sonar glass sitting on both eyes is the main goal of this paper. The major challenge lies in understanding and simulating the human vision mechanism and to realize how the field of Artificial Intelligence can be a contributor in producing technologies for the visually impaired. We are using log-polar transform to simulate human retinal image mapping. The Scale Invariant Feature Transform (SIFT) algorithm has also been implemented. It is the first time that both human eyes can be replaced by vision sensors. After comparing the estimated obstacle information from one sensor pair with that of the other sensors, the voice track is activated. The blind person uses the nearest obstacle information to avoid the obstacle and to extract spatial information about obstacles ahead of the user and provide an early warning. Unique in its design, the sonar Glass's synchronization protocol for a pair of related sensors provides possible object information in that direction. The executions were simulated in MATLAB and the results obtained in real time are found to be promising as the tests were carried out both indoor and outdoor. The sonar Glass

Rider Optimization With Deep Learning Based Image Encryption for Secure Drone Communication

Publisher: IEEE

Cite This

PDF

N. Kannaiya Raja ; E. Laxmi Lydia ; Thumpala Archana Acharya ; K. Radhika ; Eunmok Yang ; Okyeon Yi [All Authors](#)

2 Cites in Papers

653 Full Text Views



Open Access Comment(s)

Under a Creative Commons License

Abstract

Document Sections

- I. Introduction
- II. Related Works
- III. The Proposed Model
- IV. Performance Validation
- V. Conclusion

Authors

Figures

References

Citations

Keywords

Metrics

More Like This

Abstract:

In recent years, drones or Unmanned Aerial Vehicles (UAVs) got significant attention among researchers because of their extensive application in commercial applications, border surveillance, etc. As the conventional terrestrial communication system does not work effectively on heavy calamities namely floods, landslides, cyclones, earthquakes, etc., UAVs can offer a potential solution for inexpensive, rapid, and wireless communication. Despite the drones' benefits in emergency monitoring, security is been a main factor because of the existence of wireless connections for transmission. Therefore, this article introduces optimal deep learning with image encryption-based secure drone communication (ODLIE-SDC) technique. The major intention of the ODLIE-SDC technique lies in the effectual secure communication and classification process in emergency monitoring scenarios. To accomplish this, the presented ODLIE-SDC technique designs a hyperchaotic map-based image encryption technique and its optimal keys are produced by the use of a rider optimization algorithm (ROA). The image classification process is performed encompassing EfficientNet-B4-CBAM feature extraction and enhanced stacked autoencoder (ESAE) classification. Finally, the hyperparameter tuning of the EfficientNet-B4-CBAM technique takes place using the Bayesian optimization (BO) algorithm. The experimental validation of the ODLIE-SDC technique is tested on the AIDER dataset. The comprehensive comparative analysis reported the enhanced performance of the ODLIE-SDC technique over other existing approaches.

In this article, we have developed a new ODLIE-SDC method for effectual secure communication and classification processes in emergency scenarios. The ODLIE-SDC technique ... [Show More](#)

Published in: IEEE Access (Volume: 11)

Page(s): 121646 - 121655

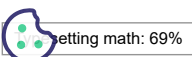
DOI: 10.1109/ACCESS.2023.3324068

Date of Publication: 12 October 2023

Publisher: IEEE

Electronic ISSN: 2169-3536

Funding Agency:



SECTION I.

Introduction

The reliance and usage of drones have been steadily increasing in various fields. This is because of the drones' capability to provide image capture, live-stream and real-time video, in conjunction with the capability to fly and transport goods [1]. Consequently, over 10,000 drones come into existence for commercial usage within the next five years. This is primarily a result of their benefits over commercial helicopters when it comes to budget and costs. Furthermore, technological development allows easier manipulation through smartphones to fly mini-drones rather than using remote controllers. Indeed, the usage of drones is not constrained to commercial and personal purposes [2]. Currently, drones are described as aircraft that fly with no pilots at the controls but are instead supported by automated flight or ground operators without human interference. Now, they are available for different applications and are utilized for crop monitoring, vegetation mapping, habitat destruction assessment, marine fauna detection, and surveillance of crime scenes. In addition, drone mapping has a large number of applications in different fields involving infrastructure inspection, construction, agriculture, and mining [3]. In recent times, the application of drones to humanitarian relief [4], [5]. Precise collection of data might be highly complicated in an emergency due to the lack of coordinated action by different agencies during the emergency [6]. Nevertheless, it was recommended that to enhance efficiency of the emergency management, recent technologies and methodologies are needed to conceptualize systems that integrate a mixture of spatial/temporal-oriented, telecommunication tools, and remote sensing databases. Even though this application was most promising to offer comfort and safety to all, it could bring disastrous results if the drone transmission link was misused and hacked [7].

Being resource-constraint, drones are extremely vulnerable to cyber and physical threats or attacks [8]. The battery and storage capacity of drones is limited and if appropriate management is not provided, it becomes easier to hack the sensors and the chips installed on the drone circuits to attain the information stored. As a result, it is extremely imperative to emphasise the safety requirements for drone transmission as their application increases [9]. The reliance on wireless communication makes drones vulnerable to different attacks. This type of attack might have dramatic effects, involving commercial and non-commercial losses. In that regard, there is a lack of clear understanding on how hacker hijacks a drone and performs their attacks, to crash or even interrupt it [10]. Indeed, drones could also be compromised for malicious purposes.

This article introduces optimal deep learning with image encryption-based secure drone communication (ODLIE-SDC) technique. The presented ODLIE-SDC technique designs a hyperchaotic map-based image encryption technique and its optimal keys are produced by the use of a rider optimization algorithm (ROA). The image classification process is performed encompassing EfficientNet-B4-CBAM feature extraction and enhanced stacked autoencoder (ESAE) classification. Finally, the hyperparameter tuning of the EfficientNet-B4-CBAM technique takes place using the Bayesian optimization (BO) algorithm. The experimental validation of the ODLIE-SDC technique is tested on the AIDER dataset

SECTION II.

Related Works

Alrayes et al. [11] establish an AI-oriented Secure Communication and Classification for Drone-Enabled Emergency Monitoring System (AISCC-DE2MS). This system mostly utilizes encrypt and classifier methods for emergency conditions. Primarily, the proposed technique utilizes an artificial gorilla troops optimizer (AGTO) technique with an ECC-related ElGamal Encryption system for accomplishing security. For the emergency condition classifier, the proposed scheme includes a DenseNet extraction feature, penguin search optimizer (PESO) based hyperparameter tuning, and LSTM-based classifier. Rabieh et al. [12] present a proxy re-encryption-based sharing method for enabling 3rd party for accessing only restricted videos with no need for an original encrypted key. The expensive pairing functions in proxy re-encrypt could not be utilized for allowing quick access and delivery of surveillance video for 3rd party. The basic management was controlled by a trusted control centre that performs as a proxy to re-encryption the data.

Ingle et al. [13] examined an earlier fusion-based video synopsis. Primarily, the authors fused the 2-D camera and 3-D LIDAR point cloud data; secondarily, the authors executed abnormal object recognition utilizing customized sensor on the integrated dataset and lastly extracting only the basic information to create a synopsis. In [14], the authors examine that UAVs are utilized for distributing virus-related tests to probal sick patients. A new technique which the authors present is to utilize the present drone structure for performing this task, whereas drones maintained and worked by distinct private and public entities can be retrofitted for the distribution of necessities in crises. Miao et al. [15] introduce a drone-supported smart air agent from a 6-G edge fusion scheme. Primarily, the energy-effective dynamic routing scheme dependent upon a joint air-ground control optimizer was planned for improving fusion sensing efficacy and extending

RESEARCH ARTICLE


 OPEN ACCESS

Received: 19-10-2023

Accepted: 28-10-2023

Published: 05-12-2023

Citation: Radha M, Kiran MA, Ravikumar C, Raghavendar K (2023) A Comparative Study of Machine Learning Models for Early Detection of Skin Cancer Using Convolutional Neural Networks. Indian Journal of Science and Technology 16(45): 4186-4194. <https://doi.org/10.17485/IJST/v16i45.2658>

* **Corresponding author.**chrk5814@gmail.com**Funding:** None**Competing Interests:** None

Copyright: © 2023 Radha et al. This is an open access article distributed under the terms of the [Creative Commons Attribution License](https://creativecommons.org/licenses/by/4.0/), which permits unrestricted use, distribution, and reproduction in any medium, provided the original author and source are credited.

Published By Indian Society for Education and Environment ([iSee](https://www.indjst.org/))

ISSN

Print: 0974-6846

Electronic: 0974-5645

A Comparative Study of Machine Learning Models for Early Detection of Skin Cancer Using Convolutional Neural Networks

Marepalli Radha¹, Medikonda Asha Kiran², Ch Ravikumar^{3*}, K Raghavendar⁴

¹ Associate professor, Department, of Computer Science and Engineering, CVR College of Engineering, Mangalapally, Hyderabad, 501510, India

² Assistant Professor, Department of Artificial Intelligence & Machine Learning, Chaitanya Bharathi Institute of Technology, 500075, Hyderabad, India

³ Assistant Professor, Department of Artificial Intelligence & Data Science, Chaitanya Bharathi Institute of Technology, 500075, Hyderabad, India

⁴ Assistant Professor, Department of Computer Science and Engineering, Teegala Krishna Reddy Engineering College, Meerpet, Hyderabad, 500097

Abstract

Objectives: The purpose of this research is to enhance the early diagnosis of skin cancer, with a particular emphasis on melanoma, by utilizing machine learning methods such as transfer learning and Convolutional neural networks (CNNs). The main objective is to differentiate between benign and malignant skin lesions in order to improve the chances of survival for this potentially lethal illness. **Method:** The SIIM-ISIC 2020 Challenge Dataset is a useful resource for comparing machine learning models that use CNNs to identify skin cancer early on. Including 33,126 DICOM images from a variety of sources, including Memorial Sloan Kettering Cancer Center, Hospital Clinic de Barcelona, and Medical University of Vienna, this large dataset was published by ISIC in 2020. A rigorous, well-structured technique is essential to guarantee the reliability and validity of the findings. For every model, the study uses a 70/30 train-test split, providing a thorough and exacting method for assessing each model's performance in this crucial area. **Findings:** This study emphasizes the value of early skin cancer identification. Significant differences are noted in the 5-year survival rates of the various stages of melanoma, with stage 1 having a 90-95% survival rate and stage 4 having just a 15-20% survival rate. Machine learning algorithms' potential to distinguish between benign and malignant skin lesions in images holds the promise of improving early detection and treatment outcomes. **Novelty:** This research introduces innovation by concentrating on melanoma and blending cutting-edge deep learning methods with the pressing requirement for enhanced skin cancer diagnosis. The distinctive contributions of this work encompass novel model architectures, data augmentation techniques, and innovative evaluation metrics. These innovations set this approach apart from existing methods, providing a fresh avenue for early diagnosis and underscoring the value of continuous research

and data collection in the critical realm of cancer detection.

Keywords: Melanocytic Lesions; Epidermal Lesions; Image Feature Extraction; Skin Cancer; And Transfer Learning

1 Introduction

The rising global incidence of skin cancer, particularly melanoma, presents a critical public health challenge. Skin cancer is the most commonly diagnosed form of cancer, affecting approximately one in three individuals⁽¹⁾. Early detection is paramount to improving patient outcomes, yet there are significant research gaps in this field.

Melanoma, squamous cell carcinoma, and basal cell carcinoma are the primary skin cancer categories. While melanoma is less prevalent, it carries a disproportionate risk and accounts for a significant number of skin cancer-related fatalities⁽²⁾. Early detection of melanoma is essential for effective treatment, making it a top priority for both researchers and healthcare professionals.

Recent studies have revealed limitations in dermatologists' accuracy in detecting early-stage skin cancer, underscoring the need for improved diagnostic methods, including those based on artificial intelligence⁽³⁾. Deep learning, particularly Convolutional Neural Networks (CNNs), has shown promise in automating skin cancer detection by identifying subtle details and patterns that may elude the human eye.

However, existing research has not provided a comprehensive comparative analysis of machine learning models, leaving critical research gaps. This study aims to address these gaps by evaluating the accuracy, sensitivity, specificity, and area under the receiver operating characteristic (ROC) curve of various machine learning models, particularly in the context of melanoma detection. By shedding light on both the strengths and limitations of these models, this research seeks to contribute to the development of more precise and user-friendly diagnostic tools, ultimately enhancing patient outcomes and reducing the global incidence of skin cancer.

1.1 Models

a) CNN model: Convolutional Neural Networks are essential in image analysis, as they can automatically learn hierarchical representations from data⁽⁴⁾.

b) VGG16 model: VGG16 is well-suited for images with simple features, making it valuable for skin cancer analysis⁽⁵⁾.

c) ResNet-50: Its deep architecture allows it to extract complex image features, overcoming the vanishing gradient problem⁽⁶⁾.

d) AlexNet: AlexNet's use of ReLU activation in hidden layers accelerates the training process and prevents overfitting, and it is a model trained on the ImageNet dataset, making it valuable for skin cancer image classification⁽⁷⁾.

These models, especially those employing transfer learning, possess unique capabilities for feature extraction, potentially improving skin cancer detection⁽⁸⁾.

1.2 Research Gap

Despite significant medical advancements, skin cancer, particularly melanoma, remains a serious and potentially lethal disease. This study addresses research gaps by introducing an innovative approach to early skin cancer detection, focusing on epidermal and Melanocytic lesions. The current research landscape lacks a comprehensive comparative analysis of machine learning models, leaving critical gaps. This study aims to enhance early diagnosis and treatment outcomes for a common and potentially lethal disease by utilizing state-of-the-art deep learning techniques to distinguish between benign and malignant lesions from photos.

RESEARCH ARTICLE



Optimization of Facial Images to Predict Gender Using HDSON and Bidirectional Associative Memory

 OPEN ACCESS

Received: 26-12-2022

Accepted: 03-02-2023

Published: 02-05-2023

Shoba Rani Salvadi^{1*}, D Nagendra Rao², S Vathsai³¹ Research scholar, Jawaharlal Nehru Technological University, Hyderabad, Telangana, India² Professor and Principal, Abhinav-Hitech College of Engineering, Moinabad, Telangana, India³ Retired DRDO Scientist

Citation: Salvadi SR, Rao DN, Vathsai S (2023) Optimization of Facial Images to Predict Gender Using HDSON and Bidirectional Associative Memory . Indian Journal of Science and Technology 16(17): 1276-1283. <https://doi.org/10.17485/IJST/v16i17.2481>

* **Corresponding author.**

reddymallashobarani2@gmail.com

Funding: None

Competing Interests: None

Copyright: © 2023 Salvadi et al. This is an open access article distributed under the terms of the [Creative Commons Attribution License](https://creativecommons.org/licenses/by/4.0/), which permits unrestricted use, distribution, and reproduction in any medium, provided the original author and source are credited.

Published By Indian Society for Education and Environment ([iSee](https://www.indjst.org/))

ISSN

Print: 0974-6846

Electronic: 0974-5645

Abstract

Objective: To enhance the Gender prophecy by employing facial images using imaginative algorithm and to resolve real time applications. **Method:** Initially, we make use of shared deep octonion network and the Octonion-Valued Neural Network (OVNN) to develop a generic framework for a Hybrid Deep Sparse Octonion Network (HDSON). Sparse Coding Octonion data Algorithm (SCOA) is exploited to depict the face images up to seven color channels and improves the weight of HDSON. Furthermore, to take advantage of the maximum storage we make use of Bidirectional Associative Memories (BAM). **Findings:** The proposed approach resolves both the issues of depiction of the facial image and its storage, since the present study combines the characteristics of SCOA to improve HDSON weight and BAM to enhance the storage. Moreover, the present study is simple to apply and effective in real time applications. **Novelty:** The proposed approach can be used in paramilitary to minimize cross border terrorism; in addition, the presented scheme can enhance the probability of child detection and may help local police to a large extent.

Keywords: Automatic Gender Classification; BAM; DCN; HDSON; Octonion; SCOA; OVNN

1 Introduction

Technological developments in medical science grows rapidly; as a result, it becomes very complicated to identify the sex from facial image. So, to recognize the sex from facial image will become a vital problem and leads security issues. Consequently, this issue switches the attitude of signal and image processing researchers to exploit the problem; numerous theories and model have been developed to mitigate these issues. However, most approaches used complex image processing algorithms and make use neural networks to study the image performance and increases the delay thereby reduces the overall throughput.

Characteristics of the human face may be used to get information about a person's age, gender, emotional state, and ancestry^(1,2). Among these characteristics, age and gender recognition can be particularly useful, where gender must be determined by

their faces, but there are still various issues with age and gender credentials that pose open difficulties. Despite being state-of-the-art, predictions from unfiltered real life face photos have not yet met the demand for commercial and real time applications. Hence, it is crucial to have a reliable and precise system for age and gender identification, since this research focuses on gender prediction based on data collected and openly available datasets^(3,4). It has been stated that many different in real time neural network models have been built, as a whole⁽⁵⁾, these models may be split into two classes: shallow and deep. Non-deep models are typically built using a multilayer perception module, which makes training challenging with the real-valued back propagation (BP) technique. One can roughly build deep models using pretrained methods like deep belief nets^(6,7), deep auto-encoder⁽⁸⁾, LeNet-5, Alex Net, Inception etc.⁽⁹⁾.

Real Convolution neural network (RCNN) has widespread success in various applications, however correlations between convolution kernels are rarely considered, and i.e., no specific link or connection is created among convolution kernels. Moreover, real-value recurrent neural networks (Real RNNs) acquire the correlations by connecting and learning the weights of convolution kernels and the training difficulty is much increased.

Moumen et al⁽¹⁰⁾ used Complex algebra and quaternion algebra to increase performance during model the connections between convolution kernels. Subsequently, lot of effort is required to design neural networks to work in the complex, quaternion, and octonion spaces, which are outside the existing domain. In⁽¹¹⁾ a deep learning model is used to determine a gender based on photographs of their retinas. In these approach authors used multiple stored images to train the model. However, to predict a person’s gender based on the image requires a good explanatory power, which is not currently available, since the doctors currently have lack of information about gender-specific differences in retinal features. It is possible that the suggested deep learning may allow for the automatic discovery of new images and illness biomarkers under the direction of clinicians. In^(12,13) authors discussed how age and gender can be determined using CNN, cell phone and machine learning technologies, however the authors need strong CNN to be available in the cell phone which may not be optimum with the currently available hardware. Katna et al⁽¹⁴⁾ used machine learning to identify gender. The suggested technique achieved an accuracy of 81.2% for gender prediction. Various approaches⁽¹⁵⁻¹⁷⁾ based on octonion-valued neural network (OVNN) have been presented to investigate the image property. The two approaches run on static data, hence may not be the optimum solution for real time application. Xiao et al⁽¹⁸⁾ introduces fractional-order octonion-valued bidirectional attention mechanism. The system is too complex and reduced the overall throughput of the system.

In this paper an enhanced algorithm called hybrid of HDSON and Bidirectional Associative Memory Model(HHBM). In this approach we make use of HDSON to consider the facial image and BAM to improve the storage capacity of the system. Consequently, a hybrid model is developed having both the properties of HDSON and BAM and improves the performance of the existing systems⁽¹⁵⁻¹⁷⁾.

The rest of the paper is organized as follows, in section 2 we are presenting our proposed model, section 3 presents results and discussion and finally we are concluding our paper in section 4.

1.1 Proposed Model

The proposed model presented has the following folds.

- **Sparse coding step:** The complex and quaternions sparse coding difficulties are generalizations of the problem posed in⁽¹⁹⁾. After multiplication, the generated matrix is represented in Table 1 having orthogonal columns. The study acquired a structured coefficient matrix to maintain the orthogonality property and the correlation between spectral channels. Contemporary, it can still rely on the tried-and-true linear correlation method across color channels to keep colors accurate. Compared to the standard concatenation model, this method enhanced connection between the image channels. It has been observed that the '1-norm minimization issue for octonionic signals may be transformed into a genuine convex optimization problem. To minimize the issue modified OMP for the octonion settings is employed. The presented algorithm chooses the atom d_k at each step k that minimizes the residual $\|r^k\|_2^2 = \|r^{k-1} - d_k x_k\|_2^2$, where $r^0 = y$

In the context of an octonion, it has been proven that this is identical to picking the atom with the highest correlation with the residual vector $\langle r^k, d_k \rangle$. Explicitly, the active dictionary is created as $D^k = (D^{k-1}, d_k]$ by selecting the atom that yields the highest absolute value in the inner product with the residual. Where, 'x' is the coding coefficient to minimize the norm $\|y - D^k x\|_2^2$. The Octonion-based linear least-squares problems are hard to solve; therefore, the study employs a new technique that involves changing the minimization issue into a genuine vector minimization problem represented in⁽¹⁹⁾ and can be represented as

$$\|y - D^k x\|_2^2 = \|v(y - D^k x)\|_2^2 = \|v(y) - \mathcal{X}(D^k) v(x)\|_2^2 \tag{1}$$

RESEARCH ARTICLE


 OPEN ACCESS

Received: 17-02-2023

Accepted: 12-03-2023

Published: 02-05-2023

Citation: Salvadi SR, Rao DN, Vathsal S (2023) Visual Mapping for Gender Identification from Facial Images using BAM and DON. Indian Journal of Science and Technology 16(17): 1295-1301. <https://doi.org/10.17485/IJST/v16i17.349>

* Corresponding author.

[reddymallashobarani2@gmail.com](mailto:redmashobarani2@gmail.com)**Funding:** None**Competing Interests:** None

Copyright: © 2023 Salvadi et al. This is an open access article distributed under the terms of the [Creative Commons Attribution License](https://creativecommons.org/licenses/by/4.0/), which permits unrestricted use, distribution, and reproduction in any medium, provided the original author and source are credited.

Published By Indian Society for Education and Environment (ISEE)

ISSN

Print: 0974-6846

Electronic: 0974-5645

Visual Mapping for Gender Identification from Facial Images using BAM and DON

Shoba Rani Salvadi^{1*}, D Nagendra Rao², S Vathsal³¹ Research scholar, Jawaharlal Nehru Technological University, Hyderabad, Telangana, India² Professor and Principal, Abhinav-Hitech College of Engineering, Moinabad, Telangana, India³ Retired DRDO Scientist

Abstract

Objective: To Develop an intelligent and innovative method to categorize the Gender by focusing facial images. **Method:** We integrate the characteristics of Bidirectional Associative Memory (BAM) and Deep Octonion Networks (DON) to enhance the Gender detection in real time applications. The developed hybrid model is called Visual Mapping of BAM and DON (VMBAD). To validate the projected system, we make use of 4000 images and 126 different subjects as a data set to train the proposed approach and simultaneously compare our results with the existing methods using the same data set. **Findings:** The projected technique improves the performance of the system by 3 -5 % in terms of sensitivity, accuracy, and precision when compared with the existing approaches (vide figures 4-7). **Novelty:** The designed method enhances both the accuracy and precision of image by nearly 4% and 2% respectively when compared with the reported work.

Keywords: Artificial Intelligence; Bidirectional Associative Memories; Gender Identification; Deep Octonion Networks; Deep Quaternion Networks

1 Introduction

Many methods of gender detection have been suggested to improve the identification. However, no or very less attention was given toward a hybrid model of image algorithm and storage to improve the training of the desired identification system. Because conventional methods of artificial intelligence and image processing algorithms were employed to verify the depth of the image, as a result, some methods reduce overall output due to more delay and some experienced storage problems. To overcome the storage gap and analyze images more deeply, a model has been suggested that not only mitigates the gaps but also improves the performance of the identification system.

In the present environment, there has been a rise in the usage of hyper complex values in digital signal processing to study complex signals⁽¹⁾. Many commonly used algorithms, ranging from simple real-valued to hyper complex algorithms are employed⁽²⁻⁴⁾ to analyze the image characteristics. In⁽⁵⁻⁸⁾ the authors exploit octonion linear canonical transform and Quaternion based algorithm to investigate the mathematical analysis of an image signal. Takahashi et al⁽⁹⁾ suggested Remarks on Octonion-valued Neural Networks to control the Robot applications. Cariow and

Cariowa,⁽¹⁰⁾ proposed a quaternion-valued linear convolution algorithm to decrease the arithmetic complexity. In this study the author’s make use of notion that quaternion multiplication can be expressed as a matrix-vector product in the synthesis of the procedure mentioned. For the classification of data Wu et al⁽¹¹⁾ employed general outline for DON and the fundamental building elements of DON to initialize the weight and normalization of octa- norm algorithm. Rasheed et al⁽¹²⁾ presented a gender identification model based on complete face, however the authors didn’t consider changing image characteristics and it may not be valid in a real time application. Rani and Pushpalatha⁽¹³⁾ presented an approach to improving the application of IOT using a distributed mining algorithm. However, this may not be helpful to recognize the gender.

Garai et al⁽¹⁴⁾ suggested a method to identify the gender based on Gate technology. However, this is a binary classification problem, whereas age estimation is a regression problem and may not be the optimum solution for real time applications. Abirami et al⁽¹⁵⁾ employed CNN to identify the age and sex from same face, since the approach showed less accuracy and precision and didn’t meet the requirement of gender identification in real time applications. The authors of^(16–18) suggested an Artificial intelligence based methods to analyze age group and gender of a human the methods have more delay and reduces overall throughput. Swaminathan et al⁽¹⁹⁾ proposed a technique in which numerous Machine Learning Classification Procedures on Facial image has been considered to identify the gender. However, due to additional features of machine learning, the algorithm has become more complex, which reduces the overall performance of the desired system. Xiao et al⁽²⁰⁾ proposed a fractional-order octonion-valued to improve gender identification property. However, the system is too multifaceted and compact the overall performance of the system.

In this paper, visual mapping of Bidirectional Associative Memory and Deep Octonion Networks have collectively employed to optimize the gender identity and is called Visual Mapping of BAM and DON (VMBAD). Bidirectional Associative Memory improves the access speed and storage capacity of the desired system. Moreover, the Deep Octonion Network Algorithm utilizes the benefits of Bidirectional Associative Memory by analyzing the image very deeply to enhance the Gender determination process from a facial image in the Augmented Reality (AR) data base.

The remaining sections of the paper is systematized as section 2 describes the proposed approach. Section 3 enlightens about results and discussion, and finally the conclusion of the paper has been presented in section 4.

2 Methodology

2.1 Proposed Approach

The heart of the proposed approach is the Octonion values and can be calculated as

$$O_V = \sum_{i=0}^7 x_i e_i \in 0 \tag{1}$$

Where ‘0’ indicates the Octonion sum ‘ x_i ’ $\in R$ and represents the real sum, in addition to this

$e_0 = 1$ and $e_i, i = 1, 2, 3 \dots, 7$ represents the seven pretended entities to model the rule and has to follow equation (2)

$$\begin{cases} e_i^2 = -1 \\ e_i e_j = -e_j e_i \quad \forall i \neq j \neq k : 1 \leq i, j, k \leq 7 \\ (e_i e_j) e_k = -e_i (e_j e_k) \end{cases} \tag{2}$$

The above-mentioned analysis only finds characteristics of the image and didn’t provide any storage to compare the end result. So, to eliminate the storage dilemma in Octonion analysis we introduced an octonion-valued bidirectional associative memory to enhance the gender probability detection.

2.2 Bidirectional associative octonion-valued memories

The bidirectional Associative memory is commonly used in neural networks to store the training algorithms and the processor compatible with the memory unit. In this paper the bidirectional Associative memory is employed to store the entire training data of an image and enhances the probability of gender detection using Octonion approach.

Once the octonion data are stored using bidirectional associative memories, it must be retrieved for identification of gender. The identification process is carried out by one of the methods of Octonion approach called deep octonion network.

2.3 Deep octonion networks

In this we make use of numerous mathematical models such as batch normalization module, convolution module and octonion initialization technique of Octonion networks to analyze the image and improves the performance of the designed system.

An Statistical Analysis of Gated Recurrent Unit Based Predictive Modelling for Dynamic Obstacle Avoidance in Autonomous Aerial Vehicles

¹Dr. Nisha Wankhade, ²Dr Srilatha Pulipati, ³Dr. Manoj Vasantrya Bramhe, ⁴Dr. R. B. Raut, ⁵Dr. Snehlata Dongre, ⁶Dr. Piyush K. Ingole

¹Assistant professor, Department of information Technology, Yeshwantrao Chavan College of Engineering, Nagpur, Maharashtra, India

nisha.ycce@gmail.com

²Associate Professor, Department of AI & DS, Chaitanya Bharathi Institute of Technology, Hyderabad , Telangana, India.

pulipatisrilatha_aids@cbit.ac.in

³Professor, Department of Information Technology, St. Vincent Pallotti College of Engineering and Technology, Nagpur, Maharashtra, India.

mbramhe@stvincentngp.edu.in

⁴Associate Professor, Department of Electronics and Communication Engineering, Shri Ramdeobaba College of Engineering and Management, Nagpur, Maharashtra, India

rautrb@rknc.edu

⁵Department of Computer Science and Engineering, G H Raisoni College of Engineering, Nagpur, Maharashtra, India.

dongre.sneha@gmail.com

⁶Department of Computer Science and Engineering, Jhulelal Institute of Technology, Nagpur, Maharashtra, India.

piyush.ingole@gmail.com

Article History:

Received: 24-03-2024

Revised: 12-05-2024

Accepted: 25-05-2024

Abstract:

More and more, autonomous aerial vehicles (AAVs) are being used for a wide range of tasks, such as monitoring, search and rescue, and item delivery. One important part of AAVs' liberty is that they can safely move through changing surroundings. To be successful at dynamic obstacle avoidance, you need to be able to guess how objects will move in real time using good predictive modeling. In this work, we suggest a new way to use Gated Recurrent Units (GRUs) for predictive models in AAVs' dynamic obstacle avoidance. This is a type of recurrent neural network (RNN) called the GRU. It works well for handling linear data and has shown promise in many areas, such as natural language processing and time series prediction. Through our method, we use GRUs to predict how dynamic objects move by looking at past data. The model projects where the obstacles will be in the future based on where the AAV is now and where they have been in the past. The AAV can change its direction to avoid hitting things by constantly changing its predictions in real time. We use a collection of synthetic AAV flights in changing settings to train the GRU model. The file has details about the AAV's location, speed, and direction, as well as the locations of moving objects. We preprocess the data to get the important traits out of it and make it more uniform so that the training process works better. Then, we train the GRU model using both past data and real-world information about where obstacles will be in the future. We use a set of measures, such as impact rate, forecast accuracy, and processing speed, to judge how well our method works. The outcomes show that the GRU-based predictive modeling method greatly enhances dynamic obstacle avoidance performance when compared to conventional approaches. The AAV that has our model can successfully

move through complex settings with changing objects, staying on a smooth path without running into any problems.

Keywords: Autonomous Aerial Vehicles, Dynamic Obstacle Avoidance, Predictive Modeling, Gated Recurrent Units, Real-time Decision-making.

1. Introduction

In the past few years, autonomous aerial vehicles (AAVs) have gotten a lot of interest because they could change many fields, such as transportation, monitoring, and farmland. One of the biggest problems with using AAVs in real life is making sure they can safely move through changing surroundings. It is very important for the safety and speed of AAV operations to avoid accidents with moving objects like other vehicles, people, and animals. This is called dynamic obstacle avoidance. Traditional ways of making AAVs avoid moving obstacles depend on rules or paths that are set up ahead of time using static maps or sensor data. These methods may work in some situations, but they often fail to adapt to settings that are uncertain or change quickly [1]. Also, they might not be able to handle how multiple moving objects interact with each other in complicated ways. To deal with these problems, academics have looked to machine learning methods, especially prediction modeling, to help AAVs guess how moving objects will affect their paths and plan their flights accordingly. In this study, we suggest a new way to use Gated Recurrent Units (GRUs), a type of recurrent neural network (RNN), to predict how AAVs will avoid obstacles in the real world. There are several reasons why using GRUs is better than using standard methods. First, GRUs are great for modeling sequential data, which makes them perfect for showing how the movement patterns of moving objects change over time. Second, GRUs can find complicated trends in data, which lets them adapt to a lot of different settings that change quickly [2]. Lastly, GRUs use little computing power, which makes them good for real-time apps that need to have low delay. This paper gives a thorough look at our method, covering the creation of the GRU-based predictive model, the preparation of the input data, the training process, and the evaluation metrics used to check how well the model worked. We also show testing results that show how well our method works in a virtual AAV setting. The rest of this paper is organized in this way. In Section 2, we talk about similar work that has been done in the area of dynamic object avoidance for AAVs. In Section 3, we talk about the structure of our GRU-based prediction model and the steps that were taken to prepare the raw data for it. In Section 4, we talk about the training process and the setting we used to test how well the model worked. In Section 5, we show the outcomes of our tests and contrast them with the standard methods. Finally, Section 6 wraps up the study with an outline of our results and suggestions for more research.

2. Related Work

Predictive modeling for dynamic obstacle avoidance in autonomous aerial vehicles (AAVs) is an important area of study that aims to make AAV activities safer and more efficient in complex settings. Several similar works have looked at different ways to solve this problem by using predictive modeling to successfully predict and avoid moving objects. This part talks about the most important study efforts in this area, focusing on their methods, main results, and limits. One way to use predictive modeling to help AAVs avoid moving objects is to guess their paths based on how the obstacles are moving. For instance, [10] suggested a way to use a Long Short-Term Memory (LSTM) neural network to guess

A CAD Method for Early Detection of Glaucoma Employing CNN from Fundus Photographs

Deepak Parashar^{*1}, Pulipati Shrilatha², Kachapuram Basava Raju³, Kanhaiya Sharma⁴

Submitted: 25/01/2024 Revised: 03/03/2024 Accepted: 11/03/2024

Abstract: Early detection and diagnosis of glaucoma, a crippling eye illness that causes irreversible vision loss, are essential for effective care. In this study, convolutional neural networks are used to diagnose glaucoma in a novel way (CNNs). The methodology incorporates local binary pattern (LBP) for image preprocessing using a rigorously curated dataset of Fundus Photos, which includes 1450 images with 899 cases of glaucoma and 551 non-glaucomatous images. Ten layers make up the proposed CNN architecture, including a Conv2D layer for feature extraction, a MaxPooling2D layer for down sampling, a Flatten layer for vectorization, and seven Dense levels for classification. By detecting glaucoma with an accuracy of 99% during training and a loss of 4%, this CNN model has demonstrated outstanding performance. On the test dataset, the model achieves a test loss of 30% and an accuracy of 94%. Confusion matrix, precision, recall, F1-score, support, Matthew's correlation coefficient (MCC), and Area Under the Receiver Operating Characteristic Curve are just a few of the metrics used to assess this model (AUC). The model's strong performance in evaluation measures, along with its high accuracy and low loss, point to its potential for early glaucoma detection and, consequently, its critical role in maintaining vision and improving patient treatment. In order to achieve the goal of prompt diagnosis and treatment, this research advances automated glaucoma detection systems.

Keywords: Glaucoma, CNN, Precision, F1 Score, Recall, Matthews correlation, Local binary pattern

1. Introduction

If undiagnosed and untreated, glaucoma is a dangerous eye ailment that can cause irreversible vision loss. Convolutional Neural Networks are one of the cutting-edge techniques for glaucoma early detection [1-7]. Early detection of glaucoma is essential for preventing additional damage (CNNs). Convolutional Neural Networks are a family of deep learning models that were created primarily for image-related tasks [8]. Since glaucoma detection requires the processing of retinal pictures and scans of the optic nerve head, these models are excellent for this task. An overview of glaucoma detection with CNNs is provided below: The Importance of Glaucoma Detection. A collection of eye conditions known as glaucoma generally result from elevated intraocular pressure and damage the optic nerve. It is one of the main causes of permanent blindness in the world. Vision loss can be avoided with early detection and prompt treatment. Retinal imaging in glaucoma detection: Ophthalmologists use a variety of diagnostic procedures, such as retinal imaging, to identify glaucoma. OCT and fundus photography, which take high-resolution pictures of the retina and the optic nerve head, are two typical methods [9-13]. CNNs in Medical Image Analysis: CNNs have completely changed the way that

medical image analysis is done. They work effectively for jobs like spotting anomalies and diseases in medical imaging because they excel at automatically learning pertinent aspects from photos. CNNs' benefits in glaucoma detection: Traditional image processing methods may find it difficult to automatically learn and extract complex features from retinal pictures using CNNs. They offer a data-driven methodology that enables the model to evolve and enhance its performance over time. CNN-based systems' rapid picture processing speed makes it possible to efficiently screen lots of patients [14]. Increased intraocular pressure and eventual vision loss are typical symptoms of glaucoma, a chronic and progressive eye condition that affects the optic nerve. It is the main contributor to permanent blindness globally. Early identification is critical for optimal care and the preservation of vision because glaucoma frequently develops gradually and without obvious symptoms in its early stages. Individuals with glaucoma suffer from damage to the optic nerve, which is in charge of carrying visual information from the eye to the brain. This leads to a progressive loss of peripheral vision and, eventually, central vision. Glaucoma can cause serious vision loss or perhaps total blindness if ignored. Therefore, early glaucoma diagnosis is essential to start the right therapy and stop future vision loss. Convolutional Neural Networks (CNNs) have demonstrated astounding efficiency in a range of medical imaging applications, including the identification of glaucoma. CNNs are a class of deep learning models that are especially made for processing visual data, making them perfect for examining medical images like retinal scans, which are essential for glaucoma

^{1,4}Symbiosis Inst. of Tech., Symbiosis International University Pune, India
ORCID ID : 0000-0002-4189-4560, 0000-0002-5810-801X

²AI & DS Dept., Chaitanya Bharathi Inst. of Tech., Hyderabad, TS, India
ORCID ID : 0000-0003-0181-2943

³AI Department, Anurag University, Hyderabad, TS, India
ORCID ID : 0000-0002-0192-0592

* Corresponding Author Email: parashar.deepak08@gmail.com

diagnosis. We can automate the process of analyzing these photos and help medical practitioners identify glaucoma in early stages by utilizing CNN [7]. In this paper, we explore the use of CNNs for retinal imaging-based glaucoma identification. We investigate how these sophisticated neural networks can extract complex patterns and information from retinal pictures to assist in the detection of glaucoma-related symptoms. We want to use CNNs to build a reliable and effective automated system that could revolutionise glaucoma screening and help with early detection and proactive management of this illness that could cause blindness. The remaining sections are given as. In Section 2, we described literature review. Problem formulation given in Section 3. Methodology provided in Section 4. Results are discussed in Section 5. Conclusion given in Section 6.

2. Literature Review

In this section we will go through several published research work based on similar domain. Explainable Machine Learning Model for Glaucoma Diagnosis and Its Interpretation Sejong Oh, Yuli Park, Kyong Jin Cho, and Seong Jae Kim³. The study aims to create a machine learning model for diagnosing glaucoma and provide an explanation for its predictions. Clinical data, including visual field tests, retinal nerve fiber layer optical coherence tomography (RNFL OCT) tests, intraocular pressure measurements, and fundus photography, were used for feature selection. Five features were chosen for the prediction model, which was tested using several algorithms. All models demonstrated high diagnostic performance, with accuracy ranging from 0.903 to 0.947. The XGboost model achieved the highest accuracy at 0.947, along with good sensitivity, specificity, and AUC values. Three statistical charts were employed to explain the XGboost model's predictions. This study represents a pioneering effort in applying explainable artificial intelligence to eye disease diagnosis [15-20].

Glaucoma Diagnosis with Machine Learning Based on Optical Coherence Tomography and Color Fundus Images Guangzhou An, Kazuko Omodaka, Kazuki Hashimoto, Satoru Tsuda, Yukihiro Shiga, Naoko Takada. The study aimed to develop a machine learning algorithm for diagnosing glaucoma in patients with open-angle glaucoma using three-dimensional optical coherence tomography (OCT) data and color fundus images. They enrolled 208 glaucomatous and 149 healthy eyes, capturing OCT data and fundus images. A convolutional neural network (CNN) was trained using different input images, including grayscale fundus images, thickness maps, and deviation maps. Data augmentation and dropout were applied for training the CNN. A random forest (RF) was used to combine the results from each CNN model and classify healthy and glaucomatous eyes. The 10-fold cross-

validation area under the receiver operating characteristic curve (AUC) results for the CNNs ranged from 0.940 to 0.952, and the RF combining all models achieved an AUC of 0.963. This machine learning system accurately distinguishes between healthy and glaucomatous subjects based on OCT and fundus image data, potentially improving glaucoma diagnostic accuracy [1].

R. N. Weinreb and P. T. Khaw, "Primary open-angle glaucoma," *The Lancet*, vol. 363, no. 9422, pp. 1711–1720, 2004. Primary open-angle glaucoma is a common and progressive eye condition that can lead to irreversible vision loss if not detected and treated early. Early diagnosis relies on examining the optic disc, retinal nerve fiber layer, and visual field. Recent advancements in imaging and psychophysical tests have enhanced the ability to detect and monitor disease progression. Long-term clinical trials have shown that reducing intraocular pressure can effectively prevent glaucoma progression, with the extent of protection linked to the degree of pressure reduction. Ongoing improvements in treatment include more effective and better-tolerated medications and surgical procedures to lower intraocular pressure. Additionally, there are promising developments in treatments aimed at directly protecting the retinal ganglion cells, which are damaged in glaucoma [21].

M. A. Kass, D. K. Heuer, E. J. Higginbotham et al., "The ocular hypertension treatment study," *Archives of Ophthalmology*, vol. 120, no. 6, pp. 701–713, 2002 Primary open-angle glaucoma (POAG) is a leading cause of blindness in the United States and globally, affecting millions. Many people in the U.S., estimated at three to six million, are at a heightened risk of developing POAG due to elevated intraocular pressure (IOP) or ocular hypertension. However, there is no consensus on the effectiveness of medical treatment in delaying or preventing the onset of POAG in individuals with elevated IOP. To address this, the Ocular Hypertension Treatment Study was conducted. The study involved 1,636 participants aged 40 to 80 years with no signs of glaucomatous damage but with IOP levels ranging from 24 mm Hg to 32 mm Hg in one eye and between 21 mm Hg and 32 mm Hg in the other eye. These participants were randomly assigned to either an observation group or a group receiving commercially available topical ocular hypotensive medication. The medication group aimed to reduce IOP by 20% or more, with a target IOP of 24 mm Hg or lower [9].

M. C. Leske, A. Heijl, L. Hyman et al., "Predictors of long-term progression in the early manifest glaucoma trial," *Ophthalmology*, vol. 114, no. 11, pp. 1965–1972, 2007. The study found that overall progression of primary open-angle glaucoma (POAG) was 67% by the end of the follow-up period (median of 8 years). Treatment with ocular

Enhancing digital security using Signa-Deep for online signature verification and identity authentication

Ravikumar Ch¹, Mulagundla Sridevi², M Ramchander³, Vankudoth Ramesh⁴, Vadapally Praveen Kumar⁵

¹Assistant Professor, Department of Artificial Intelligence & Data Science,
Chaitanya Bharathi Institute of Technology, Hyderabad, India-500075.

²Associate Professor, Department of Computer Science and Engineering,
CVR College of Engineering, Hyderabad, India-501510

³Assistant Professor, Department of Master of Computer Applications,
Chaitanya Bharathi Institute of Technology, Hyderabad, India-500075.

⁴Assistant Professor, Department of Emerging Technologies,
CVR College of Engineering, Hyderabad-500039.

* Corresponding author E-mail: chrk5814@gmail.com

(Received 23 October 2023; Final version received 61 January 2024; Accepted 16 April 2024)

Abstract

In the contemporary digital realm, the utilization of online services has surged, facilitated by the seamless integration of deep learning technology, which is paramount in applications demanding precision and efficiency. A pivotal use case in this context is online handwritten signature verification, where the need for exceptional accuracy is indisputable. This paper introduces 'Signa-Deep,' an innovative approach designed to address the challenge of online signature verification and the determination of an individual's authorization status. The study explores a range of methodologies, including Convolutional Neural Networks (CNN), Long Short-Term Memory (LSTM), GoogleNet, and MobileNet, to discern the authenticity of signatures and affirm the identity of the signatory. The results of our proposed method are promising, showcasing its potential to significantly enhance the security of digital transactions and identity verification processes. In summary, 'Signa-Deep' harnesses deep learning technology to bolster the accuracy and reliability of online signature verification, thereby contributing to the overall robustness of digital interactions and identity validation processes.

Keywords: Deep Learning, Online Signature Verification, Authorization Status, Identity Authentication, Digital Transactions Security

1. Introduction

As a biometric feature used for user identification, the human signature makes signature verification a persistent area of study. Online and offline signatures are the two main categories into which signatures fall. Signatures are widely used as a form of authentication. Online signatures, also called dynamic signatures, are digital signatures that are recorded in databases after being digitally taken with electronic equipment. Dynamic characteristics include things like the number and sequence of strokes, the speed at which the signature is made, and the pressure distribution at different points, which make the signature difficult to copy and

distinctly unique. After the signature is preprocessed, certain attributes are taken out. User enrollment in an online signature verification system begins with the submission of reference signatures or samples of signatures. Following that, if a user signs a document (called a test signature) to prove who they are, the test signature is compared to the reference signatures linked to that person. The user's request is rejected if the discrepancy is more than a set quantity. Offline signatures, also known as static signatures, originate as ink-on-paper signatures, which are subsequently preserved by scanning to create a digital copy. In practice, it is essential to verify the authenticity of both online and offline signatures. Nevertheless, verifying offline

signatures poses a greater challenge since, unlike their online counterparts, they lack dynamic data (N. Abbas et 2012 & Neha et. 2022).

Numerous sectors, including banks, official documents, and receipts, rely on online signatures to enhance security and establish the identity of the respective individuals. Although each person possesses a unique signature, the challenge lies in consistently reproducing the same signature. The primary objective of signature verification is to reduce intra-individual variations. Online signature verification constitutes the process of confirming the author's identity through a signature verification system (O.Shapran & M. C. Fairhurst 2009). This system can serve as a security measure, facilitating verification for purposes such as access control and password replacement. Utilizing signature verification enables organizations to validate the legitimacy of customer signatures (Y. Ren et 2020.)

Signature verification is a method employed by banks, intelligence agencies, and prestigious organizations to authenticate an individual's identity. This technique is frequently utilized for comparing signatures within bank offices and other branch capture processes. Online signature verification utilizes signatures recorded using pressure-sensitive tablets, which capture not only the signature's shape but also its dynamic properties (C. Y. Low et 2007).

During the verification process, various distance measures are produced by comparing the test signature to every signature in the reference set. Consequently, a methodology for combining these distance values into a single metric that represents the difference between the test signature and the reference set must be implemented. After that, a predetermined threshold is compared to this statistic to make a decision. One can determine the single dissimilarity value by taking the average, maximum, or minimum of all the distance measurements. A verification system usually selects one of these measures and ignores the others.

Determining if a handwritten signature is real or fake is part of the online handwritten signature verification process. It is possible to fake signatures, and these fakes fall into five different categories: self-forgery, random, skilful, basic, and fluent.

- a) **Random forgery:** Generated without any prior knowledge of the signature, its shape, or the signer's identity.
- b) **Simple forgery:** Produced with only knowledge of the signer's name, lacking any reference to the signer's signature style.
- c) **Skilled forgery:** Crafted by observing an authentic signature sample and endeavoring to replicate it as faithfully as possible. This type of forgery involves having access to a sample of the signature to be duplicated. The quality of a skilled forgery relies on factors such as the forger's practice, their skill level, and their meticulous attention to detail in mimicking the original signature. A skilled forgery closely resembles a genuine signature.
- d) **Fluent forgery:** The forger aims to imitate the motion of the signature, often resulting in rapid scribbling that overlooks design elements such as the shape of letters.
- e) **Self-forgery:** A specific type of forgery in which an individual forges their signature intending to deny it at a later stage."

The complexity of the signature verification task increases notably when transitioning from simple to skilled forgery. Consequently, crafting an effective signature verification system poses a significant and critical challenge (Chang et.2023).

The vital and complex field of signature verification, which is essential for user identification using the biometric characteristic of a human signature, is the subject of this study. Differentiating between offline and online signatures, the study emphasizes how online signatures are more dynamic and difficult to duplicate. Reference signatures are submitted as part of the registration procedure, and these signatures serve as the foundation for identity verification utilizing comparison with test signatures that are later submitted. Because they are not dynamic, offline signatures which started as ink on paper and were subsequently digitized present a unique set of challenges. Despite these difficulties, online and offline signatures are essential for improving security and verifying personal identity in a variety of industries, such as banking, intelligence services, and elite institutions. The main objective of the work is to tackle the crucial problem of intra-individual differences in signatures, which is necessary for the creation of efficient signature verification systems with security, access control, and

A comparative analysis for deep-learning-based approaches for image forgery detection

Ravikumar Ch¹, Marepalli Radha², Maragoni Mahendar³, Pinnapureddy Manasa⁴

¹Assistant Professor, Department of Artificial Intelligence & Data Science, Chaitanya Bharathi Institute of Technology, Hyderabad, India-500075

²Associate Professor, Department of Computer Science and Engineering, CVR College of Engineering, Hyderabad, India-501510

^{3,4}Assistant Professor, Department of Computer Science and Engineering, Neil Gogte Institute of Technology, Hyderabad-500039

* Corresponding author E-mail: chrk5814@gmail.com

(Received 23 October 2023; Final version received 04 December 2023; Accepted 27 December 2023)

Abstract

The detection of counterfeit photographs is critical in the digital age because of the widespread development of digital media and its significant impact on social networks. The legitimacy of digital content is being threatened by the growing sophistication of picture counterfeiting. With the help of pre-trained VGG-16 models and deep learning techniques that integrate Error Level Analysis (ELA) and Convolutional Neural Networks (CNNs), this study presents a fresh solution to this problem. The study thoroughly assesses and contrasts these models with a dataset that has been carefully chosen to bring the presented findings into perspective. To ensure a reliable evaluation of each model's performance 5000 experiments were carried out in total. With an accuracy rate of 99.87% and an accurate identification rate of 99% of hidden forgeries, the results demonstrate the exceptional effectiveness of the ELA-CNN model. However, despite its robustness, the VGG-16 model only achieves a significantly lower accuracy rate of 97.93% and a validation rate of 75.87%. This study clarifies the relevance of deep learning in the identification of image forgeries and highlights the practical ramifications of various models. Moreover, the research recognizes its constraints, especially for highly advanced counterfeits, and proposes possible paths for enhancing the accuracy and scope of detection algorithms. In the ever-changing world of digital media, the thorough comparative analysis provided in this study offers insightful information that can direct the creation of accurate forgery detection tools, protecting digital content integrity and reducing the effects of image manipulation.

Keywords: Counterfeit images, Image forgery detection, deep learning, ELA-CNN, VGG-16 model.

1. Introduction

The advent of the digital era has seen an unprecedented surge in the creation and dissemination of images across various online platforms, from social media networks to news outlets (Smith, 2018). This proliferation of digital imagery has dramatically altered the landscape of information sharing and communication, emphasizing the critical concern for the integrity of digital content in this digital ecosystem dominated by visual communication (Kumar & Yadav, 2019). In this context, the need to ensure the authenticity of images has become paramount.

To address this concern, image forgery, encompassing the manipulation or alteration of digital images to

deceive, misinform, or distort reality, has proliferated in tandem with the rise of digital media (Farid, 2019). Image forgeries take various forms, including spurious images intended to manipulate public perception, retouched photographs altering perceived reality, and visually manipulated content designed to deceive (Barni & Piva, 2019). The consequences of such manipulations can be severe, from the spread of misinformation eroding public trust in media (Baker & Tabaka, 2020) to potential damage to individual and institutional reputations (Baluja, 2018), and even legal ramifications in cases of fraudulent activities (Ahmed & Hu, 2021).

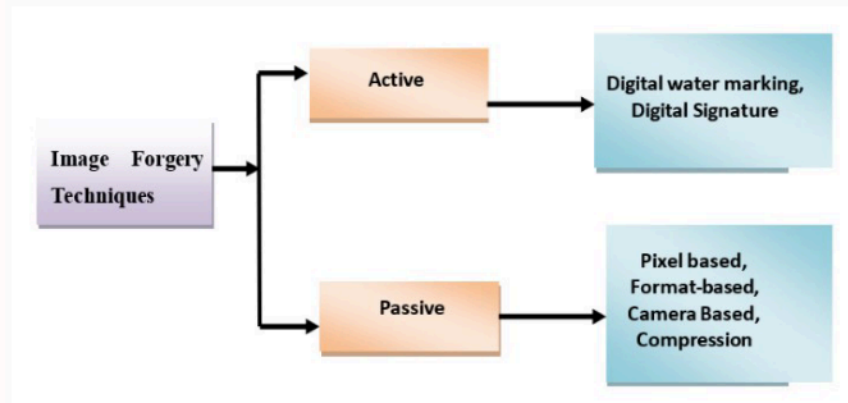


Fig 1: Image Forgery Techniques

Given the gravity of these consequences, the ability to detect and thwart image forgery has become an imperative requirement in preserving the trustworthiness of digital content in the modern age. This research paper aims to contribute to this endeavor by introducing and evaluating a novel deep learning-based approach for image forgery detection. To provide a more explicit transition from the general context to the specific research problem addressed in this study, the paper is structured as follows: Section 2 presents an overview of the digital age's impact on image integrity and the rise of image forgery. Section 3 introduces the methodology, emphasizing the integration of Error Level Analysis (ELA) with Convolutional Neural Networks (CNNs) and the VGG-16 model. Section 4 presents the findings of the comprehensive comparative analysis of these models, highlighting the remarkable efficacy of the ELA-CNN model. Section 5 discusses the implications of the results, acknowledges study limitations, and suggests potential enhancements for image forgery detection algorithms. Finally, Section 6 concludes the paper by emphasizing the contribution to the field and the importance of advancing techniques to maintain the integrity of digital content in the face of evolving image manipulation challenges.

2. Literature review

The literature review sheds light on the transformative impact of digital media on social networks and its influence on information sharing through images. Jones provides a compelling analysis of this influence, emphasizing the altered dynamics of social interactions in the digital age. The review underscores the critical role of images in shaping online communication, setting the

stage for the exploration of image forgery detection techniques (Ahmed et. Al.,2021).

In addressing the challenges to digital media integrity, Patel and Gupta discuss threats and vulnerabilities in the digital media landscape. They emphasize the potential consequences of misinformation and image manipulation, reinforcing the need for advanced solutions to protect the credibility of digital content. This discussion forms the backdrop for the exploration of image forgery detection methods (Jones 2019, Patel et al.,2020). Chang and Chen's comprehensive survey delves into the application of deep learning for image forensics, providing valuable insights into the evolution of image forgery detection. Their work lays a strong foundation for understanding the technical aspects of image forensics, paving the way for the discussion of advanced methods. Similarly, Wang and Farid focus on image authentication and tamper detection, emphasizing the significance of ensuring the integrity of digital images. Their study discusses various methods for verifying image authenticity, contributing to a nuanced understanding of image forgery detection techniques (Chang et. al.,2017, Wang et.al.,2020).

Ochoa and Rueda explore the challenges posed by deep fake technology in image forgery detection. Their examination of the evolving landscape of image manipulation techniques emphasizes the need for advanced detection methods in the era of deepfake. Additionally, Wang and Zhou's survey provides a comprehensive overview of image forgery detection methods, offering insights into the challenges and opportunities in the field Ochoa et.al.,2019, Wang et.al.,2018).

Brown and Black's review focuses on the detection of deep fake videos, closely related to image forgery detection. The paper discusses techniques and challenges associated with identifying manipulated video content, providing valuable insights into the broader context of

Joint effects of thermal diffusion and diffusion thermo on MHD three dimensional nanofluid flow towards a stretching sheet

G. Murali¹, G. Deepa², Nirmala Kasturi V³, T. Poornakantha⁴

¹Sreenidhi University, Hyderabad, India

²Chaitanya Bharathi Institute of Technology, Gandipet, India

³Gokaraju Lailavathi Womens Engineering College, Bachupally, India

⁴Gayatri Vidya Parishad College of Engineering for Women, Visakhapatnam, India

¹Corresponding author

E-mail: ¹murali.maths81@gmail.com, ²deepagadipally@gmail.com, ³nirmalakasturi279@gmail.com,

⁴purnakantha19@gvpcew.ac.in

Received 27 August 2023; accepted 6 November 2023; published online 30 December 2023

DOI <https://doi.org/10.21595/mme.2023.23590>



Copyright © 2023 G. Murali, et al. This is an open access article distributed under the Creative Commons Attribution License, which permits unrestricted use, distribution, and reproduction in any medium, provided the original work is properly cited.

Abstract. This communication reports the joint effects of Thermal Diffusion and Diffusion Thermo on viscous and incompressible three-dimensional nanofluid flow towards a stretching sheet in connection to the influence of a magnetic field. In this study, nanofluid model is employed for the effects of thermophoresis and Brownian motion. Following that, similarity variables are chosen to turn the dimensional nonlinear system into dimensionless expressions and the resultant transformed equations are solved numerically using Finite Element method. Special emphasis has been given to the parameters of physical interest. These findings are visually presented through graphical representations, providing a clear and insightful understanding involved in this flow scenario. In addition, the final results are examined in light of past research and it is determined that they meet the convergence standards to an exceedingly satisfactory degree. The study's findings are beneficial for many technical and commercial endeavours.

Keywords: thermal diffusion, diffusion thermo, MHD, three-dimensional, nanofluid, stretching sheet.

Nomenclature

u, v, w	Velocity components in x, y and z , Axes respectively (m/s)
x, y, z	Cartesian coordinates
f	Dimensionless stream function along x -direction (kg/m.s)
f'	Fluid velocity along x -direction (m/s)
g	Dimensionless stream function along y -direction (kg/m.s)
g'	Fluid velocity along y -direction (m/s)
Pr	Prandtl number
T	Fluid temperature (K)
T_w	Temperature at the surface (K)
B_o	Uniform magnetic field (Tesla)
M	Magnetic field parameter
T_∞	Temperature of the fluid far away from the stretching sheet (K)
Cf	Skin-friction coefficient along x -direction (s^{-1})
$u_w(x)$	Stretching velocity of the fluid along x -direction (m/s)
$v_w(y)$	Stretching velocity of the fluid along y -direction(m/s)
Nu	Rate of heat transfer coefficient (or) Nusselt number
Sh	Rate of mass transfer coefficient (or) Sherwood number
C_p	Specific heat capacity of nano particles (J/kg/K)
a	Constant

Re_x	Reynolds number
C	Fluid nanoparticle volume concentration (mol/m ³)
C_∞	Dimensional ambient volume fraction (mol/m ³)
Nb	Brownian motion parameter
Nt	Thermophoresis parameter
A	Coefficient related to stretching sheet
Le	Lewis number parameter
D_B	Coefficient of Brownian diffusion (m ² /s)
C_w	Dimensional nanoparticle volume concentration at the stretching surface (mol/m ³)
D_T	Coefficient of Thermophoresis diffusion (m ² /s)
n	Velocity power index parameter
Du	Diffusion thermo (or) Dufour number
Sr	Thermal diffusion (or) Soret number
C_s	Concentration susceptibility
K_T	Thermal diffusion ratio
D_m	Solutal diffusivity of the medium
T_m	Fluid Mean temperature
η	Dimensionless similarity variable (m)
θ	Dimensionless temperature (K)
ν	Kinematic viscosity (m ² /s)
σ	Electrical Conductivity
μ	Dynamic viscosity of the fluid
κ	Thermal conductivity of the fluid
ρ_f	Density of the fluid (kg/m ³)
τ	Effective heat capacitance
ϕ	Nanoparticle volume concentration at the stretching surface (mol/m ³)
κ_B	Boltzmann constant (J/K)
/	Differentiation w.r.t z
f	Fluid
w	Condition on the sheet
∞	Ambient conditions

1. Introduction

In-depth research has been started to examine the thermophysical characteristics of typical heat transfer fluids. However, the escalating demands of contemporary technologies cannot be met by these fluids. Thus, the addition of nanoparticles to such fluids is started in order to overcome these obstacles. Engineered nanofluids are made up of a base fluid and nanoparticles. The base fluid is used to produce these liquids by incorporating nano-sized particles into it. Recent research have demonstrated through experimentation that the inclusion of nanoparticles increases the thermal conductivity of conventional fluids significantly. A connection between micro and macro molecular structures has been established thanks to the new inherent properties of nanofluids. Nanofluids are extremely important in many heat transfer processes such as fuel cells, microelectronics, hybrid-powered engines, and so on because of their remarkable qualities. Because of its utility in the creation of high-quality lubricants and oils, nanofluids are utilized in industrial technologies. Fluid mass and heat transfer vary as a consequence of the difference in density between fluid flux and fluid flow regime. The interaction between composition gradients (Dufour) and temperature gradients is one of two possible processes that might lead to the generation of thermal diffusion (Soret). Although their advantages in hydrology, petrology, geosciences, isotope separation, and other fields have been shown [1], their influence on the fluid density differential in fluid flow regimes is still significant. Kaladhar et al. [2] investigated the

impact of Soret and Dufour on chemically reacting mixed convection flow in an annulus with Navier slip and convective boundary conditions. The effects of thermophoresis, Soret, and Dufour on the heat and mass transfer flow of a magnetohydrodynamics non-Newtonian nanofluid over an inclined plate were examined by Idowu and Falodun [3]. In order to investigate the combined effects of Soret, Dufour, and radiation of a viscoelastic fluid over an exponentially growing surface, Kasali et al. [4] employed the Cattaneo-Christov heat flux model. In an inclined rectangular enclosure with a partly saturated porous wall, Hu and Mei [5] studied the combined effects of heat and moisture convection and entropy production in the presence of Soret and Dufour numbers. The combined effects of Dufour and Soret on three-dimensional compressed flow and heat transfer in a spinning tube were examined by Yinusa et al. [6]. The effect of Soret and Dufour on thermo-solute convection was examined by Rghif et al. [7]. In double diffusive mixed convection, Hussain et al. [8] examined the effect of Dufour and Soret on the power law fluid and magnetic field parameters. Using the finite difference approach, Khan et al. [9] examined the Darcy-Forchheimer flow of a viscous fluid with Dufour and Soret effects. Numerical solutions for the MHD flow with Soret and Dufour effects were created by Hayat et al. [10]. The Soret and Dufour effects were taken into consideration when Hayat et al. [11] investigated the influence of chemical processes on the peristaltic motion of an MHD-coupled fluid in a channel. The effects of Soret-Dufour, heat radiation, and binary chemical reaction on the Darcy-Forchheimer flow of nanofluids were studied by Rasool et al. [12]. In a Hall MHD generator system, Usman et al study's team [13] looked into the impacts of Soret, Dufour, and activation energy on the double diffusive convective pair stress micropolar nanofluid flow. The effects of chemical reaction, thermo-diffusion, and diffusion-thermo on the MHD flow of an incompressible nanofluid over a uniformly elongating sheet were examined by Reddy and Chamkha [14]. In a container holding liquid metal, Arun and Satheesh [15] explain MHD double diffusive natural convection and entropy generation. The slip effects of MHD unsteady Maxwell nanofluid flow across a permeable stretched sheet with radiation and thermo-diffusion in the presence of a chemical reaction were examined by Ali et al. [16] using the finite element method. The combined effects of thermo-diffusion and heat radiation on a porous sheet that could contract and stretch while carrying a Williamson nanofluid were investigated by Bhatti and Rashidi [17]. In a porous cage containing nanofluid, Aly [18] investigated thermo-diffusion-influenced spontaneous convection across circular cylinders. M. C. Krishna Reddy et al. [19] studied Heat and mass transfer effects on unsteady MHD free convection flow past a vertical permeable moving plate with radiation. S. Sivaiah et al. [20] Found the solution for Unsteady MHD mixed convection flow past a vertical porous plate in presence of radiation. M. Gundagani et al. [21] analysed the Radiation Effects on an Unsteady MHD Convective Flow Past a Semi-Infinite Vertical Permeable Moving Plate Embedded in a Porous Medium with Viscous Dissipation. Deepa Gadipally et al. [22] Studied on Analysis of soret and dufour effects on unsteady MHD flow past a semi infinite vertical porous plate via finite difference method. G. Deepa et al. [23] Studied the Effects of viscous dissipation on unsteady MHD free convective flow with thermophoresis past a radiate inclined permeable plate. Murali G. et al. [24] applied FEM on numerical study of chemical reaction effects on unsteady MHD fluid flow past an infinite vertical plate embedded in a porous medium with variable suction. For better understanding of the concept and its applications are covered by references [25-30].

It is crucial to evaluate thermal diffusion and thermal diffusion effects on steady, incompressible, viscous, electrically conducting, three-dimensional, MHD-Nanofluid flow over a stretched sheet in the presence of magnetic field, Brownian motion, and thermophoresis effects. The intellectual curiosity and technical applications of non-Newtonian rheology have greatly piqued academics' attention. Because of its generous and prized application in industrial production mechanisms, power engineering, petroleum production, and a wide range of chemical processes, non-Newtonian fluids have been the subject of several studies in recent years. A single constitutive relation is insufficient to fully describe the features of all non-Newtonian fluids, hence they are classified categorically into several models. Visco-inelastic fluids, visco-elastic fluids, polar fluids, anisotropic fluids, and fluids with microstructure are the main classifications of these

models. Visco-inelastic fluids, which integrate the combined effects of elastic and viscous characteristics, are among them and represent the most important subclass of non-Newtonian fluid.

This review is motivated by the aforementioned sources as well as the different potential industrial applications of the topic. The current study is considered to examine heat and mass transfer effects across a vertically stretched surface under the light of double diffusion effects due to importance in practical, industrial, and technical consequences. From the literature review mentioned above, it can be concluded that this issue has never been addressed. First, by using compatible transformations, the challenging partial equations are transformed into useful ordinary differential equations for this purpose. To develop numerical solutions with increased computing efficiency, the finite element method is utilised.

The goal of this research is to elaborate on the findings of Khan et al. [25]. Along with the effects of skin friction, the rate of heat transfer and mass transfer coefficients on fluid flow, relevant variables including velocity, temperature, and concentration profiles are given.

2. Mathematical formulation

When thermophoresis, Brownian motion, and the effects of magnetic fields are present, the combined effects of Soret and Dufour on the flow of a nanofluid that is viscous, electrically conducting, incompressible, and three-dimensional are investigated. The nanofluid in question possesses all of these characteristics. The nanofluid under consideration is one that moves in a three-dimensional manner across a sheet that has been stretched. Investigations are now being carried out to learn more about how nanofluids behave while moving over a stretched sheet. As a result of the findings of this investigation, we are in a position to hypothesise the following things:

1) For the stretching sheet, the variable thickness is assumed as $z = A(x + y + z)^{\frac{1-n}{2}}$.

2) Also, the stretched velocity of the sheet is $u_w = a(x + y + z)^{\frac{1-n}{2}}$ and this is suitable for $n \neq 1$ since $n - 1$ demotes the flat stretching sheet.

The magnetic Reynolds number has to be as low as it is physically possible to make it in order to dismiss the magnetic field that is formed. This is the case in order to disregard the magnetic field that is created.

In this work, the authors have preferred Magnetic field of strength B_o is applied to the flow.

The following are the equations that should be used for flow control in line with the ideas that have been discussed up to this point:

Continuity equation:

$$\frac{\partial u}{\partial x} + \frac{\partial v}{\partial y} + \frac{\partial w}{\partial z} = 0. \tag{1}$$

Momentum equations:

$$u \left(\frac{\partial u}{\partial x} \right) + v \left(\frac{\partial u}{\partial y} \right) + w \left(\frac{\partial u}{\partial z} \right) = \nu \left(\frac{\partial^2 u}{\partial z^2} \right) - \left(\frac{\sigma B_o^2}{\rho_f} \right) u, \tag{2}$$

$$u \left(\frac{\partial v}{\partial x} \right) + v \left(\frac{\partial v}{\partial y} \right) + w \left(\frac{\partial v}{\partial z} \right) = \nu \left(\frac{\partial^2 v}{\partial z^2} \right) - \left(\frac{\sigma B_o^2}{\rho_f} \right) v. \tag{3}$$

Equation of thermal energy:

$$u \left(\frac{\partial T}{\partial x} \right) + v \left(\frac{\partial T}{\partial y} \right) + w \left(\frac{\partial T}{\partial z} \right) = \frac{\kappa}{\rho C_p} \left(\frac{\partial^2 T}{\partial z^2} \right) + \tau \left[D_B \frac{\partial T}{\partial z} \frac{\partial C}{\partial z} + \frac{D_T}{T_\infty} \left(\frac{\partial T}{\partial z} \right)^2 \right] + \frac{D_m K_T}{C_s C_p} \left(\frac{\partial^2 C}{\partial y^2} \right). \tag{4}$$

Equation of species concentration:

$$u \left(\frac{\partial C}{\partial x} \right) + v \left(\frac{\partial C}{\partial y} \right) + w \left(\frac{\partial C}{\partial z} \right) = D_B \left(\frac{\partial^2 C}{\partial z^2} \right) + \frac{D_T}{T_\infty} \left(\frac{\partial^2 T}{\partial z^2} \right) + \frac{D_m K_T}{T_m} \left(\frac{\partial^2 T}{\partial y^2} \right). \quad (5)$$

The boundary conditions for this flow are:

$$\begin{aligned} u = u_w(x), \quad v = v_w(x), \quad T = T_w(x), \quad C = C_w(x), \quad z = 0 \\ u \rightarrow 0, \quad v \rightarrow 0, \quad T \rightarrow T_\infty, \quad C \rightarrow C_\infty, \quad z \rightarrow \infty, \end{aligned} \quad (6)$$

where:

$$B(x) = B_o(x + y + z)^{\frac{1-n}{2}}, \quad (7)$$

$$u_w = a(x + y + z)^{\frac{1-n}{2}}, \quad v_w = a(x + y + z)^n, \quad \tau = \frac{(\rho C_p)_s}{(\rho C_p)_f}, \quad (8)$$

$$T_w = T_\infty + T_o(x + y + z)^{\frac{1-n}{2}}, \quad C_w = C_\infty + C_o(x + y + z)^{\frac{1-n}{2}}, \quad n \neq 1.$$

If you use the following similarity transformations and convert the governing equations to ordinary differential equations, you should be able to get the answers that you are seeking for:

$$\begin{aligned} u = a(x + y + z)^n f^{(\eta)}, \quad \theta = \frac{T - T_\infty}{T_w(x) - T_\infty}, \quad \phi = \frac{C - C_\infty}{C_w(x) - C_\infty}, \\ v = a(x + y + z)^n g^{(\eta)}, \quad \eta = z \left(\sqrt{\frac{(n+1)a}{2v}} \right) (x + y + z)^{\frac{1-n}{2}}, \end{aligned} \quad (9)$$

$$w = -\sqrt{\frac{2av}{n+1}} (x + y + z)^{\frac{1-n}{2}} \left\{ \left(\frac{n+1}{2} \right) [f(\eta) + g(\eta)] + \eta \left(\frac{n-1}{2} \right) [f^{(\eta)} + g^{(\eta)}] \right\}.$$

The continuity equation, which is validated by Eq. (9), is provided in the following form, which is also used by Eqs. (2), (3), (4), and (5):

$$\left(\frac{n+1}{2} \right) f''' - n f'^2 - n f' g' + \left(\frac{n+1}{2} \right) f f'' + \left(\frac{n+1}{2} \right) g f'' - M f' = 0, \quad (10)$$

$$\left(\frac{n+1}{2} \right) g''' - n g'^2 - n f' g' + \left(\frac{n+1}{2} \right) f g'' + \left(\frac{n+1}{2} \right) g g'' - M g' = 0, \quad (11)$$

$$\begin{aligned} \theta'' + Nb\theta'\phi' + Nt\theta'^2 - \left(\frac{1-n}{1+n} \right) \text{Pr}f'\theta - \left(\frac{1-n}{1+n} \right) \text{Pr}g'\theta + \left(\frac{1-n}{1+n} \right) \text{Pr}f\theta' \\ + \left(\frac{1-n}{1+n} \right) \text{Pr}g\theta' + \text{Pr}Du\phi'' = 0, \end{aligned} \quad (12)$$

$$\begin{aligned} Nb\phi'' + Nt\theta'' + LeNb \left(\frac{1-n}{1+n} \right) f'\phi - NbLe \left(\frac{1-n}{1+n} \right) g'\phi + NbLe \left(\frac{1-n}{1+n} \right) f\phi' \\ + NbLe \left(\frac{1-n}{1+n} \right) g\phi' + NbSr\theta'' = 0. \end{aligned} \quad (13)$$

As a direct consequence of this Eq. (6), the following boundary constraints are imposed on the system:

$$\begin{aligned}
 f(0) = 0, \quad g(0) = 0, \quad f'(0) = 1, \quad g'(0) = 1, \quad \theta(0) = 1, \quad \phi(0) = 1, \\
 f'(\infty) = 0, \quad g'(\infty) = 0, \quad \theta(\infty) = 0, \quad \phi(\infty) = 0.
 \end{aligned}
 \tag{14}$$

When referring to the subject matter at hand, many of the components that go into making it up are referred to as:

$$\begin{aligned}
 M = \frac{\sigma B_0^2}{\rho a}, \quad Pr = \frac{\mu C_p}{\kappa}, \quad Le = \frac{\nu}{D_B}, \quad Nb = \frac{\tau D_B (C_w - C_\infty)}{(\mu C_p)_f}, \\
 Sr = \frac{D_m K_T (T_w - T_\infty)}{T_m \nu (C_w - C_\infty)}, \quad Du = \frac{D_m K_T (C_w - C_\infty)}{C_s C_p \nu (T - T_\infty)}, \quad Nt = \frac{\tau D_T (T_w - T_\infty)}{T_\infty (\mu C_p)_f},
 \end{aligned}
 \tag{15}$$

The Sherwood number, the skin-friction coefficient, and the local Nusselt number are:

$$\begin{aligned}
 Cf_x = 2 \sqrt{\frac{n+1}{2}} \cdot \frac{1}{\sqrt{Re_x}} \cdot f''(0), \quad Cf_y = 2 \sqrt{\frac{n+1}{2}} \cdot \frac{1}{\sqrt{Re_y}} \cdot g''(0), \\
 Nu = - \sqrt{\frac{n+1}{2}} \cdot \sqrt{Re_x} \cdot \theta'(0), \quad Sh = - \sqrt{\frac{n+1}{2}} \cdot \sqrt{Re_x} \cdot \phi'(0),
 \end{aligned}
 \tag{16}$$

where $Re_x = u_x(x)(x + y + z)/\nu$ and $Re_y = v_x(x)(x + y + z)/\nu$ are local Reynolds numbers.

3. Method of solution

Numerical modelling and simulation provide an easier, cheaper and highly efficient way to find solutions to complex mathematical equations. The development of computer numerical modelling has been useful in simplifying the problem-solving procedure. Numerical models are developed to perfectly match the physical system, and the solutions can be analyzed and checked against the real system. These numerical methods allow us to improve approaches to the physical system and solve it quickly. The finite element method employed in the current study can be used in future research since it is a highly useful approach to solving linear and nonlinear partial and ordinary differential equations in physics, mechanical engineering, and other related subjects. The following are the advantages of FEM technique:

- Modelling
- Adaptability
- Accuracy
- Boundaries
- Visualization

The use of the finite element approach is shown in Fig. 1, which also serves as an example. The resolution of generated equations may be accomplished by the use of a wide variety of numerical techniques, including the LU decomposition method, the Gauss elimination method, and a great deal more besides. The solution of built equations is one of the most popular uses for these approaches. When working with real numbers, it is very necessary to bear in mind the form functions that are used to make an approximate approximation of real functions. Form functions may be used to provide a close approximation of real functions. If you follow this technique step by step, you may be certain that your calculations will be accurate. The flow domain has a total of 20,001 nodes and is divided into 10,000 quadratic components that are all the same size.

These components are all of the same shape. The flow domain is made up of 10,000 quadratic components, all of which are of the same magnitude as their counterparts in the other components. After the element equations were developed, there were a total of 80,004 nonlinear equations that

could be investigated. These equations were made accessible for study. After the boundary conditions have been applied, the Gauss approach is used to remove the remaining system of nonlinear equations, and then the Gauss technique is used to arrive at a numerical solution that is accurate to 0.00001 degrees. The use of gaussian quadrature is done so that the challenges that are connected to integration may be aided in some way.

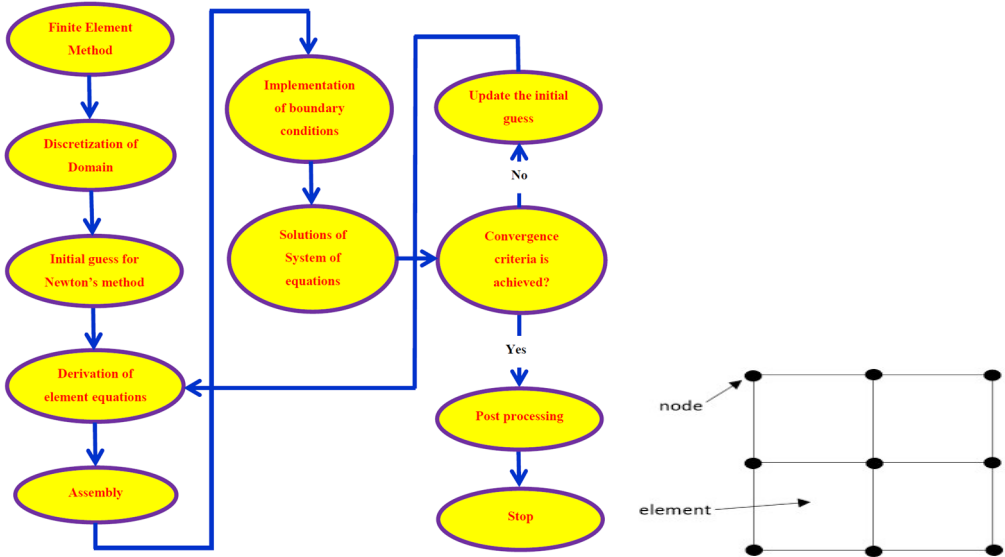


Fig. 1. Finite element method flow chart and meshing diagram

Program code validation.

Table 1. Comparison of present finite element method results with published results of Khan et al. [25] for $Sr = Du = M = Le = 0$

Pr	Present Nusselt number results	Nusselt number results of Khan et al. [25]
7.0	2.39698362139067130947561	2.404797
13.0	2.69678670983769138713347	2.705551
25.0	3.27565748503561087643423	3.287794
50.0	4.10875617938673896398386	4.115197
100.0	5.32767687587319873698139	5.336685

Table 1 compares the most recent finite element Nusselt number (rate of heat transfer) results with those that Khan et al. [25] had previously reported using the shooting method with the fourth- to fifth-order Runge-Kutta integration method without taking into account the effects of thermal diffusion, diffusion thermo, magnetic field, and Lewis number. As this table demonstrates, there is a strong correlation between the new findings and the outcomes that Khan et al. [25] previously established.

4. Results and discussion

In this results and discussion section, the authors have to study the effects of the different physical parameters namely Magnetic field parameter (M), Prandtl number (Pr), Thermophoresis parameter (Nt), Brownian motion parameter (Nb), Lewis number (Le), Diffusion thermo parameter (Du), Thermal diffusion parameter (Sr) and Velocity power index parameter (n) are presented through Fig. 3 to 16 for dimensionless velocity, temperature and concentration ($\phi(\eta)$) profiles. Also, the effects of same parameters are discussed on engineering quantities namely Skin-friction coefficient, Nusselt number (rate of heat transfer coefficient), Sherwood number

(rate of mass transfer coefficient) are discussed with help of numerical values in tabular forms.

Effect of Magnetic field parameter (M): Figs. 2 and 3 intend the velocity profiles $f'(\eta)$ and $g'(\eta)$ for various values of M (Magnetic field parameter). It is observed that velocity fields $f'(\eta)$ and $g'(\eta)$ decline when the values of M increases. The application of an applied magnetic field has the tendency to slow down the movement of the fluid, which leads to a decrease in the velocity and momentum boundary layer thickness. The influence of Magnetic field parameter (M) on Skin-friction coefficient is discussed in Table 2. From this table, it is observed that, the Skin-friction coefficient is decreasing with increasing values of Magnetic field parameter.

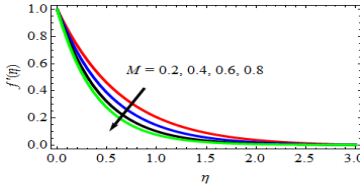


Fig. 2. $f'(\eta)$ profiles for deviations of M

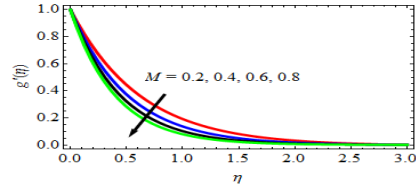


Fig. 3. $g'(\eta)$ profiles for deviations of M

Table 2. Skin-friction coefficient Cf_x values for different values of M, Pr, Nt, Nb, n, Sr, Du and Le

M	Pr	Nt	Nb	n	Sr	Du	Le	Cf_x
0.2	0.71	0.1	0.1	0.1	0.5	0.5	0.3	2.376518457634875
0.4								2.346574687580164
0.6								2.326786768709389
	1.00							2.330867069736953
	3.00							2.310560986703987
		0.3						2.404758471653743
		0.5						2.423034839876236
			0.3					2.392328956490934
			0.5					2.414467037460111
				0.2				2.406787110387667
				0.3				2.426470107340303
					0.8			2.397778556767339
					1.0			2.415656787287387
						1.0		2.402564107354705
						1.5		2.426676872736475
							0.7	2.347785290756908
							0.9	2.313567577575207

Effect of Velocity power index parameter (n): The influence of n (Velocity power index parameter) on velocity profiles ($f'(\eta)$ and $g'(\eta)$), temperature ($\theta(\eta)$) and concentration ($\phi(\eta)$) profiles are discussed in Figs. 4-7. From these figures, it is observed that the velocity profiles ($f'(\eta)$ and $g'(\eta)$), temperature ($\theta(\eta)$) and concentration ($\phi(\eta)$) profiles are increasing with increasing values of n (Velocity power index parameter). The effect of Velocity power index parameter (n) on Skin-friction coefficient, Rate of heat transfer and mass transfer coefficients are discussed in Tables 2, 3 and 4 respectively. From these tables, it is observed that, the Skin-friction, Rate of heat transfer and mass transfer coefficients are increasing with increasing values of Velocity power index parameter.

Effect of Prandtl number (Pr): Fig. 8 illustrates the link that exists between the Prandtl number and the temperature of the fluid whose temperature is being measured. As the value of Pr continues to increase, the temperature gradient of the fluid will give off the impression of being less striking. When Pr increases, so does the momentum diffusivity, which eventually overtakes the thermal diffusivity and becomes the dominant one. This happens when momentum diffusivity finally overtakes thermal diffusivity. There is a good chance that the amount of heat that can be transferred by a fluid is in some way related to the speed at which the fluid is moving. This has

the immediate effect of reducing the thickness of the boundary layer, which in turn results in an increase in the rate at which heat is carried. The effect that the Prandtl number, which is more commonly referred to as Pr , has on the rate of heat transfer coefficient is broken down and discussed in Table 3. According to the data presented in the table, the rate of the heat transfer coefficient tends to decrease as the Prandtl number rises. This is indicated by the downward trend seen in this rate.

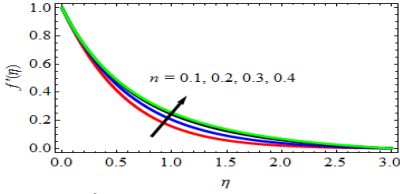


Fig. 4. $f'(\eta)$ profiles for deviations of n

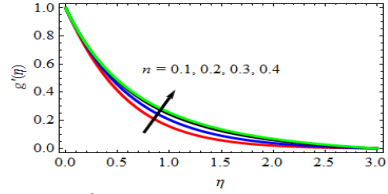


Fig. 5. $g'(\eta)$ profiles for deviations of n

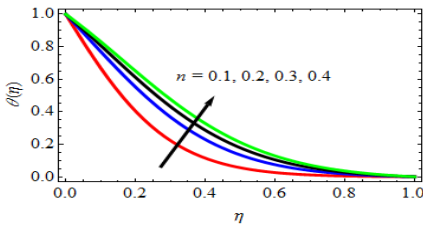


Fig. 6. $\theta(\eta)$ profiles for deviations of n

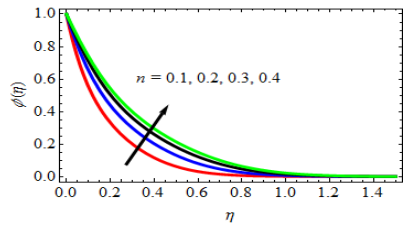


Fig. 7. $\phi(\eta)$ profiles for deviations of n

Table 3. Skin-friction coefficient Cf_x values for different values of M, Pr, Nt, Nb, n, Sr, Du and Le

M	Pr	Nt	Nb	n	Sr	Du	Le	Cf_x
0.2	0.71	0.1	0.1	0.1	0.5	0.5	0.3	1.267896398713986
0.4								1.228678209386932
0.6								1.209678676901767
	1.00							1.2180818966618944
	3.00							1.197098285694984
		0.3						1.280897892741818
		0.5						1.316786529873929
			0.3					1.285413403369393
			0.5					1.309376036137032
				0.2				1.299687200698301
				0.3				1.320986729849287
					0.8			1.296713670933986
					1.0			1.327643109334933
						1.0		1.309857666686248
						1.5		1.336790868733696
							0.7	1.245745637901711
							0.9	1.229954901934930

Effect of Brownian motion parameter (Nb): Using the data that is shown in Figs. 9 and 10, the authors came to the conclusion that an increase in the Nb , which is the parameter that describes the Brownian motion, results in a drop in the concentration fields and a rise in temperature. The thermophoresis and Brownian motion coefficients of individual nanoparticles do not all have the same values. This is a well-established scientific fact. This exemplifies the fact that New Brunswick possesses breathtakingly gorgeous natural scenery. Tables 2, 3, and 4 respectively analyse the effect that the Brownian motion parameter has on the skin friction, the rate of heat transfer, and the mass transfer coefficients. If you take a look at these tables, you'll see that the value of the Brownian motion parameter causes the skin-friction and rate of heat transfer

coefficients to increase, whilst the rate of mass transfer coefficient decreases. This is something that you can observe for yourself. In the case of the rate of mass transfer coefficient, one observes the impact that is directly opposite.

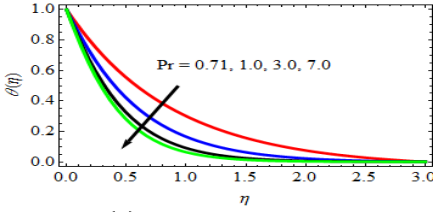


Fig. 8. $\theta(\eta)$ profiles for deviations of Pr

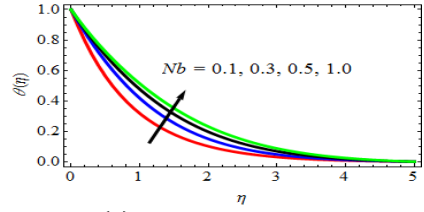


Fig. 9. $\theta(\eta)$ profiles for deviations of Nb

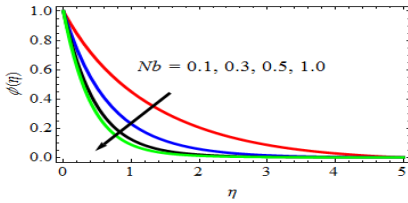


Fig. 10. $\phi(\eta)$ for deviations of Nb

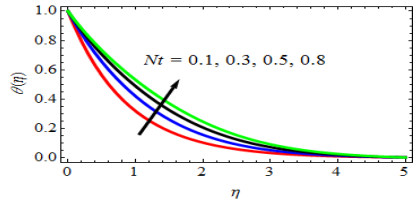


Fig. 11. $\theta(\eta)$ profiles for deviations of Nt

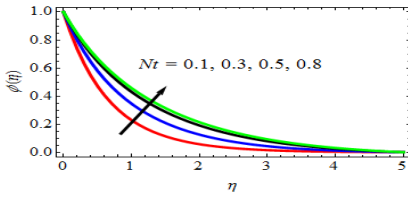


Fig. 12. $\phi(\eta)$ for deviations of Nt

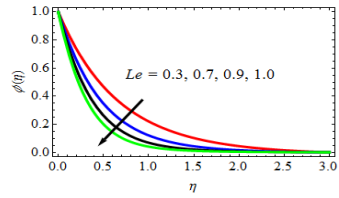


Fig. 13. $\phi(\eta)$ for deviations of Le

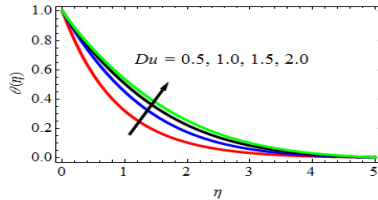


Fig. 14. $\theta(\eta)$ profiles for deviations of Du

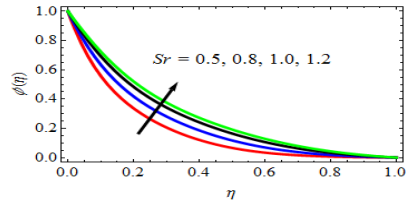


Fig. 15. $\phi(\eta)$ for deviations of Sr

Effect of Dufour number or Diffusion thermo parameter (Du): Fig. 14 showed that the fluid temperature profile rose along with the rise in the Dufour number. This phenomenon may be explained physically as what would happen if two separate fluids with the same temperature and no chemical reaction were discharged into the system and allowed to spread. The temperature differential in the system would increase. Tables 2 and 3 explore, respectively, how the Dufour number affects skin friction and the rate of heat transfer coefficients. These data show that when the Dufour number rises, both skin friction and the rate of heat transfer coefficients increase.

Effect of Soret number or Thermal diffusion parameter (Sr): The influence of the Soret number on concentration profiles and the subsequent increase in fluid concentration is seen in Fig. 15. The Soret effect takes place when an irreversible process results in a temperature gradient in a concentration field. This causes the field to have a gradient. It is likely to result in an increase in the concentration flux of the flow system. Fig. 15 gives an explanation. The effect that the Soret number has on the rate of mass transfer coefficients and the skin friction is investigated in Tables 2 and 4, respectively. According to these data, a rise in the Soret number results in an increase in the rate of mass transfer coefficients as well as an increase in the skin friction.

Table 4. Rate of heat transfer coefficient Nu_x values for different values of Pr , Nb , Nt , n and Du

Pr	Nb	Nt	n	Du	Nu_x		
0.71	0.1	0.1	0.1	0.5	0.746187561347563		
1.00	0.1	0.1	0.1	0.5	0.707856729847486		
3.00					0.670804287489651		
0.1					0.3	0.769782183756867	
					0.5	0.780298476173734	
					0.3	0.3	0.779717360931973
						0.5	0.793736631397399
					0.2	0.2	0.772556776400390
						0.3	0.797670987097368
					1.0	0.786768609816987	
					1.5	0.812598919086301	

Table 5. Rate of mass transfer coefficient Sh_x values for different values of Le , Nb and Nt

Le	Nb	Nt	n	Sr	Sh_x		
0.3	0.5	0.1	0.1	0.5	0.895678168053718		
0.7	0.1	0.1	0.1	0.5	0.853665034039290		
0.9					0.821067039160937		
0.1					0.5	0.866786908742823	
					0.8	0.849871987659872	
					0.3	0.3	0.919610369829839
						0.5	0.930896981367903
					0.2	0.2	0.903565706418738
						0.3	0.922060361073783
					0.8	0.916673187346049	
					1.0	0.931604176304393	

5. Conclusions

In this current research work, Finite element method is implemented to provide the numerical solutions of nanofluid parameters in three dimensional flows. The numerical solutions are used to study the three dimensional structures with the flow of nanofluid to investigate the influence of well-known fluid parameters and the final results are:

- 1) Increasing values of Magnetic field parameter, the fluid velocities along x and y – directions are decreasing due to Lorentz force.
- 2) Rising values of Velocity power index parameter, the fluid velocities along x and y – directions are growing.
- 3) Increasing values of Prandtl number decreases temperature profiles and the reverse effect is noticed in case of rising values of Dufour number, Velocity power index parameter, Thermophoresis parameter and Brownian motion parameters.
- 4) In case of increasing values of Thermophoresis parameter, Soret number, Velocity power index parameter, the Concentration profiles are decreases and reduce for in case of Brownian motion parameter and Lewis number.
- 5) Finally, for program code validation, the authors have compared the present research work with the published results of Khan et al. [25] and observed good agreement.

Acknowledgements

The authors have not disclosed any funding.

Data availability

The datasets generated during and/or analyzed during the current study are available from the

corresponding author on reasonable request.

Author contributions

All authors have read and approved the manuscript.

Conflict of interest

The authors declare that they have no conflict of interest.

References

- [1] M. T. Akolade, A. S. Idowu, and A. T. Adeosun, "Multislip and Soret-Dufour influence on nonlinear convection flow of MHD dissipative Casson fluid over a slendering stretching sheet with generalized heat flux phenomenon," *Heat Transfer*, Vol. 50, No. 4, pp. 3913–3933, Jun. 2021, <https://doi.org/10.1002/htj.22057>
- [2] K. Kaladhar, E. Komuraiah, and K. M. Reddy, "Soret and Dufour effects on chemically reacting mixed convection flow in an annulus with Navier slip and convective boundary conditions," *Applied Mathematics and Nonlinear Sciences*, Vol. 4, No. 2, pp. 475–488, Dec. 2019, <https://doi.org/10.2478/amns.2019.2.00045>
- [3] A. S. Idowu and B. O. Falodun, "Effects of thermophoresis, Soret-Dufour on heat and mass transfer flow of magnetohydrodynamics non-Newtonian nanofluid over an inclined plate," *Arab Journal of Basic and Applied Sciences*, Vol. 27, No. 1, pp. 149–165, Jan. 2020, <https://doi.org/10.1080/25765299.2020.1746017>
- [4] K. B. Kasali, Y. O. Tijani, M. O. Lawal, and Y. T. Lawal, "Soret, Dufour and radiation effects of a viscoelastic fluid on an exponentially stretching surface using the Cattaneo-Christov heat flux model," *Multidiscipline Modeling in Materials and Structures*, Vol. 16, No. 6, pp. 1577–1594, Jun. 2020, <https://doi.org/10.1108/mmms-11-2019-0202>
- [5] J.-T. Hu and S.-J. Mei, "Combined thermal and moisture convection and entropy generation in an inclined rectangular enclosure partially saturated with porous wall: Nonlinear effects with Soret and Dufour numbers," *International Journal of Mechanical Sciences*, Vol. 199, p. 106412, Jun. 2021, <https://doi.org/10.1016/j.ijmecsci.2021.106412>
- [6] A. A. Yinusa, M. G. Sobamowo, M. A. Usman, and E. H. Abubakar, "Exploration of three dimensional squeezed flow and heat transfer through a rotating channel with coupled Dufour and Soret influences," *Thermal Science and Engineering Progress*, Vol. 21, p. 100788, Mar. 2021, <https://doi.org/10.1016/j.tsep.2020.100788>
- [7] Y. Rghif, B. Zeghmami, and F. Bahraoui, "Soret and Dufour effects on thermosolutal convection developed in a salt gradient solar pond," *International Journal of Thermal Sciences*, Vol. 161, p. 106760, Mar. 2021, <https://doi.org/10.1016/j.ijthermalsci.2020.106760>
- [8] S. Hussain, M. Jamal, and B. P. Geridonmez, "Impact of power law fluid and magnetic field on double diffusive mixed convection in staggered porous cavity considering Dufour and Soret effects," *International Communications in Heat and Mass Transfer*, Vol. 121, p. 105075, Feb. 2021, <https://doi.org/10.1016/j.icheatmasstransfer.2020.105075>
- [9] S. A. Khan, T. Hayat, and A. Alsaedi, "Irreversibility analysis in Darcy-Forchheimer flow of viscous fluid with Dufour and Soret effects via finite difference method," *Case Studies in Thermal Engineering*, Vol. 26, p. 101065, Aug. 2021, <https://doi.org/10.1016/j.csite.2021.101065>
- [10] T. Hayat, T. Nasir, M. I. Khan, and A. Alsaedi, "Numerical investigation of MHD flow with Soret and Dufour effect," *Results in Physics*, Vol. 8, pp. 1017–1022, Mar. 2018, <https://doi.org/10.1016/j.rinp.2018.01.006>
- [11] T. Hayat, S. Asghar, A. Tanveer, and A. Alsaedi, "Chemical reaction in peristaltic motion of MHD couple stress fluid in channel with Soret and Dufour effects," *Results in Physics*, Vol. 10, pp. 69–80, Sep. 2018, <https://doi.org/10.1016/j.rinp.2018.04.040>
- [12] G. Rasool, A. Shafiq, and D. Baleanu, "Consequences of Soret-Dufour effects, thermal radiation, and binary chemical reaction on darcy forchheimer flow of nanofluids," *Symmetry*, Vol. 12, No. 9, p. 1421, Aug. 2020, <https://doi.org/10.3390/sym12091421>

- [13] A. H. Usman, Z. Shah, U. W. Humphries, P. Kumam, and P. Thounthong, "Soret, Dufour, and activation energy effects on double diffusive convective couple stress micropolar nanofluid flow in a Hall MHD generator system," *AIP Advances*, Vol. 10, No. 7, Jul. 2020, <https://doi.org/10.1063/5.0014897>
- [14] P. S. Reddy and A. J. Chamkha, "Soret and Dufour effects on MHD convective flow of Al₂O₃-water and TiO₂-water nanofluids past a stretching sheet in porous media with heat generation/absorption," *Advanced Powder Technology*, Vol. 27, No. 4, pp. 1207–1218, Jul. 2016, <https://doi.org/10.1016/j.appt.2016.04.005>
- [15] S. Arun and A. Satheesh, "Mesoscopic analysis of MHD double diffusive natural convection and entropy generation in an enclosure filled with liquid metal," *Journal of the Taiwan Institute of Chemical Engineers*, Vol. 95, pp. 155–173, Feb. 2019, <https://doi.org/10.1016/j.jtice.2018.10.015>
- [16] B. Ali, Y. Nie, S. A. Khan, M. T. Sadiq, and M. Tariq, "Finite element simulation of multiple slip effects on MHD unsteady maxwell nanofluid flow over a permeable stretching sheet with radiation and thermo-diffusion in the presence of chemical reaction," *Processes*, Vol. 7, No. 9, p. 628, Sep. 2019, <https://doi.org/10.3390/pr7090628>
- [17] M. M. Bhatti and M. M. Rashidi, "Effects of thermo-diffusion and thermal radiation on Williamson nanofluid over a porous shrinking/stretching sheet," *Journal of Molecular Liquids*, Vol. 221, pp. 567–573, Sep. 2016, <https://doi.org/10.1016/j.molliq.2016.05.049>
- [18] A. M. Aly, "Natural convection over circular cylinders in a porous enclosure filled with a nanofluid under thermo-diffusion effects," *Journal of the Taiwan Institute of Chemical Engineers*, Vol. 70, pp. 88–103, Jan. 2017, <https://doi.org/10.1016/j.jtice.2016.10.050>
- [19] M. C. K. Reddy, G. Murali, S. Sivaiah, and N. Babu, "Heat and mass transfer effects on unsteady MHD free convection flow past a vertical permeable moving plate with radiation," *International Journal of Applied Mathematical Research*, Vol. 1, No. 2, pp. 189–205, Apr. 2012, <https://doi.org/10.14419/ijamr.v1i2.45>
- [20] S. Sivaiah, G. Muraligoud, G. Murali, M. C. K. Reddy, and S. Raju, "Unsteady MHD mixed convection flow past a vertical porous plate in presence of radiation," *International Journal of Basic and Applied Sciences*, Vol. 1, No. 4, pp. 651–666, Aug. 2012, <https://doi.org/10.14419/ijbas.v1i4.106>
- [21] M. Gundagani, S. Sheri, A. Paul, and M. C. K. Reddy, "Radiation effects on an unsteady MHD convective flow past a semi-infinite vertical permeable moving plate embedded in a porous medium with viscous dissipation," *Walailak Journal of Science and Technology*, Vol. 10, No. 5, pp. 499–515, Apr. 2013.
- [22] D. Gadipally and M. Gundagani, "Analysis of Soret and Dufour effects on unsteady MHD convective flow past a semi-infinite vertical porous plate via finite difference method," *International Journal of Applied Physics and Mathematics*, Vol. 4, No. 5, pp. 332–344, 2014, <https://doi.org/10.7763/ijapm.2014.v4.306>
- [23] G. Deepa and G. Murali, "Effects of viscous dissipation on unsteady MHD free convective flow with thermophoresis past a radiate inclined permeable plate," *Iranian Journal of Science and Technology (Sciences)*, Vol. 38, No. 3.1, pp. 379–388, Oct. 2014, <https://doi.org/10.22099/ijsts.2014.2437>
- [24] G. Murali, Ajit Paul, and N. V. N. Babu, "Numerical study of chemical reaction effects on unsteady MHD fluid flow past an infinite vertical plate embedded in a porous medium with variable suction," *Electronic Journal of Mathematical Analysis and Applications*, Vol. 3, No. 2, Jul. 2015, <https://doi.org/10.21608/ejmaa.2015.310762>
- [25] J. A. Khan, M. Mustafa, T. Hayat, M. A. Farooq, A. Alsaedi, and S. J. Liao, "On model for three-dimensional flow of nanofluid: An application to solar energy," *Journal of Molecular Liquids*, Vol. 194, pp. 41–47, Jun. 2014, <https://doi.org/10.1016/j.molliq.2013.12.045>
- [26] P. Yesodha, M. Bhuvanewari, S. Sivasankaran, and K. Saravanan, "Convective heat and mass transfer of chemically reacting fluids with activation energy along with Soret and Dufour effects," *Materials Today: Proceedings*, Vol. 42, pp. 600–606, 2021, <https://doi.org/10.1016/j.matpr.2020.10.878>
- [27] S. Hazarika, S. Ahmed, and A. J. Chamkha, "Investigation of nanoparticles Cu, Ag and Fe₃O₄ on thermophoresis and viscous dissipation of MHD nanofluid over a stretching sheet in a porous regime: A numerical modeling," *Mathematics and Computers in Simulation*, Vol. 182, pp. 819–837, Apr. 2021, <https://doi.org/10.1016/j.matcom.2020.12.005>
- [28] M. Shamshuddin, A. Abderrahmane, A. Koulali, M. R. Eid, F. Shahzad, and W. Jamshed, "Thermal and solutal performance of Cu/CuO nanoparticles on a non-linear radially stretching surface with heat source/sink and varying chemical reaction effects," *International Communications in Heat and Mass Transfer*, Vol. 129, p. 105710, Dec. 2021, <https://doi.org/10.1016/j.icheatmasstransfer.2021.105710>

- [29] S. A. A. Shah, N. A. Ahammad, E. M. T. E. Din, F. Gamaoun, A. U. Awan, and B. Ali, "Bio-convection effects on prandtl hybrid nanofluid flow with chemical reaction and motile microorganism over a stretching sheet," *Nanomaterials*, Vol. 12, No. 13, p. 2174, Jun. 2022, <https://doi.org/10.3390/nano12132174>
- [30] M. A. Kumar, Y. D. Reddy, B. S. Goud, and V. S. Rao, "An impact on non-Newtonian free convective MHD Casson fluid flow past a vertical porous plate in the existence of Soret, Dufour, and chemical reaction," *International Journal of Ambient Energy*, Vol. 43, No. 1, pp. 7410–7418, Dec. 2022, <https://doi.org/10.1080/01430750.2022.2063381>



Prof. Dr. **Murali Gundagani** received Ph.D. degree in Mathematics from SHIATS Govt. funded deemed University, Prayagraj, India, in 2014. Now he works at Sreenidhi University. His current research interests include computational fluid dynamics, mathematical modeling, numerical techniques, heat and mass transfer.



Dr. **Deepa Gadipalli** received Ph.D. degree in Mathematics from Osmania University, Hyderabad, India in 2013. Now she works at Chaitanya Bharathi Institute of Technology, Gandipet. Her current research interests include computational fluid dynamics and heat and mass transfer.



Dr. **Nirmala Kasturi V** received Ph.D. degree in Mathematics from JNTU Hyderabad, India in 2017. Now she works at Gokaraju Lailavathi Womens Engineering College. Her current research interests include probability and statistics, fluid dynamics.



Dr. **Poornakantha** received Ph.D. degree in Mathematics from Andhra University, Visakhapatnam, India in 2010. Now she works at Gayatri Vidya Parishad College of Engineering for Women. His current research interests include computational fluid dynamics, heat and mass transfer.

Weakly nonlinear analysis of Darcy–Brinkman gravity modulated biothermal convection in rotating porous media

P. A. Akhila¹ | B. Patil Mallikarjun¹  | Palle Kiran²

¹Department of Studies and Research in Mathematics, Tumkur University, Tumakuru, Karnataka, India

²Chaitanya Bharathi Institute of Technology Hyderabad, Hyderabad, Telangana, India

Correspondence

B. Patil Mallikarjun, Department of Studies and Research in Mathematics, Tumkur University, Tumakuru-572103, Karnataka, India.

Email: mbp1007@yahoo.com

Funding information

Karnataka Science and Technology Promotion Society (KSTePS), Grant/Award Number: MAT-03:2022-23/1019

Abstract

The present study investigates the gyrotactic micro-organism flow in a rotating porous medium containing Newtonian fluid. Using gravity modulation, Darcy–Brinkman biothermal convection is examined. Linear theory describes the stationary convective mode which derives the expression for critical Rayleigh number. This indicates the onset of bioconvection. The system's marginal stability is demonstrated by graphical and tabular representation which has a good agreement with each other. The Ginzburg–Landau equation governs the Nusselt number, which is used to further explore heat transfer. The study provides an explanation and graphical representation of the effects of the following factors on heat transfer: cell eccentricity, modified Vadasz number and bioconvective Rayleigh–Darcy number, modulation frequency, and amplitude along with Taylor number. The mean Nusselt number has been plotted in the current study. The effect of rotating porous media and gravity modulation is explained in this work. Additionally, a comparison graph is plotted to examine the effects of gravity, both modulated and unmodulated, on the Nusselt number. This demonstrates how well gravity modulation on rotating porous media controls the system's heat



Study of double-diffusive gravity modulated biothermal convection in porous media under internal heating effect

P. A. Akhila^{1,a}, B. Patil Mallikarjun^{1,b}, Palle Kiran^{2,c}, Ali J. Chamkha^{3,d}

¹ Department of Studies and Research in Mathematics, Tumkur University, Tumakuru 572103, India

² Chaitanya Bharathi Institute of Technology, Hyderabad, Telangana 500075, India

³ Faculty of Engineering, Kuwait College of Science and Technology, 35004 Doha, Kuwait

Received: 19 April 2024 / Accepted: 3 July 2024

© The Author(s), under exclusive licence to Società Italiana di Fisica and Springer-Verlag GmbH Germany, part of Springer Nature 2024

Abstract Double diffusion combined with thermo-bioconvection in porous media under two prominent effects such as gravity modulation and internal heating are considered in the present work. The impact of considering double diffusion and porous medium in the current problem is studied graphically. We deal with linear and weakly nonlinear theory of the system. Linear theory helps in the analysis of onset of convection. The stability of the system is also discussed in this section. Onset of convection is governed by critical(threshold) Rayleigh number Ra_c . The marginal stability curves are plotted between critical Rayleigh number and wavenumber for all the parameters that exist in the study which helps in analyzing the stability of the system. Weakly nonlinear stability analysis is carried out to study heat and mass transfer in the system. Due to the gravity modulation, there arise amplitude and frequency for the corresponding fluid under convection. From such nonlinear study, we arrive at an amplitude equation called Ginzburg–Landau (GL) equation. Further, on solving GL equation, we discuss heat and mass transfer in terms of Nusselt number Nu and Sherwood number Sh . The graphical study of heat and mass transfer is performed by plotting Nu versus time scale τ and Sh against τ , respectively, for various parameters existing in the study. The convection cells arise due to temperature difference between the horizontal plates are shown in the form of streamlines and isotherms.

List of symbols

h	Thickness of the porous layer
T_d	Temperature at lower boundaries
T_u	Temperature at upper boundaries
g_0	Mean gravity
\vec{g}	Acceleration due to gravity
e	Unit vector in the direction of z -axis
δ	Amplitude of gravity modulation
ω_g	Frequency of gravity modulation
Ω	Non-dimensional frequency of gravity modulation
ε	Small dimensionless parameter
\mathbf{V}_D	Darcy velocity
V	Velocity along y -axis
ϵ	Porosity of the porous medium
ν	Kinematic viscosity ($\frac{\mu}{\rho_0}$)
T	Temperature
T_0	Reference temperature
ρ_0	Density of the fluid at reference temperature
K	Permeability of the porous medium
P	Pressure

^a e-mail: pa.akhila.1993@gmail.com

^b e-mail: mbp1007@yahoo.com (corresponding author)

^c e-mail: pallekiran_maths@cbit.ac.in

^d e-mail: achamkha@yahoo.com

Nonlinear Thermal Instability in Nanoliquid Under Magnetic-Field Modulation Within Hele-Shaw Cell

S. H. Manjula^{1*} and Palle Kiran²

¹Department of Mathematics (S and H) Vignana's Foundation for Science, Technology and Research (VFSTR) Vadlamudi, Guntur, 522213 Andhra Pradesh, India

²Department of Mathematics, Chaitanya Bharathi Institute of Technology, Hyderabad, 500075 Telangana, India

In a nanoliquid-confined Hele-Shaw cell, the effect of magnetic-modulation is investigated. The goal of this study is to conclude the work described in Rai et al. [45] for oscillatory convection. The existence of the CGLE^{42,43} model is constrained by the condition $\omega^2 > 0$ and determined transfer analysis. The magnetic fluxes in Hele-shaw cells are governed by CGLE and magnetic modulation limitations. Changes in magnetic modulation can affect heat and mass transfer in terms of modulation frequency and amplitude. In addition, the findings of earlier research on heat and mass transport indicate that oscillatory mode is preferable than stationary mode. Further, the transport analysis is compared to previous research and shown to have improved results.

KEYWORDS: Nanofluids, Nonlinear Flow, Magnetic-Field, Hele-Shaw Cell, Magnetic Modulation, CGLE.

1. INTRODUCTION

Study of magneto convection was well documented in Chandrasekhar.¹ Numerous applications of magneto-convection might be observed in Planets, earth science, convection process in earth's interior layers, day-night convection profiles, electrical coils, construction of engine oils in the presence of electric fields, controlling convection in the presence of magnetic fields, drug delivery process, formation of materials in the presence of magnetic fields, thermal and mechanical engineering works related problems etc., Human life is related to the fields of electronics and electrical applications and producing huge magnetic abnormal fluctuations. In the case of the manufacture of electronic devices magnetic fields are fluctuated in their surroundings and create other effects. These fluctuations need to be investigated and controlled. The research work in the case of magnetic field modulation on convection flows is very short. It is observed in the literature that numerous research work is counted under gravity and thermal modulation than magnetic modulation. Now let us discuss the literature survey on magneto-convection for different modulations.

Siddheshwar et al.² studied magnetoconvection in the presence of both gravity and temperature modulation using the GL model. In order to quantify heat transport, they developed a third-order finite amplitude equation.

Srivastava et al.³ expanded this magneto convection to anisotropic porous layers with the Soret effect. Bhaduria and Kiran⁴ studied magneto-convection under magnetic field modulation and concluded that magnetic modulation is superior to gravity modulation and thermal modulation. Bhaduria and Kiran^{5,6} adapted the same magneto convection issue to a two-component fluid layer subject to temperature modulation. Manjula et al.⁷ studied the influence of thermal modulation and internal heating on heat transport through weakly nonlinear thermal instability in the presence of an applied magnetic field. Aminossadati et al.⁸ carried out numerical investigation on the laminar forced convection of water-Al₂O₃ nanofluid inside a horizontal microchannel. For the ranges of Hartmann number from 0 to 1000, solid volume percent from 0 to 0.04 and Reynolds number from 0 to 1000, the results of heat transfer are observed.

The Rayleigh-Bénard convection^{10,11} is a type of natural convection, occurring in a planar horizontal layer (Hele-Shaw) of fluid heated from below, in which the fluid develops a regular pattern of convection cells known as Bénard cells. Darcy-Bénard convection is a term used to describe Bénard-Rayleigh convection in porous media. Chandrasekhar's,¹ Drazin, and Reid¹¹ works revealed the essential investigations of hydromagnetic stability analysis. Henry Selby Hele-Shaw, who investigated the issue in Ref. [12], termed the phenomenon Hele-Shaw flow, which is described as Stokes flow between two parallel flat plates separated by an incredibly tiny space. Wooding¹³ studies thermal instability in a Hele-cell using a viscous fluid having variable vertical density gradient. The problem of a

*Author to whom correspondence should be addressed.

Email: manjubknd.bk@gmail.com

Received: 18 October 2021

Accepted: 10 April 2022



Analysis of weakly nonlinear Darcy–Brinkman bio-thermal convection in a porous medium under gravity modulation and internal heating effect

Akhila P.A.^{a,1}, Patil Mallikarjun B.^{a,*,1}, Palle Kiran^{b,1}

^a Department of Studies and Research in Mathematics, Tumkur University, Tumakuru 572103, India

^b Chaitanya Bharathi Institute of Technology Hyderabad, Telangana 500075, India

ARTICLE INFO

Keywords:

Gyrotactic microorganisms
Darcy–Brinkman model
Bio-thermal convection
Internal heating
Gravity modulation

ABSTRACT

In this study, we consider Newtonian fluid with gyrotactic microorganisms flowing through a porous medium. The effects of gravity field and internal heating are investigated on Darcy–Brinkman bio-thermal convection. The threshold Rayleigh number expression in the form of stationary mode is derived to study the onset of bioconvection. Further, heat transfer is investigated using Nusselt number, which is governed by Ginzburg–Landau equation. The influence of internal Rayleigh number, Vadasz number, modified bioconvective Rayleigh–Darcy number, cell eccentricity, modulation frequency and modulation amplitude on heat transfer is explored by the research and depicted graphically. Also the effect of the above parameters on the threshold Rayleigh number against the wave number is studied graphically. These graphical study is called as marginal stability analysis. Also, a comparative graph is plotted to study modulated and unmodulated effect of gravity on Nusselt number. This highlights the effectiveness of the gravity modulation and internal heating effect in controlling heat transport within the system.

1. Introduction

The study of fluid flow in a porous medium has significant practical applications in various fields. In recent times, a new area of research known as bioconvection in porous media has emerged and created interest in researchers and scientists. Bioconvection deals with the microbial and bacterial movement especially in oil production technologies. Hence, there is a need to study the interaction between bioconvection and natural convection theoretically.

Instability in fluid layer due to temperature within porous medium was extensively studied by Ingham and Pop [1]. Nield and Bejan [2] authored on internal free convection concerning to porous medium. A detailed study on heat transport due to fluid flow in rotating porous media was provided by Vadasz [3]. The above mentioned works mainly concentrate on thermal instability in the system. Similar studies on natural convection in fluid saturated porous media were made by taking into account the factors such as magnetic field, rotational modulation, gravitational modulation and other related effects. The Darcy–Brinkman equation is extensively used to investigate flow in porous media with high porosity [4]. Zhao et al. [5] studied the same under gravity modulation. Here, the chaotic nature of the fluid is stressed on. In this regard, enormous number of problems arise related to the study

of bioconvection in high porosity medium which is based on the Darcy–Brinkman model.

The term bioconvection refers to the phenomenon where convective patterns are formed as a result of the presence of self-propelled species of microorganism that are more in density than the surrounding fluid medium [6–8]. The responsive movement of organisms to various external stimuli like light, gravity, presence of food, chemicals etc., is known as taxis. Taxis can be classified based on the type of stimulus and whether the organism moves towards or away from it. Positive taxis, means attraction that occur when an organism or cell moves in the direction of the stimulus. On the other hand negative taxis, or repulsion, describes the movement away from the stimulus. In this paper, our focus will be on gyrotactic microorganisms which describes an organism's directional movement in response to gravitational force and viscous force. The theory and mathematical model for bioconvection of gravitactic microorganisms was developed by Childress et al. [9]. This theory describes the pattern formed by the suspended microorganisms. In this view, Pedley et al. [6] developed a linear stability theory for analyzing the stability of bioconvection involving gyrotactic microorganisms within a shallow layer of a regular fluid. Hill et al. [7] developed theoretical bioconvective model for the same.

* Corresponding author.

E-mail addresses: pa.akhila.1993@gmail.com (A. P.A.), mbp1007@yahoo.com (Patil Mallikarjun B.), pallekiran_maths@chit.ac.in (P. Kiran).

¹ All the authors have contributed equally.

Stochastic Analysis of Sesame efficiency in India exhausting SARIMA exemplary

Sreedhar Reddy Bhaskar

Sr. Asst. Professor, Department of Mathematics, CBIT Gandipet, Hyderabad (TS)-500075

ABSTRACT

This is an overview of Sesame production and manufacturing in India. The facts from 1966-67 to 2020-21 have been analyzed the usage of time sequence method. Versions from 1966-67 to 2019-20 are used for generation and forecasting. Figures from 2019-20 to 2020-21 are used for version verification. Autocorrelation function (ACF) and partial autocorrelation characteristic (PACF) had been calculated for statistics. Fixed Patty Jenkins' Correct Autoregressive Integrated Moving Average. Version verification the usage of known statistical methods. The universal performance of the version is validated by an assessment criterion that includes the percentage deviation of the fee and the mean percentage absolute error (MAPE) of the prediction. To forecast the location, we forecast the key years the usage of autoregressive joint shifting common (0,1,1) and autoregressive joint transferring common (0,1,1), respectively. The effects also exhibit that the 12-month area forecast for 2021 is 8.3219 million hectares in the decrease bound state, 10.3718 million hectares in the top sure state, and the manufacturing forecast is about 6.4445 million hectares in the decrease certain state. Hectares, if the upper restriction is 8.6487 million hectares. Slope fashions are examined exponentially or linearly. The ultimate outcomes proven that integrated linear rebar loading is a fantastic and volumetric method for field and manufacturing applications.

Keywords: Sesame; Linear GR; Compound GR; Seasonal Auto Regression Integrated Moving Averages; AIC; BIC ;MAPE.

1. INTRODUCTION

Sesame (*Helianthus annuus* L.) is one of the few crop species that originated in North America. It was first added to Europe via Spain, and unfold at some point of Europe as a curiosity till it reached Russia, where it was once as soon as surely adapted. After World War II, Russia's considerable oilseeds have been reintroduced to the United States, reviving hobby in the crop. Sesame production was later developed by means of entrepreneurs as an oilseed crop, birdseed crop, and human snack meals in the Great Plains of the United States. In India, Sesame used to be delivered as an oil seed crop in 1969 and before that it was once used as an ornamental plant. Among the main Sesame producers in the country, Karnataka is among the pinnacle six states. Karnataka is the essential Sesame producing state in India with a production of 3.04 lakh tonnes from an vicinity of 7.94 lakh hectares found throughout Andhra Pradesh, Maharashtra, Bihar, Orissa and Tamil Nadu (Figure 1). As about eighty percentage of the region is rainfed, Sesame manufacturing follows systemic climatic conditions. In terms of productivity, Bihar leads with 1402 kg, followed via Tamil Nadu with 1328.7 ha, with each nation averaging less than 25000 ha of irrigated crops. The average productivity of the all India vary is 900 ha relying on climatic prerequisites and irrigation which are crucial factors for excessive yield.

2. REVIEWS OF LITERATURE

Shukla and Jharkharia (2011) Investigated the applicability of autoregressive joint transferring averages in the wholesale vegetable market through exploiting sales of onion, a perishable vegetable. Data accumulated from Ahmedabad wholesale market, India. Validation of variations used to be carried out the usage of comparable market potato sales information. The (2, 0, 1) version of the autoregressive joint moving common is in right health, and the version parameters verify that revenue in the present day period are relatively inspired when using the previous period's earnings. [2].

Adilet al. (2012) Attempted to predict name and transport in Punjab province of Pakistan the usage of the integrated shifting average model of autoregressive regression. Based on the ACF and PACF graphs, the autoregressive joint moving common (1, 1, 0) is healthy for location and production, and the autoregressive joint transferring average model (1, 1, 1) for onion consumption becomes healthful beauty. have. Onion consumption and manufacturing loss predicted in 2025. The projected location below onion cultivation may be 47,484 thousand hectares and the projected production in 2025 can also be 372,403 thousand tons.. [3].

Sudhaet al. (2013) Growth in maize location, manufacturing and yield between 1970-71 and 2008-09 used to be evaluated. Various polynomial modes, such as linear, quadratic, cubic and various incremental modes, particularly logarithmic, inverse, exponential, compound and strength modes are used. To take a look at the mode. The dice function has become a well-equipped model for predicting room, vessel and corn yields because it has a most adjustment of R2. [4].

Koujalagiet al. (2014) Predict make bigger in domestic development, production, yield and export of Karnataka between 1987-88 and 2009-10. The linear shy away version is equipped one at a time for grenade location, processing and yield. There has been an explosion in pomegranate production, which is based entirely on the leaves of the variety. The website online below these trees grows drastically in Koppal and Bagalkot districts [5].

Debnath et al. (2015) Predict the area of cotton grown and produced in India the usage of an autoregressive built-in transferring common version. Overlapping time sequence from 1950 to 2010 had been modified for the study. Auto Regressive Integrated Moving Averages(0, 1,0) Auto Regressive Integrated Moving Averages(1, 1, 4) and Auto Regressive Integrated Moving Averages(0, 1, 1) are entirely featured variations for forecasting. It seems there is. Origin, production and yield of cotton in India. This estimate suggests that if the modern-day charge expand is sustained, manufacturing and yield for 12 months 2020 could be 10.92 million ha, 39.19 million bales at 170 kg and 527 kg per hectare. Indicates the presence [6].

Sajid Ali Et Al. (2016) Check out our strive to forecast manufacturing and yield of essential mills of Pakistan, specially sugarcane and cotton crops, the usage of Autoregressive Moving Average (ARMA) and Autoregressive Integrated Moving Average forecasting methods. Data from 1948 to 2012 were used to task production and yield for each plant for 18 years from 2013 to 2030. ARMA(1, 4), ARMA(1, 1) and ARMA(0, 1) are classified as appropriate for sugarcane production. , sugarcane yield, and cotton production, respectively, and autoregressive joint transferring averages (2, 1), 1) had been transformed to the proper version with the modified cotton yield forecast. Some diagnostic exams were additionally armed mode and nicely geared up [7].

B R Sreedhar (2021) in welcome find out about erect that the model grown for the nut district presented, individually, the joint autoregressive mobile average (0, 1, 1) and the joint autoregressive affecting common (0, 1, 1). According to the handy forecasts making use of the developed model, it is clear that the field cultivated accompanying peanuts suitable to know-how a beneficial fashion in result in the coming age. The genuineness of the concluded worth perhaps established when file is accessible for lead periods. Important for the domain, the result for the study ending suggests that capable measures are wanted to adjoin fee to nut in India.[8]

3. METHODOLOGY

This discussion is principally based on secondary records on Indian Sesame yield, estimation of charge increases, area forecasting and production. Production data accrued by using the Department of Economic Statistics, Ministry of Agriculture and Cooperation, India, for the period 1966-67 to 2020-21, Sesame crop location. Agricultural data from 1966-67 to 2020-21 have been converted to construct and forecast versions. Changed from 20/2019 to 22/2021 for use in version validation.

3.1. Estimation of Growth Rates

A appear at the facts, ie from 1966-67 to 2020-21. Keeping the targets, linear incremental cost (LGR) and compound incremental value (CGR) for crop traits were expected with the help of making Sesame crop in India, subsequent functions of Sesame crop in India. [9].

3.1.1. Linear increase characteristic

Linear increase characteristic is given by $\omega_t = f + d_t + e_t$ with the aid of using

Where, t is the time in years, unbiased variable, W_t is the fashion price of the established variable c and d are constants or parameters and e_t is blunders term

The above equation is equipped with the aid of using the use of the least squares approach of estimation.

The linear increase price is calculated with the aid of using the formula: Linear increase price(LGR%) = $d/\bar{y} \times 100$

3.1.2.Compound increase characteristic

Compound increase characteristic is given with the aid of using

$$\omega_\tau = \gamma \alpha^\tau \text{ (or) } \text{Log } \omega = \log \gamma + \tau \log \alpha$$

The compound increase price (CGR %) is calculated with the aid of using the use of the formula

$$\text{CGR } (\%) = (\text{antilog } (D-1)) \times 100$$

3.2.Auto Regressive Integrated Moving Model

Auto Regressive Integrated Moving Averages technique is also known as Box-Jenkins technique. The Box-Jenkins process is associated with becoming an autoregressive joint moving average version of a given set of statistics. The styles evolved through this technique are commonly known as SAIRMA styles because they use a mixture of auto regressive (AR), integration (I)-join change contrast technique and common transfer (MA) operations to provide forecasting. (Box, and G.M. Jenkin, 1976) . A version of SAIRMA is usually called Seasonal Auto Regressive Integrated Moving Averages(p, d, q).

Autoregressive correlative shifts are expressed in a general form:

If $\varphi_t = \nabla^b r_t = (\mathbf{1} - \mathbf{B})^d r_t$ then

$$\varphi_t = \beta_1 \varphi_{t-1} + \beta_2 \varphi_{t-2} + \dots + \beta_p \varphi_{t-p} + \delta_t - \beta_1 \delta_{t-1} - \beta_2 \delta_{t-2} - \dots - \beta_p \delta_{t-p}$$

Where, ∇ is distinction operator, χ is the returned shift operator, that is $\chi(X_t) = X_{t-1}$

p is the variety of autoregressive terms, q the variety of transition common terms, d the variety of moments of stationery that results in a permutation. The primary goal of becoming this version of Auto Regressive Integrated Moving Averages is to discover the stochastic technique of the time sum and accurately anticipate destiny values. These strategies have additionally been useful in numerous state of affairs involving discrete-time addition and fashion construction for dynamical systems. But this technique does not work well for lead times or for seasonal aggregation with a large random component. A stochastic technique is neither a desk band nor a desk bond. The first aspect to note is that the time collection requirement is not desk bound and the regular version is more effective for desk bound time collection. Since the Auto Regressive Integrated Moving Averages fashion is most effective for a desk-bound period collection, the primary level of the Box-Jenkins version is to downgrade the non-desk collection to a desk-bound collection by taking first-order differences. The basic layers of building a Box-Jenkins predictive version are as follows. i) identification ii) parameter

estimation iii) diagnostic testing and predictions.

3.3. Identification Stage

A cross-check with a chronology statistics table was conducted and it was found that Sesames were produced for India. A large and robust autoregressive joint moving average model was developed from statistics and used to forecast production in India, a potential growth location. His next five years. The autoregressive joint moving average mode was identified by finding the baseline values of the order of non-seasonal parameters 'p' and 'q'. They were obtained by searching for giant spikes in the autocorrelation and partial autocorrelation functions. At the identity level, one or more methods were tentatively selected that we believed provided a statistically accurate representation of the available data. Exact estimates of the version parameters were then obtained by the method of least squares.

3.4. Estimation Stage

Auto Regressive Integrated Moving Averages fashions are outfitted and accuracy of the version turned into examined on the idea of diagnostics statistics.

3.5 Indicative Checking

The great healthy version turned into decided on primarily based totally on the subsequent diagnostics.

Low Akaike Information Criteria (AIC): - AIC is predicted through

$AIC = (-2 \log L + 2 w)$, in which $w = p + q$ and L is the probability function. Sometimes, SBC is likewise used and predicted through $SBC = \log \sigma^2 + (v \log s)/n$.

3.6. Prognostication Accuracy Checking

An excellent version is used for forecasting mainly based on screening accuracy between autoregressive joint moving averages with excellent dressings and exponential smoothing method. In particular, accuracy is tested using the RMSE and MAPE measures. A major part of the statistics used to form the version is called the school set and a small part of the statistics (usually 10%) used to test the prediction accuracy is called the check out set.

3.7. Prognostication

The latter version is used to generate predictions that approximate fate values. R software was used for time-aggregation evaluation and growing autoregressive joint moving average trends and forecasts.

4. OUTPUT AND CONFAB

4.1. Assessment of Growth Rates

The linear and composite boom expenditures had been 0.91 and 1.13 per cent per year respectively for the Sesame crop position searching at the duration for production 2.39 and 3.06 per cent per year respectively. Sesame crop in India. It displayed a high high-quality massive fashion for place and production beneath the Sesame crop in India. Table 1 suggests the linear and composite increase costs of Sesame area and manufacturing with 1 percentage magnitude degree.

Table-1: Evolution rates for area, production of Sesame crop in India

India	LGR (%)	CGR (%)
Area	0.91**	1.13**
Production	2.39**	3.06**

** Significance at 1% level

Table-2: Values of Auto Correlation Function and Partial Correlation Function of Area and Production of Sesame Data.

Lag	Auto Correlation Function(ACF)-Area	Partial Correlation Function(PACF)-Area	Auto Correlation Function(ACF)-Production	Partial Correlation Function(PACF)-Production
0	1.000		1.000	
1	-0.622	-0.411	-0.469	-0.429
2	0.212	-0.322	0.154	-0.326
3	-0.119	-0.123	-0.271	-0.289
4	0.087	-0.221	0.193	-0.163
5	0.026	0.411	0.251	0.151
6	-0.243	-0.132	-0.243	-0.324
7	0.201	-0.213	0.047	-0.238
8	-0.217	-0.112	-0.293	-0.324
9	0.221	-0.212	0.129	-0.219
10	-0.210	-0.231	-0.219	-0.516
11	0.284	0.123	0.148	0.312
12	-0.145	-0.314	-0.542	-0.214
13	0.136	0.115	-0.215	0.231
14	-0.213	-0.124	0.321	-0.114
15	0.214	0.210	0.141	0.321
16	-0.223	-0.109	-0.213	-0.215
17	0.124	0.191	0.119	0.156

Table-3:AIC and BIC values for tentative Model

S.No	Sesame	ARIMA (p, d, q)	AIC	AICc	BIC	σ^2 (Variance)
1	Area	1, 0, 1	91.37	95.17	101.4	0.2931
		1, 1, 1	91.64	90.12	94.61	0.2980
		0, 1, 1	89.13	89.20	93.04	0.2824
		0, 1, 2	90.69	91.17	96.66	0.2892
2	Production	1, 0, 1	61.49	62.29	69.52	0.1557
		1, 1, 1	56.15	56.63	62.11	0.1534
		0, 1, 1	52.17	52.41	54.15	0.1496
		0, 1, 2	56.14	56.62	62.11	0.1534

Table-4:Valuations of the fitted Auto Regressive Integrated Moving Averages model for AREA of Sesame

ME	RMSE	MAE	MPE	MAPE	MASE	ACF1
0.1164	0.1353	0.3009	1.1632	4.1328	0.9048	-0.1382

Table-5:Evaluations of the fitted Auto Regressive Integrated Moving Averages model for PRODUCTION of Sesame

ME	RMSE	MAE	MPE	MAPE	MASE	ACF1
0.0766	0.3209	0.2874	1.1747	4.3429	0.9141	-0.0102

ME- Mean Error, RMSE- Root Mean Square Error, MAE- Mean Absolute Error, MPA- Mean Percentage Error, MAPE- Mean Absolute Percentage Error, MASE- Mean absolute Scaled Error, ACF- Auto Correlation Function

Table-6: Prognostication -Area with Confidence Limits at 95%

Year	Point Forecast	Low 95%	High 95%
2019	7.1234	6.1325	9.1154
2020	7.3245	6.1458	9.0023
2021	7.2157	6.2135	9.1001
2022	7.4468	6.1457	9.2140
2023	7.108	6.2214	9.1145
2024	7.3651	6.1487	9.1234
2025	7.2301	6.2347	9.1156
2026	7.1911	6.1247	9.1212
2027	7.1241	6.0021	9.1145
2028	7.3254	6.1581	9.1231
2029	7.1234	6.1234	9.1123
2030	7.0147	6.1125	9.1231

Table-7 Prognostication --Production with Confidence Limits at 95%

Year	point Forecast	L 95%	H 95%
2019	5.5466	4.7860	7.3072
2020	5.5762	4.6575	7.4358
2021	5.5923	4.5453	7.5479
2022	5.6123	4.4445	7.6487
2023	5.6962	4.3522	7.7411
2024	5.7523	4.2665	7.8268
2025	5.8236	4.1862	7.9071
2026	6.0231	4.1104	7.9829
2027	6.1235	4.0383	8.0549
2028	6.5123	4.9696	8.1237
2029	7.0235	4.1325	8.9786
2030	7.7569	4.8675	9.0235

Table-8:ACF and PACF values of Residuals at AUTO REGRESSION INTEGRATED MOVING AVERAGES(0,1,1) Area and Production of Sesame

Lag	ACF-Area	PACF-Area	ACF-Production	PACF-Production
0	1.000		1.000	
1	0.007	0.008	0.008	0.008
2	-0.003	-0.013	-0.013	-0.003
3	-0.139	-0.119	-0.129	-0.129
4	0.113	0.117	0.113	0.107
5	0.125	0.126	0.135	0.136
6	-0.130	-0.148	-0.140	-0.168
7	-0.124	-0.179	-0.114	-0.079
8	-0.157	-0.135	-0.117	-0.165
9	0.110	0.024	0.100	0.034
10	-0.052	-0.095	-0.032	-0.085
11	0.026	0.013	0.016	0.033
12	-0.166	-0.029	-0.126	-0.079
13	-0.174	-0.238	-0.124	-0.248
14	0.039	0.011	0.069	0.121
15	0.025	0.025	0.045	0.045
16	-0.002	-0.117	-0.022	-0.137
17	-0.016	0.017	-0.026	0.077

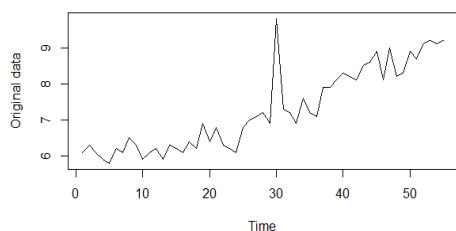


Fig-1(a): Base data-Area

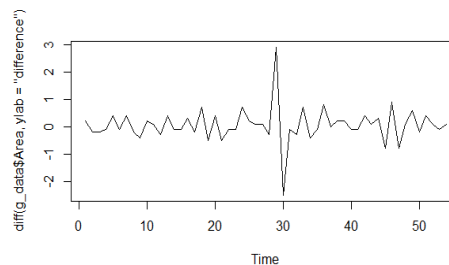


Fig1(b): I st Differences –Area

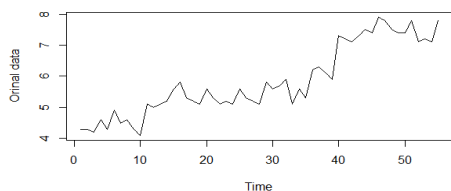


Fig-2(a): Base data-Production

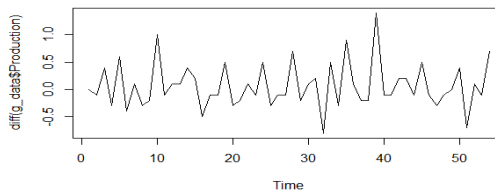


Fig-2(b): I st Differences –Production

4.2.Build Auto Regressive Integrated Moving Averages model for Area and Production of Sesame Crop

4.2.1. Identification

The first step in the analysis used to be to plot the given data. Figure 1 suggests the location and production of Indian Sesame from 1966-67 to 2017-18. Inspection of Figure 1 revealed a tremendous vogue over time, indicating nonstationarity of the series. This used to be tested via autocorrelation function (ACF) partial autocorrelation characteristic (PACF). To stabilize the series, it was originally divergent however then the facts reached a stationary region and Sesame yields, as shown in Figure 2. The subsequent step is to identify the p and q values. For this purpose, more than a few orders of autocorrelation coefficients and partial autocorrelation coefficients of X are calculated (Table 2). Figures three and 4 show the location and product data, autocorrelation characteristic (ACF) and partial autocorrelation function (PACF). We reviewed eight primary autoregressive joint shifting average models and selected the one that comfry the smallest AIC (Akaike Information Criterion) and SBC (Schwartz Bayesian Criterion). For AIC and BIC, select the terrific model: autoregressive joint moving common (0, 1, 1) for the Sesame region. Autoregressive built-in transferring average (0,1,1) for Sesame production has the lowest values for AIC and SBC. shown in Table three

4.3. Model Estimation and Verification

Indian Sesame range, manufacturing model parameters were estimated using R software program document estimation results. Predicted values the use of autoregressive joint shifting averages the usage of model fitting information such as RMSE and MAPE values are proven in Tables four and 5. Model validation entails inspecting the model residuals to see if there are still systematic patterns that can be eliminated to improve the chosen autoregressive integration. Moving average.

4.4. Diagnostic Checking

Examining the auto correlations and partial auto correlations of the residuals of various orders. Fig. 5 shown the ACF and PACF of the residual and Box L-Jung statistic non-significant result also indicate “good fit” of the model.

4.5 Prognostication

Using autoregressive joint transferring average (0,1,1) Sesame area model and autoregressive joint transferring average (0,1,1) Sesame production mannequin to predict place and yield of Indian Sesame crop over a 6-year period. to do The envisioned values are proven in Table 6. Hence, the nice overall performance is observed with autoregressive embedded shifting common (0,1,1) with R2 cost of 98.00% each Sesame vary mannequin and product model. The accuracy of both earlier than and after predictions was tested the usage of the following checks such as mean squared error (MSE) and suggest absolute proportion error (MAPE). An autoregressive joint moving average mannequin is principally designed to predict the variable in question. To assess the predictive ability of the geared up autoregressive joint transferring common model, a key measure of forecast accuracy used to be calculated for the sample period. Mean absolute percentage error (MAPE) for the Sesame region, production is 4.612, with measurements of 4.942, indicating low forecast

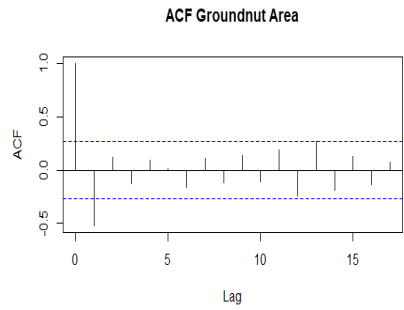


Fig-3(a): ACF- Area

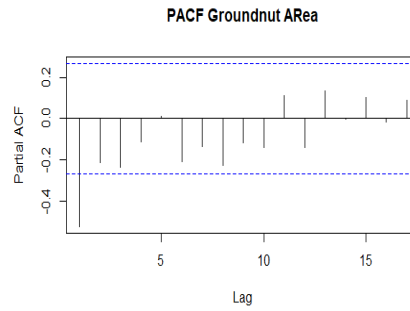


Fig-3(b):PACF- Area

uncertainty.

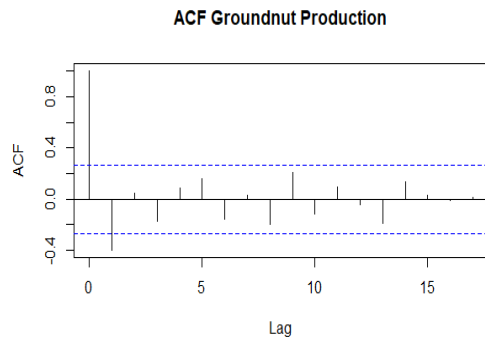


Fig-4(a): ACF-Production

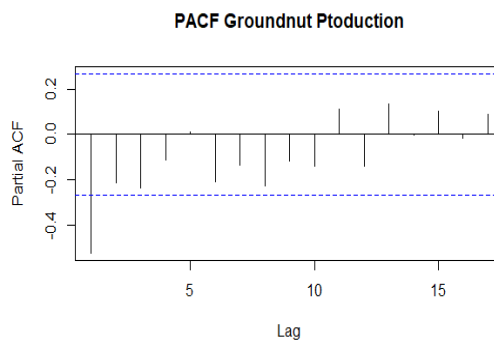


Fig-4(b): PACF- Production

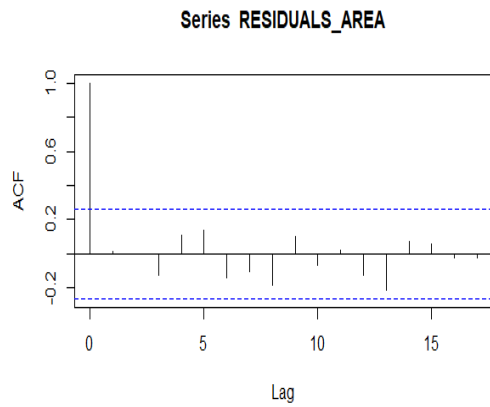


Fig-5(a): Residuals ACF -Area

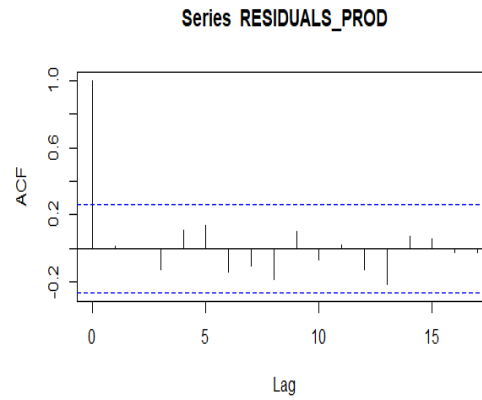


Fig-5(b): Residuals PACF -area

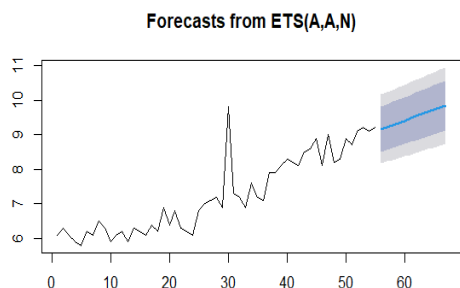
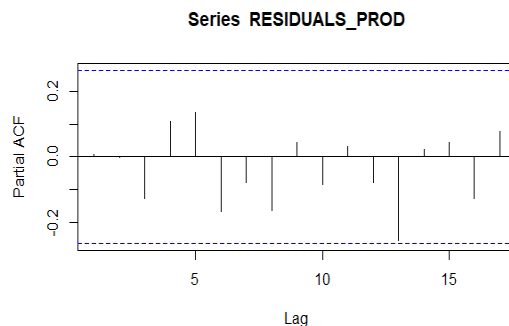
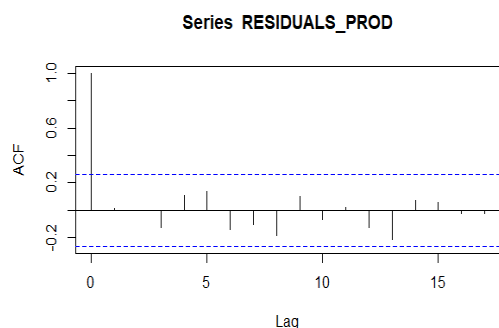


Fig-6(a): Residuals ACF – Production

Fig-7: Forecast of Sesame area

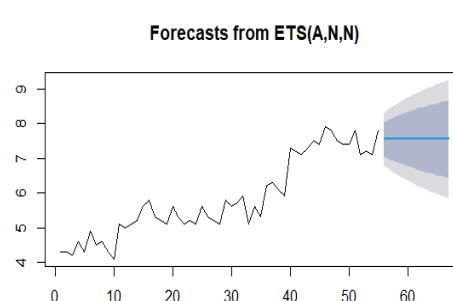


Fig-6(b): Residuals PACF - Production

Fig-8: Forecast of Sesame production

5. CONCLUSION

In this study, the developed models for Sesame place have been decided as autoregressive joint transferring common (0, 1, 1) and autoregressive joint moving average (0, 1, 1), respectively. The projections reachable the use of the developed models exhibit that the projected Sesame acreage and manufacturing will exhibit a superb fashion in the coming years. Validity of the expected price can be validated if data is reachable for the lead period. The linear and compound growth prices of Sesame at some point of the study duration proved to be wonderful and good sized for regional production, suggesting that terrific measures ought to be taken for Sesame enchantment in India.

REFERENCES

- [1] **Shukla M, Jharkharia S.** Application of ARIMA models in wholesale vegetable market: An investigation. *Int. Conference Industrial Engineering Operations Management, Kuala Lumpur, Malaysia.* 2011;24:1125-1130.
- [2] **Adil SA, Maqsood A, Bakhsh K, Hassan S.** Forecasting demand and supply of onion in Pakistani Punjab. *Pakistan J. Agric. Sci.* 2012;49(2):205-210.
- [3] **Sudha CHK, Rao VS, Suresh CH.** Growth trends of maize crop in Guntur district of Andhra Pradesh. *Int. J. Agric. Stat. Sci.* 2013;10(2):115-121.
- [4] **Koujalagi CB, Patil BL, Murthy C.** Growth trends in area, production, productivity and export of pomegranate in Karnataka: An economic analysis. *Inter. J. Commerce and Business Manage.* 2014;7(1):11-15.
- [5] **Debnath MK, KarticBera, Mishra.** Forecasting area, production and yield of cotton in India using ARIMA Model. *Res & Rev: J. Space Sci. & Tech.* 2015;2(1):16- 20.
- [6] **Sajid Ali, NoumanBadar, Hina Fatima.** Forecasting Production and Yield of Sugarcane and Cotton Crops of Pakistan for 2013-2030. *Sarhad J. Agric.* 2016;31(1):1-9.
- [7] **Mahesh M, Jain BC.** Compound Growth Rate (CGR) of area, production and productivity of papaya in Raipur district of Chhattisgarh,” *International Journal of Agriculture, Environment and Biotechnology.* 2013;6(1):139-143.

- [8] **Box GEP, Jenkin GM.** Time series of analysis, forecasting and control, Sam Franscico, Holden Day, California. USA; 1976.
- [9] **Biswa R, Bhattacharyya B.** ARIMA modelling to forecast area and production of rice in West Bengal. *Journal of Crop and Weed.* 2013;9(2):26-31.
- [10] **Indira R, Datta A.** Univariate forecasting of state-level agriculture production“, *Economic and Political Weekly.* 2003;38 (18):1800-1803.
- [11] **Saeed N, Saeed A, Zakria M, Bajwa TM.** Forecasting of Wheat production in Pakistan using ARIMA models”, *International Journal of Agriculture Biology.*2000;2(4):352-353.
- [12] **B R Sreedhar.** Forecast Analysis of Yearly Groundnut Productivity in India Using Auto Regressive Integrated Moving Averages model, “*Nat. Volatiles & Essent. Oils,*”. 2021; 8(5): 4286-4298.



Fitted Difference Scheme on a Non-uniform Mesh for Singularly Perturbed Parabolic Reaction–Diffusion with Large Negative Shift and Non-local Boundary Condition

Wakjira Tolassa Gobena^{1,2} · Gemechis File Duressa^{2,3} · Lakshmi Sireesha Challa^{1,2}

Accepted: 2 August 2023 / Published online: 21 September 2023

© The Author(s), under exclusive licence to Springer Nature India Private Limited 2023

Abstract

In this paper, we study the numerical solution of singularly perturbed parabolic reaction–diffusion problems with large delay in space, and the right end plane is non-local boundary condition. As the perturbation parameter approaches zero, the solution to this problem exhibits a parabolic boundary layers and an interior layer have been exhibited in the solution domain. To solve these problems, we develop a numerical scheme which combines the cubic spline scheme for the spatial derivatives, and backward difference scheme for the time derivative. To resolve the boundary layers, we use the piecewise uniform Shishkin types mesh (Standard Shishkin mesh, Bakhvalov–Shishkin mesh) for the spatial discretization. To treat the non-local boundary condition, numerical integration method is applied. A priori bounds for the solution and its derivatives of the continuous problem are given, which are necessary to analyze the error. Stability analysis and error estimates are obtained. Some numerical results are considered to support our theoretical result, which shows the ε -uniform convergent results.

Keywords Singular perturbation · Cubic spline · Non-uniform mesh · Parabolic reaction diffusion · Non-local boundary condition

Mathematics Subject Classification 65L11 · 65M06 · 65M12

Gemechis File Duressa and Lakshmi Sireesha Challa have contributed equally to this work.

✉ Wakjira Tolassa Gobena
wakjira.tolassa@gmail.com

Gemechis File Duressa
gammeef@gmail.com

Lakshmi Sireesha Challa
sirii.challa@gmail.com

¹ Department of Mathematics, Nekemte College of Teacher Education, 88 Nekemte, Oromia, Ethiopia

² Department of Mathematics, College of Natural Science, Jimma University, 378 Jimma, Oromia, Ethiopia

³ Department of Mathematics, University College of Science, Saifabad Osmania University, CBIT, Hyderabad, India

Research Article

Lakshmi Sireesha Challa, Ravi Ragoju, Sathishkumar Veerappampalayam Easwaramoorthy, and Jaehyuk Cho*

Linear instability of the vertical throughflow in a porous layer saturated by a power-law fluid with variable gravity effect

<https://doi.org/10.1515/phys-2024-0049>

received November 24, 2023; accepted June 05, 2024

Abstract: The present study investigates the thermal convection of a power-law fluid in a horizontal porous layer that is heated from below. The study of flow in a porous medium is important because of its applications in various fields such as agriculture, geothermal sciences, and engineering. Linear instability analysis is performed using the normal mode method to solve the governing equations after non-dimensionalization. The `bvp4c` routine in MATLAB R2020a has been used to solve the raised problem for linear instability. The impact of gravity parameter, Peclet number, and power-law index on linear instability has been investigated. Linear and quadratic variations of gravity field are considered. From the results, it is evident that the critical Rayleigh number exhibits a non-monotonic relationship with the Peclet number. Increasing the gravity variation parameter leads to a more stable system, particularly in the case of linear gravity variation.

Keywords: linear stability, porous media, power-law fluid, variable gravity

Nomenclature

d	length (m)
k	thermal diffusivity (m ² /s)
K	permeability (H/m)
T	temperature (K)
t	time (s)
P	pressure (N/m ²)
g	acceleration due to gravity (m/s ²)
$\bar{\mathbf{u}}$	fluid velocity (m/s)
$\bar{u}, \bar{v}, \bar{w}$	velocity components
w_0	prescribed vertical throughflow velocity
Dimensionless parameters	
n	power-law index
Pe	Peclet number
q	wave number
Ra	Rayleigh number
Greek symbols	
β	thermal expansion coefficient ((m/m)/°C)
σ	ratio of heat capacitance
μ	consistency factor
ϕ	porosity (mL/min)
ρ	fluid density (kg/m ³)
χ	thermal diffusivity (m ² /s)
δ	gravity parameter

* **Corresponding author: Jaehyuk Cho**, Department of Software Engineering and Division of Electronics and Information Engineering, Jeonbuk National University, Jeonju-si, 54896, Republic of Korea, e-mail: chojh@jbnu.ac.kr

Lakshmi Sireesha Challa: Department of Mathematics, CBIT Hyderabad, Hyderabad, India

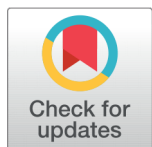
Ravi Ragoju: Department of Applied Sciences, National Institute of Technology Goa, Goa, India

Sathishkumar Veerappampalayam Easwaramoorthy: Department of Computing and Information Systems, Sunway University, 47500, Petaling Jaya, Selangor Darul Ehsan, Malaysia

1 Introduction

Throughflow is a type of irregular horizontal internal water flow within the soil mantle, which occurs when the soil is fully saturated due to high precipitation. Understanding the onset of convective phenomena and throughflow influence in porous domains holds significant importance in various geophysical applications within the Earth and in technical

RESEARCH ARTICLE


 OPEN ACCESS

Received: 08-10-2023

Accepted: 22-12-2023

Published: 13-01-2024

Citation: Kumar SR, Rao CR, Rao CP, Ramani VS (2024) Seasonal Trend Analysis of Major Air Pollutant (PM_{2.5} and PM₁₀) Concentration in Visakhapatnam During 2020 – 2022: A Case Study. Indian Journal of Science and Technology 17(3): 258-269. <https://doi.org/10.17485/IJST/v17i3.2549>

* Corresponding author.

ravikumar25450@gmail.com**Funding:** None**Competing Interests:** None

Copyright: © 2024 Kumar et al. This is an open access article distributed under the terms of the [Creative Commons Attribution License](https://creativecommons.org/licenses/by/4.0/), which permits unrestricted use, distribution, and reproduction in any medium, provided the original author and source are credited.

Published By Indian Society for Education and Environment ([iSee](https://www.indjst.org/))

ISSN

Print: 0974-6846

Electronic: 0974-5645

Seasonal Trend Analysis of Major Air Pollutant (PM_{2.5} and PM₁₀) Concentration in Visakhapatnam During 2020 – 2022: A Case Study

Sistla Ravi Kumar^{1*}, Ch Ramasanyasi Rao², Ch Prabhakara Rao³, V Sree Ramani⁴

¹ Associate Professor, Department of Physics, Vignan's Institute of Information technology, Visakhapatnam, 530049, Andhra Pradesh, India

² Associate Professor & HOD, Department of Applied Mathematics, MVR Degree & PG College, Visakhapatnam, 530026, Andhra Pradesh, India

³ Professor, Department of Mathematics (BS&H), Raghu Engineering college (Autonomous), Visakhapatnam, 531162, Andhra Pradesh, India

⁴ Assistant Professor, Department of Mathematics, Chaitanya Bharathi Institute of technology, Gandipet, Hyderabad, 50007, Telangana, India

Abstract

Objective: The main objective of the present study is to analyze the seasonal variations of major particulate air pollutants (PM_{2.5} and PM₁₀) from January 2020 to December 2022 in the industrially developed Visakhapatnam City and its comparison with previous existing studies from January 2018 - December 2020. **Methods:** The real-time daily mass concentrations of air pollutants in Visakhapatnam recorded by the Central Pollution Control Board (CPCB) are collected for the present study. The monthly average observations of pollutants such as PM_{2.5}, PM₁₀, and PM_{2.5}/PM₁₀ in each season are considered for the present study, and pollutants trends are studied from January 2020 - December 2022. The fine particles below 100µm (RSPM) and coarse particles > 100µm (TSPM) are treated as primary pollutants and pollutant concentration is determined based on prevailing meteorological and topographic factors. In the present study, the pollutant intensity is analyzed using the Pearson correlation coefficient for various seasons. Similarly, statistical analysis is also implemented on particulate air pollutants (PM_{2.5} and PM₁₀) from January 2020 to December 2022. **Findings:** From Table 1 PM_{2.5} levels fall within the range of 16 - 96 µg/m³ and the minimum PM_{2.5} level is in April 2020 and maximum in December 2020. According to AQI standards, moderate pollution indicates the fall of the PM₁₀ levels within the range of 53-196 µg/m³ during 2020-2022 minimum in April 2020 and maximum in December 2020. The present study recorded high pollutants of PM_{2.5} and PM₁₀ in Visakhapatnam in the winter season during 2020-2022. The obtained result reveals that high PM_{2.5} and PM₁₀ mass concentrations in winter exceed the NAAQS limit and better air quality is observed especially in summer and during monsoon season. The ratio

between $PM_{2.5}$ and PM_{10} is minimal in May 2020 and almost similar maximum values from November - 2020 to December 2020. This indicates that PM_{10} concentration is maximum in May 2020 and minimum during November - 2020 to December 2020. The ratio between $PM_{2.5}$ and PM_{10} is maximum in November 2021 and minimum in September - 2021. This indicates that PM_{10} concentration is less in November 2021 and maximum in September - 2021. The ratio between $PM_{2.5}$ and PM_{10} is maximum in December 2022 and minimum in April - 2022. This indicates that PM_{10} concentration is less in December 2022 and maximum in April - 2022. The Pearson correlation coefficient between PMs over the period 2020-2022 is especially high in the summer season ($r = 0.9711$) and is negative ($r = -0.7039$) in the winter season which indicates that traffic-related emissions are the main sources of pollution at this site. **Novelty:** Air pollutants from January 2018 - December 2020 for nine monitoring stations in Visakhapatnam were observed by numerous authors and concluded that maximum $PM_{2.5}$ levels fall within the range of $61-90 \mu\text{g}/\text{m}^3$. Similarly, PM_{10} falls within the range of $101-250 \mu\text{g}/\text{m}^3$ in 2019 and 2020. The maximum PM_{10} concentration was $195 \mu\text{g}/\text{m}^3$ in December 2020 and the minimum value was $53 \mu\text{g}/\text{m}^3$ in April 2020. The decrease in PM_{10} concentration is probably due to the prevailing pandemic situation in 2020. The major harmful air pollutant is particulate matter (PM_{10} and $PM_{2.5}$) in Visakhapatnam city due to rapid industrialization and its variations are analyzed during January 2020 - December 22. The data analyzed from CPCB reveals that the maximum PM_{10} concentration was $166.5 \mu\text{g}/\text{m}^3$ in January 2021 and the minimum value was $74.92 \mu\text{g}/\text{m}^3$ in May 2021. The maximum $PM_{2.5}$ concentration is $83.38 \mu\text{g}/\text{m}^3$ in January 2021 and the minimum value is $20.2 \mu\text{g}/\text{m}^3$ in April 2022. The decrease in P.M concentrations is probably due to the prevailing post-pandemic situation.

Keywords: Particulate matter; Dispersion; Pollution; Anthropogenic

1 Introduction

The atmosphere of Earth is a dynamic system that takes a variety of gases, liquids, and solids from both natural and man-made sources. These materials spread through the air, interact physically and chemically with other materials, and travel together. Most of these eventually wind up in an interceptor, such as a person, object, animal, or plant, or a depository like the ocean. A wide range of pollutants are released into the atmosphere through man made and natural activities. Man has designated the portion of these compounds as pollutants that interact with the environment to create toxicity, sickness, aesthetic distress, impacts, or environmental degradation. Air pollutants can also be broadly classified into two general groups a) Primary Pollutants and b) Secondary pollutants. The Primary pollutants emit into the atmosphere directly but the secondary pollutants are produced by chemical and photochemical reactions of primary pollutants.

At the beginning of the 21st century, industrialization and modernization are at their peak around the world. As a result, catastrophic levels of air pollution are on the rise. Air pollution is a major environmental problem affecting people and biodiversity in both developed and developing countries. Particulate matter (PM_{10} and $PM_{2.5}$), nitrogen oxides (NO and NO_2), sulfur dioxide (SO_2), Ozone (O_3), carbon monoxide (CO), volatile organic compounds (VOCs), and NH_3 are the most common air pollutants

encountered in our daily lives⁽¹⁾. The main anthropogenic sources of these particles are vehicle emissions, industry, fossil fuel combustion, and power plants.

Sulfur dioxide is released into the atmosphere by both natural and anthropogenic emissions. Natural sources are mainly volcanic eruptions, while anthropogenic sources include the combustion of all sulfur-containing fuels such as oil, coal, and diesel used to generate electricity for industrial activities. Air pollution adversely affects all life on earth. Poor air quality has become a global concern. According to one report, about 4.2 million people die prematurely every year due to exposure to poor air quality, which causes lung cancer, heart disease, asthma, and other chronic respiratory diseases⁽²⁾. In addition to health, air pollution also has negative impacts on the environment, climate, vegetation, and the economy.

Air pollution can be categorized based on its origin, chemical composition, size, and whether it originates from indoor or outdoor sources⁽³⁾. In terms of origin, air pollution can be classified into two main types: natural and man-made pollution, as well as stationary and mobile pollution. Natural pollutants are emitted directly from natural sources, such as forest fires, volcanic eruptions, dust storms, pollen grains, and radon gas⁽⁴⁾. On the other hand, man-made pollution is a result of human activities. Man-made sources of air pollution can be further divided into three categories: point source, area source, and line source. Point sources are localized and stationary, typically associated with large facilities or locations where significant amounts of air pollutants are released during manufacturing processes⁽⁵⁾. These point sources usually release pollutant substances into the atmosphere through chimneys at a sufficient height to allow for substantial dilution before reaching the ground surface. However, certain weather conditions, such as low temperatures, winds, and a stable atmosphere, can hinder the dispersion of pollutants, leading to poor air quality near the point source⁽⁶⁾. In contrast to point sources, area sources are smaller in scale but can still contribute significantly to air pollution when their cumulative effects are considered. Stationary sources of air pollution include manufacturing facilities, power plants, oil refineries, chemical plants, and other industrial utilities⁽⁷⁾. In contrast to point sources, area sources are smaller in scale but can still contribute significantly to air pollution when their cumulative effects are considered. Stationary sources of air pollution include manufacturing facilities, power plants, oil refineries, chemical plants, and other industrial utilities⁽⁷⁾.

The current COVID-19 outbreak has been reported to have a positive impact on the environment. Various workers reported that the COVID-19 lockdown showed a significant decrease in the concentrations of SO₂ (6.76%), NO₂ (5.93%), PM_{2.5} (13.66%), and PM₁₀ (24.67%) over 44 cities in northern China^(8–10). In urban areas of Malaysia, the COVID-19 lockdown has shown reductions in NO₂ and SO₂, PM_{2.5}, and PM₁₀ concentrations⁽¹¹⁾.

In Barcelona, Spain, air pollution was significantly reduced by the closure of COVID-19⁽¹²⁾. In India, air pollution levels have decreased significantly due to a massive reduction in vehicular traffic and industrial activity, resulting in cleaner and fresher air^(13,14). COVID-19 lockdown has been reported to improve air quality in 22 Indian cities⁽¹⁵⁾. The impact of COVID-19 lockdown measures on air pollution levels has been analyzed in six mega cities in India and China, and the analysis showed a drastic reduction in air pollution⁽¹⁶⁾. In this context, the present study was envisaged to evaluate the influence of the COVID-19 lockdown in the year 2020 on the concentrations of air pollutants such as PM_{2.5} and PM₁₀ at the selected locations of Visakhapatnam city, Andhra Pradesh⁽¹⁷⁾. The values of these parameters were compared with the same parameters obtained at the same locations of the city in 2018 and 2019, to document the impact of the lockdown on the evaluated parameters^(17,18).

Visakhapatnam is not meeting National Ambient Air Quality Standards (NAAQS) as identified by the Central Pollution Control Board (CPCB) and it is one of the leading industrial centers in southern India. The major industries such as Coromandel fertilizers, Visakhapatnam Port Trust, Hindustan Zinc Limited, Hindustan Petroleum Corporation Limited, LG polymers, and Essar Steel are responsible for contributing to significant air pollution. Particulate matter and gaseous emissions are identified as pollutants due to industrial and domestic activities from NAAQS. Fine particulate matter is generally in the lower portion of the atmosphere in the winter season due to the condensation process. The particulate matter is one of the major pollutants in Visakhapatnam several studies⁽¹⁷⁾ reported that particulate pollutants are emerging as critical air pollutants in the winter season which is unhealthier. The average PM₁₀ mass concentrations at the Jogannapalem and Parawada sites in Visakhapatnam exceeded the CPCB annual limit (60 mg/m³). Air pollutants from January 2018 - December 2020 for nine monitoring stations in Visakhapatnam observed that maximum PM_{2.5} levels fall within the range of 61-90 µg/m³⁽¹⁸⁾ and PM₁₀ falls within the range of 101-250 µg/m³ in 2019 and 2020. The present paper aims to analyze the seasonal trend in particulate matter from January 2020 to December 2022.

Studies on Particulate Matter (PM) and Health have demonstrated a connection between PM and detrimental health outcomes, with an emphasis on either acute or chronic short-term PM exposure. Typically, chemical reactions between the various pollutants result in the formation of particulate matter (PM) in the atmosphere. Particle size has a direct impact on how well they penetrate⁽¹⁹⁾. The United States Environmental Protection Agency categorized particulate matter (PM) as particles⁽²⁰⁾. PM₁₀, or particles having a diameter of 10 micrometers (µm) or less, and extremely fine particles, which typically have a diameter of 2.5 micrometers (µm) or less, are included in the category of particulate matter (PM) pollution.

Tiny liquid or solid droplets included in particulate matter can be ingested and have detrimental effects on one's health⁽²¹⁾. PM₁₀ (particles smaller than 10 microns in diameter) can enter the circulation and infiltrate the lungs following inhalation. PM_{2.5}, or fine particles, are more harmful to health^(22,23). Numerous epidemiological research on PM's effects on health have been conducted. A positive correlation was seen between acute nasopharyngitis and both short- and long-term exposures to PM_{2.5}⁽²²⁾. Furthermore, it has been discovered that years of prolonged exposure to PMs are linked to cardiovascular illnesses and neonatal mortality.

In addition, respiratory diseases and immune system disorders have been documented as long-term chronic consequences⁽²⁴⁾. It is important to highlight those individuals with asthma, pneumonia, and diabetes, as well as respiratory and cardiovascular conditions, are particularly susceptible and prone to the impacts of PM. PM_{2.5}, followed by PM₁₀, exhibits a strong association with various respiratory ailments⁽²⁵⁾, as their small size enables them to penetrate indoor spaces⁽²⁶⁾. These particles induce toxic effects based on their chemical and physical characteristics. These particles induce toxic effects based on their chemical and physical characteristics.

The COVID-19 pandemic is typically associated with remote areas and low population densities, and some authors⁽²⁷⁾ have suggested that the spread of the virus to high latitudes or poles is an unlikely event. However, other studies⁽²⁸⁾ have raised concerns about the virus's potential to spread to Antarctic wildlife.

Researchers and environmentalists are referring to this outbreak as a "blessing in disguise" because lockdowns have significantly decreased air pollution. Globally, air pollution caused by human activity is typically one of the main factors contributing to health crises, inequality, and fatalities^(29–31). We now have the chance to breathe in low-carbon air because of the pandemic's reduction in air pollution, which was brought on by the cancellation of additional highway transportation, the suspension of public transit, and the closure of aeroplanes⁽³²⁾. Lockdowns and restricted movement greatly enhance the quality of the environment around us, with the greatest benefit being a decrease in air pollution.

Particulate Matter (PM), which is particles of varying but extremely small diameters, enters the respiratory system through inhalation and can lead to cancer, reproductive, cardiovascular, and central nervous system disorders, as well as other health issues⁽³³⁾. Ozone protects against UV radiation in the stratosphere, but when it is concentrated too much at ground level can be hazardous and negatively impact the cardiovascular and respiratory systems. Fine particles have been linked lung cancer death rate⁽³⁴⁾ in China.

Air pollution refers to the contamination of the surrounding atmosphere due to the presence of chemical substances, gases, or particulate matter. These pollutants have the potential to cause discomfort, diseases, and even millions of deaths annually. Additionally, they can have detrimental effects on vegetation, animals, and food crops. The emission of these pollutant materials can lead to the formation of smog and acid rain, which in turn can result in respiratory and cancer-related illnesses. Furthermore, the accumulation of these pollutants over time can contribute to the depletion of the ozone layer, exacerbating global warming. The harmful impact of pollutants is influenced by factors such as the duration and intensity of exposure, the specific type of pollutants, and the overall accumulation of pollutants over time. Commonly referred to as "criteria air pollutants" or "basic pollutants," these include nitrogen oxides, sulfur oxides, carbon monoxide, ground-level ozone, lead, volatile air compounds (VOCs), and particulate matter.

Airborne particulate matter is a prevalent type of air pollution found in the atmosphere. These particles can be categorized based on their aerodynamic diameter. Coarser particles, with a diameter of 10 μm or less, are referred to as PM₁₀, while fine particles, with a diameter of 2.5 μm or less, are known as PM_{2.5}. Ultra-fine particles, on the other hand, have a diameter lower than 0.1 μm ⁽³⁵⁾. Particulate matter can originate from both natural and human activities. Natural sources include volcanic eruptions, mineral dust, sea salt, and wildfires. Anthropogenic sources, such as fuel combustion, industrial emissions, biomass burning, road dust, and combustion in vehicles and heating boilers, are the main contributors to particulate matter in the atmosphere^(35,36). The World Health Organization (WHO) has highlighted the health effects of particulate matter, particularly those with aerodynamic diameters of less than 2.5 μm and 10 μm . PM₁₀ particles can reach the bronchi and alveoli in the lungs, while PM_{2.5} particles can penetrate the bronchial capillary wall and interfere with gas exchange in the lungs. In 2014, the WHO reported that outdoor and indoor particulate matter was responsible for over 7 million deaths. Inhalation of PM₁₀ and PM_{2.5} particles has been linked to acute and chronic health issues and damage to the respiratory system^(37,38). Additionally, particulate matter can affect visibility and have impacts on crops and ecosystems. PM is a major contributor to reduced visibility due to its ability to scatter and absorb light⁽³⁹⁾.

On the other hand, NO₂ exhibited a significant impact on children, particularly those under the age of 15. Moreover, an increase of approximately 10 $\mu\text{g}/\text{m}^3$ in ambient air pollution levels resulted in a rise of approximately 2.8%, 3.6%, and 7.7% in emergency room admissions for PM₁₀, SO₂, and NO₂, respectively. These results were reported by⁽⁴⁰⁾. Furthermore, the association between respiratory disease mortality and lung cancer mortality with the major air pollutants (SO₂, NO₂, and PM₁₀) was examined. The study found that a 10 $\mu\text{g}/\text{m}^3$ increase in SO₂, NO₂, and PM₁₀ levels led to a respective increase of

approximately 7.69%, 4.38%, and 1.55% in respiratory disease mortality. Notably, only SO₂ showed a significant association with lung cancer mortality, as reported by⁽⁴¹⁾.

2 Materials and methods

The real-time daily mass concentrations of air pollutants in Visakhapatnam city are recorded by the Central Pollution Control Board (CPCB). It is a single recording station that records real-time precise air pollution data of Visakhapatnam used for the present study. This real-time air pollution data (<https://cpcb.nic.in>) is maintained by the Greater Visakhapatnam Municipal Corporation (GVMC, Ramnagar). The monthly average observations of major pollutants such as PM_{2.5}, PM₁₀, and the ratio of PM_{2.5}/PM₁₀ in each season are considered for the present study. The trends of major harmful air pollutants such as PM_{2.5}, PM₁₀, and the ratio of PM_{2.5}/PM₁₀ are analyzed seasonally from January 2020 - December 2022. The present data analyzed and results were compared with previously available data. The conclusions are made based on seasonal variations of major pollutants and also prevailing pandemic situation at that time. The trends of harmful pollutants (PM_{2.5}, PM₁₀) are measured using the Pearson correlation coefficient. The present data is analyzed statistically from January 2020 - December 2022 and conclusions are made based on obtained results.

3 Results and Discussions

Air pollutants from January 2018 - December 2020 for nine monitoring stations in Visakhapatnam are observed that maximum PM_{2.5} levels fall within the range of 61-90 $\mu\text{g}/\text{m}^3$ ⁽¹⁸⁾. Similarly, PM₁₀ falls within the range of 101-250 $\mu\text{g}/\text{m}^3$ in 2019 and 2020 which indicates moderate pollution according to AQI⁽¹⁸⁾.

Typically, chemical reactions between the various pollutants result in the formation of particulate matter (PM) in the atmosphere. Particle size has a direct impact on how well they penetrate. The US Environmental Protection Agency identified particles as part of the category known as particulate matter (PM)⁽²⁰⁾.

PM₁₀, or particles having a diameter of 10 micrometers (μm) or less, and extremely fine particles, which typically have a diameter of 2.5 micrometers (μm) or less, are included in the category of particulate matter (PM) pollution. Particulate matter is made up of microscopic solid or liquid droplets that are harmful to the lungs when inhaled. After inhalation, particles with a diameter less than 10 μm , or PM₁₀, can penetrate the lungs and potentially enter the bloodstream. PM_{2.5}, or fine particles, are more harmful to health.

The studies conducted rely on PM_{2.5} monitors and have limitations in terms of the area they cover, either restricted to a specific study area or city due to the absence of detailed daily PM_{2.5} concentration data. Consequently, these studies cannot be considered representative of the entire population. A recent epidemiological study conducted by the Department of Environmental Health at Harvard School of Public Health (Boston, MA)⁽⁴²⁾ highlighted that the spatial variation in PM_{2.5} concentrations leads to an exposure error (known as Berkson error) and the complete understanding of the short- and long-term effects is still lacking. To address this, the team developed a PM_{2.5} exposure model utilizing remote sensing data, enabling the assessment of both short- and long-term human exposures across different spatial resolutions for the entire population⁽⁴²⁾.

In addition, long-term chronic consequences include immune system affection and respiratory illnesses. It is important to remember that persons who have diabetes, asthma, pneumonia, or other respiratory or cardiovascular conditions are particularly vulnerable to the negative effects of PM's. Because PM_{2.5} and PM₁₀ are small enough to penetrate interior spaces, they are strongly linked to a variety of respiratory system disorders. The chemical and physical characteristics of the particles cause harmful effects.

It has been determined how environmental contamination contributed to the COVID-19 pandemic's spread and severity. Particulate matter (PM) in the atmosphere has the potential to transmit several viruses. Inhaled particles, particularly those smaller than 2.5 μm (PM_{2.5}) and their associated microorganisms, can enter the deep lung and facilitate the growth of viruses that cause infections in the respiratory tract⁽⁴³⁾.

Since fine and ultrafine PM (PM_{2.5} and PM_{0.1}) are thought to be responsible for several million fatalities annually worldwide, they are currently regarded as one of the most significant environmental risk factors^(44,45). In addition to compromising immunological functions, atmospheric pollution can cause pro-inflammatory and oxidative pathways in the lungs and other organs. These data suggest that air pollution may have a detrimental impact on COVID-19 patients' prognosis. Additionally, in Italy during the early stages of the COVID pandemic, noticeably higher death rates were noted in the northern regions, which are known to be more polluted than the other regions which suggest a possible role for pollution in the pandemic's spread⁽⁴⁶⁾. India exhibits geographic heterogeneity, whereby regions with disparate climatic conditions, populations, and educational attainment levels produce varying indoor air quality. North Indian states have been shown to have higher PM_{2.5} levels (557–601 $\mu\text{g}/\text{m}^3$)

in comparison to the Southern States (183–214 $\mu\text{g}/\text{m}^3$)^(47,48).

The present paper aims to analyze the trend in particulate matter from January 2020 - December 2022. Table 1 shows air pollutants from January 2020 - December 2022 in Visakhapatnam and $\text{PM}_{2.5}$ levels fall within the range of 16 - 96 $\mu\text{g}/\text{m}^3$. The minimum $\text{PM}_{2.5}$ level is in April 2020 and the maximum in December 2020. Similarly, PM_{10} levels fall within the range of 53-196 $\mu\text{g}/\text{m}^3$ during 2020-2022. The minimum PM_{10} level is in April 2020 and maximum in December 2020 which indicates moderate pollution according to AQI. This study plays a vital role because the detailed trend analysis of major pollutants like $\text{PM}_{2.5}$ and PM_{10} is not made from January 2020 to December 2022.

Table 1. Monthly variations in $\text{PM}_{2.5}$ and PM_{10} ($\mu\text{g}/\text{m}^3$)

Year	Month	$\text{PM}_{2.5}$	PM_{10}	Year	$\text{PM}_{2.5}$	PM_{10}	Year	$\text{PM}_{2.5}$	PM_{10}
2020	January	59.18	120.04	2021	83.38	166.55	2022	63.73	126.99
	February	44.95	95.12		64.52	153.76		55.63	134.76
	March	29.89	78.34		47.24	136.36		53.24	140.27
	April	16.76	53.16		34.47	98.70		20.22	78.76
	May	17.92	68.89		24.46	74.92		33.35	97.64
	June	23.71	81.91		31.86	94.40		36.01	98.40
	July	25.39	75.04		25.1	77.82		29.65	91.80
	August	35.47	93.41		30.83	87.17		29.34	94.38
	September	28.96	75.77		25.22	81.06		29.83	87.23
	October	48.66	107.58		44.05	108.24		40.41	91.31
	November	59.94	121.70		49.37	85.74		69.32	151.44
	December	95.98	195.57		61.43	121.60		80.33	159.79
Mean		40.567	97.210		43.494	107.193		45.088	112.730
Standard deviation		22.855	37.179		18.623	30.800		18.911	28.0115

Table 2 shows monthly variations of $\text{PM}_{2.5}/\text{PM}_{10}$ from 2020-22. The most prominent pollutant at the study site is PM_{10} which is more intense in December 2020. $\text{PM}_{2.5}$ is also a more intense pollutant in December 2020. The maximum intensity of PM_{10} decreased by 26% in December 2021 and the maximum intensity of $\text{PM}_{2.5}$ decreased by 27% in December 2021. The maximum intensity of PM_{10} increases by 20% in December 2022 and the maximum intensity of $\text{PM}_{2.5}$ increases by 21% in December 2022. The ratio of $\text{PM}_{2.5}/\text{PM}_{10}$ is minimum (0.260) in May 2020 (Figure 4) and the ratio of $\text{PM}_{2.5}/\text{PM}_{10}$ is minimum (0.311) in September 2021 (Figure 5) and $\text{PM}_{2.5}/\text{PM}_{10}$ is minimum (0.257) in April 2022 (Figure 6). The gradual decrease of $\text{PM}_{2.5}/\text{PM}_{10}$ shows that PM_{10} is a significant pollutant. A low ratio of $\text{PM}_{2.5}/\text{PM}_{10}$ indicates the dominance of dust, and a high ratio denotes anthropogenic aerosols during the season. The ratio of $\text{PM}_{2.5}/\text{PM}_{10}$ less than 0.5 for the entire study period indicates the existence of higher coarse particle masses.

The average monthly variations of particulate matter (PM_{10} and $\text{PM}_{2.5}$) are shown in Figure 1a, b, and c for 2020-2022. The average PM_{10} concentration exceeded the national air quality standard from October to December 2020. The highest average value of $195.57\mu\text{g}/\text{m}^3$ was recorded in December 2020, and the second-highest was registered in January 2021 ($166.5\mu\text{g}/\text{m}^3$). The PM_{10} concentration was lower than national air quality standards from April - October for almost all the years, with a minimum average value of $70\mu\text{g}/\text{m}^3$. The low values of PMs in the summer months can be attributed to dispersion conditions, and higher values in winter were due to inversion conditions and condensation of fine particulate matter in the lower atmosphere.

Seasonal variations of PMs are displayed in Figures 2 and 3. Seasonal average mass concentrations of PMs clearly show that air quality is clearest in summer. Season-wise variations exhibited a linear trend from summer to winter (2020 - 2022). In 2020, the particulate matter mass concentrations show a fluctuating trend, and changes in the meteorological conditions also affect the annual changes in pollutant levels. There is a decrease in particulate matter concentrations in the 2020 summer season when compared to the 2020 winter season due to the stringent lockdown imposed in March 2020 because of the COVID-19 pandemic. The ratio of $\text{PM}_{2.5}/\text{PM}_{10}$ decreases from January to May 2020 and increases afterward as shown in Figure 4. The ratio of $\text{PM}_{2.5}/\text{PM}_{10}$ decreases from January to March 2021 becomes uniform up to September 2021 and increases afterward as shown in Figure 5. The ratio of $\text{PM}_{2.5}/\text{PM}_{10}$ decreases up to April 2022 and has an irregular trend up to December 2022 as shown in Figure 6. The ratio of $\text{PM}_{2.5}/\text{PM}_{10}$ is maximum in the post-monsoon period in November 2021 and minimum in the summer period (April 2022) as shown in Figure 7.

Table 2. Monthly variations in PM_{2.5}/PM₁₀

Year	Month	PM _{2.5} /PM ₁₀	Year	PM _{2.5} /PM ₁₀	Year	PM _{2.5} /PM ₁₀		
2020	January	0.493	2021	January	0.501	2022	January	0.502
	February	0.473		February	0.420		February	0.413
	March	0.382		March	0.346		March	0.380
	April	0.315		April	0.349		April	0.257
	May	0.260		May	0.327		May	0.342
	June	0.289		June	0.338		June	0.366
	July	0.338		July	0.323		July	0.323
	August	0.380		August	0.354		August	0.311
	September	0.382		September	0.311		September	0.342
	October	0.452		October	0.407		October	0.443
	November	0.493		November	0.576		November	0.458
	December	0.491		December	0.505		December	0.503
Mean		0.3956		0.3964		0.3866		
Standard deviation		0.0838		0.0869		0.0779		

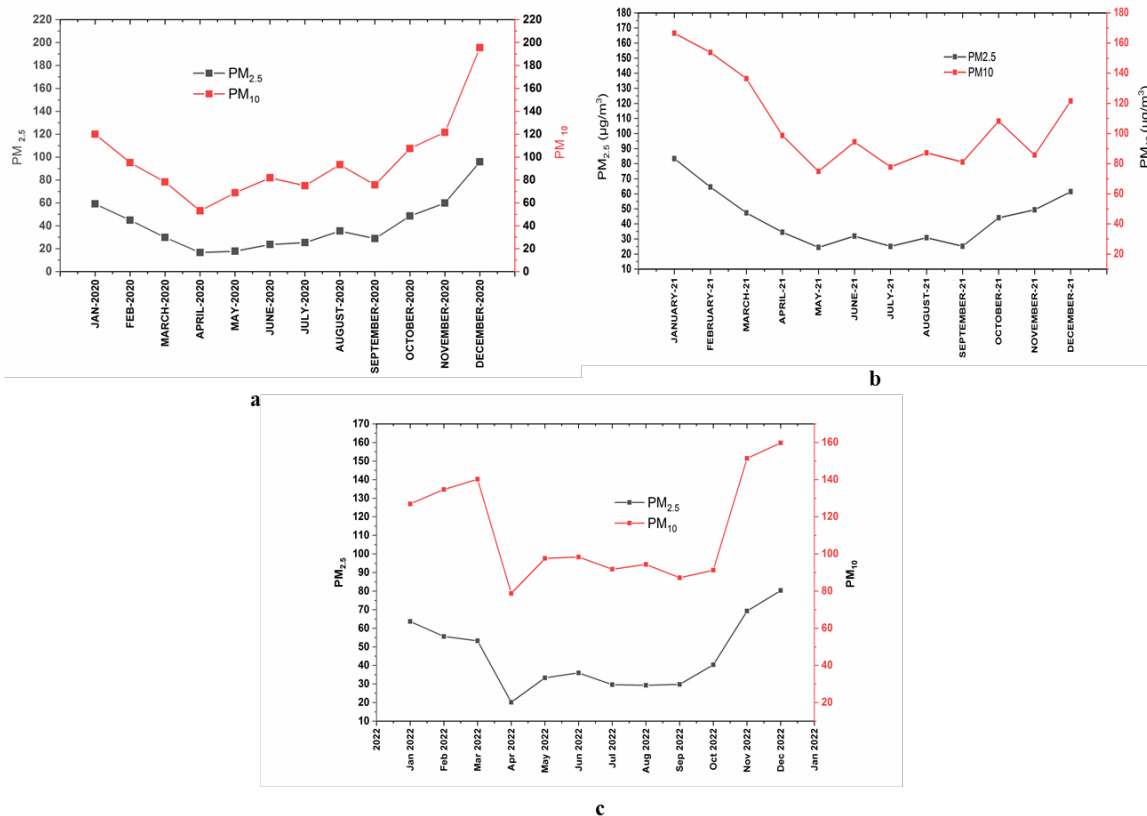


Fig 1. a. Average daily variation of PM concentrations for various months in 2020, b. Average daily variation of PM concentrations for various months in 2021, c. Average daily variation of PM concentrations for various months in 2022

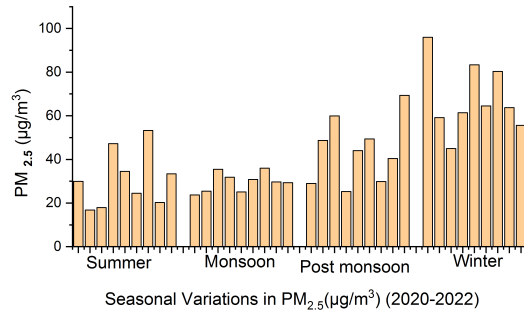


Fig 2. Seasonal variations in PM_{2.5} (µg/m³) during 2020-22

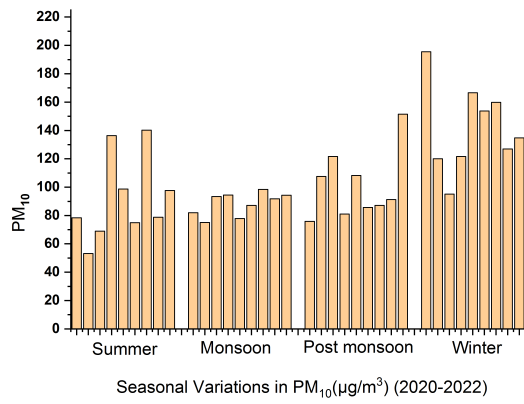


Fig 3. Seasonal variations in PM₁₀ (µg/m³) during 2020-22

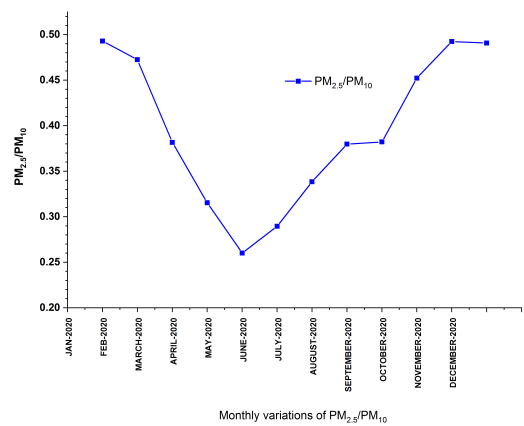


Fig 4. Monthly variations of PM_{2.5}/PM₁₀ in 2020

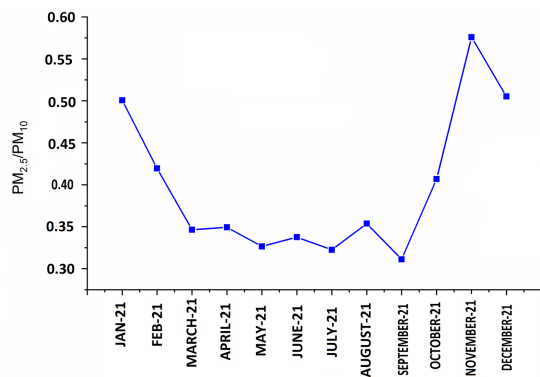


Fig 5. Monthly variations of PM_{2.5}/PM₁₀ in 2021

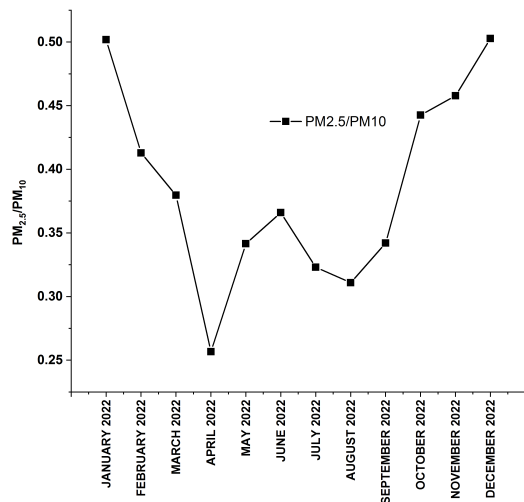


Fig 6. Monthly variations of PM_{2.5}/PM₁₀ in 2022

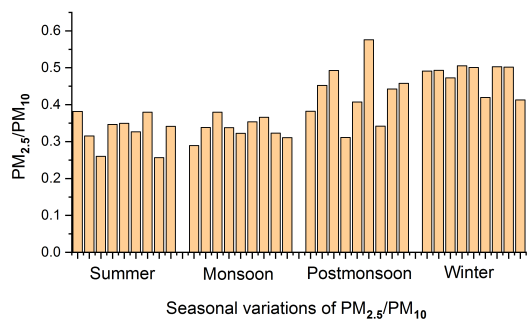


Fig 7. Seasonal variations of PM_{2.5}/PM₁₀ from 2020-2022

The meteorological parameters (relative humidity, wind speed, temperature, and precipitation) influence the air pollutants (particulate matter and gaseous pollutants). The distribution and spread of air pollutants were significantly influenced by meteorological parameters in Visakhapatnam city. The Pearson correlation coefficient results suggest that meteorological parameters influence the concentration of air pollutants. The temperature had the strongest negative effect on pollutant concentrations, and all other meteorological parameters investigated had both negative (decreased) and positive (increased) effects on air pollutant concentrations.

4 Conclusions

The low values of PMs in the summer months can be attributed to dispersion conditions, and higher values in winter were due to inversion conditions and condensation of fine particulate matter in the lower atmosphere. The Pearson correlation coefficient during January 2020–December 2022 is especially high in the summer season and negative in the winter season which indicates traffic-related emissions. It can be concluded that Visakhapatnam recorded high pollutants of PM_{2.5} and PM₁₀ in the winter season from Jan 2020 to Dec 2022 due to traffic-related emissions when compared to January 2018– December 2019. Due to the increased moisture storage capacity during non-monsoon summers, particles become larger and are deposited on the ground through dry deposition processes. In winter, water storage capacity decreases, leaving water vapor suspended along with air pollutants, further deteriorating air quality. High wind speeds promote dispersion and dilution, but high wind speeds can add dust particles and increase pollutant levels. The variation of PM_{2.5}/PM₁₀ showed that the cumulative effect of relative humidity was stronger in PM_{2.5} than in PM₁₀ (winter season).

The highest standard deviation of 37.17 occurred in 2020 which indicates that the data points deviate from the average with low contamination. Conversely, a lower standard deviation indicates a lower variance and more tightly clustered datasets occurred in 2021 and 2022 which indicates high contamination. Numerous authors have already examined the diurnal variations in harmful PM concentrations (PM_{2.5}, PM₁₀) and other gaseous pollutants in Visakhapatnam City between 2018 and 2020 and concluded the study that residents of Visakhapatnam City are at high health risk due to fine particulate matter.

According to the previous study, air pollution levels for NO₂, SO₂, and NH₃ fall between 0 and 40 μg/m³. While NH₃ levels fall between 0 and 200 μg/m³, the minimum PM_{2.5} levels in 2019 and 2020 fall between 0 and 30 μg/m³, and the minimum PM₁₀ levels fall between 0 and 50 μg/m³, indicating a good air pollution status according to the AQI. However, in 2019 and 2020, the highest PM_{2.5} levels were found to be between 61 and 90 μg/m³ and 101 and 250 μg/m³, respectively, indicating that the AQI classifies air pollution as moderately polluted. They identified that the concentration levels of NH₃, PM_{2.5}, and PM₁₀ did not significantly decrease throughout the lockdown period, which may be due to the sources of these parameters were not impacted by the COVID-19 lockdown. Prior research indicates that all monitoring sites of Visakhapatnam had acceptable levels of air quality; however, from January 2018 to December 2020, the only metric that showed a decrease across all monitoring stations was NH₃.

However, the current study analyzed the data for seasonal variations of dangerous pollutants like PM_{2.5} and PM₁₀ for the years 2020–2022. This study had a favourable impact on improving air quality, particularly during the COVID season which met AQI norms. The present study may be improved effectively if blood samples of living people in the polluted areas corresponding to industrial and seashore areas of Visakhapatnam were collected seasonally and analysis is carried out corresponding to sensitive biodiversity variations. Air pollution may cross AQI standards due to man made activities arising due to the failure of solid waste management policies in moderate economic countries like India. This present study may help policymakers and environmentalists to reduce air pollution in the future by strategically enacting lockdowns at pollution hotspots that cause the least amount of economic damage. The pollution prevention methods and current challenges in reducing air pollution also need to be elaborated. This study may not provide a proper reason if air pollution occurs from nonpoint sources. This study may be improved drastically if various pollution due to point and nonpoint sources were measured using remote sensing techniques.

5 Acknowledgement

The authors sincerely thank the anonymous reviewers and look forward to receiving valuable comments to improve the quality of the article.

References

- 1) Guo H, Chang Z, Wu J, Li W. Air pollution and lung cancer incidence in China: Who are faced with a greater effect? *Environment International*. 2019;132:105077. Available from: <https://doi.org/10.1016/j.envint.2019.105077>.
- 2) Gupta A, Bherwani H, Gautam S, Anjum S, Musugu K, Kumar N, et al. Air pollution aggravating COVID-19 lethality? Exploration in Asian cities using statistical models. *Environment, Development and Sustainability*. 2021;23(4):6408–6417. Available from: <https://doi.org/10.1007/s10668-020-00878-9>.

- 3) Bernstein JA, Alexis N, Barnes CN, Bernstein IL, Nel AL, Peden D, et al. Health effects of air pollution. *Journal of Allergy and Clinical Immunology*. 2004;114(5):1116–1123. Available from: <https://doi.org/10.1016/j.jaci.2004.08.030>.
- 4) Appannagari RRR. Environmental Pollution Causes and Consequences: A Study. *North Asian International Research Journal of Social Science & Humanities*. 2017;3(8):151–161. Available from: https://www.researchgate.net/publication/323944189_Environmental_Pollution_Causes_and_Consequences_A_Study#:~:text=The%20destruction%20of%20ozone%20layer,in%20many%20low%20lying%20coastal.
- 5) Khallaf M, editor. The impact of air pollution on health, economy, environment and agricultural sources. In Tech Publishing. 2011. Available from: <https://www.intechopen.com/books/489>.
- 6) Bian Y, Huang Z, Ou J, Zhong Z, Xu Y, Zhang Z, et al. Evolution of anthropogenic air pollutant emissions in Guangdong Province, China, from 2006 to 2015. *Atmospheric Chemistry and Physics*. 2019;19(18):11701–11719. Available from: <https://doi.org/10.5194/acp-19-11701-2019>.
- 7) Fujita EM, Campbell DE, Arnott WP, Johnson T, Ollison W. Concentrations of mobile source air pollutants in urban microenvironments. *Journal of the Air & Waste Management Association*. 2014;64(7):743–758. Available from: <https://doi.org/10.1080/10962247.2013.872708>.
- 8) Duthel F, Navel V, Clinchamps M. The Indirect Benefit on Respiratory Health From the World's Effort to Reduce Transmission of SARS-CoV-2. *Chest*. 2020;158(2):467–468. Available from: <https://doi.org/10.1016/j.chest.2020.03.062>.
- 9) Muhammad S, Long X, Salman M. COVID-19 pandemic and environmental pollution: A blessing in disguise? *Science of The Total Environment*. 2020;728:1–5. Available from: <https://doi.org/10.1016/j.scitotenv.2020.138820>.
- 10) Wang Q, Su M. A preliminary assessment of the impact of COVID-19 on environment – A case study of China. *Science of The Total Environment*. 2020;728:1–10. Available from: <https://doi.org/10.1016/j.scitotenv.2020.138915>.
- 11) Kanniah KD, Zaman NAFK, Kaskaoutis DG, Latif MT. COVID-19's impact on the atmospheric environment in the Southeast Asia region. *Science of The Total Environment*. 2020;736:1–13. Available from: <https://doi.org/10.1016/j.scitotenv.2020.139658>.
- 12) Tobías A, Carnerero C, Reche C, Massagué J, Via M, Minguillón MC, et al. Changes in air quality during the lockdown in Barcelona (Spain) one month into the SARS-CoV-2 epidemic. *Science of The Total Environment*. 2020;726:1–4. Available from: <https://doi.org/10.1016/j.scitotenv.2020.138540>.
- 13) Lokhandwala S, Gautam P. Indirect impact of COVID-19 on environment: A brief study in Indian context. *Environmental Research*. 2020;188:1–10. Available from: <https://doi.org/10.1016/j.envres.2020.109807>.
- 14) Mahato S, Ghosh KG. Short-term exposure to ambient air quality of the most polluted Indian cities due to lockdown amid SARS-CoV-2. *Environmental Research*. 2020;188:1–15. Available from: <https://doi.org/10.1016/j.envres.2020.109835>.
- 15) Sharma AK, Balyan P. Air pollution and COVID-19: Is the connect worth its weight? *Indian Journal of Public Health*. 2020;64(6):132–134. Available from: https://journals.lww.com/ijph/fulltext/2020/64060/air_pollution_and_covid_19_is_the_connect_worth.16.aspx.
- 16) Agarwal A, Kaushik A, Kumar S, Mishra RK. Comparative study on air quality status in Indian and Chinese cities before and during the COVID-19 lockdown period. *Air Quality, Atmosphere & Health*. 2020;13(10):1167–1178. Available from: <https://doi.org/10.1007/s11869-020-00881-z>.
- 17) Chandu K, Dasari M. Variation in Concentrations of PM_{2.5} and PM₁₀ During the Four Seasons at the Port City of Visakhapatnam, Andhra Pradesh, India. *Nature Environment and Pollution Technology*. 2020;19(3):1187–1193. Available from: [https://neptjournal.com/upload-images/\(32\)B-3657.pdf](https://neptjournal.com/upload-images/(32)B-3657.pdf).
- 18) Grace LK, Raliengoane TP. Effect of Covid-19 on air quality in Visakhapatnam-A comparative study. *International Journal of Ecology and Environmental Sciences*. 2021;3(3):102–105. Available from: <https://www.ecologyjournal.in/archives/2021/vol3/issue3/3-3-22>.
- 19) Wilson WE, Suh HH. Fine Particles and Coarse Particles: Concentration Relationships Relevant to Epidemiologic Studies. *Journal of the Air & Waste Management Association*. 1997;47(12):1238–1249. Available from: <https://doi.org/10.1080/10473289.1997.10464074>.
- 20) Particulate Matter (PM) Basics. Available from: <https://www.epa.gov/pm-pollution/particulate-matter-pm-basics>.
- 21) Cheung K, Daher N, Kam W, Shafer MM, Ning Z, Schauer JJ, et al. Spatial and temporal variation of chemical composition and mass closure of ambient coarse particulate matter (PM_{10-2.5}) in the Los Angeles area. *Atmospheric Environment*. 2011;45(16):2651–2662. Available from: <https://doi.org/10.1016/j.atmosenv.2011.02.066>.
- 22) Zhang L, Yang Y, Li Y, (min) Qian Z, Xiao W, Wang XW, et al. Short-term and long-term effects of PM_{2.5} on acute nasopharyngitis in 10 communities of Guangdong, China. *Science of The Total Environment*. 2019;688:136–142. Available from: <https://doi.org/10.1016/j.scitotenv.2019.05.470>.
- 23) Kelishadi R, Poursafa P. Air pollution and non-respiratory health hazards for children. *Archives of Medical Science*. 2010;6(4):483–495. Available from: <https://doi.org/10.5114/aoms.2010.14458>.
- 24) Current and Forecasted Air Quality in New Hampshire. Environmental Fact Sheet . 2019. Available from: <https://www.des.nh.gov/organization/commissioner/pip/factsheets/ard/documents/ard-16.pdf>.
- 25) Kappos AD, Bruckmann P, Eikmann T, Englert N, Heinrich U, Höppe P, et al. Health effects of particles in ambient air. *International Journal of Hygiene and Environmental Health*. 2004;207(4):399–407. Available from: <https://doi.org/10.1078/1438-4639-00306>.
- 26) Boschi N. Defining an Educational Framework for Indoor Air Sciences Education. In: Education and Training in Indoor Air Sciences;vol. 60 of NATO Science Series. Dordrecht, Netherlands. Springer. 1999;p. 3–6. Available from: https://doi.org/10.1007/978-94-011-4511-4_1.
- 27) Oktorie O, Berd I. Spatial model of COVID 19 distribution based on differences a climate characteristics and environment of according to the earth latitude. *Sumatra Journal of Disaster, Geography and Geography Education (SJDGGE)*. 2020;4(1):17–21. Available from: <https://doi.org/10.24036/sjdgge.v4i1.322>.
- 28) Barbosa C, Cowell AJ, Dowd WN. Alcohol Consumption in Response to the COVID-19 Pandemic in the United States. *Journal of Addiction Medicine*. 2021;15(4):341–344. Available from: <https://doi.org/10.1097/adm.0000000000000767>.
- 29) Yang T, Liu W. Does air pollution affect public health and health inequality? Empirical evidence from China. *Journal of Cleaner Production*. 2018;203:43–52. Available from: <https://doi.org/10.1016/j.jclepro.2018.08.242>.
- 30) Lin B, Zhu J. Changes in urban air quality during urbanization in China. *Journal of Cleaner Production*. 2018;188:312–321. Available from: <https://doi.org/10.1016/j.jclepro.2018.03.293>.
- 31) Zhang H, Wang S, Hao J, Wang X, Wang S, Chai F, et al. Air pollution and control action in Beijing. *Journal of Cleaner Production*. 2016;112(2):1519–1527. Available from: <https://doi.org/10.1016/j.jclepro.2015.04.092>.
- 32) Monks P. Here's How Lockdowns Have Improved Air Quality Around the World. 2020. Available from: <https://www.weforum.org/agenda/2020/04/coronavirus-lockdowns-air-pollution>.
- 33) Manisalidis I, Stavropoulou E, Stavropoulos A, Bezirtzoglou E. Environmental and Health Impacts of Air Pollution: A Review. *Frontiers in Public Health*. 2020;8:1–13. Available from: <https://doi.org/10.3389/fpubh.2020.00014>.
- 34) Kan H, Chen R, Tong S. Ambient air pollution, climate change, and population health in China. *Environment International*. 2012;42:10–19. Available from: <https://doi.org/10.1016/j.envint.2011.03.003>.

- 35) Samek L, Stegowski Z, Styszko K, Furman L, Fiedor J. Seasonal contribution of assessed sources to submicron and fine particulate matter in a Central European urban area. *Environmental Pollution*. 2018;241:406–411. Available from: <https://doi.org/10.1016/j.envpol.2018.05.082>.
- 36) Jeong CH, Mcguire ML, Herod D, Dann T, Dabek-zlotorzynska E, Wang D, et al. Receptor model based identification of PM_{2.5} sources in Canadian cities. *Atmospheric Pollution Research*. 2011;2(2):158–171. Available from: <https://doi.org/10.5094/APR.2011.021>.
- 37) Ezeh GC, Obioh IB, Asubiojo OI, Abiye OE. PIXE characterization of PM₁₀ and PM_{2.5} particulates sizes collected in Ikoyi Lagos, Nigeria. *Toxicological & Environmental Chemistry*. 2012;94(5):884–894. Available from: <https://doi.org/10.1080/02772248.2012.674133>.
- 38) Orok U. Contamination and health risk assessment of suspended particulate matter (SPM) in Uyo. *Nigeria Journal of Scientific Research and Reports*. 2015;6(4):276–286. Available from: <https://doi.org/10.9734/JSRR/2015/16296>.
- 39) Gourджи S. Review of plants to mitigate particulate matter, ozone as well as nitrogen dioxide air pollutants and applicable recommendations for green roofs in Montreal, Quebec. *Environmental Pollution*. 2018;241:378–387. Available from: <https://doi.org/10.1016/j.envpol.2018.05.053>.
- 40) Ma Y, Yang S, Zhou J, Yu Z, Zhou J. Effect of ambient air pollution on emergency room admissions for respiratory diseases in Beijing, China. *Atmospheric Environment*. 2018;191:320–327. Available from: <https://doi.org/10.1016/j.atmosenv.2018.08.027>.
- 41) Zhu F, Ding R, Lei R, Cheng H, Liu J, Shen C, et al. The short-term effects of air pollution on respiratory diseases and lung cancer mortality in Hefei: A time-series analysis. *Respiratory Medicine*. 2019;146:57–65. Available from: <https://doi.org/10.1016/j.rmed.2018.11.019>.
- 42) Kloog I, Ridgway B, Koutrakis P, Coull BA, Schwartz JD. Long- and short-term exposure to PM_{2.5} and mortality using novel exposure models. *Epidemiology*. 2013;24(4):555–561. Available from: <https://doi.org/10.1097/ede.0b013e318294beaa>.
- 43) Comunian S, Dongo D, Milani C, Palestini P. Air Pollution and COVID-19: The Role of Particulate Matter in the Spread and Increase of COVID-19's Morbidity and Mortality. *International Journal of Environmental Research and Public Health*. 2020;17(12):1–20. Available from: <https://doi.org/10.3390/ijerph17124487>.
- 44) Lelieveld J, Evans JS, Fnais M, Giannadaki D, Pozzer A. The contribution of outdoor air pollution sources to premature mortality on a global scale. *Nature*. 2015;525(7569):367–371. Available from: <https://doi.org/10.1038/nature15371>.
- 45) Lelieveld J, Klingmüller K, Pozzer A, Pöschl U, Fnais M, Daiber A, et al. Cardiovascular disease burden from ambient air pollution in Europe reassessed using novel hazard ratio functions. *European Heart Journal*. 2019;40(20):1590–1596. Available from: <https://doi.org/10.1093/eurheartj/ehz135>.
- 46) Conticini E, Frediani B, Caro D. Can atmospheric pollution be considered a co-factor in extremely high level of SARS-CoV-2 lethality in Northern Italy? *Environmental Pollution*. 2020;261:1–3. Available from: <https://doi.org/10.1016/j.envpol.2020.114465>.
- 47) Saud T, Gautam R, Mandal TK, Gadi R, Singh DP, Sharma SK, et al. Emission estimates of organic and elemental carbon from household biomass fuel used over the Indo-Gangetic Plain (IGP), India. *Atmospheric Environment*. 2012;61:212–220. Available from: <https://doi.org/10.1016/j.atmosenv.2012.07.030>.
- 48) Singh DP, Gadi R, Mandal TK, Saud T, Saxena M, Sharma SK. Emissions estimates of PAH from biomass fuels used in rural sector of Indo-Gangetic Plains of India. *Atmospheric Environment*. 2013;68:120–126. Available from: <https://doi.org/10.1016/j.atmosenv.2012.11.042>.

Novel Encryption and Decryption Technique Using ATP & New Sequent Rules in Three Variables

¹ K. Kanthi Sowjanya, *²Talari Surendra, ³Suryaprakash Nalluri, ⁴V.Sree Ramani,
⁵Subrahmanya S Meduri, ⁶P S V S Sridhar,

¹Research Scholar, Department of Mathematics, GSS, GITAM Deemed to be University, Visakhapatnam - 45,
Andhra Pradesh, India

²Department of Mathematics, GSS, GITAM Deemed to be University,
Visakhapatnam - 45, Andhra Pradesh, India

³Department - Information Security, Affiliation-University of Cumberland, Williamsburg, USA

⁴Department of mathematics, Chaitanya Bharati Institute of Technology,
Gandipet-500075, Telangana, India

⁵Technical Architect, Wipro Technologies, USA

⁶Department of Computer Science and Engineering, Koneru Lakshmaiah Education Foundation, Vaddeswaram,
AP, India

Abstract:-The act of safeguarding digital information from unauthorized access, corruption or theft is called Data Security. The secured encryption and decryption method gives more security from unauthorized access. Here we developed a new Encryption and Decryption technique using ATP (Automatic Theorem Proving) and new antecedent & consequent rules in three variables assigned with conversion systems. As it involves various degrees of encryptions and decryptions, the security is more and this technique is infeasible to attacks.

Keywords: ATP, New antecedent rules, New consequent rules, Encryption, Decryption and Security.

1. Introduction

This paper discusses novel encryption and decryption method using Automatic Theorem Proving and new sequent rules in two and three variables with connectives. In this method, the difficulty of the technique depends on number elements in the domain set. The number of elements in the domain set is directly proportional to the length the block.

T. Surendra et al. [21] proposed cryptosystem developed by ATP and sequent rules assigned by existing ciphers is very feasible for the attackers even though it contains various levels of encryptions and decryptions.

T. Surendra et al. [22] proposed cryptosystem developed by ATP and new sequent rules in two variable and new ciphers is infeasible for the attackers as the sequent rules assigned by new ciphers, which contain alphabets.

We proposed in this paper a novel crypto system using ATP and new developed antecedent and consequent rules in three variables. Which are treating as encryption and decryption rules. For these developed sequent rules we assigned various number conversion system such as Binary Number System, Octal number system, Hexadecimal number system and ASCII Number System for these variables. For two variable sequent rules we used [22] new developed ciphers such as Tree fence technique, Slash fair cipher, Jelly cipher, Triangular cipher and Passing key cipher. Since this cryptosystem contain various levels of encryption, decryption, it is very difficult to the attacker to decrypt the plain text. So security levels are more and for attackers, it is infeasible [19,23].

1.1 Description of Automatic Theorem Proving: [2]

To check the validity of a given statement from the set of premises, Automatic Theorem Proving which includes antecedent rules, consequent rules, sequent, axioms, statements, premises is used. To build each step of derivation in a specific method without any barrier to any ingenuity and finally arriving at the last step, set of rules and procedure are followed. In spite of being a mechanical procedure, more than any other previously available methods, it is an exponential procedure for the verification of the validity of the statement/conclusion. This system includes the procedures of techniques of derivation like 10 rules, an axiom schema and rules of well-formed sequent & formulas and is more competent than the previous methods.

1. The capital letters K, L, M... used as statement variables and statement formulas are considered to be the variables.
2. The connectives appear in the formulas with the order of precedence as given.
3. String of formulas: A string of formulas is defined as follows:
 - (a) Any formula is considered a string of formulas
 - (b) If alpha and beta are strings of formulas, then alpha-beta and beta-alpha are the strings of formulas
 - (c) Only those strings obtained by steps (a) and (b) are considered strings of formulas, with the exception of the empty string which is also a string of formulas.

Note: The order in which the formulas appear in a string is not significant and hence, the strings P, Q, R; Q, R, P; P, R, Q; etc., are the same.

4. Sequent: If alpha and beta are strings of formulas, they are called a *sequent* in which alpha is denoted as the antecedent and beta as the consequent of the sequent.

Thus P, Q, R, S, T, U is true if and only if PQRSTU is true. i.e., A sequent is true if and only if either at least one of the formulas of the antecedent is false or at least one of the formulas of the consequent is true. Hence, the symbol is a generalization of the connection to strings of formulas. Similarly, the symbol applied to the strings of formulas is used as a generalization of the symbol. Thus $P \Rightarrow Q$ means "P implies Q" or is a tautology which means that is true. Ex: $X, Y, Z \Rightarrow X, N$

The empty antecedent is described as the logical constant "true" (T) and the empty consequent is described as the logical constant "false" (F).

5. Axiom Schema: If alpha and beta are strings of formulas such that every formula in both alpha and beta is a variable only, then the sequent is an axiom if and only if alpha and beta have at least one variable in common.

Ex: $M, N, O \Rightarrow X, N, Y$ is an axiom, where M, N, O, X&Y are variables

6. Theorem: The following sequents are theorems of our system
 - (a) Every axiom is a theorem.
 - (b) If a sequent alpha is a theorem and a sequent beta result from alpha through the use of one of the above rules of the system, then beta is a theorem.
 - (c) Sequents obtained by (a) and (b) are the only theorems.

1.2 Rules:

1.2.1 Rules for two variables : [21, 22]

To combine formulas within strings we used following set of connectives { @, ⊕, ⊗, ⊙, ⚬ }. Corresponding to each of these connectives there are two rules, one for the introduction of the connective in the antecedent and the other for its introduction in the consequent. The strings of formulas while P and Q are formulas to which the connectives are applied [24] in the description of these enhanced antecedent and consequent rules.

Antecedent Rules:

1. Rule $\bar{\ } \Rightarrow$: If $a_1, a_2 \Rightarrow A, a_3$ then $a_1, \bar{A}, a_2 \Rightarrow a_3$
2. Rule $\wedge \Rightarrow$: If $A, B, a_1, a_2 \Rightarrow \eta$, then $a_1, A \wedge B, a_2 \Rightarrow a_3$

3. Rule $\vee \Rightarrow$: If $A, a1, a2 \Rightarrow a3$ and $B, a1, a2 \Rightarrow a3$, then $a1, A \vee B, a2 \Rightarrow a3$
4. Rule $\rightarrow \Rightarrow$: If $B, a1, a2 \Rightarrow a3$ and $a1, a2 \Rightarrow A, a3$, then $a1, A \rightarrow B, a2 \Rightarrow a3$
5. Rule $\leftrightarrow \Rightarrow$: If $A, B, a1, a2 \Rightarrow a3$ and $a1, a2 \Rightarrow A, B, a3$, then $a1, A \leftrightarrow B, a2 \Rightarrow a3$

where $A, B, a1, a2$ & $a3$ are atomic variables of compound statements.

Defined Antecedent Rules for two variables:

6. Rule $@ \Rightarrow$: If $A1, AB, A2 \Rightarrow B, A3$ then $A1, A @ B, A2 \Rightarrow A3$
7. Rule $\odot \Rightarrow$: If $A1, A, A2 \Rightarrow AB, A3$ then $A1, A \odot B, A2 \Rightarrow A3$
8. Rule $\otimes \Rightarrow$: If $A1, B, A2 \Rightarrow BA, A3$ then $A1, A \otimes B, A2 \Rightarrow A3$
9. Rule $\circ \Rightarrow$: If $A1, BA, A2 \Rightarrow A, A3$ then $A1, A \circ B, A2 \Rightarrow A3$
10. Rule $\ddot{o} \Rightarrow$: If $A1, B, A2 \Rightarrow AB, A3$ then $A1, A \ddot{o} B, A2 \Rightarrow A3$

where $A, B, A1, A2$ & $A3$ are atomic variables of compound statements. [17,18]

Defined Antecedent Rules for three variables:

1. $K1, (X1 \text{ } \text{ } X2) \text{ } X3, K2 \Rightarrow^S K3$ then $K1, X1 X2 X3, K2 \Rightarrow K3$
2. $K1, (X1 \text{ } \text{ } X2) \text{ } \cap X3, K2 \Rightarrow^S K3$ then $K1, X1, K2 \Rightarrow K1, X2 X3, K2$
3. $K1, (X1 \text{ } \text{ } X2) \text{ } \forall X3, K2 \Rightarrow^S K3$ then $K1, X1 X3, K2 \Rightarrow X2, K3$

where $X1, X2, X3, K1, K2$ & $K3$ are atomic variables of compound statements.

Consequent Rules: [21]

1. Rule $\Rightarrow \lceil$: If $A, A1 \Rightarrow A2, A3$ then $A1 \Rightarrow A2, \lceil A, A3$
2. Rule $\Rightarrow \wedge$: If $A1 \Rightarrow A, A2, A3$ and $A1 \Rightarrow B, A2, A3$, then $A1 \Rightarrow A2, A \wedge B, A3$
3. Rule $\Rightarrow \vee$: If $A1 \Rightarrow A, B, A2, A3$ then $A1 \Rightarrow A2, A \vee B, A3$
4. Rule $\Rightarrow \rightarrow$: If $A, A1 \Rightarrow B, A2, A3$ then $A1 \Rightarrow A2, A \rightarrow B, A3$
5. Rule $\Rightarrow \leftrightarrow$: If $A, A1 \Rightarrow B, A2, A3$ and $B, A1 \Rightarrow A, A2, A3$ then $A1 \Rightarrow A2, A \leftrightarrow B, A3$

where $A, B, A1, A2$ & $A3$ are atomic variables of compound statements. [14,15]

Defined Consequent Rules for two variables : [22]

1. Rule $\Rightarrow @$: If $A1, B \Rightarrow A, A2, A3$ then $A1 \Rightarrow A2, A @ B, A3$
2. Rule $\Rightarrow \odot$: If $A1, A \Rightarrow A2, BA, A3$ then $A1 \Rightarrow A2, A \odot B, A3$
3. Rule $\Rightarrow \otimes$: If $A1, B \Rightarrow A2, AA, A3$ then $A1 \Rightarrow A2, A \otimes B, A3$
4. Rule $\Rightarrow \circ$: If $A1 \Rightarrow A2, BA, A3$ then $A1 \Rightarrow A2, A \circ B, A3$
5. Rule $\Rightarrow \ddot{o}$: If $A1 \Rightarrow A1, AB, A3$ and $A1 \Rightarrow A, A2, A3$ then $A1 \Rightarrow A2, A \ddot{o} B, A3$

where $A, B, A1, A2$ & $A3$ are atomic variables of compound statements. [9,11]

Defined Consequent Rules for three variables :

1. $K1 \Rightarrow^S K2, (X1 \text{ } \text{ } X2) \text{ } X3, K3$ then $K1 \Rightarrow K1, X1 X2 X3, K3$
2. $K1 \Rightarrow^S K2, (X1 \text{ } \text{ } X2) \text{ } \cap X3, K3$ then $K1, X1 X2, K2 \Rightarrow X3, K3$
3. $K1 \Rightarrow^S K2, (X1 \text{ } \text{ } X2) \text{ } \forall X3, K3$ then $K1, X2, K2 \Rightarrow K1, X1 X3, K3$

where $X1, X2, K1, K2$ & $K3$ are atomic variables of compound statements

2. Literature Review

2.1 Binary Number System:

The binary number system is a base-2 numeral system, which means it uses only two digits: 0 and 1. It's the foundation of all modern digital electronics and computing systems. In contrast to the decimal system, which uses 10 digits (0 through 9), binary relies on powers of 2. Each digit in a binary number represents a power of 2. Starting from the rightmost digit, each digit's place value doubles as you move left. To convert a binary number to its decimal equivalent, you multiply each digit by its corresponding power of 2 and then add up the results. Converting decimal numbers to binary involves repeatedly dividing the decimal number by 2 and noting the remainders, then reading those remainders from bottom to top to get the binary representation. The binary system's simplicity makes it well-suited for electronic systems since it's easy to represent with switches (on/off), which are the basic building blocks of digital circuits.

In mathematics and in computing systems, a binary digit, or bit, is the smallest unit of data. Each bit has a single value of either 1 or 0, which means it can't take on any other value. Computers can represent numbers using binary code in the form of digital 1s and 0s inside the central processing unit (CPU) and RAM [10,13].

Example: SECRET

S	E	C	R	E	T
18	4	2	17	4	19

Binary code: 10010 100 10 10001 100 10011

2.2 Octal number system:

The octal number system is a numeral system with base-8 which means it uses 8 digits: 0, 1, 2, 3, 4, 5, 6, and 7. It's often used in computing systems, particularly in the past, as it was a convenient way to represent binary data. Each digit in an octal number represents a power of 8. Starting from the rightmost digit, each digit's place value increases by a power of 8 as you move left. To convert an octal number to its decimal equivalent, multiply each digit by its corresponding power of 8 and then add up the results. Converting decimal numbers to octal involves repeated division of the decimal number by 8 and noting the remainders, then reading those remainders from bottom to top to get the octal representation. While octal was more prevalent in the past, it's less commonly used today in favor of hexadecimal or binary, especially in computing contexts. However, it's still occasionally encountered in certain applications, such as file permissions in Unix-like operating system.

Octal refers to the numbering system with base-8. It comes from the Latin word for eight. The numerals, 0-1-2-3-4-5-6-7 are used in the octal numbering system. It is frequently used as a shorter representation of binary numbers by grouping binary digits into threes in computing environments. [6,8]

Example:

E	N	C	R	Y	P	T	I	O	N
4	13	2	17	24	15	19	8	14	13

Octal code: 4 15 2 21 30 17 23 10 16 15

2.3 Hexadecimal number system:

The hexadecimal number system is a numeral system, with base-16 which means it uses 16 digits: 0-9 followed by the letters A-F (representing 10 to 15). It's widely used in computing because it provides a suitable way to constitute large binary numbers in a more compact and human-readable or an intelligible format.

Each digit in a hexadecimal number represents a power of 16. Starting from the rightmost digit, each digit's place value increases by a power of 16 as you move left.

To convert a hexadecimal number to its decimal equivalent, multiply each digit by its corresponding power of 16 and then add up the results.

Converting decimal numbers to hexadecimal involves repeated division of the decimal number by 16 and noting the remainders, then reading those remainders from bottom to top to get the hexadecimal representation.

In computing, hexadecimal is particularly useful because each hexadecimal digit corresponds to exactly four binary digits (bits). This one-to-one correspondence makes it easy to represent binary data, such as memory addresses, byte values, or color codes, in a more concise and manageable way. Additionally, hexadecimal is commonly used in programming languages, debugging, and digital communication protocols.

The number system, that has a base value equal to 16 hexadecimal number system. It is also pronounced sometimes as 'hex'. Hexadecimal numbers are represented by only 16 symbols. These symbols or values are 0, 1, 2, 3, 4, 5, 6, 7, 8, 9, A, B, C, D, E and F, each digit representing a decimal value.

Example:

	C	R	Y	P	T	O	L	O	G	Y
	2	17	24	15	19	14	11	14	6	24
Hexadecimal:	2	11	18	15	13	14	11	14	6	18

2.4 ASCII Number System:

The ASCII (American Standard Code for Information Interchange) system is not exactly a number system like binary, octal, decimal, or hexadecimal but, it's a character encoding standard that allocates numerical values to characters. In ASCII, each character is represented by a unique 7-bit binary number (extended ASCII uses 8 bits). Originally developed for telegraphy, ASCII has become the basis for encoding text in computers and communication equipment. The ASCII standard includes codes for letters, numbers, punctuation marks, and control characters, such as carriage return and line feed. Here's a basic ASCII table showing some characters and their corresponding decimal values. While ASCII uses decimal numbers for representation in tables and documentation, it's often more convenient to work with hexadecimal representations, particularly in programming contexts. For example, the letter 'A' in ASCII is represented as 41 in hexadecimal. Because ASCII only covers characters used in English text, it's been superseded by more comprehensive character encoding standards like Unicode, which supports a wider range of characters from various languages and symbol sets. ASCII, a standard data-encoding format for electronic communication between computers assigns standard numeric values to letters, numerals, punctuation marks, and other characters used in computers. In full: American Standard Code for Information Interchange.

Example:

	C	O	M	P	U	T	E	R
ASCII:	67	79	77	80	85	84	69	82

P.A. Kameswari et al. [20] solved DLP using pollard Rho algorithm, the cryptosystem based on above DLP useful for transmitting the data securely, but security levels are weak. Surendra, T et al. [21] developed cryptosystem based on ATP and antecedent and consequent rules assigned to the ciphers. In this cryptosystem as the ciphers used already known there is a possibility for attacks. P.A. Kameswari et al. [20] solved DLP using pollard Rho algorithm, the cryptosystem based on above DLP useful for transmitting the data securely, but security levels are weak. Surendra, T et al. [21] developed cryptosystem based on ATP and antecedent and consequent rules assigned to the ciphers. In this cryptosystem as the ciphers used already known there is a possibility for attacks. Surendra, T et al. [22] developed cryptosystem based on ATP and antecedent and consequent rules assigned to the ciphers. In this cryptosystem as the ciphers used already known there is a possibility for attacks. The present developed cryptosystem which is based on Automatic Theorem Proving and new sequent rules in three variables assigned with various number systems overcomes above limitations.

3. Proposed Algorithms:

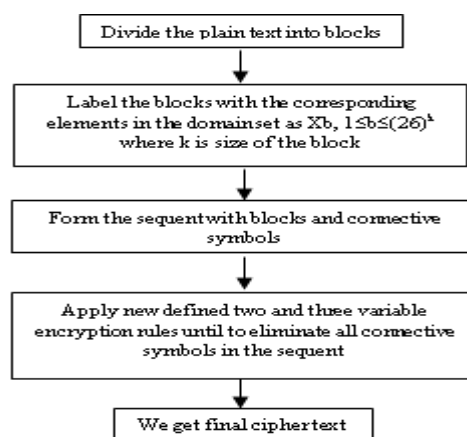
3.1 Encryption process: [21]

Based on the length of the block, the number of elements in the domain set varies. If block length is $r > 0$, domain set will contain $(26)^r$ number of elements. Here we considered block length 2, so the domain set contain $(26)^2 = 676$ elements. Consider the domain set as $\{X_1, X_2, \dots, X_{676}\}$ where $X_1 = AA, X_2 = AB, \dots, X_{676} = ZZ$. Divide the plain text into 'm' blocks with block length k where $m > 0$ and $k > 0$. Label the blocks with the corresponding elements in the domain set which contain $(26)^k$ elements with $k=2$. Then form the sequent with these blocks and connective symbols $\{\wedge, \vee, \ë, \&uarr, \&circledast, \&circledat, \&circledb, \&circledv\}$ using ATP and make sure that the statement formula, either single variable or compound formula may contain in antecedent part or consequent or both. After this apply newly defined two and three variables antecedent and consequent rules until to get eliminate all the connective symbols. Here we get various levels of cipher texts. As it involves different levels of cipher text, it is difficult to the attacker to decrypt the plain text. Here the 1st secret is set of number of systems assigned to the sequent rules. The public key the set contain two parts, first part variables to be used in antecedent part while forming first decryption sequent. Similarly, variables in the second part of the public key are to be used in consequent part while forming first decryption sequent. In the public key, [7] these two parts were separated by the symbol ';'. The second secret key is the set of "antecedent and consequent rules used in order to get level-1 to final level cipher texts". The second secret key contains the order of the connective symbols removed in the encryption sequent's. In the second secret key one connective symbol is to be applied to two variables or two statement formulas only in the process of decryption. The public key is set of "variables X_j with $1 \leq j \leq (26)^2$ in the final encryption sequent".

3.2 Encryption algorithm:

1. Divide the plain text into finite number of blocks say m, where each block contain 'k' number of alphabets ($k > 0$). If any block contain less than k number of numerals then make it k number block by filling with dummy alphabet say x. we can fill with any other alphabet by our choice.
2. Label these blocks as with the elements in the domain set, where the domain set contain X_1, X_2, \dots, X_r where $r = 26^k$ the number of elements in the domain set which we use for plain text labeling.
3. Form sequent with these blocks in such way that can apply defined two or three variables sequent rules.
4. Then apply sequent rules, we get various levels of ciphers texts.
5. Repeat the process until all the connective symbols will get eliminated and then we get final cipher text.
6. Here public key is connective symbols in order wise eliminated and private key is set of two variable sequent rules assigned ciphers and Three variable sequent rules assigned with different number systems. Also through private key will agree block length.

Encryption flow chart:



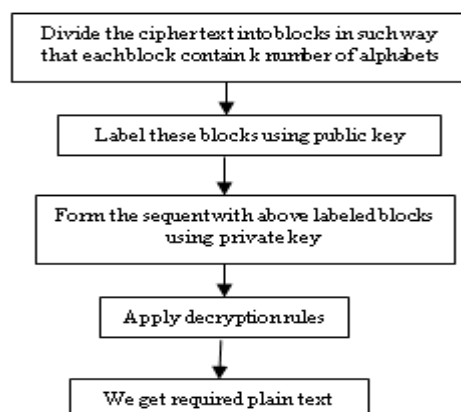
3.3 Decryption process:

The cipher text obtained from the sender have to divide into m number blocks where each block contain ‘k’ number of alphabets ($k > 0$). Label these blocks with $X_j, 1 \leq j \leq (2)^{26}$, using the public key [7]. Then form the decryption sequent with these blocks secret key 2. Then apply two and three variable decryption rules by following secret key 1 and secret key 2. The connectives in the secret key are used in reverse order i.e., from backward direction to decode the cipher text. The implications in the secret key are used from the right and ‘c followed by connective symbol represents rules that has to be applied in decryption consequent part. Similarly, ‘a followed by connective symbol’ represents that rule to be applied in decryption antecedent part’. With one connective symbol in the secret key, compound statement is formed by taking two variables or two compound statements or one variable and compound statement by considering the order. The process is repeated until all the connectives are used in the secret key. In this process we get required plain text [16,24].

3.4 Decryption algorithm:

1. Divide the cipher text into m number of blocks as block length agreed through secret key.
2. Label these blocks using public key.
3. Form the sequent with these using another public key.
4. Apply Decryption process using public and private keys then we get required plain text.

Decryption flow chart



4. Implementation of Encryption and Decryption:

Symbol	Name
$X@Y$	Jelly cipher
$X\odot Y$	Tree fence cipher
$(X\oslash Y)\#Z$	Octal system
$(X\text{I}Y)\forall Z$	ASCII system
$(X\text{I}Y)\text{I} Z$	Hexa decimal system
a-0, b-1, c-2, z-25 \Rightarrow^{S_n}	Alphabets and its values in encryption sequent
\Rightarrow^{SD_n}	n- decryption sequent
a-connective	connective symbol used in antecedent part
c-connective	connective symbol used in consequent part

4.1 Implementation 1. [4,5]

Plain text: CHANDRAYAN IS READY FOR LAUNCHING

Divide the this plain text as 2 letter blocks as ‘CH|AN|DR|AY|AN|IS|RE|AD|YF|OR| LA|UN|CH|IN|GX’ where $X_{62}=CH, X_{14}=AN, X_{122}=DR, X_{25}=AY, X_{14}=AN, X_{253}=IS, X_{473}=RE, X_4=AD, X_{656}=YF, X_{408}=OR, X_{313}=LA, X_{560}=UN, X_{86}=CH, X_{248}=IN, X_{206}=GX$. So divided plain text blocks equivalent to $(X_1|X_2|X_3|X_4|X_5|X_6|X_7|X_8|X_9|X_{10})$. For the first sequent with these variables as $[(X_{248} \otimes X_{560}) \cap X_{408}] \Delta X_{4A} [(X_{253} \boxtimes X_{25}) \boxdot X_{14}] \Rightarrow^{S1} (X_{206} \odot X_{86}) \vee (X_{313} \oplus X_{656}) \vee X_{473} \vee [(X_{14} \delta X_{122}) \forall X_{62}]$. Then apply first ‘rule $\Delta \Rightarrow$ ’ and ‘rule $\Rightarrow \vee$ ’ we get $[(X_{329} \otimes X_{641}) \cap X_{489}, X_{111}, [(X_{334} \boxtimes X_{106}) \boxdot X_{121}] \Rightarrow^{S2} (X_{220} \odot X_{185}), (X_{642} \oplus X_{131}), X_{181}, [(X_{471} \delta X_4) \forall X_{388}]$ where $X_{329}=LQ, X_{641}=XQ, X_{489}=RU, X_{111}=DG, X_{334}=LV, X_{106}=DB, X_{121}=DQ, X_{220}=HL, X_{185}=GC, X_{642}=XR, X_{131}=EA, X_{181}=FY, X_{471}=RC, X_4=AD, X_{388}=NX$. Now again apply ‘rule $\otimes \Rightarrow$ ’ now the above sequent we get $X_{323}, X_{111}, [(X_{334} \boxtimes X_{106}) \boxdot X_{121}] \Rightarrow^{S3} (X_{220} \odot X_{185}), (X_{642} \oplus X_{131}), X_{181}, [(X_{471} \delta X_4) \forall X_{388}]$, $X_{479} X_{327}$ where $X_{323}=LK, X_{479}=RK, X_{327}=LO$, now again apply ‘rule $\boxtimes \Rightarrow$ ’ now the above sequent we get $X_{323}, X_{111}, X_{390} X_{106} X_{125} \Rightarrow^{S4} (X_{220} \odot X_{185}), (X_{642} \oplus X_{131}), X_{181}, [(X_{471} \delta X_4) \forall X_{388}]$, $X_{479} X_{327}$ where $X_{390}=NZ, X_{106}=DB, X_{125}=DU$ now again apply ‘rule $\Rightarrow \odot$ ’, on the above sequent then we get $X_{323}, X_{111}, X_{390} X_{106} X_{125} \Rightarrow^{S5} X_{90} X_{215}, (X_{642} \oplus X_{131}), X_{181}, [(X_{471} \delta X_4) \forall X_{388}]$, $X_{479} X_{327}$ where $X_{215}=HG, X_{90}=CL$, now again apply ‘rule $\Rightarrow \oplus$ ’, on the above sequent then we get $X_{323}, X_{111}, X_{390} X_{106} X_{125}, X_{347} \Rightarrow^{S6} X_{90} X_{215}, X_{182}, X_{181}, [(X_{471} \delta X_4) \forall X_{388}]$, $X_{479} X_{327}$ where $X_{182}=FZ, X_{347}=MI$ now again apply ‘rule $\Rightarrow \delta$ ’, on the above sequent then we get $X_{323}, X_{111}, X_{390} X_{106} X_{125}, X_{347}, (X_{385}^{(L)} X_{150}^{(X)}) \Rightarrow^{S7} X_{90} X_{215}, X_{182}, X_{181}, (X_{107}^{(1)} X_{514}^{(X)}) (X_{96} X_{150}^{(B)}), X_{479} X_{327}$ where $X_{107}^{(1)} X_{514}^{(X)} = DC1 STX X_{385}^{(L)} X_{150}^{(X)} = NUL ETX X_{96} X_{150}^{(B)} = CR ETB$ stop the processes since all the connective symbols where eliminated in the last sequence so final level cipher is LQDGNZDBDU MINULETX \Rightarrow CLHGFZFYDC1STXCRETBR KL O. The public key is $\{X_{323}, X_{111}, X_{390} X_{106} X_{125}, X_{347}, X_{107}^{(1)} X_{514}^{(X)} X_{385}^{(L)} X_{150}^{(X)}; X_{90} X_{215}, X_{182}, X_{181}, X_{107}^{(1)} X_{514}^{(X)} X_{96} X_{150}^{(B)}, X_{479} X_{327}\}$ and secret key 1 is $\{\oplus\text{-Jelly}, \odot\text{-Tree fence}, \boxtimes\text{-A-Octal}, \delta\text{-ASCII}, \otimes\text{-Hexa}\}$ and secret key 2 is $\{a\Delta, cv, a\otimes, a\boxtimes, c\odot, c\oplus\}$.

5. Results and Discussion:

Fig. 1: The execution time of Encryption

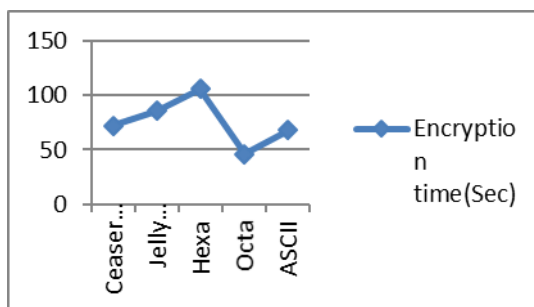


Fig. 2: The execution time of Decryption

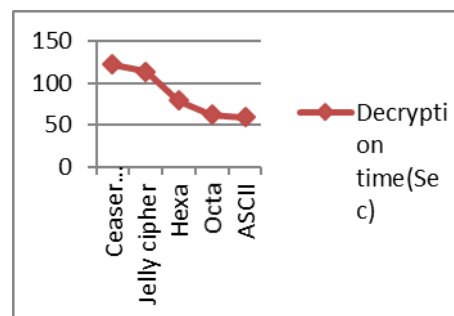
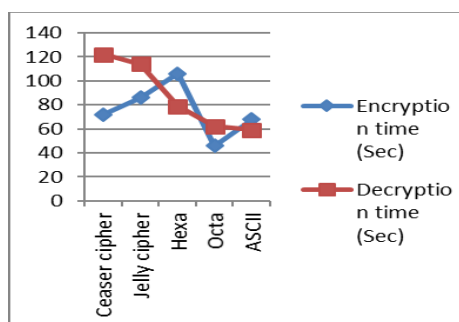


Fig. 3: The execution time of Encryption & Decryption



5. Cryptanalysis:

New cryptosystems with automatic theorem proving with novel encryption and decryption rules using three or more variables assigned to different methods can be developed [3] in future and these rules can be extended for n variables also and we can apply programming techniques, so that more data also we can do encryption and decryption easily.

6. Acknowledgements:

The authors would like to express their gratitude for the support extended by the Department of Mathematics, GSS, and GITAM Deemed to be University.

References








- [1] A.J. Menezes, P.C. Van Oorschot, and S.A. Vanstone, "Hand book of Applied Cryptography." CRC Press Series on Discrete Mathematics and its Applications. CRC Press, Boca Raton, FL, 1997. With a foreword by Ronald L. Rivest.
- [2] Bhishma Rao, "A text of Mathematical Foundations of Computer Science", SciTech Publications (India) Pvt Ltd., ISBN- 10: 8183710433.
- [3] Douglas R. Stinson "Cryptography theory and practice" Second edition.
- [4] Geoff Sutcliffe, "Automated Theorem Proving: Theory and Practice A Review", AI Magazine Volume 23 Number 1 (2002) (© AAAI).
- [5] Gerhard Frey "The arithmetic behind cryptography" AMS volume 57, Number 3.
- [6] Hans Delfs Helmut Knebl "Introduction to cryptography" Principles and its Applications, second edition.
- [7] Harry Yosh "The key exchange cryptosystem used with higher order Diophantine equations" IJNSA VOL.3, 15. No.2, March 2011.
- [8] I. Niven, H.S. Zuckerman and J.H. Silverman "An Introduction to the Theory of Numbers", 5th ed., John Wiley and Sons, New York, 1991.
- [9] J. Buchmann "Introduction to cryptography", Springer Verlag 2001.
- [10] J.P. Tremblay & R. Manohar, "A text book of Discrete Mathematical Structures with Applications to Computer Science", McGraw Hill Education (India) Edition 1997.
- [11] Keith M. Martin, Rei Safavi-Naini, Huaxiong Wang and Peter R.Wild "Distributing the encryption and decryption of a block cipher".
- [12] K.H. Rosen, "Elementary number theory and its applications" Third edition, Addison- Wesley.
- [13] Menzes A. and Vanstone S. "Hand book of applied cryptography", The CRC-Press series of Discrete Mathematics and its Applications CRC-Press, 1997.
- [14] Neal Koblitz "A course in number theory and cryptography" ISBN 3-578071-8, SPIN 10893308.
- [15] Peter J. Smith and Michael J.J. Lennon, "A New Public Key System" LUC Partners, Auckland UniServices Ltd, The University of Auckland, Private Bag92019m Auckland, New Zealand.
- [16] Phillip Rogaway Mihir Bellare John Black Ted Krovetz "OCB: A block-cipher mode of operation for efficient authenticated encryption".
- [17] P.Rogaway, M-Bellare, J. Black,T-Korvetz "A Block Cipher mode of operation for efficient authenticated encryption" Eighth ACM conference on computer and communication security (CCS-8) ACM Press, 2001.
- [18] Serge Vaudenay "A classical introduction to cryptography applications for communication security" Springer International Edition.
- [19] Song Y. Yan, "Number Theory for computing", 2nd edition, Springer, ISBN: 3- 540-43072-5.
- [20] Surendra Talari & P. Anuradha Kameswari, Pollard RHO algorithm implemented to Discrete Log with Lucas sequences, International Journal on Recent and Innovation Trends in Computing and Communication, ISSN:2321-8169 Volume: 4, Issue: 3.
- [21] Surendra Talari, S.S. Amiripalli, P. Sirisha, D.S. Kumar and V.K. Deepika, An Improved Cipher Based Automatic Theorem Proving Technique for encryption and Decryption, "Advances in Mathematics: Scientific Journal", page numbers 3121-3134, volume 9/5, June, 2020.

- [22] Surendra Talari, K.K. Sowjanya, G. Yojana, and V. Prasad, New Cryptosystem Using Enhanced Automatic Theorem Proving and Enhanced Ciphers, "Journal of Theoretical and Applied Information Technology", page numbers 6434-6443, volume 101/20, October, 2023.
- [23] W. Diffie and M. E. Hellman "New directions in Cryptography." IEEE Transactions on Information theory, 22, 644654, 1976.
- [24] William Stallings "Cryptography and network security principals and practice" 5th ed.

Modern Physics Letters B
 (2024) 2450477 (20 pages)
 © World Scientific Publishing Company
 DOI: 10.1142/S0217984924504773



Behavior of suspended natural rubber balls in water at small Reynolds numbers

K. Madhukar ^{*,||}, M. C. Jayaprakash ^{†,**}, M. Santoshi Kumari ^{††,‡‡},
 H. Y. Shrivalli ^{*,‡‡}, K. V. Nagaraja ^{§,§§}, Raman Kumar ^{†,¶¶}
 and R. Naveen Kumar ^{§,|||}

^{*}*Department of Mathematics, BMS College of Engineering,
 Bull Temple Road, Basavanagudi, Bangalore 560019, Karnataka, India*

[†]*Department of Information Technology,
 University of Technology and Applied Sciences,
 Al Musanna, Sultanate of Oman*

[‡]*Department of Mathematics, Chaitanya Bharathi Institute of Technology,
 Gandipet, Hyderabad 500075, India*

[§]*Computational Science Lab, Amrita School of Engineering,
 Amrita Vishwa Vidyapeetham, Bengaluru, India*

[¶]*Department of Mechanical Engineering,
 University Centre for Research & Development,
 Chandigarh University, Mohali, India*

^{||}*madhukar.maths@bmsce.ac.in*

^{**}*jayaprakashmc@gmail.com*

^{††}*santoshinagaram@gmail.com*

^{‡‡}*hys.maths@bmsce.ac.in*

^{§§}*kv_nagaraja@blr.amrita.edu*

^{¶¶}*raman.me@cumail.in*

^{|||}*nkrmaths@gmail.com*

Received 4 April 2024

Revised 15 April 2024

Accepted 5 May 2024

Published

This study explores the experimentally verifiable rheological parameters of sparsely spaced suspensions of periodically forced rubber spheres in water at low Reynolds numbers. The experimentally verifiable rheological parameters are first normal stress difference, second normal stress difference, intrinsic pressure, and relative viscosity. These parameters are observed to be dependent on the amplitude of the periodic force, particle Reynolds numbers and the volume fraction. The main aim of this study is to determine how well the neutrally buoyant rubber balls (isoprene) flow with the solutions at low Reynolds numbers when forced periodically. The motivation of the problem consideration is to study the collective behavior of the balls when suspended in a dilute limit. An interesting and novel feature of these balls is their non-Newtonian behavior in the Newtonian frame of reference. The model obtained was an

^{|||} Corresponding author.

K. Madhukar et al.

integro-differential-equation, which was solved using the Runge–Kutta fourth-order method. Results reveal that the relation between the intrinsic pressure and relative viscosity depicts a nonlinear relation with Reynolds number and proportional to volume fraction. When Rubber balls are forced periodically, they exhibit the non-Newtonian behavior. The relation between the intrinsic pressure and relative viscosity depicts a nonlinear relation with Reynolds number and proportional to volume fraction.

Keywords: Natural rubber; neutrally buoyant; spheres; low Reynolds numbers; periodic force.

PACS Nos.: 66.20.Cy, 51.20.+d

Nomenclature

a	:	Characteristic particle dimension
\mathbf{Y}_s	:	Integrated particle displacement
m_p	:	Particle mass
$\mathbf{p} = \frac{\mathbf{Y}_s(t) - \mathbf{Y}_s(s)}{ \mathbf{Y}_s(t) - \mathbf{Y}_s(s) }$:	Unit vector in align with the x axis
$\text{Re} = aU_c/\vartheta$:	Reynolds number
$\mathbf{U}^\infty(t)$:	Uniform velocity of the time dependent uniform flow about the particle.
$[\text{Re}_{F1}, \text{Re}_{F2}, \text{Re}_{F3}]$:	Amplitudes of the periodic force
$\text{Sl} = \frac{a}{U_c} / \tau_c$:	Strouhal number
τ_c	:	Characteristic time scale
\mathbf{F}_s^{H}	:	Pseudo steady Stokes' drag
$\mathbf{F}_s^{\text{H}_\parallel}(t) = -6\pi\mathbf{U}_s \cdot \mathbf{pp}$:	Tangential part of Stokes' drag
ϑ	:	Kinematic viscosity
\mathbf{F}^{ext}	:	External force
\mathbf{A}	:	$A = \frac{\text{Re}}{2} \left(\frac{t-s}{\text{ReSl}} \right)^{1/2} \left(\frac{\mathbf{Y}_s(t) - \mathbf{Y}_s(s)}{t-s} \right)$
\mathbf{U}_p	:	Particle velocity
U_c	:	Characteristic particle slip velocity
\mathbf{F}^{H}	:	Hydrodynamic force
$\mathbf{F}_s^{\text{H}_\perp}(t) = -6\pi\mathbf{U}_c \cdot (\boldsymbol{\delta} - \mathbf{pp})$:	Normal part of Stokes' Drag
$\mathbf{U}_s = \mathbf{U}_p - \mathbf{U}^\infty$:	Stream velocity
$1, \omega, \omega_1$:	Phase(s) of periodic force
φ	:	Volume fraction
$\overline{U_{px}}$:	Mean of U_{px}

1. Introduction

Due to their unique characteristics, neutrally buoyant particle suspensions are important in developing various composite materials. The neutrally buoyant particles are neither afloat nor sink, this means that when the liquid like water is still, they stay at the same position at which they are left in the water. That is, they balance buoyancy. Such property of materials is essential for seaplanes, sea submarines, scuba divers and other water/ocean equipment. Hence, the study of neutrally buoyant large suspensions in water becomes very important. The tides in the ocean can be considered as a periodic forcing on the submarines mainly submarine spheres or the wheels of the ship and ocean planes. The periodically forced neutrally buoyant suspensions are considered very little in the literature. Zaidi¹ studied vortex evacuation features of distributed dilute suspensions. Haffner and Mirbod² studied dilute particle suspension velocity over porous mediums. Kuznetsov *et al.*³ studied the

physical and magnetic stability of a semi-dilute magnetic multicore nanoparticle solution. A suitable rheology for dilute microswimmer suspensions was studied by Girodroux-Lavigne.⁴ Corona *et al.*⁵ used Rheo-SANS to estimate suspension closure in diluted and undiluted solutions. Natural rubber is the chemical compound isoprene, which is neutrally buoyant in water and studied and also synthetically produced, called poly isoprene, for it has various industrial and scientific applications. The rheological calculations done here are the first normal stress difference, second normal stress difference, intrinsic pressure, and relative viscosity. The analysis of heat transmission of the wavy extended surface with radiation impact was examined by Prakash *et al.*⁶ The forced rigid neutrally buoyant spheres in a Newtonian liquid at low Reynolds numbers are studied mathematically in this investigation. The literature has long established that the DC electric force causes a spherical particle to drift and that the electric force causes the sphere to spin when a fluid is in an electrostatic field. In 1984, Thomas Jones published a review on the Quincke rotation of spheres. He notes that Quincke discovered that tiny solid spheres spin on their own when submerged in liquid exposed to a strong electrostatic field in 1896. Khan *et al.*⁷ explored the stream of nanofluid via a stretchy sphere using numerical simulation. Gkormpatsis *et al.*⁸ discussed the flow of a viscoelastic liquid past a sphere with a slip surface. Albalawi *et al.*⁹ inspected the flow of liquid via the cylinders with heat transport attributes. Morimoto *et al.*¹⁰ examined pore network models critically for fluid flow simulation using sphere-shaped particles. Peng *et al.*¹¹ examined the effects of sphere-shaped rough surfaces on the fluid flow of argon atoms entering the microchannel under boiling conditions.

Various studies have been conducted to highlight the motion of particles at zero Reynolds numbers while discussing particle motion concerning Reynolds numbers. When studying the motions of microparticles, microswimmers, or microorganisms in a fluid, the particles' zero Reynolds number flow is crucial. Arosemena *et al.*¹² examined the channel stream of Newtonian liquids under turbulent circumstances at low Reynolds numbers. The stream of liquid via a stretchy surface using the collocation approach was deliberated by Madhu *et al.*¹³. The metachronous patterns of artificial cilia for fluid propulsion were studied by Milana *et al.*¹⁴. Ran *et al.*¹⁵ investigated the dispersed blowing management of flow around a square cylinder at a low Reynolds number. Zargartalebi *et al.*¹⁶ explained the viscoelastic fluid flow utilizing constrained forms at low Reynolds numbers. Many scholars have recently investigated the flow of various liquids when periodic stresses are present. Krishnamurthy *et al.*¹⁷ looked at the effects of periodic and electrical stresses on spherical particles that float in a Newtonian fluid. Alsulami *et al.*¹⁸ evaluated fluid flow via a permeable media under the magnetic impact. Raut *et al.*¹⁹ extended the obliquely propagating solitary waves in a relativistic gyrating magnetized plasma with a periodic force. Using flow equations, Noviĉenko *et al.*²⁰ investigated the amplitude-modulated time-periodic force caused by quantum systems. Srilatha *et al.*²¹ explored the impact of variable thermal attributes of the fluid stream via a gyrating disk.

K. Madhukar et al.

The dynamics and rheology of periodically forced particles were studied by Ramamohan *et al.*²². Hence, in this work, we extend the study to rubbers that are naturally neutrally buoyant and study their rheological parameters. These parameters are calculated for the low Reynolds number regime, which can be considered the ocean water and the submarines spherical in shape made of neutrally buoyant surfaces. There is a large gap in the literature about the natural rubber rheology. In this work, we have taken the first step in probing the questions of what are the rheological parameters of the natural rubber when suspended in water and what is their ensemble averages particularly when the balls are placed in such a way that they cannot interact and at low Reynolds numbers. It has turned out that the rheological parameters, such as normal stress differences, the pressure and intrinsic viscosity can be calculated through simulations and numerically method in place of it. The question answered here is how well the neutrally buoyant rubber balls (isoprene) flow with the solutions at low Reynolds numbers when forced periodically. It is expected that the wheels of flight, submarines, or ships will sometimes be exposed to marshy or concentrated or viscous media whose Reynolds numbers are low.

This paper is arranged as follows. Section 2 discusses the mathematical formulation for dynamics and rheology calculations. Section 3 deals with the solution method and its verification are discussed. Section 4 deals with results and discussions. Section 5 concludes.

2. Mathematical Formulation

Considering the Lovalenti and Brady²³ expression for the hydrodynamic force at low but nonzero Reynolds numbers for a time-dependent flow.

$$\begin{aligned} \mathbf{F}^{\mathbf{H}}(t) = & \text{ReSl} \dot{\mathbf{U}}^\infty(t) - 6\pi \mathbf{U}_s(t) - \frac{2\pi}{3} \text{ReSl} \dot{\mathbf{U}}_s(t) + \frac{3}{8} \left(\frac{\text{ReSl}}{\pi} \right)^{\frac{1}{2}} \\ & \times \left\{ \int_{-\infty}^t \left\{ \frac{2}{3} \mathbf{F}_s^{\mathbf{H}_\parallel}(t) - \left[\frac{1}{|\mathbf{A}|^2} \left(\frac{\sqrt{\pi}}{2|\mathbf{A}|} \text{erf}(|\mathbf{A}|) - \exp(-|\mathbf{A}|^2) \right) \right] \mathbf{F}_s^{\mathbf{H}_\parallel}(s) \right. \right. \\ & + \frac{2}{3} \mathbf{F}_s^{\mathbf{H}_\perp}(t) - \left[\exp(-|\mathbf{A}|^2) - \frac{1}{2|\mathbf{A}|^2} \left(\frac{\sqrt{\pi}}{2|\mathbf{A}|} \text{erf}(|\mathbf{A}|) - \exp(-|\mathbf{A}|^2) \right) \right] \\ & \left. \left. \times \mathbf{F}_s^{\mathbf{H}_\perp}(s) \right\} \frac{2ds}{(t-s)^{3/2}} \right\} + o(\text{Re}). \end{aligned} \quad (1)$$

$\mathbf{F}_s^{\mathbf{H}}(t)$ is the pseudo-steady Stoke's drag, which can be decomposed to $\mathbf{F}_s^{\mathbf{H}_\parallel}(t) + \mathbf{F}_s^{\mathbf{H}_\perp}(t)$. $\mathbf{F}_s^{\mathbf{H}_\parallel}(t) = -6\pi \mathbf{U}_s \cdot \mathbf{pp}$ and $\mathbf{F}_s^{\mathbf{H}_\perp}(t) = -6\pi \mathbf{U}_s \cdot (\boldsymbol{\delta} - \mathbf{pp})$ where $\boldsymbol{\delta}$ is the idem tensor of order 2. The unit vector \mathbf{p} is given by $\frac{\mathbf{Y}_s(t) - \mathbf{Y}_s(s)}{|\mathbf{Y}_s(t) - \mathbf{Y}_s(s)|}$, here $\mathbf{Y}_s(t) - \mathbf{Y}_s(s)$ is the integrated displacement of the particle relative to the fluid from time s to the current time t . $\mathbf{A} = \frac{\text{Re}}{2} \left(\frac{t-s}{\text{ReSl}} \right)^{1/2} \left(\frac{\mathbf{Y}_s(t) - \mathbf{Y}_s(s)}{t-s} \right)$. Velocity terms are made non-dimensional by characteristic particle slip velocity. Forced term defined by $\mu a U_c$.

It can be noted here that there is a singularity at $t = s$. To take account of that, the integral is split into 0 to $t - \varepsilon$ and $t - \varepsilon$ to t . Hydrodynamic force hence becomes

$$\mathbf{F}^{\mathbf{H}}(t) = -6\pi\mathbf{U}_s(t) - \frac{2\pi}{3}\text{ReSl}\dot{\mathbf{U}}_s(t) + \frac{3}{8}\sqrt{\left(\frac{\text{ReSl}}{\pi}\right)}(\mathbf{P} + \mathbf{Q}), \quad (2)$$

$$\mathbf{P} = \int_0^{t-\varepsilon} \frac{-8\pi\mathbf{U}_s(t)ds}{(t-s)^{3/2}} - \left[\frac{1}{|\mathbf{A}|^2} \left(\frac{\sqrt{\pi}}{2|\mathbf{A}|} \text{erf}(|\mathbf{A}|) - \exp(-|\mathbf{A}|^2) \right) \right] \frac{-12\pi\mathbf{U}_s(s)ds}{(t-s)^{\frac{3}{2}}}, \quad (3)$$

$$\mathbf{Q} = \int_{t-\varepsilon}^t \frac{-8\pi\mathbf{U}_s(t)ds}{(t-s)^{3/2}} - \left[\frac{1}{|\mathbf{A}|^2} \left(\frac{\sqrt{\pi}}{2|\mathbf{A}|} \text{erf}(|\mathbf{A}|) - \exp(-|\mathbf{A}|^2) \right) \right] \frac{-12\pi\mathbf{U}_s(s)ds}{(t-s)^{\frac{3}{2}}}. \quad (4)$$

Transforming the integral with respect to \mathbf{A} , we have

$$Q = \int_0^{c\sqrt{\varepsilon}} \frac{8\pi U_s^2 \text{Red}A}{(\text{ReSl})^{1/2} A^2} - \left[\frac{1}{|\mathbf{A}|^2} \left(\frac{\sqrt{\pi}}{2|\mathbf{A}|} \text{erf}(|\mathbf{A}|) - \exp(-|\mathbf{A}|^2) \right) \right] \frac{12\pi U_s^2 \text{Red}A}{(\text{ReSl})^{1/2} A^2}. \quad (5)$$

Now as s tends to t , the term $-\left[\frac{1}{|\mathbf{A}|^2} \left(\frac{\sqrt{\pi}}{2|\mathbf{A}|} \text{erf}(|\mathbf{A}|) - \exp(-|\mathbf{A}|^2)\right)\right]$ tends to $2/3$. Hence, Q vanishes in the limiting case of s tending to t . Therefore, the governing equation is

$$\mathbf{F}^{\mathbf{H}}(t) = -6\pi\mathbf{U}_s(t) - \frac{2\pi}{3}\text{ReSl}\dot{\mathbf{U}}_s(t) + \frac{3}{8}\sqrt{\left(\frac{\text{ReSl}}{\pi}\right)}(\mathbf{J} + \mathbf{I}), \quad (6)$$

where

$$\mathbf{J} = \int_0^{t-\varepsilon} \left[\frac{1}{|\mathbf{A}|^2} \left(\frac{\sqrt{\pi}}{2|\mathbf{A}|} \text{erf}(|\mathbf{A}|) - \exp(-|\mathbf{A}|^2) \right) \right] \frac{-12\pi\mathbf{U}_s(s)ds}{(t-s)^{\frac{3}{2}}}, \quad (7)$$

and

$$\mathbf{I} = 16\pi\mathbf{U}_s(t) \left(\frac{1}{\sqrt{t}} - \frac{1}{\sqrt{\varepsilon}} \right). \quad (8)$$

By Newton's second law, we have

$$\frac{m_p \dot{\mathbf{U}}_{\mathbf{p}}}{\mu a U_c} = \mathbf{F}^{\mathbf{H}} + \mathbf{F}^{\text{ext}}, \quad (9)$$

where

$$\mathbf{F}^{\text{ext}} = \begin{pmatrix} F_x \sin t \\ F_y \sin \omega_1 t \\ F_z \sin \omega_2 t \end{pmatrix}, \quad \mathbf{U}_s = \begin{pmatrix} U_{px} - u_x \\ U_{py} - u_y \\ U_{pz} - u_z \end{pmatrix}, \quad \dot{\mathbf{U}}_{\mathbf{p}} = \begin{pmatrix} \dot{U}_{px} \\ \dot{U}_{py} \\ \dot{U}_{pz} \end{pmatrix},$$

K. Madhukar et al.

$$\mathbf{F}^H = \begin{pmatrix} F_x^H \\ F_y^H \\ F_z^H \end{pmatrix} = \begin{bmatrix} -6\pi U_{px}(t) - \frac{2\pi}{3} \text{ReSl} \dot{U}_{px}(t) + \frac{3}{8} \sqrt{\left(\frac{\text{ReSl}}{\pi}\right)} (J_1 + I_1) \\ -6\pi U_{py}(t) - \frac{2\pi}{3} \text{ReSl} \dot{U}_{py}(t) + \frac{3}{8} \sqrt{\left(\frac{\text{ReSl}}{\pi}\right)} (J_2 + I_2) \\ -6\pi U_{pz}(t) - \frac{2\pi}{3} \text{ReSl} \dot{U}_{pz}(t) + \frac{3}{8} \sqrt{\left(\frac{\text{ReSl}}{\pi}\right)} (J_3 + I_3) \end{bmatrix},$$

$$J_1 = \int_0^{t-\varepsilon} \left[\frac{1}{|\mathbf{A}|^2} \left(\frac{\sqrt{\pi}}{2|\mathbf{A}|} \text{erf}(|\mathbf{A}|) - \exp(-|\mathbf{A}|^2) \right) \right] \frac{-12\pi U_{px}(s) ds}{(t-s)^{\frac{3}{2}}},$$

$$J_2 = \int_0^{t-\varepsilon} \left[\frac{1}{|\mathbf{A}|^2} \left(\frac{\sqrt{\pi}}{2|\mathbf{A}|} \text{erf}(|\mathbf{A}|) - \exp(-|\mathbf{A}|^2) \right) \right] \frac{-12\pi U_{py}(s) ds}{(t-s)^{\frac{3}{2}}},$$

$$J_3 = \int_0^{t-\varepsilon} \left[\frac{1}{|\mathbf{A}|^2} \left(\frac{\sqrt{\pi}}{2|\mathbf{A}|} \text{erf}(|\mathbf{A}|) - \exp(-|\mathbf{A}|^2) \right) \right] \frac{-12\pi U_{pz}(s) ds}{(t-s)^{\frac{3}{2}}},$$

$$I_1 = 16\pi U_{px}(t) \left(\frac{1}{\sqrt{t}} - \frac{1}{\sqrt{\varepsilon}} \right), \quad I_2 = 16\pi U_{py}(t) \left(\frac{1}{\sqrt{t}} - \frac{1}{\sqrt{\varepsilon}} \right),$$

$$I_3 = 16\pi U_{pz}(t) \left(\frac{1}{\sqrt{t}} - \frac{1}{\sqrt{\varepsilon}} \right), \tag{10}$$

$\varepsilon = 0.01,$

$$\mathbf{A} = \begin{bmatrix} A_x \\ A_y \\ A_z \end{bmatrix} = \begin{bmatrix} \frac{\text{Re}}{2} \left(\frac{t-s}{\text{ReSl}} \right)^{1/2} \left(\frac{Y_{px}(t) - Y_{px}(s)}{t-s} \right) \\ \frac{\text{Re}}{2} \left(\frac{t-s}{\text{ReSl}} \right)^{1/2} \left(\frac{Y_{py}(t) - Y_{py}(s)}{t-s} \right) \\ \frac{\text{Re}}{2} \left(\frac{t-s}{\text{ReSl}} \right)^{1/2} \left(\frac{Y_{pz}(t) - Y_{pz}(s)}{t-s} \right) \end{bmatrix}, \quad |\mathbf{A}| = \sqrt{A_x^2 + A_y^2 + A_z^2},$$

Therefore, the governing equations of the problem are

$$\frac{dY_{px}}{dt} = U_{px}, \tag{11}$$

$$\frac{dY_{py}}{dt} = U_{py}, \tag{12}$$

$$\frac{dY_{pz}}{dt} = U_{pz}, \tag{13}$$

$$\frac{dU_{px}}{dt} = \frac{1}{\text{REST}} \left(\text{Re}_{F1} \sin t - 6\pi U_{px}(t) + \frac{3}{8} \sqrt{\left(\frac{\text{ReSl}}{\pi}\right)} (J_1 + I_1) \right), \tag{14}$$

$$\frac{dU_{py}}{dt} = \frac{1}{\text{REST}} \left(\text{Re}_{F2} \sin \omega_1 t - 6\pi U_{py}(t) + \frac{3}{8} \sqrt{\left(\frac{\text{ReSl}}{\pi}\right)} (J_2 + I_2) \right), \tag{15}$$

Behavior of suspended natural rubber balls

$$\frac{dU_{pz}}{dt} = \frac{1}{\text{REST}} \left(\text{Re}_{F3} \sin \omega_2 t - 6\pi U_{pz}(t) + \frac{3}{8} \sqrt{\left(\frac{\text{ReSl}}{\pi}\right)} (J_3 + I_3) \right), \quad (16)$$

$$\text{REST} = \frac{2\pi \text{ReSl} + 4\pi \text{Re}}{3} \quad \text{and} \quad \text{Re}_{F1} = \frac{F_x}{\mu a U_c}, \quad \text{Re}_{F2} = \frac{F_y}{\mu a U_c}, \quad \text{Re}_{F3} = \frac{F_z}{\mu a U_c}.$$

2.1. Rheology calculations

The Batchelor's²⁴ expression for non-interacting particles in a fluid, the bulk stress is given by

$$\Sigma^P = \frac{1}{V} \sum_i \mathbf{S}_i - \frac{\text{Re}}{V} \sum_i \int \frac{1}{2} (\mathbf{ax} + \mathbf{xa}) dV_i - \frac{\text{Re}}{V} \int \mathbf{u}' \mathbf{u}' dV, \quad (17)$$

where the stress term at zero Reynolds number is the first term. According to Bardy and Bossis,²⁵ this phrase is as follows:

$$\frac{1}{V} \sum_i \mathbf{S}_i = \left(\frac{N}{V}\right) \{ \langle \mathbf{S}^H \rangle + \langle \mathbf{S}^P \rangle + \langle \mathbf{S}^B \rangle \}, \quad (18)$$

where $\langle \mathbf{S}^H \rangle$ is the ensemble average of stress transmitted by the fluid due to shear flow. Since the particles are in dilute suspension, the shear force on them is negligible and taken as zero.

$\langle \mathbf{S}^P \rangle = -\langle \mathbf{xF}^P \rangle$ and $\langle \mathbf{S}^B \rangle = \langle \mathbf{S}^P \rangle$ = ensemble average of stress due to Brownian motion which is zero for this problem.

Hence, the bulk stress is given by Brady and Bossis²⁵ as

$$\Sigma^P = \frac{-N}{V} \langle \mathbf{xF}^P \rangle - \frac{\text{Re}}{V} \sum_i \int \frac{1}{2} (\mathbf{ax} + \mathbf{xa}) dV_i - \frac{\text{Re}}{V} \int \mathbf{u}' \mathbf{u}' dV. \quad (19)$$

We calculated the bulk stress numerically using the following matrix equation:

$$\Sigma^P = -\varphi \text{Re} \begin{bmatrix} \overline{Y_{px} U_{px}} & \overline{Y_{px} U_{py}} & \overline{Y_{px} U_{pz}} \\ \overline{Y_{py} U_{px}} & \overline{Y_{py} U_{py}} & \overline{Y_{py} U_{pz}} \\ \overline{Y_{pz} U_{px}} & \overline{Y_{pz} U_{py}} & \overline{Y_{pz} U_{pz}} \end{bmatrix} \\ - \varphi \text{Re} \begin{bmatrix} \sum \frac{dU_{px}}{dt} Y_{px} & \frac{1}{2} \left(\sum \frac{dU_{px}}{dt} Y_{py} + \sum \frac{dU_{py}}{dt} Y_{px} \right) & \frac{1}{2} \left(\sum \frac{dU_{px}}{dt} Y_{pz} + \sum \frac{dU_{pz}}{dt} Y_{px} \right) \\ \frac{1}{2} \left(\sum \frac{dU_{px}}{dt} Y_{py} + \sum \frac{dU_{py}}{dt} Y_{px} \right) & \sum \frac{dU_{py}}{dt} Y_{py} & \frac{1}{2} \left(\sum \frac{dU_{py}}{dt} Y_{pz} + \sum \frac{dU_{pz}}{dt} Y_{py} \right) \\ \frac{1}{2} \left(\sum \frac{dU_{px}}{dt} Y_{pz} + \sum \frac{dU_{pz}}{dt} Y_{px} \right) & \frac{1}{2} \left(\sum \frac{dU_{py}}{dt} Y_{pz} + \sum \frac{dU_{pz}}{dt} Y_{py} \right) & \sum \frac{dU_{pz}}{dt} Y_{pz} \end{bmatrix} \\ - \varphi \text{Re} \begin{bmatrix} \sum (U_{px} - \overline{U_{px}})^2 & \sum (U_{px} - \overline{U_{px}})(U_{py} - \overline{U_{py}}) & \sum (U_{px} - \overline{U_{px}})(U_{pz} - \overline{U_{pz}}) \\ \sum (U_{px} - \overline{U_{px}})(U_{py} - \overline{U_{py}}) & \sum (U_{py} - \overline{U_{py}})^2 & \sum (U_{py} - \overline{U_{py}})(U_{pz} - \overline{U_{pz}}) \\ \sum (U_{px} - \overline{U_{px}})(U_{pz} - \overline{U_{pz}}) & \sum (U_{py} - \overline{U_{py}})(U_{pz} - \overline{U_{pz}}) & \sum (U_{pz} - \overline{U_{pz}})^2 \end{bmatrix}. \quad (20)$$

K. Madhukar *et al.*

From the above expression (9), we get the numerical values for bulk stress as

$$\boldsymbol{\Sigma}_p = \begin{pmatrix} \Sigma_{xx}^p & \Sigma_{yx}^p & \Sigma_{zx}^p \\ \Sigma_{xy}^p & \Sigma_{yy}^p & \Sigma_{zy}^p \\ \Sigma_{xz}^p & \Sigma_{yz}^p & \Sigma_{zz}^p \end{pmatrix}. \quad (21)$$

Following Kulkarni and Morris's equations,²⁶ the following rheological parameters are computed:

$$\text{First normal stress difference} = \Sigma_{xx}^p - \Sigma_{yy}^p, \quad (22)$$

$$\text{Second normal stress difference} = \Sigma_{yy}^p - \Sigma_{zz}^p, \quad (23)$$

$$\text{Intrinsic pressure} = \frac{-1}{3} (\Sigma_{xx}^p + \Sigma_{yy}^p + \Sigma_{zz}^p), \quad (24)$$

$$\text{Relative viscosity} = 1 + \frac{\Sigma_{xy}^p}{\mu \dot{\gamma}}, \quad (25)$$

where $\dot{\gamma}$ is the frequency rate assumed to be 0.001.

3. Methodology and Validation of the Codes

To calculate the velocities and displacements, the Runge–Kutta method was used and the rheological parameters were calculated with the known values of Reynolds numbers and periodic force amplitudes. All the codes were written in Octave and validated by reproducing the works of Ramamohan *et al.*,²² Lovalenti and Brady²³ and Krishnamurthy *et al.*¹⁷ The time series at zero velocity at infinity and with finite

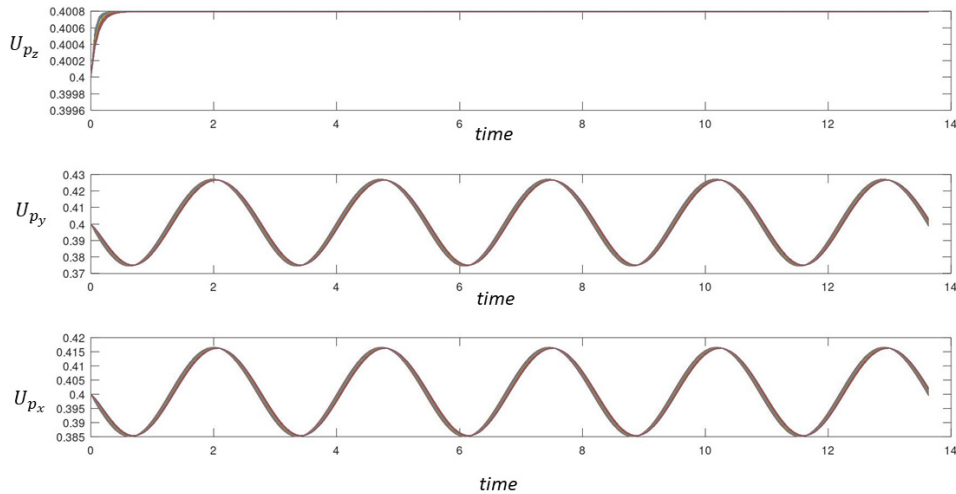


Fig. 1. (Color online) Time series plots for each coordinate showing (a) with zero amplitude of the periodic force and high velocity at infinity, (b) with low amplitude along x and (c) with low amplitude along y -axis keeping the velocity at infinity the same.

Behavior of suspended natural rubber balls

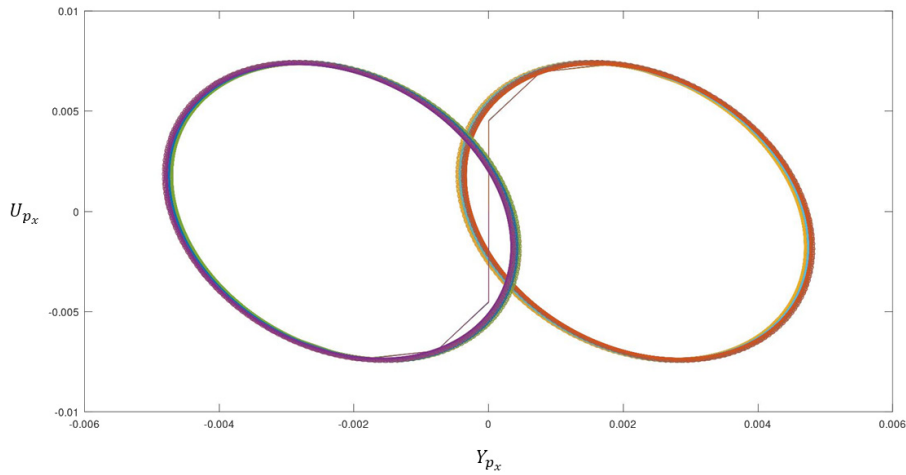


Fig. 2. (Color online) Reproducing the reflection property of one-dimensional flow.

velocity at infinity were reproduced. The finite velocity at infinity gave a time series at a finite amplitude of the periodic force. Whereas, at zero velocity, Fig. 4 of Lovalenti and Brady²³ was obtained. Similarly, when periodic force was applied, Krishnamurthy *et al.*¹⁷ and Ramamohan *et al.*²² Figures 1 and 2 were obtained, respectively. These figures are shown in Fig. 1. Figure 2 shows the reflection property of the phase plots. Here, the plot is obtained for both the positive and negative amplitudes. This phase plot represents the positive amplitude phase plot moving in the clockwise direction and the negative amplitude phase plot in the anticlockwise direction, forming or tending to form a circle. Figure 3 again is a phase plot

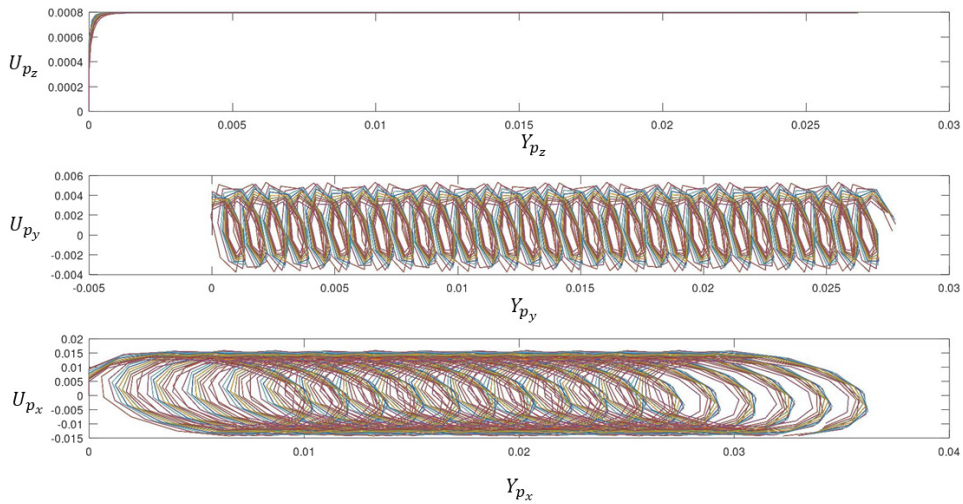


Fig. 3. (Color online) Phase space plots (a) with zero amplitude, (b) with low amplitude (c) with high amplitude, all at zero velocity at infinity.

K. Madhukar *et al.*

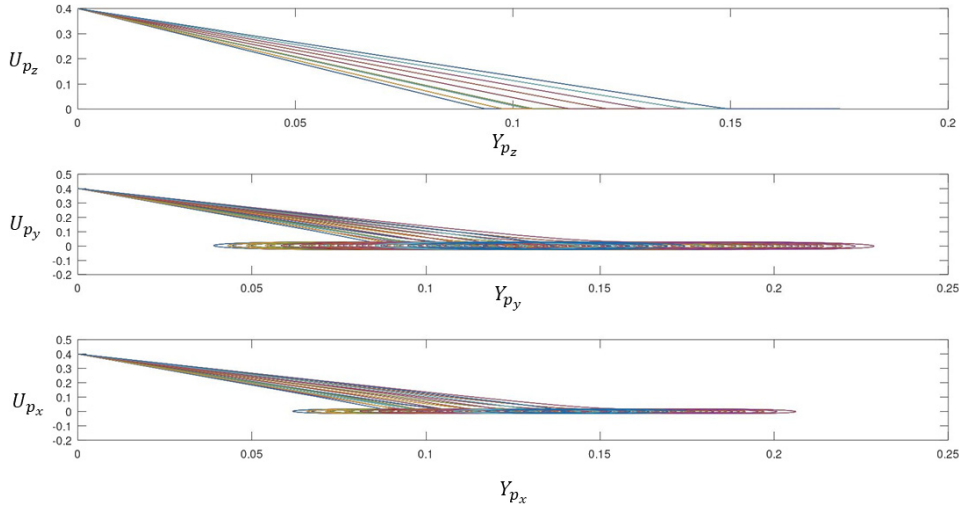


Fig. 4. (Color online) Phase space plots with 0.4 velocity at infinity (a) with zero amplitude of periodic force, (b) and (c) with moderate periodic force applied on the sphere.

reproducing the results of Lovalenti and Brady²³ (Fig. 4) with Krishnamurthy *et al.*¹⁷. Hence, the codes are robust and correct at best possibility.

4. Results and Discussions

4.1. The dynamics

The system considered here is experimentally verifiable as it does not exhibit chaos or absurdity. This phenomenon is observed in Fig. 4. It shows that even at moderate to high velocity at infinity, the phase plots come to the position where it starts oscillating. This explains the phenomena of a cricketer who takes a run and throws the rubber ball whose density is equal to the density of air and the bounce of the ball is in the phase path shown in Fig. 3, but in Fig. 4, the phase path is of a throw of the ball, and it settles at that position owing to no force beyond that point (Fig. 4(a)). Figure 4(b) shows a ripple where a rubber ball is thrown into the water. However, there is no reflection property being satisfied by these phase paths as here it's only ripple formation and the motion of the water is from the center position where the ball is pitched. Figures 4(a)–4(c) represent phase space plots with 0.4 velocities at infinity, zero amplitude of periodic force, and moderate periodic force applied on the sphere.

Figure 5 shows the linear distribution of the mean of the particle velocity with respect to the amplitude of the periodic force and the Reynolds numbers. This is an obvious result as the greater the amplitude of the throw of the ball greater the velocity and due to inertia, which is very less in this system, there will be damping on the motion of the rubber ball and hence will exhibit resistance to change in motion, hence not much effect of Reynolds numbers can be observed in Fig. 5.

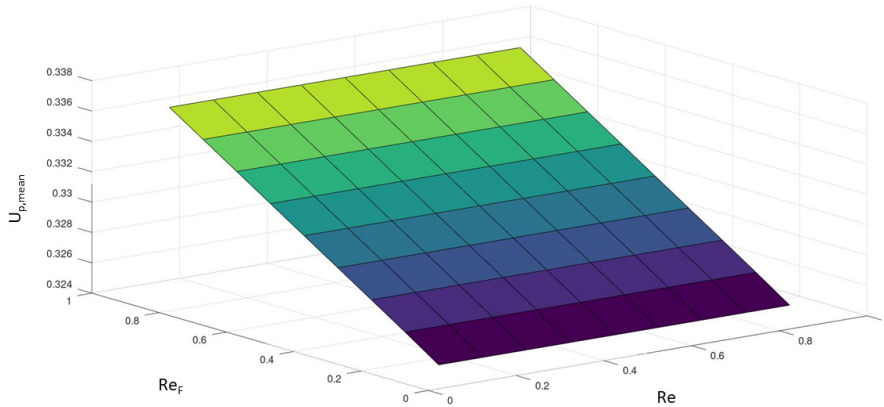
Behavior of suspended natural rubber balls

Fig. 5. (Color online) The mean of particle velocity with the Reynolds numbers and amplitude of the periodic force.

Figure 6 similarly shows the nonlinear relation between the particle displacement with the amplitude of the ball's throw and the Reynolds number. The relation is exactly similar to Fig. 5, but the displacement tends to settle down at higher amplitude, which is the effect of inertia. The Reynolds number gives a resistance to change in the motion; hence, the ball's amplitude, when pitched on the water or floor, bounces again and gives multiple pitches with reduced oscillation to settle down finally at rest. These explanations must be taken as an analogy of the phenomena occurring between a ball and a fluid with the same density as that of the ball.

4.2. The Rheology results

All the rheological parameters, first normal difference, second normal difference, intrinsic pressure and relative viscosity are calculated for various volume fractions,

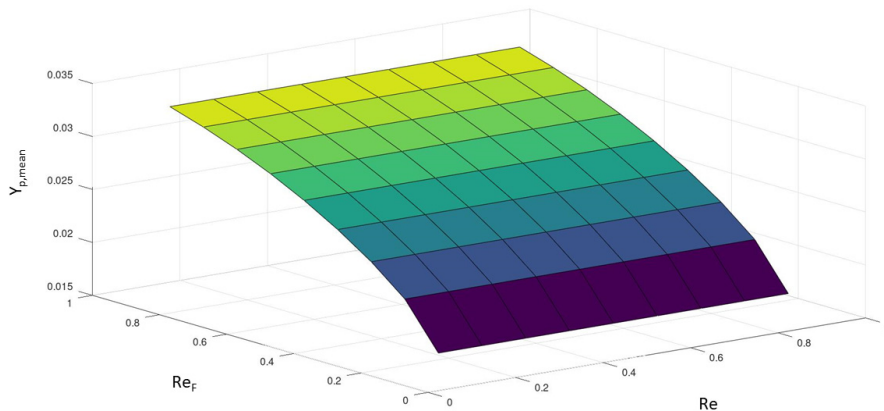


Fig. 6. (Color online) The mean of the displacement with respect to the Reynolds numbers and the amplitude of the periodic force.

K. Madhukar et al.

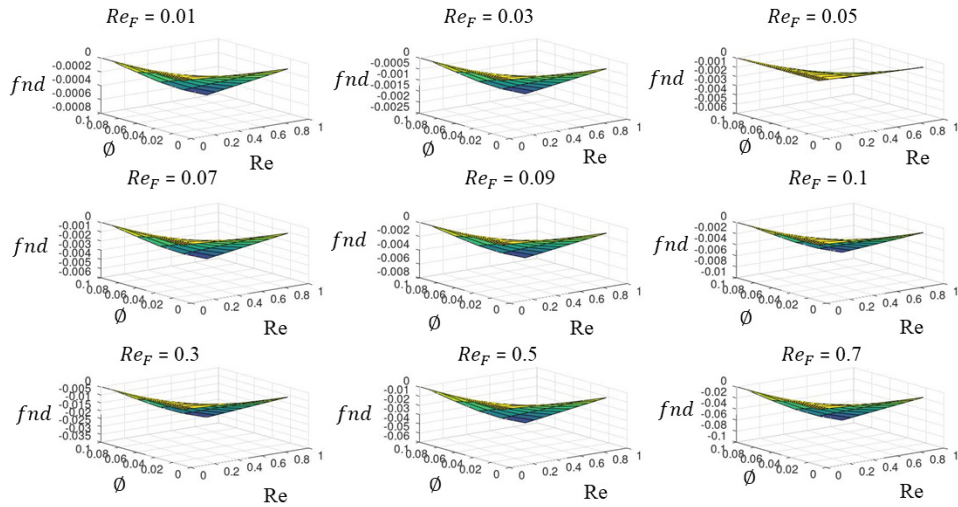


Fig. 7. (Color online) The first normal difference with respect to particle Reynolds numbers and volume fraction.

Reynolds numbers and amplitude of the periodic force. This shows that the system exhibits non-Newtonian behavior for the Newtonian fluid. Here only one of such results is presented. In Fig. 7, an observation can be made that the first normal stress difference is directly proportional to the Reynolds number and volume fraction. In Fig. 8, the second normal stress difference has a nonlinear dependence with the Reynolds number and volume fraction at lower volume fraction values. It is high and dips at high values of the Reynolds number. Figures 9 and 10 show the relation

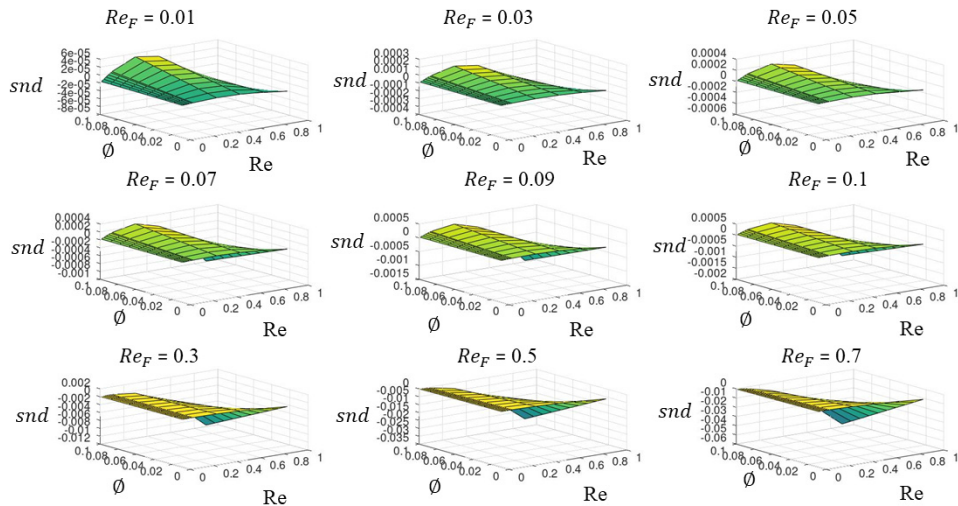


Fig. 8. (Color online) The second normal difference with respect to particle Reynolds numbers and volume fraction.

Behavior of suspended natural rubber balls

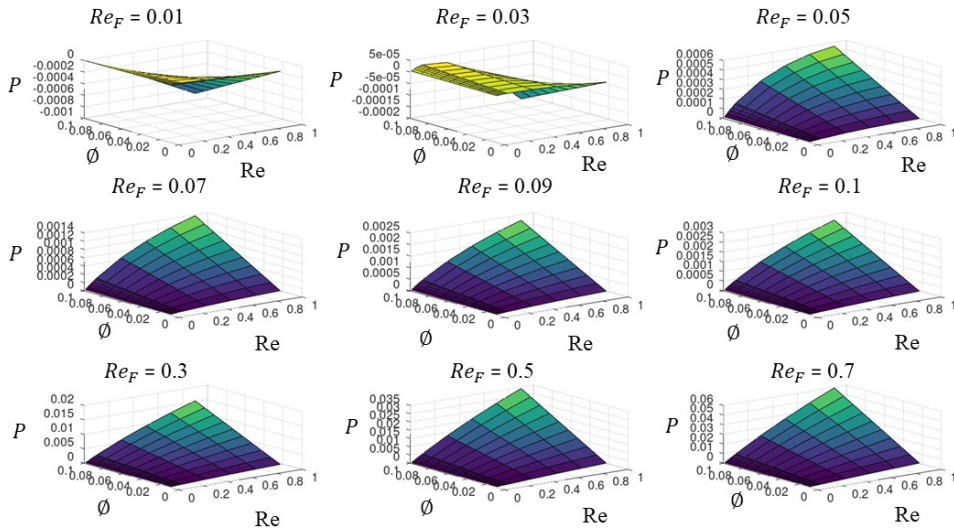


Fig. 9. (Color online) The intrinsic pressure variation with respect to Reynolds numbers and volume fraction.

between the intrinsic pressure and relative viscosity with the volume fraction and Reynolds numbers, respectively. They depict a nonlinear relation with the Reynolds number and are proportional to volume fraction.

Table 1 shows the values of the first normal difference with respect to the amplitude of the periodic force $Re_F = 0.9$ and various values of Reynolds numbers

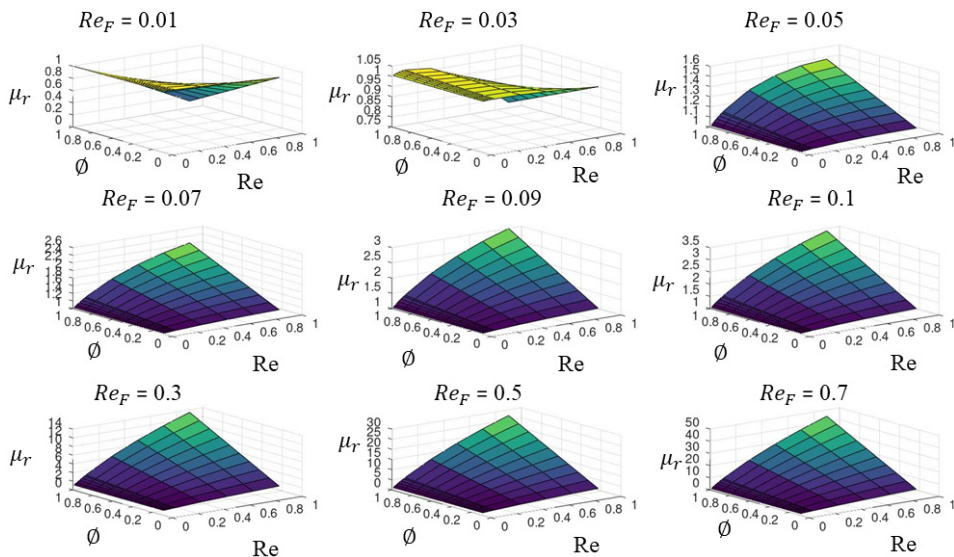


Fig. 10. (Color online) The relative viscosity variation with respect to Reynolds numbers and volume fraction.

K. Madhukar et al.

Table 1. The first normal difference for typical values of Re and volume fraction at $Re_F = 0.9$.

Vol. fraction	0.01	0.02	0.03	0.04	0.05	0.06	0.07	0.08	0.09	0.1
Re	-4.80E-05	-0.00033	-0.00062	-0.00093	-0.00126	-0.00143	-0.005	-0.00835	-0.01109	-0.01318
$Re_F = 0.9$	-9.60E-05	-0.00065	-0.00123	-0.00186	-0.00253	-0.00287	-0.01001	-0.01669	-0.02218	-0.02636
	-0.00014	-0.00098	-0.00185	-0.0028	-0.00379	-0.0043	-0.01501	-0.02504	-0.03327	-0.03954
	-0.00019	-0.00131	-0.00247	-0.00373	-0.00506	-0.00573	-0.02001	-0.03339	-0.04437	-0.05271
	-0.00024	-0.00163	-0.00308	-0.00466	-0.00632	-0.00717	-0.02501	-0.04173	-0.05546	-0.06589
	-0.00029	-0.00196	-0.0037	-0.00559	-0.00758	-0.0086	-0.03002	-0.05008	-0.06655	-0.07907
	-0.00034	-0.00229	-0.00432	-0.00653	-0.00885	-0.01004	-0.03502	-0.05842	-0.07764	-0.09225
	-0.00038	-0.00261	-0.00493	-0.00746	-0.01011	-0.01147	-0.04002	-0.06677	-0.08873	-0.10543
	-0.00043	-0.00294	-0.00555	-0.00839	-0.01137	-0.0129	-0.04503	-0.07512	-0.09982	-0.11861
	-0.00048	-0.00327	-0.00617	-0.00932	-0.01264	-0.01434	-0.05003	-0.08346	-0.11092	-0.13179

Behavior of suspended natural rubber balls

Table 2. The second normal difference for typical values of Re and volume fraction at $Re_F = 0.9$.

Re	Vol. fraction	0.01	0.02	0.03	0.04	0.05	0.06	0.07	0.08	0.09	0.1
$Re_F = 0.9$	0.01	-0.00013	-0.00015	-0.00021	-0.00027	-0.00034	-0.00038	-0.00151	-0.00343	-0.00608	-0.00928
	0.03	-0.00026	-0.0003	-0.00042	-0.00055	-0.00069	-0.00076	-0.00301	-0.00686	-0.01216	-0.01856
	0.05	-0.0004	-0.00045	-0.00063	-0.00082	-0.00103	-0.00114	-0.00452	-0.01029	-0.01824	-0.02784
	0.07	-0.00053	-0.0006	-0.00084	-0.0011	-0.00137	-0.00152	-0.00603	-0.01372	-0.02432	-0.03712
	0.09	-0.00066	-0.00075	-0.00105	-0.00137	-0.00172	-0.0019	-0.00753	-0.01715	-0.0304	-0.0464
	0.1	-0.00079	-0.0009	-0.00126	-0.00165	-0.00206	-0.00228	-0.00904	-0.02058	-0.03648	-0.05568
	0.3	-0.00092	-0.00105	-0.00147	-0.00192	-0.0024	-0.00266	-0.01055	-0.02401	-0.04255	-0.06496
	0.5	-0.00106	-0.0012	-0.00168	-0.0022	-0.00275	-0.00304	-0.01205	-0.02744	-0.04863	-0.07424
	0.7	-0.00119	-0.00135	-0.00189	-0.00247	-0.00309	-0.00342	-0.01356	-0.03088	-0.05471	-0.08352
0.9	-0.00132	-0.0015	-0.00211	-0.00275	-0.00344	-0.0038	-0.01507	-0.03431	-0.06079	-0.0928	

K. Madhukar et al.

Table 3. The intrinsic pressure for typical values of Re and volume fraction at $Re_F = 0.9$.

Re	Vol. fraction	0.01	0.02	0.03	0.04	0.05	0.06	0.07	0.08	0.09	0.1
$Re_F = 0.9$	0.01	5.91E-06	0.000286	0.000536	0.000778	0.001015	0.001132	0.003356	0.005405	0.007311	0.00907
	0.03	1.18E-05	0.000573	0.001071	0.001555	0.00203	0.002265	0.006711	0.010811	0.014622	0.018141
	0.05	1.77E-05	0.000859	0.001607	0.002333	0.003045	0.003397	0.010067	0.016216	0.021932	0.027211
	0.07	2.37E-05	0.001146	0.002143	0.003111	0.00406	0.00453	0.013422	0.021622	0.029243	0.036282
	0.09	2.96E-05	0.001432	0.002678	0.003888	0.005075	0.005662	0.016778	0.027027	0.036554	0.045352
	0.1	3.55E-05	0.001718	0.003214	0.004666	0.00609	0.006795	0.020133	0.032433	0.043865	0.054423
	0.3	4.14E-05	0.002005	0.00375	0.005444	0.007105	0.007927	0.023489	0.037838	0.051176	0.063493
	0.5	4.73E-05	0.002291	0.004285	0.006221	0.00812	0.009059	0.026844	0.043243	0.058487	0.072564
	0.7	5.32E-05	0.002578	0.004821	0.006999	0.009136	0.010192	0.0302	0.048649	0.065797	0.081634
0.9	5.91E-05	0.002864	0.005357	0.007777	0.010151	0.011324	0.033556	0.054054	0.073108	0.090705	

Behavior of suspended natural rubber balls

Table 4. The relative viscosity for typical values of Re and volume fraction at $Re_F = 0.9$.

Re	Vol. fraction	0.01	0.02	0.03	0.04	0.05	0.06	0.07	0.08	0.09	0.1
$Re_F = 0.9$	0.01	0.982001	1.244311	1.463898	1.671227	1.870504	1.967736	3.683957	5.117088	6.377914	7.503018
	0.03	0.964002	1.488622	1.927796	2.342455	2.741008	2.935473	6.367914	9.234175	11.75583	14.00604
	0.05	0.946002	1.732933	2.391695	3.013682	3.611512	3.903209	9.051871	13.35126	17.13374	20.50905
	0.07	0.928003	1.977244	2.855593	3.68491	4.482017	4.870946	11.73583	17.46835	22.51166	27.01207
	0.09	0.910004	2.221556	3.319491	4.356137	5.352521	5.838682	14.41979	21.58544	27.88957	33.51509
	0.1	0.892005	2.465867	3.783389	5.027365	6.223025	6.806418	17.10374	25.70253	33.26749	40.01811
	0.3	0.874006	2.710178	4.247288	5.698592	7.093529	7.774155	19.7877	29.81961	38.6454	46.52113
	0.5	0.856007	2.954489	4.711186	6.36982	7.964033	8.741891	22.47166	33.9367	44.02331	53.02414
	0.7	0.838007	3.1988	5.175084	7.041047	8.834537	9.709628	25.15561	38.05379	49.40123	59.52716
0.9	0.820008	3.443111	5.638982	7.712274	9.705041	10.67736	27.83957	42.17088	54.77914	66.03018	

K. Madhukar et al.


and the volume fractions. It can be observed that the first normal difference increases with the increase in volume fraction and decreases with the decrease in Reynolds numbers. This is true even with the second normal stress difference, as seen in Table 2. Figures 7 and 8 show a similar pattern. This suggests that the normal stress components are more or less equal to each other and the principle diagonal elements are constant. They increase with volume fraction and decrease with the increase in Reynolds numbers and the amplitudes of the periodic force, as seen in Table 3 and Fig. 9. The shear stress component is slightly greater than the normal stress component and they increase with the amplitude of the periodic force and decrease with the Reynolds numbers. As mentioned, the Reynolds number specifies the unsteady inertia, which is the resistance to change in motion. This is visible in the rheological parameters and the dynamics of the periodically forced natural rubber balls at low Reynolds numbers. The relative viscosity for typical values of Re and volume fraction at $Re_F = 0.9$ is depicted in Table 4.


5. Conclusion


The experimentally verifiable rheological parameters of dilute suspensions of periodically forced rubber spheres in water at low Reynolds numbers are calculated in this study. The rheological parameters which can be experimentally verifiable have been theoretically derived in this paper. The non-Newtonian behavior of these balls in the Newtonian frame of reference is an intriguing and unique trait. An integro-differential equation model was created and solved using the fourth-order Runge–Kutta technique. The work closes a gap in the literature by studying rubber rheology at low Reynolds numbers. Here, the particle is a rubber ball, a non-interacting ensemble of rubber balls in water. When these balls are forced periodically, they exhibit this non-Newtonian behavior. However, these are nonchaotic and not absurd. The relation between the intrinsic pressure and relative viscosity depicts a nonlinear relation with Reynolds number and proportional to volume fraction. Here, there is no reflection property being satisfied by the mentioned phase paths as here it's only ripple formation and the motion of the water is from the center position where the ball is pitched.


In the future, we can analyze the system's nonlinear dynamics at various forcing frequencies and amplitudes. Examine bifurcation situations to learn more about the system's behavior outside of linear approximations, such as intermittency, chaos, and period doubling. Create control mechanisms to alter the spheres' motion. This may include optimization approaches or feedback control systems to accomplish desired trajectories or behaviors. Examine the effects that confinements or boundaries have on the system's dynamics. Insights into particle aggregation, self-assembly, or rheological characteristics may result from interactions with walls, other spheres, or intricate geometries.

ORCID

K. Madhukar  <https://orcid.org/0000-0002-7837-864X>


M. C. Jayaprakash  <https://orcid.org/0000-0002-0674-7952>

M. Santoshi Kumari  <https://orcid.org/0000-0002-0391-1171>

H. Y. Shrivalli  <https://orcid.org/0000-0002-0282-5474>

K. V. Nagaraja  <https://orcid.org/0000-0002-2190-5015>

Raman Kumar  <https://orcid.org/0000-0002-5040-7920>

R. Naveen Kumar  <https://orcid.org/0000-0002-0056-1452>

References

1. A. A. Zaidi, *Phys. Fluids* **32**(9) (2020) 093310, doi:10.1063/5.0011538.
2. E. A. Haffner and P. Mirbod, *Phys. Fluids* **32**(8) (2020) 083608, doi:10.1063/5.0015207.
3. A. A. Kuznetsov, E. V. Novak, E. S. Pyanzina and S. S. Kantorovich, *J. Mol. Liq.* **359** (2022) 119373, doi:10.1016/j.molliq.2022.119373.
4. A. Girodroux-Lavigne, *SIAM J. Math. Anal.* (2023) 6305, doi:10.1137/22M148776X.
5. P. T. Corona, K. Dai, M. E. Helgeson and L. G. Leal, *J. Non-Newtonian Fluid Mech.* **315** (2023) 105014, doi:10.1016/j.jnnfm.2023.105014.
6. S. B. Prakash, K. Chandan, K. Karthik, S. Devanathan, R. S. V. Kumar, K. V. Nagaraja and B. C. Prasannakumara, *Phys. Scr.* **99**(1) (2023) 015225, doi:10.1088/1402-4896/ad131f.
7. U. Khan, R. N. Kumar, A. Zaib, B. C. Prasannakumara, A. Ishak, A. M. Galal and R. J. P. Gowda, *Therm. Sci. Eng. Prog.* **36** (2022) 101521, doi:10.1016/j.tsep.2022.101521.
8. S. D. Gkormpatsis, E. A. Gryparis, K. D. Housiadas and A. N. Beris, *J. Non-Newtonian Fluid Mech.* **275** (2020) 104217, doi:10.1016/j.jnnfm.2019.104217.
9. K. S. Albalawi *et al.*, *Appl. Therm. Eng.* **244** (2024) 122757, doi:10.1016/j.applthermaleng.2024.122757.
10. T. Morimoto, B. Zhao, D. M. G. Taborda and C. O'Sullivan, *Comput. Geotech.* **150** (2022) 104900, doi:10.1016/j.compgeo.2022.104900.
11. Y. Peng, M. Zarringhalam, A. A. Barzinjy, D. Toghraie and M. Afrand, *J. Mol. Liq.* **297** (2020) 111650, doi:10.1016/j.molliq.2019.111650.
12. A. A. Arosemena, H. I. Andersson and J. Solsvik, *J. Fluid Mech.* **908** (2021) A43, doi:10.1017/jfm.2020.903.
13. J. Madhu, K. Karthik, R. S. V. Kumar, R. J. P. Gowda, R. N. Kumar and B. C. Prasannakumara, *Numer. Heat Transf. Part Appl.* (2024) 1, doi:10.1080/10407782.2024.2319349.
14. E. Milana, R. Zhang, M. R. Vetrano, S. Peerlinck, M. D. Volder, P. R. Onck, D. Reynaerts and B. Gorissen, *Sci. Adv.* **6**(49) (2020) eabd2508, doi:10.1126/sciadv.abd2508.
15. Y. Ran, W.-L. Chen, Y. Cao, H. Li and D. Gao, *Ocean Eng.* **285** (2023) 115240, doi:10.1016/j.oceaneng.2023.115240.
16. A. Zargartalebi, M. Zargartalebi and A. M. Benneker, *AIP Adv.* **11**(8) (2021) 085213, doi:10.1063/5.0059041.
17. M. Krishnamurthy, R. G. Reddy, M. D. Alsulami and B. C. Prasannakumara, *Int. Commun. Heat Mass Transfer* **135** (2022) 106157, doi:10.1016/j.icheatmasstransfer.2022.106157.

K. Madhukar et al.

18. M. D. Alsulami, R. N. Kumar, R. J. P. Gowda and B. C. Prasannakumara, *ZAMM — J. Appl. Math. Mech. Z. Für Angew. Math. Mech.* **103**(5) (2023) e202100360, doi:10.1002/zamm.202100360.
19. S. Raut, K. K. Mondal, P. Chatterjee and A. Roy, *Pramana–J. Phys.* **95**(2) (2021) 73, doi:10.1007/s12043-021-02104-1.
20. V. Novičenko, G. Žlabys and E. Anisimovas, *Phys. Rev. A* **105**(1) (2022) 012203, doi:10.1103/PhysRevA.105.012203.
21. P. Srilatha, R. S. V. Kumar, R. N. Kumar, R. J. P. Gowda, A. Abdulrahman and B. C. Prasannakumara, *Heliyon* **9**(11) (2023) e21189, doi:10.1016/j.heliyon.2023.e21189.
22. T. R. Ramamohan, I. S. Shivakumara and K. Madhukar, *Fluid Dyn. Res.* **43**(4) (2011) 045502.
23. P. M. Lovalenti and J. F. Brady, *J. Fluid Mech.* **256** (1993) 561.
24. G. K. Batchelor, *J. Fluid Mech.* **41**(3) (1970) 545.
25. J. F. Brady and G. Bossis, *Annu. Rev. Fluid Mech.* **20**(1) (1988) 111, doi:10.1146/annurev.fl.20.010188.000551.
26. P. M. Kulkarni and J. F. Morris, *Phys. Fluids* **20**(4) (2008) 040602.



Energizing Inventory Management to Optimize Energy Consumption of Handling Shortages by Neutrosophic Fuzzy Trapezoidal Number

N. Sindhuja¹, M. Santoshi Kumari², K. Kalaiarasi^{3a*,b}, Manjula G. J.⁴, Shrivalli H. Y.⁵

¹Ph.D Research Scholar, PG and Research Department of Mathematics, Cauvery College for Women (Autonomous), Affiliated to Bharathidasan University, Tiruchirappalli-620018, Tamil Nadu, India.

²Department of Mathematics, Chaitanya Bharathi Institute of Technology, Gandipet, Hyderabad – 500075, India.

^{3a*}PG and Research Department of Mathematics, Cauvery College for Women (Autonomous), Affiliated to Bharathidasan University, Tiruchirappalli-620018, Tamil Nadu, India.

^{3b}D. Sc (Mathematics) Researcher Fellow, Srinivas University, Surathkal, Mangaluru, Karnataka-574146, India.

⁴Department of Mathematics, Siddaganga Institute of Technology, Tumakuru – 572103, Karnataka, India.

⁵Department of Mathematics, BMS College of Engineering, Bengaluru – 560019, Karnataka, India.

Emails: sindhujanagaraj13@gmail.com; santoshinagaram@gmail.com; kalaishruthi120@gmail.com; gjm@sit.ac.in; hys.maths@bmsce.ac.in

Abstract

Embarking on the exploration of integrating environmental sustainability principles and neutrosophic fuzzy theory in inventory management, this study aims to effectively tackle shortages. It underscores the vital balance between economic efficiency and ecological responsibility in contemporary inventory management practices. Neutrosophic fuzzy theory emerges as a robust tool for navigating the inherent uncertainties in inventory optimization, offering a versatile framework for modelling intricate problems. Strategies for optimizing resource consumption and minimizing waste generation within inventory management are scrutinized, emphasizing the imperative of harmonizing economic objectives with environmental concerns. Introducing a novel framework that melds neutrosophic fuzzy with environmental metrics, the research aims to optimize inventory management processes while mitigating environmental impacts. Furthermore, it delves into the challenges of managing energy consumption, advocating for innovative approaches to address fluctuating energy prices, data limitations, and evolving regulatory requirements. Neutrosophic sets are introduced for energy consumption analysis and cost evaluation, showcasing their efficacy in managing uncertainty and variability in real-world scenarios. The study concludes with a Python-based analysis of neutrosophic mean in energy consumption, offering insights into central tendencies and uncertainties associated with energy-related costs. Utilizing visualization techniques to enhance comprehension and decision-making in energy management, this research contributes to advancing inventory management practices by integrating environmental sustainability principles and sophisticated mathematical techniques, thereby fostering more resilient and sustainable supply chain operations.

Keywords: Environmental sustainability; Neutrosophic fuzzy theory; Shortage management; Energy consumption; Visualization techniques.

1. Introduction

In today's interconnected global economy, managing inventory isn't just about operational efficiency—it's about shaping the environmental impact of businesses. Environmental sustainability within inventory management goes beyond day-to-day operations; it encompasses the entire lifecycle of products, from production to disposal or reuse.

Brown, A. B., & Smith, C. D [1] At its core, environmental sustainability means finding a balance between economic success and ecological responsibility. It acknowledges that the resources used in producing, storing, and distributing goods are finite and intimately tied to the health of our planet. Therefore, striving for sustainability in inventory management involves optimizing processes not only to boost economic efficiency but also to minimize harmful environmental effects. Chen, L., & Wang, Y [2] One of the main goals of environmental sustainability in inventory management is to optimize resource usage. This involves using techniques like demand forecasting, lean manufacturing principles, and just-in-time inventory practices to ensure resources are used efficiently and waste is minimized. Garcia, E. M., & Rodriguez, J. M [3] By aligning inventory levels with actual demand and production capacity, businesses can cut down on excess inventory, conserving raw materials, energy, and water resources. Johnson, P. R., & Anderson, K. L [4] Another key aspect is reducing waste generation. Having surplus inventory not only strains finances but also leads to the production of surplus or obsolete products and packaging materials, contributing to environmental pollution. Kim, S., & Lee, J [5] By implementing strategies such as product standardization, inventory optimization algorithms, and waste reduction initiatives, businesses can minimize waste throughout the supply chain, thereby lessening environmental harm and preserving resources.

Central to environmental sustainability in inventory management is the need to balance economic efficiency with environmental responsibility. Li, H., & Zhang, G [6] While businesses aim to optimize inventory levels to maximize profits and meet customer demands, they must also recognize their duty to minimize environmental harm and protect natural resources for future generations. Liu, Q., & Wang, H [7] These calls for a shift towards sustainable business practices that prioritize long-term viability over short-term gains. Ultimately, environmental sustainability in inventory management represents a proactive approach toward aligning economic prosperity with ecological integrity. By optimizing inventory processes to reduce resource consumption, waste generation, and environmental pollution, businesses can contribute to building a more sustainable and resilient economy where prosperity doesn't come at the expense of the planet. Martinez, R. S., & Perez, L. M [8] In the realm of inventory management, where decisions are often made amidst fluctuating demand, evolving market conditions, and incomplete information, traditional optimization models may not be sufficient. This is where neutrosophic fuzzy theory comes into play as a powerful tool to address uncertainties and vagueness inherent in inventory management systems. Nguyen, T. H., & Tran, T. M [9] Neutrosophic fuzzy theory goes beyond classical fuzzy set theory by introducing the concept of neutrosophic sets, which include a third parameter—indeterminacy—to capture ambiguity and uncertainty in real-world situations. By accommodating incomplete, indeterminate, and inconsistent information, neutrosophic fuzzy logic provides decision-makers with a flexible framework to model and analyze complex inventory management problems. Park, J. H., & Kim, Y. S [10] This ability to handle uncertain data makes neutrosophic fuzzy logic particularly suitable for addressing challenges in inventory optimization, where precise information may be lacking, and demand patterns are unpredictable.

By incorporating neutrosophic fuzzy logic into inventory optimization models, decision-makers can make more informed decisions in the face of uncertainty. This enables the development of adaptive inventory management strategies that can respond dynamically to market changes and disruptions. Rodriguez, M. A., & Garcia, N. P [11] Leveraging neutrosophic fuzzy logic empowers businesses to effectively manage imprecise data, uncertain demand patterns, and fluctuating market conditions, leading to more resilient and sustainable inventory management practices. This integration of advanced mathematical techniques with practical inventory management applications holds promise for enhancing operational efficiency, minimizing costs, and promoting environmental sustainability in supply chain management. Smith, J. D., & Brown, K. R [12] Shortages in inventory management present a critical challenge with wide-ranging implications, both economically and environmentally. Economically, these shortages can lead to lost sales, decreased customer satisfaction, and increased production costs due to expedited shipping or emergency ordering. Addressing shortages is vital not only to prevent economic losses but also to minimize environmental impacts. Tran, V. L., & Le, A. Q [13] Rush orders and expedited shipping methods used to address shortages can intensify carbon emissions and fuel consumption, further exacerbating environmental harm. Wang, L., & Zhang, Y [14] Additionally, the pressure on suppliers to meet sudden demand spikes may lead to unsustainable extraction practices and environmental degradation. Effectively managing shortages is thus essential for optimizing resource utilization, minimizing waste, and reducing environmental impacts associated with inventory management. Zhang, X., & Li, Y [15] By implementing strategies to mitigate shortages, businesses can move towards a more sustainable future where economic prosperity aligns with environmental responsibility. Broumi [16, 17] explained the importance of the neutrosophic number in the decision-making problem at the complexity.

The main process of this research involves examining the integration of environmental sustainability principles within inventory management, particularly focusing on addressing shortages through the application of neutrosophic fuzzy

theory. Initially, the research delves into the concept of environmental sustainability in inventory management, emphasizing its significance in balancing economic efficiency with ecological responsibility. It then explores the application of neutrosophic fuzzy theory as a robust tool to handle uncertainties and complexities inherent in inventory optimization. The study proceeds by investigating strategies to optimize resource consumption and minimize waste generation within inventory management, highlighting the importance of balancing economic objectives with environmental considerations. Subsequently, the research evaluates the effectiveness of integrating neutrosophic fuzzy theory with environmental sustainability objectives in addressing shortages, both from economic and environmental perspectives. This involves developing and implementing a novel framework that combines neutrosophic fuzzy logic with environmental metrics to optimize inventory management processes while mitigating environmental impacts. Finally, the research assesses the outcomes of the proposed framework through case studies or simulations, aiming to demonstrate its potential in promoting economic resilience and environmental sustainability within supply chain management.

1.1 Objective of the research:

- Enhancement of inventory management processes, especially in shortage scenarios, by addressing uncertainties effectively.
- Evaluation of environmental impacts of inventory-related activities and promotion of sustainable practices.
- Development of mathematical models incorporating neutrosophic fuzzy and environmental sustainability metrics.
- Optimization of inventory management strategies to minimize economic losses and environmental impacts while balancing economic objectives with sustainability goals.

2. Neutrosophic fuzzy theory and environmental sustainability in inventory optimization with shortages:

This integrated framework combines neutrosophic fuzzy set theory with environmental sustainability metrics to enhance inventory management processes, particularly in scenarios involving shortages. The neutrosophic fuzzy set theory introduces the concept of neutrosophic sets, which effectively handle incomplete, indeterminate, and inconsistent information. By employing neutrosophic fuzzy logic in inventory optimization models, decision-makers can better navigate uncertainties related to factors like demand fluctuations and supplier reliability, leading to more informed decisions regarding inventory levels and replenishment strategies. This approach enhances the adaptability and efficiency of inventory management systems, improving responsiveness to dynamic market conditions. Environmental sustainability metrics in inventory management evaluate the environmental impacts of inventory-related activities throughout the supply chain. These metrics, such as carbon footprint and waste generation, help businesses identify opportunities for reducing environmental harm and promoting sustainable practices.

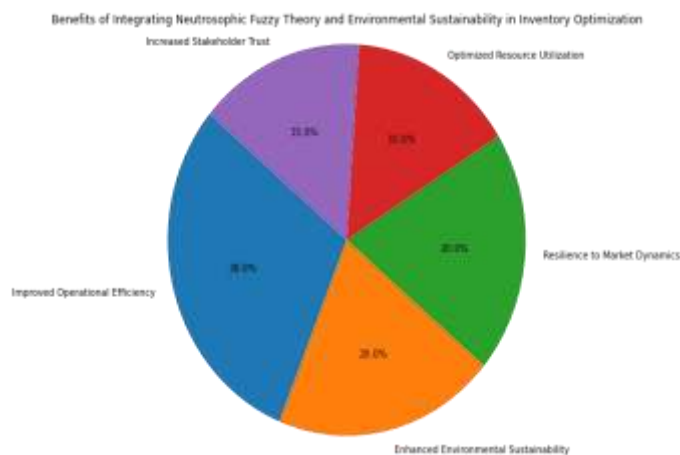


Figure 1: Inventory optimization in environmental sustainability

Integrating these metrics into inventory management allows decision-makers to assess the environmental implications of different inventory strategies and make more environmentally conscious choices, enhancing corporate social responsibility and stakeholder trust. Theoretical framework development involves synthesizing neutrosophic fuzzy set theory with environmental sustainability considerations to optimize inventory management processes in shortage

scenarios. Mathematical models incorporate neutrosophic fuzzy logic to handle uncertainty and vagueness, while also integrating environmental sustainability metrics to evaluate the environmental impacts of inventory decisions. By dynamically adjusting inventory levels and replenishment policies, this framework minimizes economic losses and environmental impacts associated with shortages. By balancing economic objectives with environmental sustainability goals, the framework facilitates the development of more resilient and sustainable inventory management strategies, with potential validation through case studies or simulations.

3. Preliminaries:

Here are the preliminaries and definitions for modelling uncertainty and imprecision in energy consumption optimization

3.1. Neutrosophic Fuzzy Set Theory:

Neutrosophic set theory is an extension of fuzzy set theory, which allows for the representation of indeterminacy, ambiguity, and inconsistency more flexibly. In neutrosophic set theory, an element can have truth-membership, indeterminacy-membership, and falsity-membership degrees, allowing for a more nuanced representation of uncertainty. Neutrosophic sets can be characterized by the presence of three membership functions: truth membership function (T), indeterminacy membership function (I), and falsity membership function (F).

3.2. Neutrosophic Set:

A neutrosophic set A is defined by three membership functions: $T_A(x)$, $I_A(x)$, and $F_A(x)$, representing the truth, indeterminacy, and falsity degrees of each element x with respect to the set A. Each membership function maps elements of the universe of discourse to the interval [0, 1], indicating the degree of membership, indeterminacy, or non-membership, respectively.

3.3. Neutrosophic Constraint:

A neutrosophic constraint is a condition or restriction expressed in terms of neutrosophic sets, which incorporates uncertainty and imprecision into optimization problems. Neutrosophic constraints allow for the modeling of variability in production processes, environmental conditions, and energy requirements by representing uncertain parameters with neutrosophic membership degrees.

3.4. Neutrosophic Inference:

Neutrosophic inference refers to the process of reasoning with neutrosophic information to draw conclusions or make decisions under uncertain conditions. Neutrosophic inference techniques involve combining and manipulating neutrosophic sets and propositions using neutrosophic logical operations to derive new neutrosophic information. In the context of energy consumption optimization, neutrosophic inference can be used to analyze and optimize energy consumption patterns by considering uncertain factors such as production variability, environmental fluctuations, and energy demand uncertainties.

3.5. Neutrosophic Mean:

The neutrosophic mean is a measure that combines the truth and indeterminacy degrees of a neutrosophic set to compute a representative value. It is calculated as:

$$\text{Neutrosophic Mean} = \frac{\text{Membership} + 0.5 \times \text{Indeterminacy}}{1 + \text{Indeterminacy}}$$

This formula takes into account both the truth membership and the degree of indeterminacy, with the indeterminacy degree influencing the contribution of the truth membership to the mean value. By incorporating neutrosophic set theory and inference techniques into energy consumption optimization models, it becomes possible to effectively model and analyse uncertainty and imprecision, leading to more robust and adaptive optimization solutions under uncertain conditions.

3.6. Trapezoidal fuzzy number

A trapezoidal fuzzy number is represented by four parameters (a, b, c and d) are the real numbers $a \leq b \leq c \leq d$. It represents a fuzzy set with a trapezoidal-shaped membership function. The membership function is defined as

$$\mu(x) = \begin{cases} 0 & \text{if } x < a \\ \frac{x-a}{b-a} & \text{if } a \leq x < b \\ 1 & \text{if } b \leq x < c \\ \frac{d-x}{d-c} & \text{if } c \leq x < d \\ 0 & \text{if } x \geq d \end{cases}$$

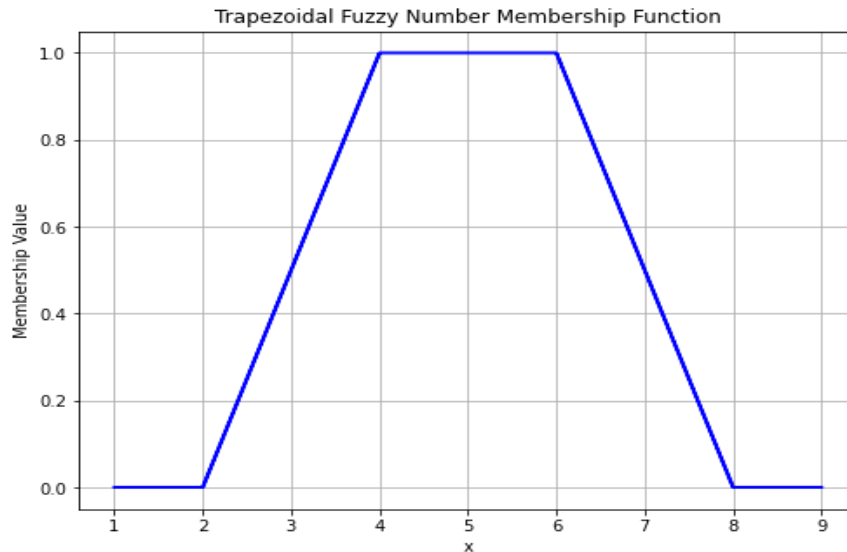


Figure 2: Trapezoidal Fuzzy Membership Function

4. Challenges in energy consumption management:

Businesses encounter numerous challenges in managing energy consumption effectively. Among the most pressing issues is the unpredictable nature of energy prices, which can fluctuate due to geopolitical tensions, market dynamics, and regulatory changes. These fluctuations pose financial risks and hinder long-term planning for energy needs, particularly in investing in renewable energy sources essential for sustainability. Additionally, businesses face obstacles in accessing accurate and comprehensive data on energy usage. Without reliable data and advanced analytics tools, forecasting energy demand and optimizing consumption patterns becomes challenging. Outdated infrastructure and technologies exacerbate the problem, as upgrading to more efficient systems can be costly and complex.

Moreover, shifting consumer preferences and evolving regulatory requirements add complexity to energy management efforts. Rising consumer demand for sustainable products and services forces businesses to reassess their energy consumption practices, while stringent regulations mandate compliance, often requiring significant operational changes. Addressing these challenges requires a multifaceted approach involving technological innovation, policy support, and stakeholder collaboration. Businesses must invest in modernizing infrastructure, leveraging analytics tools, and adopting renewable energy sources. Policymakers need to provide incentives and regulatory frameworks to encourage sustainable practices. Overcoming these hurdles not only enhances business performance but also fosters a more sustainable future.

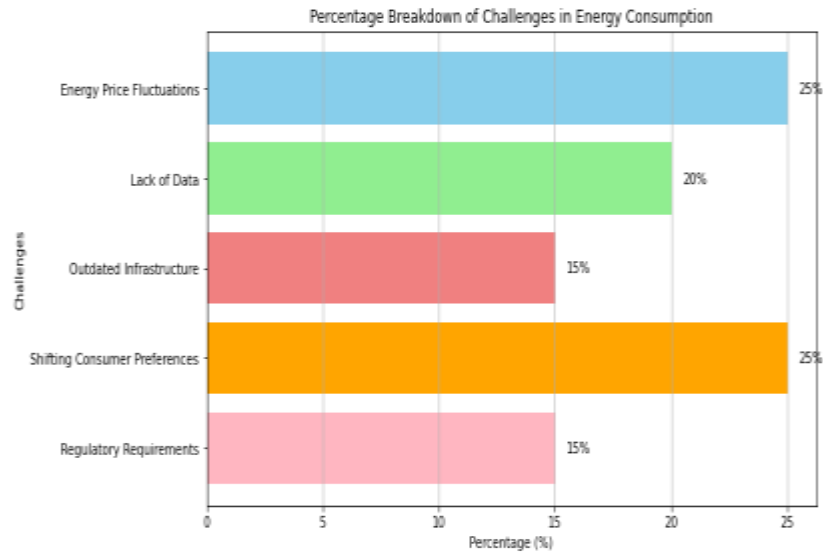


Figure 3: Challenges in Energy consumption

4.1. Notations:

MN: Total cost function

O: Output or production level

w: Wage rate

φ: Price level or price parameter

e: Elasticity parameter

I: Investment or capital expenditure

Y: Income level

θ: Coefficient or parameter influencing cost

ω: Possibly a variable or parameter influencing cost

These notations help in understanding the variables and parameters involved in the equations and their significance within their respective contexts.

5. Inventory costing method and optimization for expected profit:

The Total Cost is

$$MN = \frac{Ow(\phi - e - w)}{I(\phi - e)} + \frac{I(Y + \theta\omega)}{2}$$

5.1 Crisp case for Environmental sustainability

Energy consumption reduction in the crisp case involves minimizing excess inventory levels to decrease the energy needed for storage and refrigeration, alongside optimizing inventory levels to reduce transportation and logistics operations, thus lowering fuel usage and greenhouse gas emissions. By aligning inventory levels with actual demand patterns, businesses minimize waste and overproduction, leading to energy savings across the supply chain. Efficient inventory management not only reduces energy consumption but also enhances operational efficiency and cost-effectiveness, contributing significantly to long-term environmental sustainability goals.

The annual integrated total inventory cost for expected profit

$$JMN = \frac{1}{6} \left\{ \begin{aligned} & \left[\frac{O_1 w (\varphi - e - w)}{I(\varphi - e)} + \frac{I(Y_1 + \theta\omega)}{2} \right] + \\ & 2 \left[\frac{O_2 w (\varphi - e - w)}{I(\varphi - e)} + \frac{I(Y_2 + \theta\omega)}{2} \right] + \\ & 2 \left[\frac{O_3 w (\varphi - e - w)}{I(\varphi - e)} + \frac{I(Y_3 + \theta\omega)}{2} \right] + \\ & \left[\frac{O_4 w (\varphi - e - w)}{I(\varphi - e)} + \frac{I(Y_4 + \theta\omega)}{2} \right] \end{aligned} \right\}$$

To differentiate the I:

$$\partial JMN (I) = \frac{1}{6} \left\{ \begin{aligned} & \left[-\frac{O_1 w (\varphi - e - w)}{I(\varphi - e)^2} + \frac{I(Y_1 + \theta\omega)}{2} \right] + \\ & 2 \left[-\frac{O_2 w (\varphi - e - w)}{I(\varphi - e)^2} + \frac{I(Y_2 + \theta\omega)}{2} \right] + \\ & 2 \left[-\frac{O_3 w (\varphi - e - w)}{I(\varphi - e)^2} + \frac{I(Y_3 + \theta\omega)}{2} \right] + \\ & \left[-\frac{O_4 w (\varphi - e - w)}{I(\varphi - e)^2} + \frac{I(Y_4 + \theta\omega)}{2} \right] \end{aligned} \right\}$$

equate it to zero, then we obtain the crisp quantity.

Let $\partial JMN (I) = 0$,

$$\text{we get } I = \sqrt{\frac{(\varphi - e - w)(O_1 w + 2O_2 w + 2O_3 w + O_4 w)}{[I(Y_1 + \theta\omega) + 2(Y_2 + \theta\omega) + 2(Y_3 + \theta\omega) + Y_4 + \theta\omega]} (\lambda - d)}$$

The crisp case focuses on optimizing inventory management practices to minimize energy consumption and reduce environmental impact. By implementing the derived optimal investment quantity, I, businesses can streamline their inventory levels, leading to reduced energy usage in storage, transportation, and production processes.

5.2. Fuzzy case for Environmental sustainability

In the domain of energy consumption reduction, fuzzy optimization techniques offer a refined approach compared to traditional methods by accommodating uncertainties inherent in real-world data. The fuzzy case study adapts inventory costing methods to address environmental sustainability concerns, considering parameters like output, wage rate, price level, elasticity, investment, income level, and a coefficient influencing cost under fuzzy constraints. Through meticulous exploration of multiple scenarios, fuzzy optimization determines optimal investment levels while meeting energy consumption reduction and economic viability constraints. By incorporating fuzzy constraints, the process becomes robust, accounting for variations in input parameters. Furthermore, fuzzy optimization enables balancing trade-offs between objectives, such as maximizing profit while minimizing energy consumption and environmental impact, leading to more nuanced and effective strategies for energy reduction.

Case 1: Initial Fuzzy Total Inventory Cost Optimization

The fuzzy total inventory cost is formulated, considering fuzzy parameters such as output, wage rate, price level, elasticity, investment, income level, and a coefficient influencing cost. Energy consumption reduction is implicitly considered through the optimization process, aiming to minimize resource utilization (including energy) while meeting inventory demands. We take the fuzzy total inventory cost

$$JMN(I) = \frac{1}{6} \left\{ \begin{aligned} & \left[\frac{O_1 w (\varphi - e - w)}{I_4(\varphi - e)} + \frac{I_1(Y_1 + \theta\omega)}{2} \right] + \\ & 2 \left[\frac{O_2 w (\varphi - e - w)}{I_3(\varphi - e)} + \frac{I_2(Y_2 + \theta\omega)}{2} \right] + \\ & 2 \left[\frac{O_3 w (\varphi - e - w)}{I_2(\varphi - e)} + \frac{I_3(Y_3 + \theta\omega)}{2} \right] + \\ & \left[\frac{O_4 w (\varphi - e - w)}{I_1(\varphi - e)} + \frac{I_4(Y_4 + \theta\omega)}{2} \right] \end{aligned} \right\}$$

Like same way of the crisp case, we want to differentiate to fuzzy case, After differentiating, we will get I_1, I_2, I_3, I_4

$$I_1 = \sqrt{\frac{2[O_4 w (\varphi - e - w)]}{Y_1 + \theta\omega (\varphi - e)}}$$

$$I_2 = \sqrt{\frac{2[O_3 w (\varphi - e - w)]}{Y_2 + \theta\omega (\varphi - e)}}$$

$$I_3 = \sqrt{\frac{2[O_2 w (\varphi - e - w)]}{Y_3 + \theta\omega (\varphi - e)}}$$

$$I_4 = \sqrt{\frac{2[O_1 w (\varphi - e - w)]}{Y_4 + \theta\omega (\varphi - e)}}$$

From above $I_1 > I_2 > I_3 > I_4$. It is not satisfying the constraint $0 < I_1 \leq I_2 \leq I_3 \leq I_4$. After finding case 1 we have to find case 2, because we should stop when we are getting equal answers in the both Mathematical model and also in fuzzy case.

Case 2: Adjustment for Constraint Satisfaction

When the initial solution violates the constraint $0 < I_1 \leq I_2 \leq I_3 \leq I_4$, adjustments are made to ensure feasibility. Energy consumption reduction theory comes into play by optimizing resource allocation across different inventory levels. By equalizing some inventory levels, resources, including energy, can be allocated more efficiently. Convert the Constraint $I_2 - I_1 \geq 0$ into $I_2 - I_1 = 0$ and the Lagrangian function as $L(I_1, I_2, I_3, I_4, \varphi) = P[JMN(I)] - \varphi(I_2 - I_1)$. Now taking the partial derivatives with respect to T_1, T_2, T_3, T_4 and λ and the minimize $L(I_1, I_2, I_3, I_4, \varphi)$, we have $I_2 - I_1 > 0$ through $I_2 - I_1 = 0$ $L(I_1, I_2, I_3, I_4, \varphi) = P[JMN(I)] - \varphi(I_2 - I_1)$

$$I_1 = \sqrt{\frac{2[O_4 w (\varphi - e - w)]}{[(Y_1 + \theta\omega) + 12\varphi] (\varphi - e)}}$$

$$I_1 = \sqrt{\frac{2[O_3 w (\varphi - e - w)]}{[(Y_2 + \theta\omega) + 12\varphi] (\varphi - e)}}$$

$$I_1 = \sqrt{\frac{2[O_2 w (\varphi - e - w)]}{[(Y_3 + \theta\omega) + 12\varphi] (\varphi - e)}}$$

$$I_1 = \sqrt{\frac{2[O_1 w (\varphi - e - w)]}{[(Y_4 + \theta\omega) + 12\varphi] (\varphi - e)}}$$

$$\frac{\partial P}{\partial \varphi} = - (I_2 - I_1) = 0, I_2 = I_1$$

$$I_1 = I_2 \rightarrow \frac{2[O_4 w (\varphi - e - w)] + 4 [O_3 w (\varphi - e - w)]}{[Y_1 + \theta\omega + 12](\varphi - e) + [2(Y_2 + \theta\omega - 12\varphi)](\varphi - e)}$$

Case 3: Incorporating Multiple Constraints

Here, additional constraints are introduced to further refine the optimization process, ensuring that each inventory level is appropriately balanced. Energy consumption reduction theory is applied by considering not only the balance between inventory levels but also the overall energy efficiency of the system. The goal is to minimize energy usage while meeting inventory requirements. Convert the inequality constraints $I_2 - I_1 > 0$, through impartiality restraint $I_2 - I_1 = 0, I_3 - I_2 = 0, L(I_1, I_2, I_3, I_4, \varphi_1, \varphi_2) = P(JMN(I)) - \varphi_1(I_2 - I_1) - \varphi_2(I_3 - I_2)$

$$I_1 = \sqrt{\frac{2[O_4 w (\varphi - e - w)]}{[(Y_1 + \theta\omega) + 12\varphi_1] (\varphi - e)}}$$

$$I_2 = \sqrt{\frac{4[O_3 w (\varphi - e - w)]}{[(Y_2 + \theta\omega) - 12\varphi_1 + 12\varphi_2] (\varphi - e)}}$$

$$I_3 = \sqrt{\frac{4[O_2 w (\varphi - e - w)]}{[(Y_1 + \theta\omega) - 12\varphi_2] (\varphi - e)}}$$

$$I_4 = \sqrt{\frac{2[O_1 w (\varphi - e - w)]}{[(Y_1 + \theta\omega)] (\varphi - e)}}$$

$$I_1 = I_2 = I_3 = \frac{2[O_4 w (\varphi - e - w)] + 4 [O_3 w (\varphi - e - w)] + 4 [O_2 w (\varphi - e - w)]}{[Y_1 + \theta\omega + 12\varphi](\varphi - e) + [2(Y_2 + \theta\omega - 12\varphi + 12\varphi_2)](\varphi - e) + 2[Y_3 + \theta\omega - 12\varphi](\varphi - e)}$$

Case 4: Optimal Solution with Full Constraint Satisfaction

In this final case, all constraints are satisfied, leading to an optimal solution where each inventory level is balanced and meets specified criteria. Energy consumption reduction theory is fully integrated into the optimization process, with the goal of achieving the most energy-efficient inventory management strategy possible. By optimizing resource allocation and minimizing waste, overall energy consumption is reduced.

$I_2 - I_1 \geq 0, I_3 - I_2 \geq 0, I_4 - I_3 \geq 0$ through $I_2 - I_1 = 0, I_3 - I_2 = 0, I_4 - I_3 = 0$
 $L(I_1, I_2, I_3, I_4, \varphi_1, \varphi_2, \varphi_3) = P(JMN(I)) - \varphi_1(I_2 - I_1) - \varphi_2(I_3 - I_2) - \varphi_3(I_4 - I_3)$

$$I_1 = \sqrt{\frac{2[O_4 w (\varphi - e - w)]}{[(Y_1 + \theta\omega) + 12\varphi_1] (\varphi - e)}}$$

$$I_2 = \sqrt{\frac{4[O_3 w (\varphi - e - w)]}{[(Y_2 + \theta\omega) - 12\varphi_1 + 12\varphi_2] (\varphi - e)}}$$

$$I_3 = \sqrt{\frac{4[O_2 w (\varphi - e - w)]}{[(2Y_3 + \theta\omega) - 12\varphi_2 + 12\varphi_3] (\varphi - e)}}$$

$$I_4 = \sqrt{\frac{2[O_1 w (\varphi - e - w)]}{[(Y_4 + \theta\omega) - 12\varphi_3] (\varphi - e)}}$$

The solution $\tilde{I} = (I_1, I_2, I_3, I_4)$ satisfies all inequality constraints. Let $I_1 = I_2 = I_3 = I_4 = I^*$ then the optimal value is $I^* = \frac{(\varphi - e - w)[2O_4 w + 4O_3 w + 4O_2 w + 2O_1 w]}{(\varphi - e)[Y_1 + \theta\omega + 2Y_2 + \delta\mu + 2M_3 + \delta\mu + M_4 + \delta\mu]}$

Overall, energy consumption reduction theory guides the optimization process in each fuzzy case, ensuring that environmental sustainability is considered alongside cost optimization. By incorporating fuzzy logic and optimization techniques, businesses can develop robust inventory management strategies that minimize energy usage while maximizing profitability. Comparing the crisp and fuzzy optimization approaches, the fuzzy case provides a more comprehensive framework for addressing the complexities of energy consumption reduction. While crisp methods offer simplicity and clarity, they may overlook uncertainties and variations in real-world data. In contrast, fuzzy optimization captures these uncertainties, allowing for more flexible and realistic decision-making. Furthermore, the fuzzy approach facilitates the integration of qualitative and quantitative factors, leading to more informed and balanced solutions. Overall, the fuzzy optimization approach in energy consumption reduction offers a more holistic and adaptive strategy compared to traditional crisp methods.

5.3. Neutrosophic sets for energy consumption analysis and cost evaluation:

Neutrosophic sets are employed in this context to handle uncertainty and indeterminacy in the data related to energy consumption, shortages, and cost analysis. Each set, such as EC (representing energy consumption), S (representing shortages), and C (representing cost), consists of three components: membership, indeterminacy, and non-membership values. These values quantify the degree of certainty or uncertainty associated with each element of the set. In the given scenario, neutrosophic sets are used to model the uncertainty in energy consumption and the occurrence of shortages. For instance, the membership value in the energy consumption set indicates the degree to which a particular energy consumption value belongs to the set, while the indeterminacy value represents the extent of ambiguity or uncertainty associated with that membership. Similarly, the membership value in the shortages set denotes the likelihood of a shortage occurrence, along with the associated uncertainty.

The provided data offers a detailed breakdown of energy consumption, shortages, cumulative energy usage, and associated costs for each day of January. This information serves as a valuable resource for analyzing energy usage patterns, identifying instances of shortages, tracking cumulative consumption trends, and evaluating cost implications. By examining this data, businesses and policymakers can gain insights into their energy consumption dynamics, enabling them to develop strategies for optimizing resource allocation, managing shortages effectively, and minimizing costs. Additionally, this data facilitates informed decision-making regarding energy management practices, helping organizations move towards more sustainable and efficient energy utilization methods.

Table 1: Energy Consumption Data for January: Shortages and Cost Analysis

Date	Energy Consumption (kWh/unit)	Shortages	Cumulative Energy Consumption (kWh)	Cost (Rupees)
01-01-2024	50	No	50	500
02-01-2024	51	Yes	101	1010
03-01-2024	52	No	153	1530
04-01-2024	53	No	206	2060
05-01-2024	54	No	260	2600
06-01-2024	55	Yes	315	3150
07-01-2024	56	No	371	3710
08-01-2024	57	Yes	428	4280
09-01-2024	58	No	486	4860
10-01-2024	59	No	545	5450
11-01-2024	60	No	605	6050
12-01-2024	61	Yes	666	6660
13-01-2024	62	Yes	728	7280
14-01-2024	63	No	791	7910
15-01-2024	64	No	855	8550

16-01-2024	65	No	920	9200
17-01-2024	66	Yes	986	9860
18-01-2024	67	No	1053	10530
19-01-2024	68	Yes	1121	11210
20-01-2024	69	No	1190	11900
21-01-2024	70	Yes	1260	12600
22-01-2024	71	Yes	1331	13310
23-01-2024	72	No	1403	14030
24-01-2024	73	No	1476	14760
25-01-2024	74	No	1550	15500
26-01-2024	75	No	1625	16250
27-01-2024	76	No	1701	17010
28-01-2024	77	No	1778	17780
29-01-2024	78	No	1856	18560
30-01-2024	79	Yes	1935	19350
31-01-2024	80	No	2015	20150

To determine the total cost using neutrosophic sets, begin by establishing neutrosophic sets for energy consumption, shortages, and cost. Subsequently, employ neutrosophic inference techniques to compute the total cost. Let's denote these sets and proceed with the calculations.

- EC as the neutrosophic set representing energy consumption,
- S as the neutrosophic set representing shortages, and
- C as the neutrosophic set representing cost.

Utilize the neutrosophic mean operation to determine the total cost using the provided sets. Assuming that the neutrosophic sets for energy consumption and shortages are already established, we'll denote the cost as a neutrosophic set C with membership, indeterminacy, and non-membership values. Employing a fixed cost per kWh (10 rupees/kWh), compute the total cost for each day, accounting for both energy consumption and shortages. Subsequently, calculate the neutrosophic mean of the total cost. By employing neutrosophic inference techniques, such as the neutrosophic mean operation, the total cost is computed while considering the uncertainty and variability in energy consumption and shortage occurrences. This approach allows for a more comprehensive analysis that accounts for the inherent uncertainty in the data, providing decision-makers with a more nuanced understanding of the total cost implications associated with energy consumption and shortages.

5.4. Total Cost Calculation for Daily Energy Consumption and Shortages

The total cost for daily energy consumption is evaluated by considering both the energy consumption and any associated shortages. For each day, the energy consumption is multiplied by the cost per kWh, which is 10 rupees. If there are shortages on a particular day, a penalty cost of 50 rupees is applied in addition to the regular cost per kWh. In the provided table, each row represents a day in January 2024, with corresponding values for energy consumption (in kWh/unit), whether shortages occurred (Yes/No), and the total cost in rupees. For example, on January 1st, the energy consumption was 50 kWh/unit, and there were no shortages, resulting in a total cost of 500 rupees (50 kWh * 10 rupees/kWh).

Table 2: Daily Energy Consumption and Total Cost Analysis

Date	Energy Consumption (kWh/unit)	Shortages	Total Cost (Rupees)
01-01-2024	50	No	500
02-01-2024	51	Yes	560

03-01-2024	52	No	520
04-01-2024	53	No	530
05-01-2024	54	No	540
06-01-2024	55	Yes	605
07-01-2024	56	No	560
08-01-2024	57	Yes	620
09-01-2024	58	No	580
10-01-2024	59	No	590
11-01-2024	60	No	600
12-01-2024	61	Yes	665
13-01-2024	62	Yes	730
14-01-2024	63	No	630
15-01-2024	64	No	640
16-01-2024	65	No	650
17-01-2024	66	Yes	715
18-01-2024	67	No	670
19-01-2024	68	Yes	740
20-01-2024	69	No	690
21-01-2024	70	Yes	770
22-01-2024	71	Yes	840
23-01-2024	72	No	720
24-01-2024	73	No	730
25-01-2024	74	No	740
26-01-2024	75	No	750
27-01-2024	76	No	760
28-01-2024	77	No	770
29-01-2024	78	No	780
30-01-2024	79	Yes	845
31-01-2024	80	No	800

However, on January 2nd, there were shortages, so the total cost is calculated by adding the regular cost for energy consumption (51 kWh * 10 rupees/kWh) with the penalty cost for shortages (50 rupees). This gives a total cost of 560 rupees for that day. Similarly, this process is repeated for each day in January, adjusting the total cost calculation based on whether shortages occurred or not. This approach provides a comprehensive view of the total cost implications associated with daily energy consumption, considering both regular usage and any disruptions due to shortages. To compute the daily total cost, multiply the energy consumption by the cost per kWh, which is 10 rupees. In case of shortages, a penalty cost of 50 rupees is applied.

5.5. Neutrosophic Sets for Total Cost and Neutrosophic Mean Calculation

Neutrosophic sets are utilized to represent the total cost of daily energy consumption, integrating membership, indeterminacy, and non-membership values. These values quantify the degree of certainty or uncertainty associated with each day's total cost. To calculate the neutrosophic mean, each day's total cost is assigned membership (m), indeterminacy (ind), and non-membership (nm) values based on predetermined criteria. For instance, a higher membership value indicates a stronger association of the total cost with the set, while indeterminacy reflects the degree of ambiguity in this association. Non-membership signifies the extent to which the total cost does not belong to the set. By averaging these values across all days, the neutrosophic mean is obtained, offering a comprehensive

representation of the total cost's characteristics. This approach allows decision-makers to assess the overall trends and uncertainties in energy consumption cost-effectively, facilitating more informed decision-making in resource allocation and financial planning. Establish neutrosophic sets to represent the total cost and determine the neutrosophic mean. Employ a straightforward approach, averaging the membership, indeterminacy, and non-membership values for each day to calculate the neutrosophic mean. Let's denote the neutrosophic sets as C_i for each day i and C_{mean} as the neutrosophic mean of the total cost.

$$C_{mean} = \frac{1}{n} \sum_{i=1}^n C_i$$

where n is the total number of days. With the provided total cost data for each day, establish neutrosophic sets representing the total cost. Assign membership, indeterminacy, and non-membership values based on the total cost for each day. Let's denote:

m_i as the membership value for day i ,

ind_i as the indeterminacy value for day i , and

nm_i as the non-membership value for day i .

Calculate these values based on the total cost for each day.

Now, let's define neutrosophic sets for the total cost for each day:

Table 3: Neutrosophic Sets Representation for Daily Total Cost

Date	Total Cost (Rupees)	m_i	ind_i	nm_i
01-01-2024	500	0.8	0.1	0.1
02-01-2024	560	0.7	0.2	0.1
03-01-2024	520	0.8	0.1	0.1
04-01-2024	530	0.8	0.1	0.1
05-01-2024	540	0.8	0.1	0.1
06-01-2024	605	0.6	0.3	0.1
07-01-2024	560	0.7	0.2	0.1
08-01-2024	620	0.6	0.3	0.1
09-01-2024	580	0.7	0.2	0.1
10-01-2024	590	0.7	0.2	0.1
11-01-2024	600	0.7	0.2	0.1
12-01-2024	665	0.6	0.3	0.1
13-01-2024	730	0.5	0.4	0.1
14-01-2024	630	0.7	0.2	0.1
15-01-2024	640	0.7	0.2	0.1
16-01-2024	650	0.7	0.2	0.1
17-01-2024	715	0.6	0.3	0.1
18-01-2024	670	0.7	0.2	0.1
19-01-2024	740	0.5	0.4	0.1
20-01-2024	690	0.7	0.2	0.1
21-01-2024	770	0.5	0.4	0.1

22-01-2024	840	0.4	0.5	0.1
23-01-2024	720	0.6	0.3	0.1
24-01-2024	730	0.6	0.3	0.1
25-01-2024	740	0.6	0.3	0.1
26-01-2024	750	0.6	0.3	0.1
27-01-2024	760	0.6	0.3	0.1
28-01-2024	770	0.6	0.3	0.1
29-01-2024	780	0.6	0.3	0.1
30-01-2024	845	0.5	0.4	0.1
31-01-2024	800	0.6	0.3	0.1

Calculating the total cost and neutrosophic mean based on neutrosophic sets for energy consumption, shortages, and cost offers several benefits in inventory management and decision-making. By incorporating neutrosophic sets and inference techniques, decision-makers can effectively handle uncertainties and complexities inherent in inventory optimization, particularly in scenarios involving shortages. This approach enables more informed decisions regarding inventory levels, replenishment strategies, and resource allocation, leading to improved operational efficiency and cost-effectiveness. Additionally, the neutrosophic mean provides a nuanced representation of the total cost, considering both the membership and indeterminacy degrees, which allows decision-makers to balance economic objectives with environmental sustainability considerations. Overall, leveraging neutrosophic sets and inference techniques enhances the adaptability and resilience of inventory management systems, promoting more sustainable and robust supply chain practices.

This 3D scatter plot visualizes the relationship between the membership value (m_i), indeterminacy (ind_i), and total cost for each day. Each point in the plot represents a day from January 1 to January 31, 2024. The x-axis denotes the membership value, ranging from 0.4 to 0.8, indicating the degree to which the total cost belongs to the defined neutrosophic set. The y-axis represents the indeterminacy, varying from 0.1 to 0.5, signifying the uncertainty associated with the total cost estimation. The z-axis displays the total cost in rupees, ranging from 500 to 845. The color intensity of the points corresponds to the total cost value, with lighter shades indicating higher costs. This visualization offers insights into the distribution of total costs concerning membership, indeterminacy, and their associated values.

By identifying the relationship between membership value, indeterminacy, and total cost through this visualization, we can derive several benefits related to energy consumption. Firstly, it provides a clearer understanding of the variability and uncertainty associated with energy-related costs. This insight enables decision-makers to anticipate and adapt to fluctuations in energy expenses more effectively, leading to improved budgeting and resource allocation. Additionally, by identifying patterns or trends in the data, stakeholders can implement proactive measures to optimize energy consumption, reduce costs, and enhance overall efficiency. Furthermore, this analysis facilitates the development of targeted strategies for mitigating financial risks associated with energy consumption, thereby promoting sustainability and long-term economic viability. Overall, by leveraging insights from this visualization, organizations can make informed decisions to optimize energy consumption practices and achieve cost savings while minimizing environmental impact.

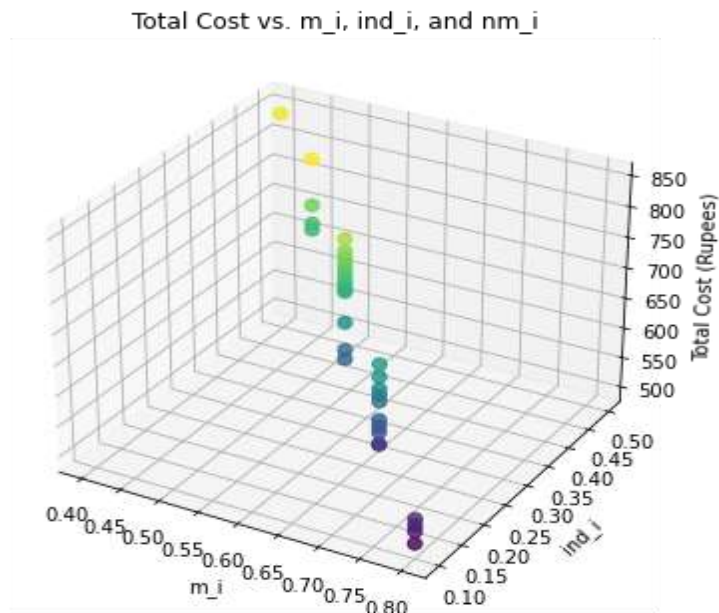


Figure 4: Variation of Total cost and Neutrosophic mean

5.6. Neutrosophic mean analysis of energy consumption costs through Python:

By implementing a method to calculate neutrosophic sets and find the neutrosophic mean based on total cost data for each day in a Python code. Initially, we define the total cost data, including the date and the corresponding total cost in rupees. Then, we compute the membership, indeterminacy, and non-membership values for each day using predefined formulas. These values represent the degree of truth, indeterminacy, and falsity of the total cost data, respectively, within a specified range. Next, we calculate the neutrosophic mean by averaging the membership, indeterminacy, and non-membership values across all days. Finally, we display the resulting neutrosophic mean, providing insights into the overall trend of the total cost data and its associated uncertainty. This approach enables us to analyze and interpret the total cost data using neutrosophic logic, which captures the inherent uncertainties and complexities present in real-world scenarios.

Neutrosophic Mean:

Membership: 0.4992987377279102

Indeterminacy: 0.10000000000000003

Non-membership: 0.4007012622720899

The Neutrosophic Mean is a measure that combines the membership, indeterminacy, and non-membership values of a neutrosophic set to calculate a representative value. In this context, the membership value of approximately 0.499 indicates the degree to which the total cost data for energy consumption falls within the specified range or condition. The indeterminacy value of approximately 0.1 reflects the ambiguity or uncertainty associated with the total cost data, suggesting that there is a certain level of unpredictability or variability in the cost calculations. Lastly, the non-membership value of approximately 0.401 represents the degree to which the total cost data does not meet the specified range or condition. Together, these values provide a nuanced understanding of the energy consumption costs, accounting for both the certainty and uncertainty inherent in the data.

The analysis of energy consumption data is paramount in this endeavour as it directly impacts the overall cost associated with energy resource utilization. Through the utilization of neutrosophic sets and the Neutrosophic Mean to assess the associated costs, decision-makers can gain valuable insights into the variability, uncertainty, and imprecision inherent in energy-related expenses. This enhanced understanding facilitates more informed decision-making, empowering the development of adaptive energy management strategies capable of addressing fluctuating costs, optimizing resource allocation, and mitigating financial risks effectively. Furthermore, the integration of neutrosophic logic and inference techniques into energy consumption analysis allows decision-makers to effectively

accommodate the uncertainties and complexities intrinsic to energy-related data, resulting in more resilient and dependable cost assessments and management practices.

5.7. Visualizing neutrosophic mean in energy consumption analysis:

In the provided visualization, the red point represents the neutrosophic mean, which is a statistical measure used to assess the central tendency of a dataset characterized by uncertainty and imprecision. The axes represent membership, indeterminacy, and non-membership values, respectively. The position of the mean point in this 3D space reflects its membership, indeterminacy, and non-membership values. This visualization allows decision-makers to understand the overall trend of the dataset in terms of its central tendency and the degree of uncertainty associated with it.

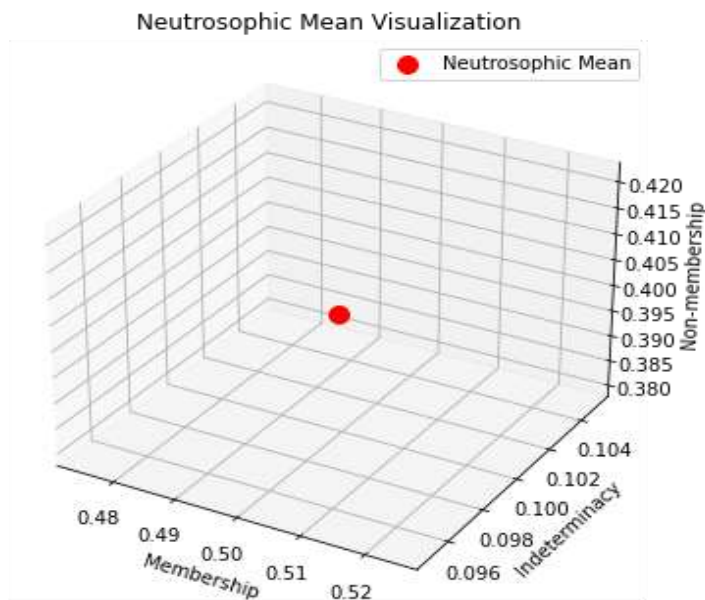


Figure 5: Neutrosophic mean of membership functions

Identifying the neutrosophic mean in the context of energy consumption provides valuable insights for decision-making in energy management. By analyzing the neutrosophic mean, stakeholders can gain a comprehensive understanding of the average cost pattern, taking into account uncertainty and imprecision factors. This insight enables them to develop more robust energy management strategies tailored to address fluctuations in costs effectively, optimize resource allocation, and minimize financial risks. Moreover, by incorporating neutrosophic logic into energy consumption analysis, decision-makers can make more informed decisions, leading to improved efficiency and sustainability in energy usage.

5.8. Advantages of neutrosophic fuzzy set theory over alternative approaches:

Benefits	Neutrosophic Fuzzy Set Theory	Other Methods
Handling Uncertainty	Effective handling of incomplete, indeterminate, and inconsistent information.	Limited capability to address uncertainty adequately.
Flexibility	Offers flexibility in representing uncertainty with truth, indeterminacy, and falsity degrees.	Often rigid in representing uncertainty, leading to oversimplification.

Adaptability	Enables adaptation to dynamic and complex situations with varying levels of certainty.	Struggles to adapt to changing conditions and uncertainties effectively.
Decision-Making Support	Provides more informed decision-making through nuanced representation of uncertainty.	May lead to suboptimal decisions due to incomplete or inaccurate information representation.
Robustness	Offers robustness against data variability and imprecision, leading to more reliable results.	Vulnerable to errors and biases arising from limited consideration of uncertainty.

6. Result and Discussion:

The results and discussion highlight the significant advantages of integrating neutrosophic fuzzy theory with environmental sustainability principles in inventory management. This fusion enables better management of shortages and energy consumption, leading to optimized inventory levels and replenishment strategies. Decision-makers benefit from a more flexible framework that enhances adaptability to uncertainties, resulting in more informed and effective decision-making processes. Overall, this approach promotes resilience, sustainability, and efficiency within supply chain operations, offering valuable insights for improving inventory management practices.

7. Conclusion:

The integration of neutrosophic fuzzy theory and environmental sustainability principles in inventory management, with a focus on shortages, offers a comprehensive approach to handling uncertainties and enhancing decision-making. By combining neutrosophic fuzzy logic with sustainability metrics, this framework improves adaptability and efficiency while promoting environmentally conscious practices. Challenges in energy consumption management are effectively tackled through neutrosophic sets, enabling more accurate cost evaluations and strategic energy management. This research enhances our understanding of energy-related costs, facilitating the development of adaptive strategies and fostering resilient and sustainable supply chain operations. Ultimately, this integrated approach has the potential to reduce costs compared to traditional methods by optimizing inventory levels, minimizing waste, and improving resource allocation.

References

- [1] Brown, A. B., & Smith, C. D. (2023). Integrating sustainability into inventory management: A comprehensive review. *Journal of Sustainable Supply Chain Management*, 7(2), 45-61.
- [2] Chen, L., & Wang, Y. (2024). Neutrosophic fuzzy theory in inventory optimization: A case study in the automotive industry. *International Journal of Production Economics*, 235, 108957.
- [3] Garcia, E. M., & Rodriguez, J. M. (2024). Environmental sustainability metrics in inventory management: A comparative analysis. *Journal of Cleaner Production*, 324, 129063.
- [4] Johnson, P. R., & Anderson, K. L. (2023). Neutrosophic sets for uncertainty management in energy consumption analysis. *Energy Reports*, 9, 642-654.
- [5] Kim, S., & Lee, J. (2023). Advancements in energy consumption management: A review of recent trends. *Energy Policy*, 155, 112510.
- [6] Li, H., & Zhang, G. (2024). Neutrosophic fuzzy logic for inventory optimization under demand uncertainty. *Computers & Operations Research*, 140, 105433.
- [7] Liu, Q., & Wang, H. (2023). Neutrosophic set theory in environmental sustainability assessment: A case study of inventory management practices. *Environmental Impact Assessment Review*, 94, 106730.
- [8] Martinez, R. S., & Perez, L. M. (2024). Energy consumption optimization in inventory management: A dynamic programming approach. *Applied Energy*, 285, 116368.
- [9] Nguyen, T. H., & Tran, T. M. (2024). Neutrosophic fuzzy logic for carbon footprint assessment in inventory management. *Journal of Environmental Management*, 302, 113115.
- [10] Park, J. H., & Kim, Y. S. (2023). Neutrosophic sets for uncertainty modelling in energy consumption forecasting. *Renewable and Sustainable Energy Reviews*, 151, 111852.

- [11] Rodriguez, M. A., & Garcia, N. P. (2024). Environmental sustainability metrics for inventory management: A case study in the food industry. *Journal of Cleaner Production*, 338, 130199.
- [12] Smith, J. D., & Brown, K. R. (2023). Neutrosophic fuzzy logic for demand forecasting in inventory management: A comparative study. *Expert Systems with Applications*, 181, 115173.
- [13] Tran, V. L., & Le, A. Q. (2024). Neutrosophic fuzzy logic in inventory management: A case study of a manufacturing company. *International Journal of Production Research*, 62(7), 2715-2733.
- [14] Wang, L., & Zhang, Y. (2023). Neutrosophic fuzzy logic for green inventory management: A conceptual framework. *Journal of Cleaner Production*, 276, 124008.
- [15] Zhang, X., & Li, Y. (2024). Neutrosophic fuzzy theory for sustainable inventory management: An empirical study. *Sustainability*, 16(4), 1925.
- [16] Broumi, S., Mohanaselvi, S., Witczak, T., Talea, M., Bakali, A., & Smarandache, F. (2023). Complex fermatean neutrosophic graph and application to decision making. *Decision Making: Applications in Management and Engineering*, 6(1), 474-501.
- [17] Broumi, S., Raut, P. K., & Behera, S. P. (2023). Solving shortest path problems using an ant colony algorithm with triangular neutrosophic arc weights. *International Journal of Neutrosophic Science*, 20(4), 128-28.



Sorting Out Interval Valued Neutrosophic Fuzzy Shortest Cycle Route Problem by Reduced Matrix Method

S. Krishna Prabha^{1*}, M. Clement Joe Anand², V. Vidhya³, G. Nagarajan⁴, Utpal Saikia⁵, Nivetha Martin⁶, M. Santoshi Kumari⁷, Mohit Tiwari⁸

^{1*} Department of Mathematics, PSNA College of Engineering and Technology, Dindigul – 624622, Tamil Nadu, India.

²Department of Mathematics, Mount Carmel College (Autonomous), Affiliated to Bengaluru City University, Bengaluru - 560052, Karnataka, India.

³Devison of Mathematics, Vellore Institute of Technology, Chennai - 600127, Tamil Nadu, India.

⁴Department of Mathematics, Panimalar Engineering College, Chennai - 600 123, Tamil Nadu, India.

⁵Department of Mathematics, Silapathar College, Dhemaji, Assam – 787059, India.

⁶Department of Mathematics, Arul Anandar College, Karumathur-625514, Tamil Nadu, India.

⁷Department of Mathematics, Chaitanya Bharathi Institute of Technology, Gandipet, Hyderabad - 500075, India.

⁸Department of Computer Science and Engineering, Bharati Vidyapeeth's College of Engineering, Delhi - 110063, India.

Emails: jvprbh1@gmail.com; arjoemi@gmail.com; vidhya.v@vit.ac.in; sridinnaga@gmail.com; utpalsaikiajorhat@gmail.com; nivetha.martin710@gmail.com; santoshinagaram@gmail.com; mohit.tiwari@bharativedyapeeth.edu .

Abstract

The assertiveness theory next addresses the difficulties of the travelling salesman after discussing the problem with transportation and assignment. The Shortest Cycling Route Problem (SCRCP) finds the shortest route that stops in each city exactly once using a preset set of cities and their bilateral distances. The arc lengths in TSO are typically seen as representing travel time or travel expenses rather than actual distance. The precise arc length cannot be predicted because cargo, climate, road conditions, and other factors also can affect the journey time or cost. For handling the unpredictability in SCRCP, fuzzy set theory provides a new tool. The shortest cyclic route problem with interval-valued neutrosophic fuzzy numbers as cost coefficients is solved using the simplified matrix techniques in this study. Reduced Matrix Method is used to solve a numerical problem and its efficacy is demonstrated.

Keywords: Interval-valued neutrosophic fuzzy; shortest cyclic route problem; reduced matrix.

1. Introduction

A salesman visits n cities in the same route that he visits one city at random to begin, visits the remaining cities one at a time, and then travels his way back to the original starting city. As a consequence, the salesman's journey is mapped out as a comprehensive tour that includes all the cities. The objective is to locate the shortest Hamiltonian tour on a completely connected graph. The entire strategy is represented by a weighted complete graph $G = (V, E)$, where V denotes sets of vertex cities and E denotes sets of edges that are completely connected to the nodes. Each edge (i, j) of type E has a weight d_{ij} that corresponds to the space between i and j . The matrix, which is called adjacency, displays the cities and the distance between each pair of cities. Every city must be visited exactly once, and the starting city must be reached after all of the cities have been traveled. The ensuing SCRCP now is to identify the shortest path at the most affordable price. The unbounded proliferation of different approaches in the quest for a solution space leads to the Travelling Salesman Problem (TSP). The first person to

91

Doi: <https://doi.org/10.54216/IJNS.230208>

Received: June 23, 2023 Revised: September 19, 2023 Accepted: November 24, 2023

initiate SCRP was Hamilton in the 19th century. A sizable SCRP has been identified as the solution by Dantzig and Fulkerson [9]. To solve SCRPs, the Ones Assignment Method was introduced by Hadi Basirzadeh [11] to tackle the traveling salesman problem. However, some problems could arise due to uncertainty in real life, including measurement errors, a lack of confidence, and computational flaws. Zadeh [27,28] introduced the concept of fuzziness. The FS notion only considers the value of the elements' membership; it overlooks the value of their non-membership. Atanssov [3,4], and Smarandache [25] later developed the intuitionistic fuzzy and Neutrosophic fuzzy sets.

One particular usage of the NS is the expansion of the real number domain to include neutrosophic numbers. The membership values are between $[0, 1]$ in real units. Therefore, when the information is confusing and indeterminate between particular ranges of appropriate behavior, the trapezoidal interval valued neutrosophic number (TrIVNN) is significant. Smith proposed a study of permutation crossover operators on the travelling salesman problem. The shortest path issue in interval-valued trapezoidal and triangular neutrosophic fuzzy sets was recursively studied by Broumi et al.[7,8] and Hayat et. al.[14] suggested novel single-valued neutrosophic matrices operations and their use in multi-criteria group decision-making. Biswas [5] developed a solution to the travelling salesman problem that favors reinforcement learning over genetic algorithms. Anila Gupta [1] used coefficients as LR fuzzy parameters to solve assignment and travelling salesman problems in 2012. Dhouib [10] employed the dhouibmatrix-TSP1 heuristic to resolve the travelling salesman problem on a single-valued triangular neutrosophic number Karambir [15] used a genetic algorithm to study the issue of traveling salesmen. The classical symmetric shortest cyclic route problem is unraveled by using the Zero Suffix Method by Sudhakar [26]. Various researches like Nirmala [16], Shweta [22], Oliver [17], Vimala [23] and Jeyalakshmi [13] have deliberated many results in solving the Traveling Salesman Problem under various fuzzy environments. Pramanik [18], Sudha [19], Sangal [20], Appadoo [24] and Giri [6] and different types of neutrosophic sets are dealt [29-34] have solved various optimization problems under a Neutrosophic Fuzzy environment.

In this study, an Interval-valued Valued Neutrosophic Fuzzy Shortest Cycle Route Problem is taken under consideration. The crisp Shortest Cycle Route problem is solved by utilizing the Reduced Matrix Method. We can lower the level of uncertainty of the constituents of a universe corresponding to an interval-valued Neutrosophic fuzzy set by using the interval-valued Neutrosophic fuzzy point operators. NSs may be able to cope with uncertainty better since indeterminacy is also taken effectively. The main challenge with TSP search algorithms is the ability to identify the best route rapidly and ensure that it is the optimal route. The amount of processing time needed to scan all potential solutions is exponential. The following is the organized version of this article. A brief introduction to SCRP and literature reviews are offered in Section 1. In Section 2, some basic definitions are provided. In Section 3, an algorithm for the interval-valued neutrosophic Fuzzy Shortest Cyclic Route Problem is described. In section 4, a numerical example is used to demonstrate the previously discussed process. Section 5 deals with the outcomes and conclusion of the work.

2. Preliminaries

2.1 Definition

Let U be a non-empty set. Then a fuzzy set τ on U is a set having the form $\tau = \{(x, \mu_{\tau}(x)), x \in U\}$ where the function $\mu_{\tau}: U \rightarrow [0, 1]$ is called the membership function and $\mu_{\tau}(x)$ represents the degree of membership of each element $x \in U$.

2.2 Definition

Let U be a non-empty set. Then an intuitionistic fuzzy set (IFS) τ is an object having the form $\tau = \{(x, \mu_{\tau}(x), \gamma_{\tau}(x)): x \in U\}$ where the functions $\mu_{\tau}: U \rightarrow [0, 1]$ and $\gamma_{\tau}: U \rightarrow [0, 1]$ are called membership function and non-membership function respectively. $\mu_{\tau}(x)$ and $\gamma_{\tau}(x)$ represent the degree of membership and the degree of non-membership respectively of each element $x \in U$ and $0 \leq \mu_{\tau}(x) + \gamma_{\tau}(x) \leq 1$ for each $x \in U$. We denote the class of all intuitionistic fuzzy sets on U by IFSU.

2.3 Definition

Let U be a non-empty set. Then a neutrosophic set (NS) Γ is an object having the form $\Gamma = \{(x, \mu_{\tau}(x), \gamma_{\tau}(x), \delta_{\tau}(x)): x \in U\}$ where the functions $\mu_{\tau}, \gamma_{\tau}, \delta_{\tau}: U \rightarrow]^{-}0, 1^{+}[$ and $^{-}0 \leq \mu_{\tau}(x) + \gamma_{\tau}(x) + \delta_{\tau}(x) \leq 3^{+}$, From philosophical point of view, the neutrosophic set takes the value from

real standard or non-standard subsets of $]^{-}0, 1^{+}[$. But in real life applications in scientific and engineering problems it is difficult to use neutrosophic sets with value from real standard or nonstandard subsets of $]^{-}0, 1^{+}[$. Hence, we consider the neutrosophic set which takes the value from the subset of $[0, 1]$ i.e; $0 \leq \mu_{\tau}(x) + \gamma_{\tau}(x) + \delta_{\tau}(x) \leq 3$ where μ_{τ} , γ_{τ} and δ_{τ} are called truth membership function, indeterminacy membership function and falsity function respectively. We denote the class of all neutrosophic sets on U by NS^U .

2.4 Definition

Let x be TrIVNN. Then its truth, indeterminacy and falsity MFs are given by

$$T_x(Z) = \begin{cases} \frac{(Z-a)t_x}{(b-a)} & a \leq z < b \\ t_x & b \leq z \leq c \\ \frac{(d-z)t_x}{(c-d)} & c < z \leq d \\ 0 & otherwise \end{cases}$$

$$I_x(Z) = \begin{cases} \frac{(b-z)(Z-a)i_x}{(b-a)} & a \leq z < b \\ i_x & b \leq z \leq c \\ \frac{(Z-c)(d-z)i_x}{(c-d)} & c < z \leq d \\ 0 & otherwise \end{cases}$$

$$F_x(Z) = \begin{cases} \frac{(b-z)(Z-a)f_x}{(b-a)} & a \leq z < b \\ f_x & b \leq z \leq c \\ \frac{(Z-c)(d-z)f_x}{(c-d)} & c < z \leq d \\ 0 & otherwise \end{cases}$$

where $0 \leq T_x(z) \leq 1, 0 \leq I_x(z) \leq 1$ and $0 \leq F_x(z) \leq 1$, also t_x, i_x, f_x are subset of $[0,1]$ and $0 \leq a \leq b \leq c \leq d \leq 1, 0 \leq \sup(t_x) + \sup(i_x) + \sup(f_x) \leq 3$; Then x is called an interval trapezoidal neutrosophic number $x = \{[a, b, c, d]; t_x, i_x, f_x\}$. We take $t_x = [\underline{t}, \bar{t}]$, $i_x = [\underline{i}, \bar{i}]$ and $f_x = [\underline{f}, \bar{f}]$.

2.5 Definition

Let U be a non empty set. Then an interval valued neutrosophic set (IVNS) Γ is an object having the form $\Gamma = \{(x, [inf\mu_{\tau}(x), sup\mu_{\tau}(x)], [inf\gamma_{\tau}(x), sup\gamma_{\tau}(x)], [inf\delta_{\tau}(x), sup\delta_{\tau}(x)]): x \in U\}$ where the functions $\mu_{\tau}, \gamma_{\tau}$ and $\delta_{\tau} : U \rightarrow \text{int}([0, 1])$ and $0 \leq sup\mu_{\tau}(x) + sup\gamma_{\tau}(x) + sup\delta_{\tau}(x) \leq 3$. We denote the class of all interval valued neutrosophic sets on U by $IVNSU$.

2.6 Definition

Let Φ, Π , be two interval neutrosophic sets on U . Then

- (a) Φ is called a subset of Π , denoted by $\Phi \subseteq \Pi$ if $inf\mu_{\Phi}(x) \leq inf\mu_{\Pi}(x), sup\mu_{\Phi}(x) \leq sup\mu_{\Pi}(x),$
 $inf\gamma_{\Phi}(x) \leq inf\gamma_{\Pi}(x), sup\gamma_{\Phi}(x) \leq sup\gamma_{\Pi}(x),$
 $inf\delta_{\Phi}(x) \leq inf\delta_{\Pi}(x), sup\delta_{\Phi}(x) \leq sup\delta_{\Pi}(x).$

- (b) The intersection of Φ and Π is denoted by $\Phi \cap \Pi$ and is defined by

$$\Phi \cap \Pi = \{([\min(\inf\mu_\Phi(x), \inf\mu_\Pi(x)), \min(\sup\mu_\Phi(x) \leq \sup\mu_\Pi(x))],$$

$$[\max(\inf\gamma_\Phi(x), \inf\gamma_\Pi(x)), \max(\sup\gamma_\Phi(x) \leq \sup\gamma_\Pi(x))],$$

$$[\max(\inf\delta_\Phi(x), \inf\delta_\Pi(x)), \max(\sup\delta_\Phi(x) \leq \sup\delta_\Pi(x))]): x \in U\}$$

(c) The union of Φ and Π is denoted by $\Phi \cup \Pi$ and is defined by

$$\Phi \cup \Pi = \{([\max(\inf\mu_\Phi(x), \inf\mu_\Pi(x)), \max(\sup\mu_\Phi(x) \leq \sup\mu_\Pi(x))],$$

$$[\min(\inf\gamma_\Phi(x), \inf\gamma_\Pi(x)), \min(\sup\gamma_\Phi(x) \leq \sup\gamma_\Pi(x))],$$

$$[\min(\inf\delta_\Phi(x), \inf\delta_\Pi(x)), \min(\sup\delta_\Phi(x) \leq \sup\delta_\Pi(x))]): x \in U\}$$

(d) The complement of Φ is denoted by Φ^c and is defined by

$$\Phi^c = \{(x, [\inf\delta_\tau(x), \sup\delta_\tau(x)][1 - \sup\gamma_\tau(x), 1 - \inf\gamma_\tau(x)], [\inf\mu_\tau(x), \sup\mu_\tau(x)]), x \in U\}$$

2.1 Ranking Technique for Trapezoidal Interval Valued Neutrosophic Numbers (TRIVNN)

Let $\tilde{\alpha}$ and \tilde{r} be two TrIVNNs, the ranking of $\tilde{\alpha}$ and \tilde{r} by score function and accuracy function is described as follows:

(i) if $s(\hat{r})^N < s(\hat{s})^N$ then $(\hat{r})^N < (\hat{s})^N$

(ii) if $s(\hat{r})^N \approx s(\hat{s})^N$

and if

(a) $a(\hat{s})^N < a(\hat{s})^N$ then $(\hat{s})^N < (\hat{s})^N$

(b) $a(\hat{r})^N > a(\hat{s})^N$ then $(\hat{s})^N > (\hat{s})^N$

(c) $a(\hat{r})^N \approx a(\hat{s})^N$ then $(\hat{s})^N \approx (\hat{s})^N$

2.2 Score Function of Trapezoidal Interval Valued Neutrosophic Number

Let $x = ([a, b, c, d]; [\underline{t}, \bar{t}], [\underline{i}, \bar{i}], [\underline{f}, \bar{f}])$ be a TrIVNN then its score function is defined by $S(x) = \frac{1}{16}(a + b + c + d)(2 + \underline{t} + \bar{t} - \underline{i} - \bar{i} - \underline{f} - \bar{f})$ and $S(x) \in [0, 1]$.-----(1)

Here we take $0 \leq a \leq b \leq c \leq d \leq 1$, t_x, i_x, f_x are subset of $[0, 1]$,

where $t_x = [\underline{t}, \bar{t}]$, $i_x = [\underline{i}, \bar{i}]$, and $f_x = [\underline{f}, \bar{f}]$

2.3 Accuracy Function of Trapezoidal Interval Valued Neutrosophic Number

Let $x = ([a, b, c, d]; [\underline{t}, \bar{t}], [\underline{i}, \bar{i}], [\underline{f}, \bar{f}])$ be a TrIVNN then its accuracy function is defined by $A_c(x) = \frac{1}{8}(c + d - a - b)(2 + \underline{t} - \bar{t} - \underline{f} - \bar{f})$ -----(2)

and $A_c(x) \in [0, 1]$. Here we take $0 \leq a \leq b \leq c \leq d \leq 1$ and t_x, i_x, f_x are subset of $[0, 1]$ where $t_x = [\underline{t}, \bar{t}]$, $i_x = [\underline{i}, \bar{i}]$, and $f_x = [\underline{f}, \bar{f}]$.

3. Shortest Cyclic Route Problem

Given a list of n cities $\{C_1, C_2, \dots, C_n\}$ and the associated distances between cities C_i and C_j , denoted by d_{ij} , the SCRP aims to find an ordering σ of $\{1, 2, \dots, n\}$ such that the tour cost, given by $c = \sum_{i=1}^{n-1} d_{\sigma(i), \sigma(i+1)} + d_{\sigma(n), \sigma(1)}$ is minimized. For the Euclidean SCRP, for instance, $d_{ij} = \|x_i - x_j\|_2$, where $x_i \in \mathbb{R}^d$ is the position of C_i . In general, however, the distance matrix $D = (d_{ij})$ does not have to be symmetric. The ordering σ can be represented as a unique permutation matrix P . Note, however, that due to the underlying cyclic symmetry, multiple orderings – corresponding to different permutation matrices – have the same cost.

SCRP can be classified into the following categories:

- (i) **Symmetric Shortest Cycle Route Problem (S - SCRP):** Let $V = v_1, v_2, \dots, v_n$ be a set of cities, $A = (p, q) : p, q \in V$ be the set of edges, and $d_{pq} = d_{qp}$ be a cost measure associated with the edge $(p, q) \in A$ which is symmetric. The s-TSP is the problem of finding then, a minimal length closed tour that visits each city once. In this case cities $v_i \in V$ are given by their coordinates (x_i, y_i) and d_r 's is the Euclidean distance between r and s then we have an Euclidean TSP.
- (ii) **Asymmetric Shortest Cycle Route Problem (A - SCRP):** From the above definition, if the cost measure $d_{pq} \neq d_{qp}$ for at least one (p, q) then the TSP becomes a SCRP.
- (iii) **Multiple Shortest Cycle Route Problem (M - SCRP):** Given a set of nodes, let there be m salesmen located at a single depot node. The remaining nodes (cities) that are to be visited are intermediate nodes. Then, the m SCRP consists of finding tours for all m salesmen, who all start and end at the same depot, such that each intermediate node is visited exactly once and the total cost of visiting all nodes is minimized.

3.1 Procedure for Framing The Reduced Matrix

This Method is similar to Branch and Bound method used for solving SCRP. This strategy can be compared to the Branch and Bound method. Here, in this method, the matrix reduction approach is used to determine the path's cost and the constraint. The presumptions for a reduced matrix are listed below:

- A particular row or column of the cost adjacency matrix is said to be reduced iff it contains at least one zero element and all remaining entries in that row or column ≥ 0 .
- The overall matrix is said to be reduced if all the rows and columns are reduced.
- Latest Tour length (new) = Previous Tour length - Total value reduced.
- All diagonal entries are replaced from 0 to Infinity in the original cost adjacency matrix.

The fundamental concept underlying to find the solution of the problem: The smallest possible cost for the travelling salesman problem is used as the cost to reduce the matrix initially. Now, at each step, we need to determine the minimum possible cost if that path is taken, i.e., a path from vertex u to v is followed.

We may achieve this by replacing the costs for the u^{th} row and v^{th} column with *infinity*, further lowering the matrix, and then adding the previously determined minimal path cost by the additional costs for reduction and cost of edge (u, v) . When at least one path has been identified, its cost is employed as the upper bound of cost to apply the branch and bound strategy to the other routes. The upper bound is revised consequently when a path with lower cost is found. Follow the illustration below for a better understanding.

3.1 Algorithm for Reduced Matrix Method

Convert the interval valued neutrosophic cost to crisp by using the score function. The processes required to carry out the above method are outlined below:

Step 1: Create a class termed as "Node" in step one that can contain the reduced matrix, cost, the current city's number, level (the total number of cities visited), and the path taken up to this point.

Step 2: Construct a queue based on priority to store the live nodes with the minimum cost at the top.

Step 3: Reduce the matrix after setting the start index's level to 0. By first lowering the row, then the column, determine the cost of the provided matrix. The price is determined in the manner described below:

Row reduction - identify and retain the minimum value for each row. After identifying the minimum element in each row subtract it from every single component in that particular row.

Column reduction - identify and save the minimum value for each column. Take the minimum element from each column and deduct it from all the other components in that particular column. The matrix has now been shrunk. In order to determine the cost, add all the minimal components to the row and column you already identified.

Step 4: Insert the element into the Priority Queue with all the data that Node needs.

Step 5: Continue the actions listed below until the priority queue is emptied.

- Eliminate the element with the minimum value from the priority queue.
- Verify that the level of the current node matches the number of nodes/cities for each pop operation.
- If so, print the path and provide the lowest cost.
- If the response is no, proceed to employ the formula to determine the cost for each and every child node of the current node.
- $\text{Child Cost} = \text{Parent_matrix_cost} + \text{Cost_from_parent to child} + \text{Child_reduced Matrix_cost}$
- It is possible to determine the cost of a reduced matrix by setting all of its row and column values to infinity and setting the index $\text{Matrix}[\text{Col}][\text{row}] = \text{infinity}$.
- After that, reorder the priority queue to include the current node.

Step 6: Continue Step 5 until we do not reach the level equal to Number of nodes minus 1.

4. Numerical Example

Consider the shortest cycle route problem with 4 nodes. The cost functions are given as Interval Valued Neutrosophic Fuzzy Shortest Cycle Route Problem.

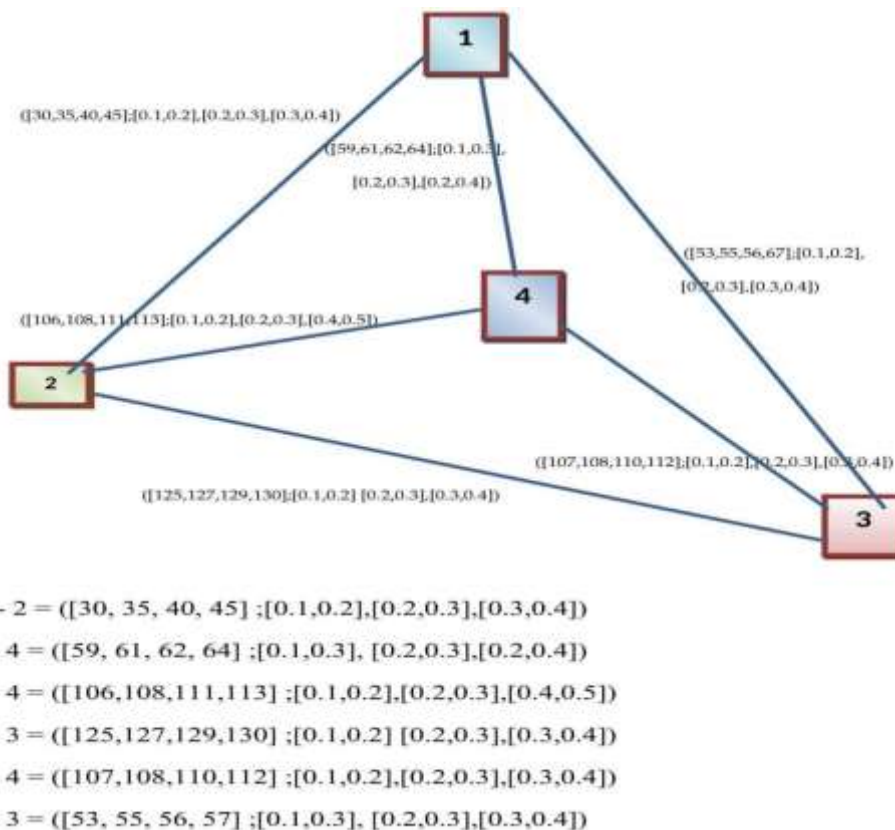


Figure 1: Interval Valued **Neutrosophic** Fuzzy Shortest Cycle Route Problem.

Defuzzifying the score function using (1), $S(x) = \frac{1}{16} (a + b + c + d) (2 + \underline{t} + \bar{t} - \underline{i} - \bar{i} - \underline{f} - \bar{f})$

$$1 \leftrightarrow 2 = ([30, 35, 40, 45]; [0.1, 0.2], [0.2, 0.3], [0.3, 0.4])$$

$$\begin{aligned}
 &= \frac{1}{16} (30 + 35 + 40 + 45) (2 + 0.1 + 0.2 - 0.2 - 0.3 - 0.3 - 0.4) \\
 &= \frac{1}{16} (150) (1.1) = 10.3 \approx 10.
 \end{aligned}$$

$$1 \leftrightarrow 4 = ([59, 61, 62, 64]; [0.1, 0.3], [0.2, 0.3], [0.2, 0.4])$$

$$\begin{aligned}
 &= \frac{1}{16} (59 + 61 + 62 + 64) (2 + 0.1 + 0.3 - 0.2 - 0.3 - 0.2 - 0.4) \\
 &= \frac{1}{16} (246) (1.3) = 19.98 \approx 20,
 \end{aligned}$$

Proceeding like this, we can defuzzify all the cost values by above score function.

$$1 \leftrightarrow 3 = 15.19 \approx 15,$$

$$2 \leftrightarrow 4 = 24.6 \approx 25,$$

$$2 \leftrightarrow 3 = 35.13 \approx 35,$$

$$3 \leftrightarrow 4 = 30.04 \approx 30.$$

The cost matrix of the given shortest cycle route problem is given below,

Table 1: Cost Matrix after Defuzzifying

ROW/COLUMN	N1	N 2	N 3	N 4
N 1	∞	10	15	20
N 2	10	∞	35	25
N 3	15	35	∞	30
N 4	20	25	30	∞

The row minimum for the corresponding rows is given as $R_1 \rightarrow 10, R_2 \rightarrow 10, R_3 \rightarrow 15, R_4 \rightarrow 20$. After reducing the corresponding elements from each row, the outcome is given below.

Table 2: Row Deduction

ROW/COLUMN	N1	N 2	N 3	N 4
N 1	∞	0	5	10
N 2	0	∞	25	15
N 3	0	20	∞	15
N 4	0	5	10	∞

The column minimum for the corresponding column is $C_1 \rightarrow 10, C_2 \rightarrow 0, C_3 \rightarrow 5, C_4 \rightarrow 10$. After reducing the corresponding elements from each column, the outcome is given below. After row and column reduction the matrix will be:

Table 3: Column Reduction

ROW/COLUMN	N1	N 2	N 3	N 4
N 1	∞	0	0	0
N 2	0	∞	20	5
N 3	0	20	∞	5

N 4	0	5	5	∞
------------	---	---	---	----------

So the cost reduction of the matrix is $(10 + 10 + 15 + 20 + 5 + 10) = 70$. Now let us consider movement from 1 to 2. Initially after substituting the 1st row and 2nd column to infinity, the matrix will be:

Table 4: Cost Matrix- movement from 1 to 2

ROW/COLUMN	N1	N 2	N 3	N 4
N 1	∞	∞	∞	∞
N 2	∞	∞	20	5
N 3	0	∞	∞	5
N 4	0	∞	5	∞

The row minimum for the corresponding rows are given as, $R_2 \rightarrow 5$, $R_3 \rightarrow 0$, $R_4 \rightarrow 0$. After reducing the corresponding elements from each row, the outcome is given below.

Table 5: Cost Matrix after row reduction

ROW/COLUMN	N1	N 2	N 3	N 4
N 1	∞	∞	∞	∞
N 2	∞	∞	15	0
N 3	0	∞	∞	5
N 4	0	∞	5	∞

and the column minimum will be 0, 5, 0. The column minimum for the corresponding column is $C_2 \rightarrow 0$, $C_3 \rightarrow 0$, $C_4 \rightarrow 0$. After reducing the corresponding elements from each column, the outcome is given below. After row and column reduction the matrix will be

Table 6: Cost Matrix after Column reduction

ROW/COLUMN		N1	N 2	N 3	N 4
N 1		∞	∞	∞	∞

N 2	∞	∞	10	0
N 3	0	∞	∞	5
N 4	0	∞	0	∞

So the cost reduction of the matrix is $70 + \text{cost}(1, 2) + 5 + 5 = 70 + 0 + 5 + 5 = 80$. Keep performing this until the traverse is finished, and then calculate the least expensive route. The optimal path is given by $1 - 2 - 4 - 3 - 1$.

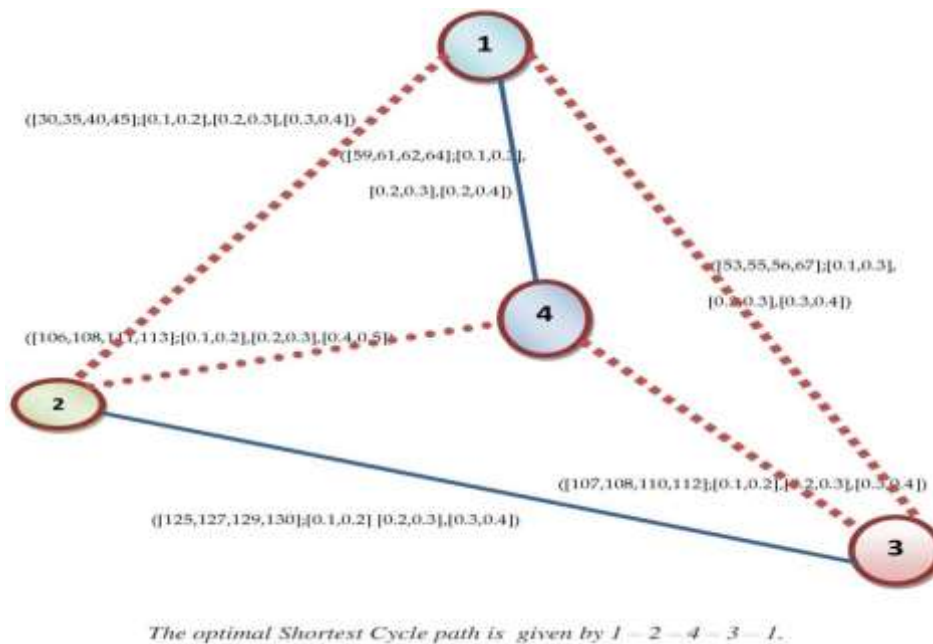
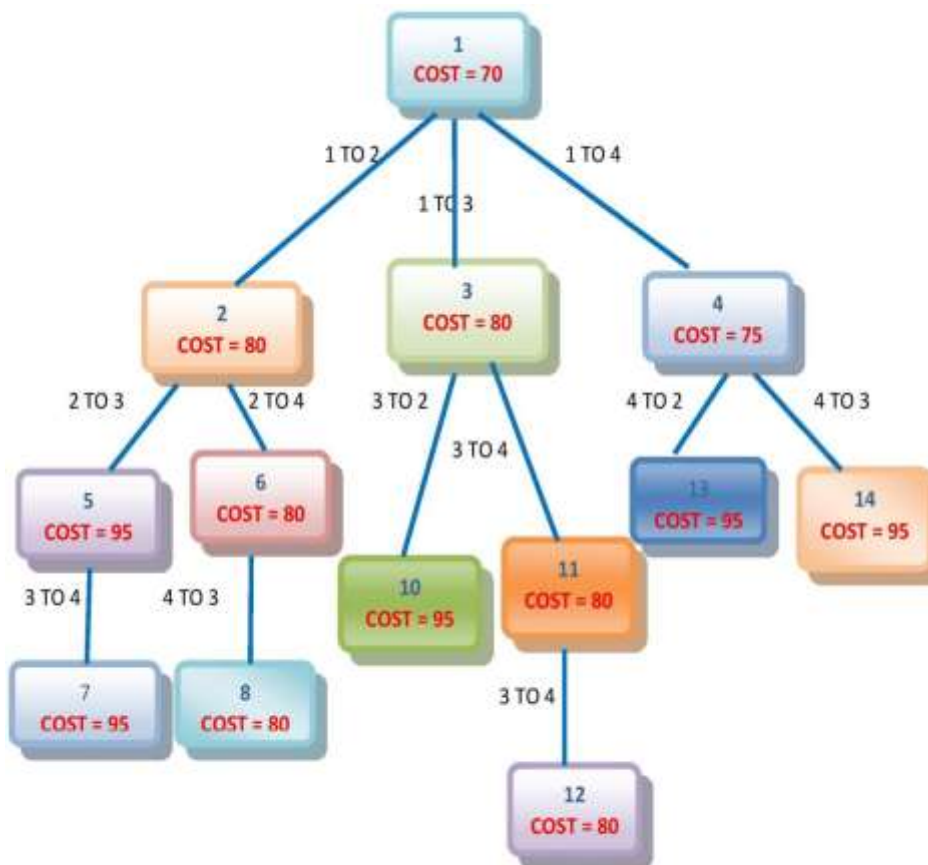


Figure 2: Optimal Path

The recursion tree method is a visual representation of an iteration method that is in the form of a tree where at each level nodes are expanded. In general, we consider the second term in recurrence as root. 3. It is useful when the divide & conquer algorithm is used. Sometimes it's hard to make an accurate prediction. Each root and child of a recursion tree indicates the cost of a single sub problem. We add the costs for each level of the tree to get a list of pre-level costs, which we then add together to get the total cost for all recursive levels. The Substitution Method should be used to obtain a solid guess from a recursive tree. Initially we'll examine node 1 with the objective to create a state-space tree. As seen in the diagram below, we can travel from node 1 to nodes 2, 3, or 4 respectively. The cost of node 1 would be the cost of 70, which is what we were able to achieve in the above-reduced matrix. The upper bound is kept in this case as well. The upper bound started out as infinite. The boundaries and the framework of the recursion tree is provided below,



Structure of the recursion tree along with the bounds

Figure 3: Framework of the Recursion Tree

The Time Complexity and various space complexity of SCRП using various algorithms are presented below.

Table 7: Time Complexity and various Space Complexity

	Greedy Approach	Dynamic Programming	Back Tracking	Reduced Matrix
Time Complexity	$O(n^2 * \log_2 n)$	$O(n^2 * 2^n)$	$O(n!)$	$O(2^n * n^2)$
Auxiliary Space	$O(n)$	$O(n * 2^n)$	$O(n)$	$O(n^2)$

5. Conclusion

This attempt investigates an Interval Valued Neutrosophic Fuzzy SCRП. The results show that the suggested procedures can successfully dismantle the Interval Valued Neutrosophic Fuzzy. This plan is simple to understand and provides a methodical approach to dissecting SCRП. The least expensive optimal path is found and a recursion tree is drawn based on the results obtained by traversing the path. This method is more efficient since the time complexity is given by $O(2^N * N^2)$ and Space complexity is given by $O(N^2)$ where N = number of nodes / City. Many Heuristic methods can be tested by utilizing under this fuzzy environment. Numerous real-world applications, Applications of SCRП includes proper deployment of cloud computing resources, optimal path search for transportation, computational modeling of proteins, microchip production, X-ray crystallography, scheduling the resources, and recently SCRП can be implemented in drone routing, all involve combinatorial optimization problems.

References

- [1] Kumar, A., Gupta, A., "Assignment and Travelling Salesman Problems with Coefficients as LR Fuzzy Parameters", *International Journal of Applied Science and Engineering*, vol. 10, no. 3, pp. 155-170, 2012. [https://doi.org/10.6703/IJASE.2012.10\(3\).155](https://doi.org/10.6703/IJASE.2012.10(3).155)
- [2] Angelo. P.P., "Optimization in an intuitionistic fuzzy environment". *Fuzzy Sets and Systems*, Vol.86, pp.299-306, 1997. [https://doi.org/10.1016/S0165-0114\(96\)00009-7](https://doi.org/10.1016/S0165-0114(96)00009-7)
- [3] Atanassov, K. T., Gargov, G., "Interval valued intuitionistic fuzzy sets," *Fuzzy Sets and Systems*, Vol. 31, No. 3, pp. 343–349.1989. [https://doi.org/10.1016/0165-0114\(89\)90205-4](https://doi.org/10.1016/0165-0114(89)90205-4)
- [4] Atanassov. K. T, "Intuitionistic fuzzy sets," *Fuzzy Sets and Systems* ", 1986,Vol. 20, No. 1, pp. 87–96,1986. [https://doi.org/10.1016/S0165-0114\(86\)80034-3](https://doi.org/10.1016/S0165-0114(86)80034-3)
- [5] Biswas, B., Mitra, A., Sengupta. S., " A Study of Travelling Salesman Problem using Reinforcement Learning Over Genetic Algorithm", *Turkish Journal of Computer and Mathematics Education* ,Vol.11, No.02 pp.963-981, 2020.
- [6] Biswas, P., Pramanik, S., and Giri.C., "Aggregation of triangular fuzzy neutrosophic set information and its application to multi attribute decision making," *Neutrosophic Sets and Systems*, vol. 12, No.1,pp. 20–40,2016. https://digitalrepository.unm.edu/nss_journal/vol12/iss1/4
- [7] Broumi, S., Nagarajan, D., and Bakali. A., "The shortest path problem in interval valued trapezoidal and triangular neutrosophic environment", *Complex Intell. Syst.* Vol.5, pp. 391–402.2019. <https://doi.org/10.1007/s40747-019-0092-5>
- [8] Broumi, S., Bakali,A., Talea, M., Smarandache, F., and Vladareanu, L., "Shortest path problem under triangular fuzzy neutrosophic information", in Proceedings of the 2016, 10th *International Conference on Software, Knowledge, Information Management & Applications (SKIMA)*, Chengdu, China.2016.
- [9] Dantzig, G. B., Fulkerson, D. R., and Johnson, S.M., "Solution of a large- scale traveling salesman problem", *Operations Research*, vol. 2, pp. 393-410, 1954.
- [10] Dhoub, S., "Optimization of travelling salesman problem on single valued triangular neutrosophic number using dhoubmatrix-TSPI heuristic", *International Journal of Engineering*, Vol. 34, No. 12, pp. 1–6, 2021. <https://doi.org/10.5829/ije.2021.34.12C.09>.
- [11] Hadi Basirzadeh., "Ones Assignment Method for Solving Traveling Salesman Problem", *Journal of mathematics and computer science*, Vol.10, pp.258-265, 2014.
- [12] Hitchcock, F. L., "The distribution of a product from several sources to numerous localities", *Journal of mathematics and physics*, Vol.20 (1-4), pp.224-230, 1941. <http://dx.doi.org/10.1002/sapm1941201224>
- [13] Jeyalakshmi, K., and Prabha, S. K., "Unraveling Type-3 Fuzzy Shortest Cycle Route Problem By RMM", *Journal Of Critical Reviews*,Vol. 7,No. 15, pp.4854-4858, 2020.
- [14] Karaaslan, F., and Hayat, K., "Some new operations on single valued neutrosophic matrices and their applications in multicriteria group decision making," *Applied Intelligence*, Vol. 48, No. 12, pp. 4594–4614.2018. <https://doi.org/10.1007/s10489-018-1226-y>
- [15] Kumar, N., Karambir and Rajiv Kumar., "A study of genetic algorithm approach to study travelling salesman problem", *Journal of Global Research in Computer Science*, Vol. 3, 3,pp.33-37, 2012.
- [16] Nirmala, G., and Anju, R., "Travelling Salesman Problem (SCR) Using Fuzzy Quantifier", *International Journal of Science and Research* ,Vol.3, No.12, pp.184-186, 2012. www.ijsr.net/archive/v3i12/U1VCMTQxNjI=.pdf
- [17] Oliver, I.M., Smith, D.J., and Holland, J.R.C., "A Study of Permutation Crossover Operators on the Travelling Salesman Problem". In J.J. Grefenstette (ed.). *Genetic Algorithms and Their Applications: Proceedings of the 2nd International Conference on Genetic Algorithms*. Lawrence Erlbaum Associates, Hilladale, NJ, 1987.
- [18] Pramanik, S., Dey, P.P., "Multi-level linear programming problem with neutrosophic numbers: a goal programming strategy", *Neutrosophic Sets Syst*, 29:242–254, 2020. https://digitalrepository.unm.edu/nss_journal/vol29/iss1/19
- [19] Sudha. S, Nivetha Martin, M. Clement Joe Anand, P. G. Palanimani,T. Thirunamakkani, B. Ranjitha. "MACBETH-MAIRCA Plithogenic Decision-Making on Feasible Strategies of Extended Producer's Responsibility towards Environmental Sustainability." *International Journal of Neutrosophic Science*, Vol. 22, No. 2, 2023 ,PP. 114-130.
- [20] Saini, R.K., and Sangal, A.,"Application of single valued trapezoidal neutrosophic numbers in transportation problem",*Neutrosophic Sets and System*, Vol.35,pp.563583,2020.https://digitalrepository.unm.edu/nss_journal/vol35/iss1/33

- [21] Saloni Gupta, Poonam Panwar., “Solving Travelling Salesman Problem Using Genetic Algorithm”, *International Journal of Advanced Research in Computer Science and Software Engineering* , Volume 3, No. 6, pp.376-380, June 2013.
- [22] Shweta, R., and Saurabh Ranjan. S., “Solving Travelling Salesman Problem Using Improved Genetic Algorithm”, *Indian Journal of Science and Technology*, Vol.10, No.30, pp.1-6, 2017. 10.17485/ijst/2017/v10i30/115512
- [23] Sikkannan, K.P., Vimala. S., “Unraveling neutrosophic transportation problem using costs mean and Complete contingency cost table,” *Neutrosophic Sets and Systems*, vol. 29, pp. 165–173, 2019. https://digitalrepository.unm.edu/nss_journal/vol29/iss1/13
- [24] Singh, A., Kumar. A., and Appadoo. S. S., “Modified approach for optimization of real life transportation problem in neutrosophic environment,” *Mathematical Problems in Engineering*, Article ID 2139791, pp.1-10, pages, 2017. <https://doi.org/10.1155/2017/2139791>
- [25] Smarandache, F., “A Unifying Field in Logics: Neutrosophic Logic. Neutrosophy, Neutrosophic Set”, *Neutrosophic Probability and Statistics*, InfoLearnQuest, Philadelphia, PA, USA ,6th edition.2007. https://digitalrepository.unm.edu/math_fsp/163/
- [26] Sudhakar, V.J., Navaneetha Kumar, V., “A New Approach to Solve the Classical Symmetric Shortest Cyclic Route Problem by Zero Suffix Method”, *Int. J. Contemp. Math. Sciences*, Vol. 6, no. 23, pp. 1111 – 1120, 2011.
- [27] Zadeh, L.A., “Fuzzy sets as a basis for a theory of possibility”, *Fuzzy sets and systems*, Vol.1, No.1, pp. 3-28, 1978. [https://doi.org/10.1016/0165-0114\(78\)90029-5](https://doi.org/10.1016/0165-0114(78)90029-5)
- [28] Zadeh. L.A., “Fuzzy sets”, *Information and Computation*”, vol. 8, pp. 338–353, 1965. [http://dx.doi.org/10.1016/S0019-9958\(65\)90241-X](http://dx.doi.org/10.1016/S0019-9958(65)90241-X)
- [29] Manshath, E., Kungumaraj, E., Lathanayagam, M. C. Joe Anand, Nivetha Martin, Elangovan Muniyandy, S. Indrakumar. "Neutrosophic Integrals by Reduction Formula and Partial Fraction Methods for Indefinite Integrals." *International Journal of Neutrosophic Science*, Vol. 23, No. 1, 2024 ,PP. 08-16.
- [30] Rajesh, Sharmila Rathod, Jyoti Kundale, Nilesh Rathod, M. Clement Joe Anand, Utpal Saikia, Mohit Tiwari, Nivetha Martin. "A Study on Interval Valued Temporal Neutrosophic Fuzzy Sets." *International Journal of Neutrosophic Science*, Vol. 23, No. 1, 2024 ,PP. 341-349.
- [31] Broumi, S., Mohanaselvi, S., Witczak, T., Talea, M., Bakali, A., & Smarandache, F. (2023). Complex fermatean neutrosophic graph and application to decision making. *Decision Making: Applications in Management and Engineering*, 6(1), 474-501.
- [32] Broumi, S., Raut, P. K., & Behera, S. P. (2023). Solving shortest path problems using an ant colony algorithm with triangular neutrosophic arc weights. *International Journal of Neutrosophic Science*, 20(4), 128-28.
- [33] Bharatraj J., Clement Joe Anand, M., “Power harmonic weighted aggregation operator on single-valued trapezoidal neutrosophic numbers and interval-valued neutrosophic sets”. In: *Fuzzy Multi-criteria Decision-Making Using Neutrosophic Sets*. Springer International Publishing, Cham, pp. 45–62, 2019.
- [34] Clement Joe Anand M, Janani Bharatraj, “Interval-Valued Neutrosophic Numbers with WASPAS”. In: Kahraman, C., Otay, İ. (eds) *Fuzzy Multi-criteria Decision-Making Using Neutrosophic Sets*. *Studies in Fuzziness and Soft Computing*, Springer, Cham, pp.435-453, 2019

MHD WILLIAMSON HYBRID NANOFUID FLOW WITH CATTANEO-CHRISTOV FLUX MODEL

Kankanala Sharada

Assistant Professor, Department of Mathematics
Chaitanya Bharathi Institute of Technology(A),
Kokapet(V), Gandipet(M), Hyderabad-500075, Telangana, India
kankan.sharada@gmail.com

Acceptance Date: 25 Oct 2023

Published date: 30 Dec 2023

Abstract

In this research, the numerical simulation of the Williamson hybrid nanofluid's MHD heat and mass transfer flow over a porous stretched sheet with Cattaneo-Christov heat and mass flux was found. The underlying physics of the situation are modelled by governing equations. After applying a suitable similarity transformation, these equations were converted into an ODE system and solved numerically using MATLAB and the BVP4C tool. The study's findings indicate that while raising the mass relaxation flux raises concentration distributions, increasing the heat relaxation flow raises temperature. To improve temperature and velocity distributions, an additional value of thermal radiation, heat generation, and Eckert number were observed. Due to the imposed electromagnetic force, a higher value of the magnetic field is observed. Also, the enhance in the thermal radiation parameter is observed to increase the velocity and temperature distributions. This research benefits from biomedical engineering, biological sciences, astrophysics, and geophysics.

Keywords: Williamson fluid, MHD, velocity, temperature, concentration.

1. Introduction

Numerous scholars have examined the connection between heat transmission and viscous dissipation and thermal radiation. Thermal radiation and viscous dissipation are used in underground storage systems and in the extraction of geothermal energy. Thermal radiation is highly important in satellites, nuclear power plants, gas turbines, and the alteration of high temperature energy processes. This fluid was subjected to Chemical reaction and ionizing radiation by Kataria et al (2016). Electricity was used to illuminate the Soret-Dufour mechanism, the MHD buoyancy force, and dissipative viscous significance in a conducting fluid. Analysis of radiation's impact on stagnation flow with second order slip and melting heat transfer was carried out by Hayat et al [2017]. Ahmed Alsaedi et al [2017] investigated the possibility of radiative flow because of a circulating disk with different thicknesses. An investigation of the effect of joule heating along with viscous dissipation and magnetic field on Power-law fluid was conducted by Motahar Reza et al [2022]. A colloidal nanoparticle suspension in a base fluid was first developed by Chaio [1995] as a mixture of chemical nanoparticles such as nitride-AiN, metals-Al, nonmetals-Graphite, oxide ceramics, and metal carbides-SiC. There are numerous uses for nanofluids in cancer therapy; industrial cooling; biomedical engineering; biological science; and the solar sector. Murthy et al [2016] studied boundary layer motion of Williamson nanofluid in the passable region using MHD boundary layer motion. Hashim et al [2020] was studied by the Williamson fluid flow time is dependent on a heated surface. Reddy et al [2018] address the impacts of radiation and warm

dissemination on MHD heat move stream of a dusty viscoelastic liquid between two moving equal plates. Synthetic response impact on MHD stream of Casson liquid with permeable extending sheet concentrated by Makinde et al [2018]. Krishna et al [2018] showed the mathematical arrangements of precarious MHD stream heat move over an extending surface with pull or infusion. Reddy et al [2018] thoroughly searched in the impacts of radiation and Soret on a shaky progression of a Casson liquid through permeable vertical channel with development and constriction. Warm radiation and compound response consequences for MHD stream along a moving vertical permeable plate was investigated by Sreedevi et al [2017]. Many researchers [Sharada and Shankar 2015, Dulal Pal and Gopinath Mandal 2021, Sugunamma et al. 2022, Surya kanta Mondal and Dulal Pal 2022, Kankanala Sharada 2022, Sudarshan Reddy et al. 2022, Vishvambhar S. Patil et al. 2022, K Sharada and B Shankar 2017, Reddy et al. 2014, S Jagadha et al. 2021] have studied and analysed the solution of MHD flows on radiation and chemical reaction effects of the Newtonian and non-Newtonian fluid flows. Using non-isothermal and non-isosolutal limitations, Dawar et al [2021] studied convective flow over a cone and wedge of Williamson nanofluid. The influence of thermal radiation on nanofluid mixed convective flow on an inclined wavy surface was studied by Srinivasacharya et al [2018]. Chemically reacting nanofluid convective flow via mobile or stationary vertical plate was the subject of research by Gireesha et al [2016]. The effect of a constant heat source/sink on the convective nonlinear flow of nano Oldroyd-B fluid over a stretchy surface was examined by Ganesh kumar et al [2018]. Ahmad Farooq et al [2021] investigated the flow of a stretchy sheet of Maxwell viscoelastic MHD nanofluid. Nadeem et al [2021] studied the effects of natural convection motion and heat transfer in two upright plates on fuzzy nano-hybrid fluids. Idowu et al [2020a] studied the simultaneous motion of Casson-Walters-B fluid over a vertical porous plate by altering thermal conductivity and viscosity.

The MHD Falkner-Skan-Sutter by nanofluid was studied using the nanofluid model and the Cattaneo-Christov heat flux theory by Khan et al [2020]. Williamson hybrid engine oil nanofluids and Cattaneo-Christov heat flux. The MHD Casson-Ferro fluid's heat radiative transport was modelled numerically by Ali et al [2017]. Zhang Yan et al [2021] investigated the melting heat reaction in a von Karman circulating motion of hybrid nanofluids by employing a Cattaneo-Christov heat flux. The Cattaneo-Christov model and a chemical process on an exponentially stretchable surface were used by Hayat Tanzila et al [2018] to address the motion of 3D Eyring-Powell. The Cattaneo-Christov model was used to investigate the flow of Carreau fluid across a thin sheet of material. The Cattaneo-model Christov's was used in the work to connect viscoelastic fluid flow with heat transport processes by Shihao Han et al [2014].

The magnetic and electric field-induced flow of highly conducting fluids is explained by MHD. Astrophysicists and geophysicists use a variety of techniques to study astrophysics, geophysics, MHD power generation, and heat exchanger design. A large number of researchers have investigated MHD flows on non-Newtonian fluids over stretched surfaces. Plasma research, flowmeters, aerodynamics, and solar energy devices are examples of MHD processes. As a result of the wide range of MHD applications, the studies listed below have documented the flow phenomena associated with MHD. Falodun et al [2016] evaluated the flow of a chemically reactive fluid past a half infinite upright plate with heat radiation and Soret-Dufour significance was studied. Multiple slides on the relevance of MHD and the non-Newtonian flow of nanofluids across a stretchable cylinder were explored by Khan et al [2018]. Mishra Satya Ranjan et al [2018] investigated the dissipation relevance of Casson

fluid's MH stagnation-point motion past a stretchy sheet. MHD mass transport via a slanting plate with thermophoresis, a non-constant heat source/sink, chemical reaction, and Soret-Dufour significance was studied by Mondal et al [2018]. Ramzan et al [2021] used heat transport analysis across a stretchy sheet with thermal and velocity slip limitations to investigate MHD hybrid nanofluids with heat transport. Omowaye et al [2018] elucidated the MHD flow of viscosity-elastic fluid past an accelerating penetrable surface. Reddy et al [2016] studied Soret-Dufour effects on MHD convective flow of Al_2O_3 -water and TiO_2 -water nanofluids past a stretching sheet. Rashidi et al [2022] did an extensive survey of energy examination of shell and tube heat exchangers. Farooq Umar et al [2022] as of late analysed the calculation of nonlinear warm radiation in magnetized nanofluid stream with entropy age. Bhatti et al [2022] concentrated on normal convection non-Newtonian EMHD dissipative flow through a microchannel containing a non-Darcy porous medium utilizing the homotopy method technique. Therefore, mentioned above authors show that Cattaneo-Christov models are used to study magnetohydrodynamic with a distinct approach. To the absolute best of our insight, no concentrate in the writing has considered MHD intensity and mass exchange stream of Williamson Half and half nanofluids over a permeable extending sheet with Cattaneo-Christov hypotheses. Subsequently, this paper zeroed in on intensity and mass exchange on Williamson mixture nanofluid stream by means of an extending penetrable surface with attractive and electromagnetic powers. This paper investigated the exploration on crossover nanofluid stream by means of an extended sheet by inspecting Cattaneo-Christov models and the Soret-Dufour system, as well as MHD Williamson stream by taking both attractive field and electromagnetic power importance on stream course into account. Tables and charts are utilized to delineate the effect of stream boundaries on speed, temperature, and fixation in a way that is straightforward. For instance, MHD gas pedals, biomedical and cell research, heat exchangers, and subsurface stockpiling gadgets all advantage from the discoveries of this review.

2. Mathematical analysis

This work considers a 2-D free convective flow of MHD Williamson hybrid nanofluids that is laminar and incompressible, passing through a stretched sheet that is saturated in the passable zone. In Figure 1 treats the x -axis along the stretching surface, while the y -axis is evaluated at the surface. In order to coordinate the electric current, a uniform Magnetization B_0 is forced while Magnetic force is applied to the stretched surface. According to the earliest research, the magnetism is unaffected by the produced magnetic field. The stretching surface is kept at a constant temperature (T_w) and concentration (C_w). Both the temperature T_∞ and concentration C_∞ are far away from the plate. A state of thermal equilibrium is maintained because no slip considerations exist. The water-based nanofluids are considered to have nonlinear viscous dissipative effects. Estimates of radiative heat flux are made using the Rosseland approximation Soret-Dufour mechanisms are also significant because of the high concentrations of the compounds.

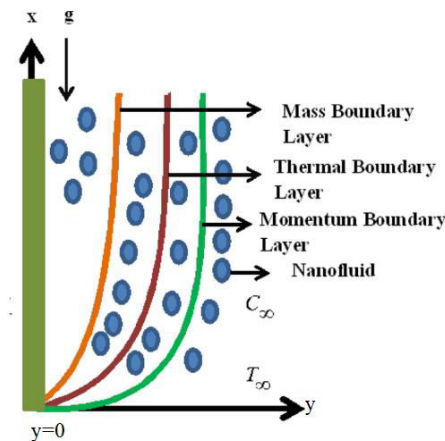


Figure-1: The physical model of the problem.

In view of the assumptions, the governing equations are designed as follows.

$$u_x + v_y = 0 \quad (1)$$

$$uu_x + vv_y = \frac{\mu_{nf}}{\rho_{nf}} u_{yy} + \sqrt{2}\Gamma u_y u_{yy} - \frac{\sigma_{nf}}{\rho_{nf}} B_0^2 u - \frac{\sigma_{nf}}{\rho_{nf}} E_0 B_0 - \frac{\mu_{nf}}{\rho_{nf}} \frac{u}{K} \quad (2)$$

$$uT_x + vT_y = \left[\alpha_{nf} T_{yy} - \frac{1}{(\rho C_p)_{nf}} q_{ry} + \frac{\mu_{nf}}{(\rho C_p)_{nf}} \left[u_y + \frac{\Gamma}{\sqrt{2}} u_y^2 \right] + \frac{1}{(\rho C_p)_{nf}} q''' + \frac{D_C}{(\rho C_p)_{nf}} C_{yy} \right] + \frac{\sigma B_0^2}{(\rho C_p)_{nf}} u^2 - \lambda_1 \{ uu_x T_x + vv_y T_y + uv_x T_y + v^2 T_{yy} + vu_y T_x + 2uv T_{xy} + u^2 T_{xx} \} \quad (3)$$

$$uC_x + vC_y = \left[D_M C_{yy} + D_T T_{yy} - Kr^*(C - C_\infty) - \lambda_2 \left\{ uu_x C_x + vv_y C_y + uv_x C_y + v^2 C_{yy} + vu_y C_x + 2uv C_{xy} + u^2 C_{xx} \right\} \right] \quad (4)$$

The appropriate boundary conditions for the model under consideration are given by:

$$u = bx, v = 0, T = T_w, C = C_w \quad \text{at} \quad y = 0 \quad (5)$$

$$u \rightarrow 0, T \rightarrow T_\infty, C \rightarrow C_\infty \quad \text{as} \quad y \rightarrow \infty$$

u and v are velocity features along x and y direction. b is stretching rate, C is concentration of the fluid, T is temperature of the fluid, Kr^* is chemical rate of reaction, σ is electrical conductivity, ρ_{nf} is the density of nanofluid, α_{nf} is the thermal diffusivity of nanofluid, μ_{nf} is dynamic viscosity of nanofluid, K is permeability parameter, D_M is diffusivity of species, (ρC_p) is heat capacitance of nanofluid, D_T indicates mass flux in temperature gradient, D_C indicates heat flux in concentration gradient.

The stretching sheet stretches on its plane with surface velocity $U(x) = bx$ where b is stretching rate considered to be positive constant.

In the view of the Rosseland approximation q_r is defined as

$$q_r = - \left(\frac{4\sigma^*}{3k_{nf}} \right) \left(\frac{\partial T^4}{\partial y} \right) \quad (6)$$

where σ^* stands for the Stefan-Boltzmann constant and k_{nf} is the coefficient of mean absorption. Under the above assumptions that the variation of temperature is low between the layers, the following relationship is used

$$T^4 \cong 4T_2^3 T - 3T_2^4 \quad (7)$$

The non-uniform heat Source or Sink

$$q''' = \frac{k_{nf}}{\nu_f} a [A(T_w - T_\infty) f' + (T - T_\infty) B] \quad (8)$$

The similarity transformations considered for the problem are:

$$\eta = \sqrt{(b/\nu_f)}, \psi = \sqrt{(b\nu_f)} xf(\eta), u = bxf'(\eta), v = -\sqrt{b\nu_f} f(\eta) \quad (9)$$

$$\zeta(\eta) = \frac{T - T_\infty}{T_w - T_\infty}, \varpi(\eta) = \frac{C - C_\infty}{C_w - C_\infty}$$

Employing the Equations (7-10) on the governing Equations (1-4), subjected to the boundary conditions (5):

$$f''' + K_1 K_2 \left[ff'' - f'^2 - \frac{M}{K_2} f' + E_0 M \right] - A_1 f' + We f'' f''' = 0 \quad (11)$$

$$\left(1 + \frac{4}{3} R \right) \zeta'' + Pr \frac{K_3}{K_5} \left[f \zeta' - 2 f' \zeta + \frac{Ec}{K_4} f'^2 + 0.5 We f''^3 \right. \\ \left. + \frac{1}{K_3} (K_1 f' + L_1 \zeta + Du \varpi'') - \beta_1 (ff' \zeta' + f^2 f'^2) \right] \quad (12)$$

$$\varpi'' Sc (f \zeta' - Kr \varpi + Sr \zeta'' - \beta_2 (ff' \varpi' + f^2 \varpi'^2)) = 0 \quad (13)$$

The associated boundary conditions are:

$$f = 0, f' = 1, \zeta = 1, \varpi = 1 \text{ at } \eta = 0 \quad (14)$$

$$f' \rightarrow 0, \zeta \rightarrow 0, \varpi \rightarrow 0 \text{ as } \eta \rightarrow \infty$$

where

$$M = \frac{\sigma B_0^2}{\rho_f}, Pr = \frac{\nu_f}{\alpha_f}, K = \frac{\nu_f}{K_p}, We = \Gamma x \sqrt{\frac{2b^3}{\nu_f}}, E_0 = \frac{E}{B_0 U_w}, \beta_1 = \frac{A}{b(\rho C_p)_f}, Kr = \frac{Kr^*}{b}$$

$$Sc = \frac{\nu_f}{D_M}, So = \frac{D_T (T_w - T_\infty)}{\nu_f (C_w - C_\infty)}, Du = \frac{D_C (C_w - C_\infty)}{\nu_f (\rho C_p)_f (T_w - T_\infty)}, \beta_2 = \frac{B}{b(\rho C_p)_f}, Ec = \frac{U_w^2}{(C_p)_f (T_w - T_\infty)}$$

The thermal properties of nanofluid are defined as follows:

$$K_{nf} = k_f \frac{k_s + 2k_f - 2\phi(k_f - k_s)}{k_s + 2k_f + 2\phi(k_f - k_s)}, (\rho C_p)_{nf} = (1 - \phi)(\rho C_p)_s + \phi(\rho C_p)_f, \quad (15)$$

$$\alpha_{nf} = \frac{K_{nf}}{(\rho C_p)_{nf}}, \mu_{nf} = (1 - \phi)^{-2.5} \mu_f, \rho_{nf} = (1 - \phi)\rho_f + \phi\rho_s, \nu_f = \frac{\mu_f}{\rho_f}.$$

4. Result and discussion

The limit esteem issue conditions (11)- (13) were settled mathematically utilizing the capability BVP4C from MATLAB. This BVP4C capability is planned to utilize the 3-stage Lobatto IIIa equation under the limited contrast conspire with fourth request accuracy. Thetables and charts introduced in this part thus compares to these qualities aside from where it is otherwise expressed.

The influence of attractive term (M) on the profile of velocity is displayed in figure 2. The velocity circulation and the whole hydrodynamic limit layer are worked on because of an expansion in M . A forced attractive field produces Lorentz force and this power influences the electrically conductive liquids. For instance, Lorentz force significantly affects speed dissemination in figure 2, since electric component boundary is available in stream system.

The permeability parameter (K) affects the velocity appropriation, as displayed in Figure 3. The porousness boundary increments, bringing about a remarkable change in the velocity profile. The penetrability boundary in a limit layer stream permits liquids to venture out starting with one layer then onto the next genuinely. While expanding K builds the permeable system, it likewise permits more liquid particles to go through. Along these lines, the thickness of the hydrodynamic limit layer continues to rise.

Prandtl (Pr) effect on velocity and temperature appropriations should be visible in Figures 4(a) and 4(b). The velocity and temperature diagrams degenerate emphatically when the Pr is expanded. Since any liquid with a bigger Prandtl will have an extremely high thickness, this outcome is sensibly right. As per the result displayed in Figure 4, the plate has started to cool from the wall up. Due to the low plate surrounding consistency, this is valid. Pr checks the stream conduct of liquid warm and energy boundaries during heat move. Truly, the thickness of the hydrodynamic and warm limit layer upgrades because of expansion in Pr .

On the velocity and fixation charts, Soret (Sr) has an impact displayed in Figure 5. Solutal and hydrodynamic limit layers seem to accelerate because of an expansion in Sr . To settle two-fold diffusive stream, a more noteworthy Sr esteem has been found. For instance, on the off chance that the fixation inclination is more prominent than nothing, the thickness of the nanoparticles falls because of this slope, and they diffuse to a cooler medium. Nonetheless, when the liquid temperature climbs to Sr , the thickness of the liquid ascents and the nanoparticles spread to a hotter climate.

Williamson boundary (Weissenberg number) (We) effects on the profile of velocity is found in Figure 6. The hydrodynamic layer and speed profile are upgraded by expanding We . With regards to speed, the effect of We is most perceptible when you're near the wall and nearly non-existent when you're a long way from the plate. Along these lines, liquid stream is impacted by the wall's thickness.

Figures 7(a) and 7(b) portrays the impact of Dufour (Du) on the velocity and temperature designs in the district. For the dispersion warm nature of the cycle, the meaning of Du should be visible. The energy transition inside the layer is dispersed by the focus inclinations depicted by the Du .

This outcomes in a synchronous decrease of the Solutal and hydrodynamic limit layers. Eckert's (Ec) impact on velocity and temperature conveyances is found in Figures 8(a) and 8(b). The Eckert number is a proportion of the enthalpy and dynamic energy in the stream. In a high incompressible stream, Ec fundamentally affects the temperature, which is the reason it is significant at high rates in compressible streams. The result, which indicates that the flow gains more energy and hence improves the thermal and hydrodynamic boundary layers.

To represent the effect of synthetic response term (Kr) on velocity and concentration circulations, Figures 9(a) and 9(b) was made. Destructive outcomes are gotten by decreasing the convergence of species and the energy limit layer at the pace of substance response. Species focus and rubbing coefficient are decreased by the destructive responsive cycle.

Figure 10(a) and 10(b) shows that the velocity and temperature profiles for different values of thermal radiation parameter. The electromagnetic radiation produced by the material medium in view of intensity energy is called warm radiation. The climb in temperature is a

consequence of the energy delivered because of warm radiation. Nonetheless, convective stream is supported.

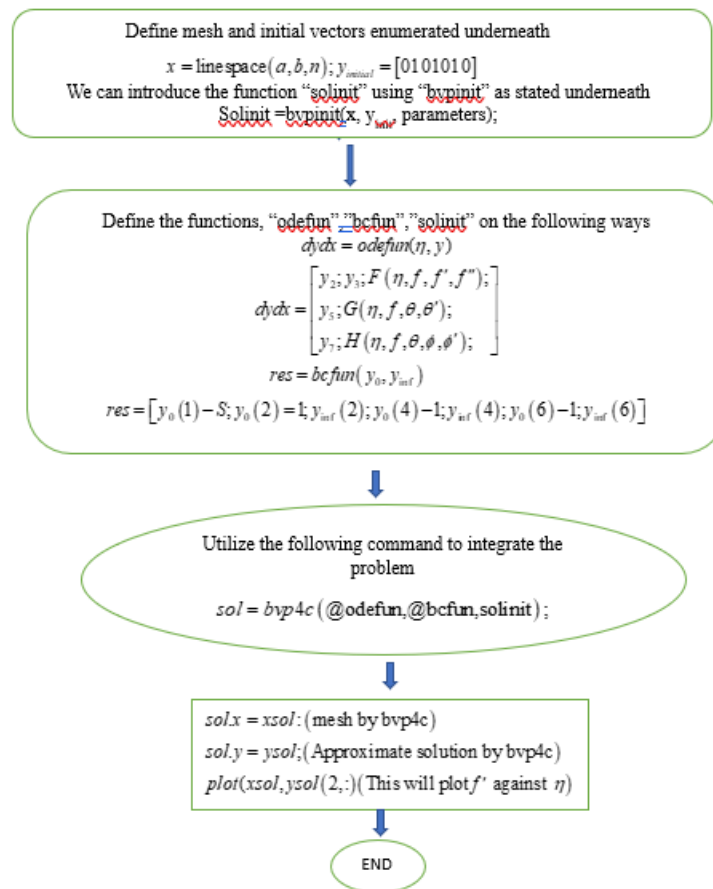
Table I shows the comparison of the present study and that of Sudarshana Reddy and Ali J Chamkha[2016] when $E = We = \beta_1 = \beta_2 = 0$. The present study was found to be in good agreement.

Table II shows that designing amounts is essentially influenced by the flow parameters. Expansion of 'Pr' will speed up the coefficient of skin contact and heat transport. No matter how quickly mass is transferred, Prandtl's significance remains constant. As the 'M' boundary expands, the coefficient of skin rubbing decreases. The rate of intensity and mass transfer remain constant at the point when 'M' expands. There is an expansion in the coefficient of skin grinding and the change of intensity transmission with an expansion in Du, R, Ec, and β_1 . Table - II shows that rising the worth of Kr, Sc diminishes the Sherwood coefficient and skin erosion.

5. Conclusion

The following observations can be concluded from the above:

- If the fluid velocity is raised, then the two factors heat generation and thermal radiation enhances the warm fluid particles and fluid temperature.
- A component in the energy equation known as the viscous dissipation term is responsible for the reduction of heat energy into the flow of a fluid. So, heat energy increases the thickness of hydrodynamic and thermal layers.
- This study has shown that the local mass transfer and skin friction increases due to chemical reaction. As the thermal layer thickens, a higher heat relaxation flow and a higher mass relaxation flux were shown to improve fluid particle concentrations and the overall concentration layer.



Flow chart

Table I: Comparison of the present study with the details of Sudarshana Reddy and Ali J Chamkha[2016] when $We = \beta_1 = \beta_2 = 0$

M	ϕ	Ramana Reddy et al[14]				Present study			
		$-f''(0)$		$-\theta'(0)$		$-f''(0)$		$-\theta'(0)$	
		Al ₂ O ₃	TiO ₂	Al ₂ O ₃	TiO ₂	Al ₂ O ₃	TiO ₂	Al ₂ O ₃	TiO ₂
0.0	0.05	1.00657	1.01167	1.62258	1.63832	1.00659	1.01169	1.62253	1.63829
	0.10	1.01002	1.01032	1.49187	1.51984	1.01001	1.01031	1.49185	1.51983
	0.15	0.98954	0.99666	1.37561	1.41387	0.98953	0.99665	1.37559	1.41385
	0.20	0.95601	0.97294	1.27153	1.31856	0.95600	0.97294	1.27151	1.31855
0.5	0.05	1.20481	1.20961	1.57892	1.59484	1.20479	1.20960	1.57894	1.59486
	0.10	1.17592	1.18502	1.45312	1.48162	1.17590	1.18501	1.45312	1.48164
	0.15	1.13924	1.15183	1.34128	1.37981	1.13922	1.15181	1.34130	1.37981
	0.20	1.09601	1.10857	1.24152	1.28814	1.09589	1.10754	1.24153	1.28819

Table II: The significance of flow parameters on the skin friction, Nusselt and Sherwood numbers.

Pr	M	K	Sc	Sr	Du	Ec	Kr	R	β_1	β_2	We	Cf	Nu	Sh
0.71												0.0574	0.3380	0.6781
3.0												1.2168	0.3447	0.6781
7.0												1.4571	0.3697	0.6781
	0.0											0.7676	0.7000	0.0561
	0.5											0.4220	0.7000	0.0561
	1.0											0.1846	0.7000	0.0561
		0.3										0.8929	0.4111	0.5261
		0.6										0.1437	0.4111	0.5261
		1.0										1.1804	0.4111	0.5261
			0.61									1.2363	0.3377	0.5918
			1.0									0.3856	0.3377	0.6352
			3.0									0.1034	0.3377	0.6866
				1.0								0.5045	0.7141	0.1205
				2.0								1.5431	0.7141	0.4484
				3.0								2.3307	0.7141	0.5353
					1.0							0.1042	0.1066	0.3971
					2.0							1.1989	0.2226	0.3971
					3.0							2.2937	0.5518	0.3971
						0.2						0.5565	0.2584	0.6121
						0.4						1.7755	0.8541	0.6121
						0.6						2.9945	1.4498	0.6121
							0.1					0.4467	0.3141	0.7761
							0.3					0.7770	0.3141	0.8430
							0.5					1.2266	0.3141	1.0361
								0.0				0.0845	0.3427	0.8120
								0.5				0.9431	0.3597	0.8120
								1.0				1.8569	0.3777	0.8120
									2.0			0.4343	0.1581	0.1782
									4.0			1.0864	0.2812	0.1782
									6.0			2.4042	0.3318	0.1782
										2.0		0.7126	0.5858	0.0176
										4.0		0.8710	0.5858	0.3897
										6.0		1.2396	0.5858	0.4858
											0.0	1.3434	0.5240	0.6015
											0.5	2.7060	0.5240	0.6015
											1.0	3.0687	0.5240	0.6015

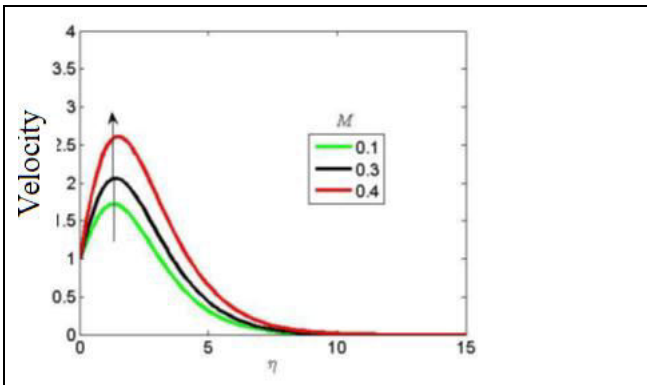


Figure 2: Impact of Magnetic parameter on velocity profiles.

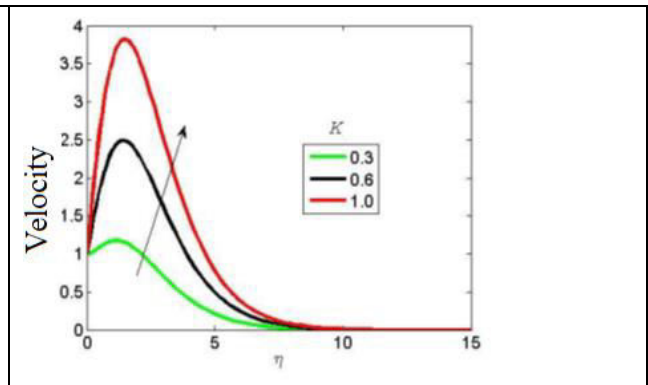


Figure 3: Impact of Permeability parameter on velocity profiles.

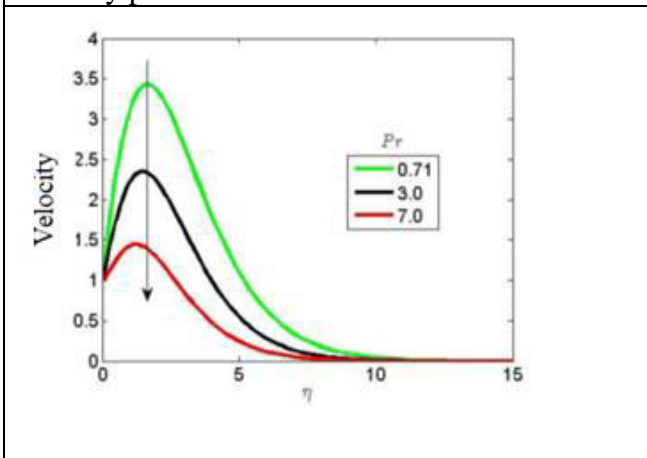


Figure 4(a): Impact of velocity profiles for various values of Prandtl number.

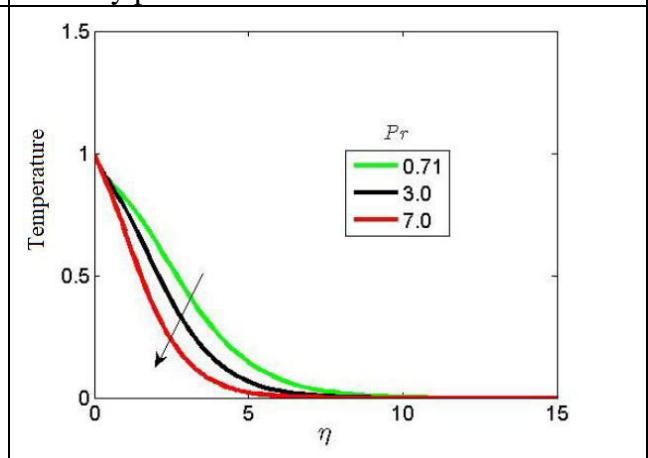


Figure 4(b): Impact of temperature profiles for various values of Prandtl number.

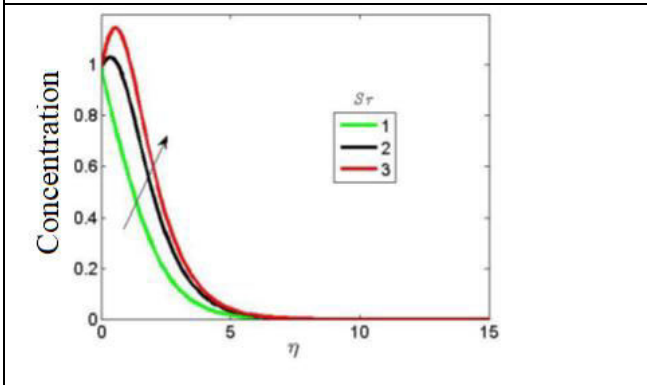


Figure 5: Impact of Soret number on Velocity profiles.

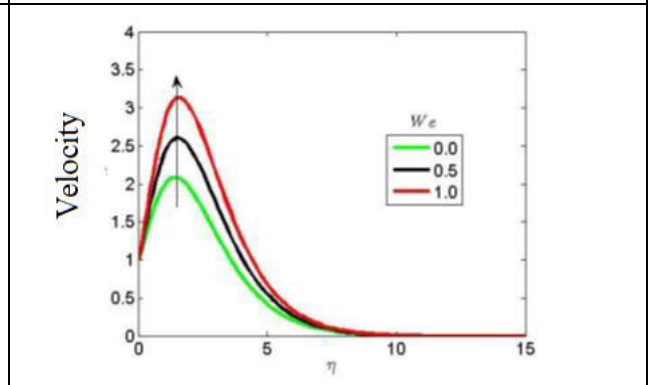


Figure 6: Impact of Weissenberg number on velocity profiles.

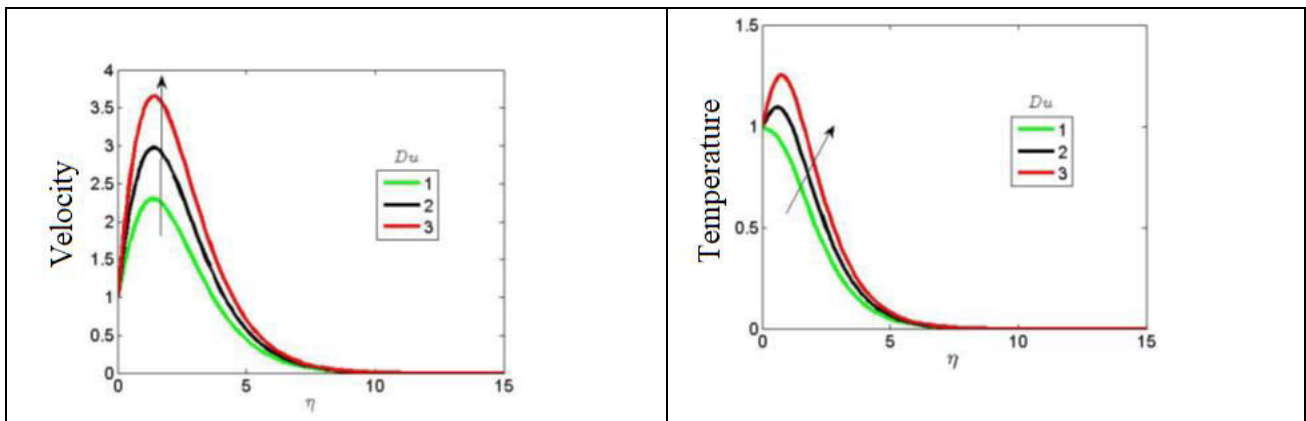


Figure 7(a): Impact of Dufour number on velocity profiles.

Figure 7(b): Impact of Dufour number on temperature profiles

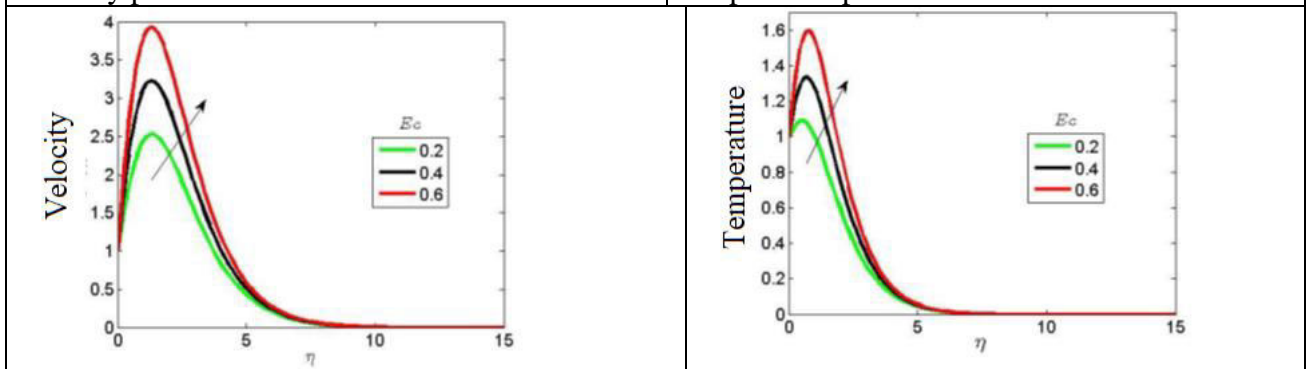


Figure 8(a): Impact of Eckert number on velocity profiles.

Figure 8(b): Impact of Eckert number on temperature profiles.

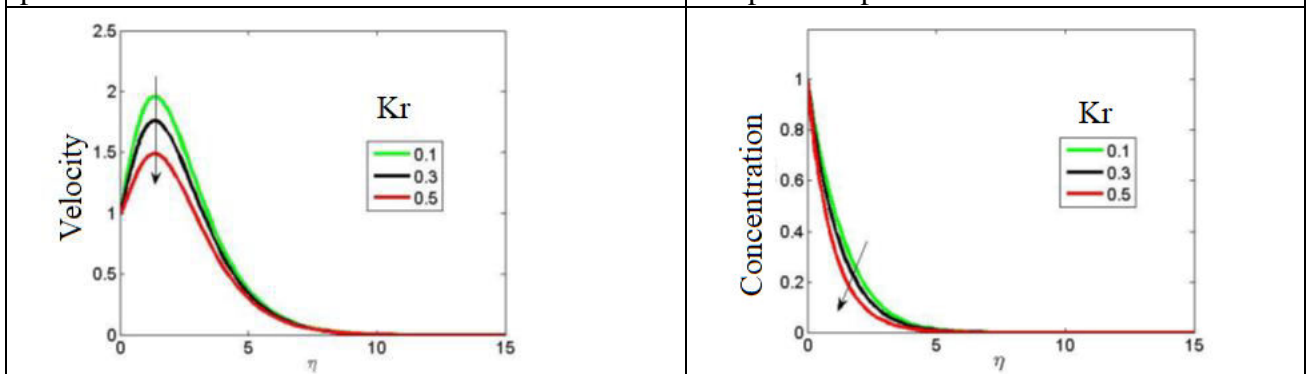


Figure 9(a): Impact of chemical reaction on velocity profiles.

Figure 9(b): Impact of Chemical reaction on concentration profiles.

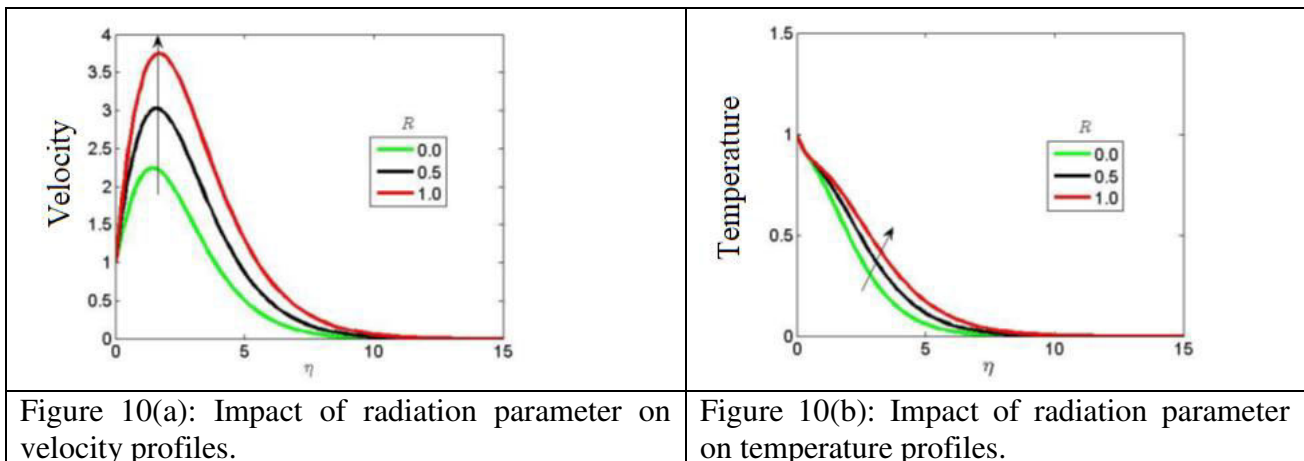


Figure 10(a): Impact of radiation parameter on velocity profiles.

Figure 10(b): Impact of radiation parameter on temperature profiles.

REFERENCES

1. Hari R. Kataria, and Patel Harshad R. (2016). "Radiation and chemical reaction effects on MHD Casson fluid flow past an oscillating vertical plate embedded in porous medium." *Alexandria Engineering Journal* 55: pp 583–595.
2. Mabood, F., Shafiq, A., Hayat, T., and Abelman, S. (2017). "Radiation effects on stagnation point flow with melting heat transfer and second order slip", *Results in Physics* 7: pp 31–42.
3. Hayat Tasawar, Sumaira Qayyum, Maria Imtiaz, Ahmed Alsaedi (2017). "Radiative flow due to stretchable rotating disk with variable thickness." *Results in Physics*, 7:pp 156–165.
4. Amalendu Rana and Motahar Reza and K. Maruthi Prasad and G. Chandra Shit (2022). "Effects of different viscous dissipation and Joule heating on Electromagnetohydrodynamic flow of power-law fluid in porous microchannel." *International Journal of Ambient Energy*:pp 1-40. DOI:10.1080/01430750.2022.2142289
5. Choi, S. (1995). "Enhancing thermal conductivity of fluids with nanoparticles." *ASEM Publ.Fed* 231: pp 99-106. <https://www.osti.gov/servlets/purl/196525>.
6. Krishnamurthy, M.R., Prasanna kumara, B.C., Giresha, B.J., Rama Subba Reddy Gorla (2016). "Effect of chemical reaction on MHD boundary layer flow and melting heat transfer of Williamson nanofluid in porous medium." *Engineering Science and Technology, an International Journal* 9: pp 53–61.
7. Hashim, Aamir Hamid, Masood Khan (2020), "Heat and mass transport phenomena of on time dependent flow of Williamson fluid towards heated surface." *Neural Computing and Applications* 32:3253–3263.
8. Reddy, B.M., Kesavaiah, D.C., Reddy, G.V.R.(2018). "Effects of radiation and thermal diffusion on MHD heat transfer flow of a dusty viscoelastic fluid between two moving parallel plates." *ARPJ Journal of Engineering and Applied Sciences* 13 (22):pp. 8863-8872.
9. Krishna, Y.H., Reddy, G.V.R., Makinde, O.D. (2018). "Chemical reaction effect on MHD flow of Casson fluid with porous stretchingsheet." *Defect and Diffusion forum* 389: pp 100-109. DOI: 10.4028/www.scientific.net/DDF.389.100
10. Reddy, G.V.R., Krishna, Y.H. (2018). "Numerical solutions of unsteady MHD flow heat transfer over a stretching surface with suction or injection." *Fluid Dynamics and Material Processing* 14 (3): pp. 213-222. DOI: 10.3970/fdmp.2018.00411

11. Vijaya, N., Hari Krishna, Y., Kalyani, K., Reddy, G.V.R. (2018). "Soret and radiation effects on an unsteady flow of a Casson fluid through porous vertical channel with expansion and contraction." *Frontiers in Heat and Mass Transfer* 11, art. no. 19. DOI: 10.5098/hmt.11.19
12. Sreedevi, G., Prasada Rao, D.R.V., Makinde, O.D., Venkata Ramana Reddy, G. (2017). "Soret and DuFour effects on MHD flow with heat and mass transfer past a permeable stretching sheet in presence of thermal radiation." *Indian Journal of Pure and Applied Physics* 55 (8): pp. 551-563.
13. K. Sharada and B. Shankar. (2015). "MHD mixed convection flow of a Casson fluid over an exponentially stretching surface with the effects of Soret, Dufour, thermal radiation and chemical reaction." *World Journal of Mechanics* 5(9), pp 165–177.
14. Dulal Pal & Gopinath Mandal.(2021). "Magnetohydrodynamic nonlinear thermal radiative heat transfer of nanofluids over a flat plate in a porous medium in existence of variable thermal conductivity and chemical reaction." *International Journal of Ambient Energy* 42(10): pp 1167-1177.
15. K. Anantha Kumar, A.C. Venkata Ramudu, V. Sugunamma & N. Sandeep. (2022). "Effect of non-linear thermal radiation on MHD Casson fluid flow past a stretching surface with chemical reaction." *International Journal of Ambient Energy* 43(1): pp 8400-8407
16. Surya Kanta Mondal, Dulal Pal. (2022). "Performance of activation energy and variable thermal conductivity on bioconvection heat transfer of Williamson nanofluid undergoing binary chemical reaction with multiple slip." *International Journal of Ambient Energy* 43(1): pp 6108-6120.
17. KankanalaSharada. (2022). "Heat and mass transfer effects on MHD mixed convection flow of viscoelastic fluid with constant viscosity and thermal conductivity.", *Heat Transfer* 51(1): pp 1213–1236.
18. P. Sudarsana Reddy & P. Sreedevi (2022), "Impact of chemical reaction and double stratification on heat and mass transfer characteristics of nanofluid flow over porous stretching sheet with thermal radiation", *International Journal of Ambient Energy*, 43:1, pp1626-1636, DOI: [10.1080/01430750.2020.1712240](https://doi.org/10.1080/01430750.2020.1712240)
19. Vishwambhar S. Patil, Pooja P. Humane & Amar B. Patil (2022). "MHD Williamson nanofluid flow past a permeable stretching sheet with thermal radiation and chemical reaction", *International Journal of Modelling and Simulation*, DOI: [10.1080/02286203.2022.2062166](https://doi.org/10.1080/02286203.2022.2062166).
20. K Sharada, B Shankar. (2017). "Soret and Dufour Effects on MHD Mixed Convection Flow of Carreau Nanofluid Over an Exponentially Stretching Sheet with Concentration Slip", *Journal of Nanofluids* 6(6): pp 1143-1148.
21. Reddy, G.V.R., Ibrahim, S.M., Bhagavan, V.S. (2014). "Similarity transformations of heat and mass transfer effects on steady MHD free convection dissipative fluid flow past an inclined porous surface with chemical reaction", 11 (2), pp. 157-166. DOI: 10.3329/jname.v11i2.18313.
22. S. Jagadha, S. Hari Shing Naik, P. Durgaprasad, A. Naresh Kumar & Kishan Naikoti. (2021). "Radiative Newtonian Carreau nanofluid through stretching cylinder considering the first-order chemical Reaction" *International Journal of Ambient Energy* 43(1) : pp 4959-4967,doi: 10.1080/01430750.2021.1929473.
23. Dawar Abdullah, Zahir Shah, Asifa Tassaddiq, Poom Kumam, Saeed Islam, Waris Khan (2021). "A convective flow of Williamson nanofluid through cone and wedge with non-isothermal and non-isosolutal conditions: A revised Buongiorno model", *Case Studies in Thermal Engineering* 24:100869

24. Srinivasacharya, D. and Kumar P. Vijay (2018). "Effect of thermal radiation on mixed convection of a nanofluid from an inclined wavy surface embedded in a non-Darcy porous medium with wall heat flux", *Propulsion and Power Research*, 7(2): pp 147–157.
25. Mahanthesh, B., Giresha, B.J., Rama Subba Reddy Gorla (2016). "Heat and mass transfer effects on the mixed convective flow of chemically reacting nanofluid past a moving/stationary vertical plate", *Alexandria Engineering Journal*, 55(1), pp 569–581.
26. Giresha, B.J., Ganesh Kumar, K., Ramesh, G.K., Prasannakumara, B.C. (2018). "Nonlinear convective heat and mass transfer of Oldroyd-B nanofluid over a stretching sheet in the presence of uniform heat source/sink", *Results in Physics*, 9, 1555–1563.
27. Ahmad Farooq, Sohaib Abdal, Hela Ayed, Sajjad Hussain, Suleman Salim, A. Othman Almatroud (2021). "The improved thermal efficiency of Maxwell hybrid nanofluid comprising of graphene oxide plus silver / kerosene oil over stretching sheet", *Case Studies in Thermal Engineering*, 27(2), 101257.
28. Nadeem Muhammad, Ahmed Elmoasry, Imran Siddique, Fahd Jarad, Rana Muhammad Zulqarnain, Jawdat Alebraheem, and Naseer S. Elazab (2021). "Study of Triangular Fuzzy Hybrid Nanofluids on the Natural Convection Flow and Heat Transfer between Two Vertical Plates", *Computational Intelligence and Neuroscience* 2021: Article ID 3678335.
29. Idowu, A.S., and Falodun B.O. (2020). "Variable thermal conductivity and viscosity effects on non-Newtonian fluids flow through a vertical porous plate under Soret-Dufour influence", *Mathematics and Computers in Simulation* 177: pp 358–384.
30. Khan Umair, Anum Shafiq, A. Zaib, Abderrahim Wakif, and Dumitru Baleanu (2020). "Numerical exploration of MHD falkner-skansutterby nanofluid flow by utilizing an advanced non-homogeneous two-phase nanofluid model and non-Fourier heat-flux theory", *Alexandria Engineering Journal* 59: pp 4851–4864.
31. Ali, M.E. and Sandeep, N. (2017). "Cattaneo-Christov model for radiative heat transfer of magnetohydrodynamic Casson-ferrofluid: A numerical study", *Results in Physics* 7: pp 21–30.
32. Zhang Yan, Nazia Shahmir, Muhammad Ramzan, Hammad Alotaibi, and Hassan M. Aljohani (2021). "Upshot of melting heat transfer in a Von Karman rotating flow of gold silver/ engine oil hybrid nanofluid with Cattaneo-Christov heat flux", *Case Studies in Thermal Engineering* 26(4): 101149
33. Hayat Tanzila, and S. Nadeem (2018). "Flow of 3D Eyring-Powell fluid by utilizing Cattaneo-Christov heat flux model and chemical processes over an exponentially stretching surface", *Results in Physics* 8: pp 397–403.
34. Shihao Han, Liancun Zheng, Chunrui Li, and Xinxin Zhang (2014). "Coupled flow and heat transfer in viscoelastic fluid with Cattaneo-Christov heat flux model", *Applied Mathematics Letters* 38: 87–93
35. Alao, F.I., Fagbade, A.I., Falodun, B.O., (2016). "Effects of thermal radiation, Soret and Dufour on an unsteady heat and mass transfer flow of a chemically reacting fluid past a semi-infinite vertical plate with viscous dissipation", *Journal of the Nigerian Mathematical Society* 35(6): pp 142–158.
36. Tlili, I., Khan, W.A., Khan, I. (2018). "Multiple slips effects on MHD SA-Al₂O₃ and SACu non-Newtonian nanofluids flow over a stretching cylinder in porous medium with radiation and chemical reaction", *Results in Physics* 8: 213–222.

37. Mishra Satya Ranjan, Asmat Ara and Najeeb Alam Khan (2018). "Dissipation Effect on MHD Stagnation-Point Flow of Casson Fluid Over Stretching Sheet Through Porous Media", *Mathematical. Sciences Letters* 7(1): pp 13-20.
38. MondalHiranmoy, Dulal Pal, Sewli Chatterjee, and Precious Sibanda (2018). "Thermophoresis and Soret-Dufour on MHD mixed convection mass transfer over an inclined plate with non-uniform heat source/sink and chemical reaction", *Ain Shams Engineering Journal* 9(4): pp 2111–2121.
39. Ramzan, M, Dawar A, Saeed A, Kumam P, Wathayu W, and Kumam W (2021). "Heat transfer analysis of the mixed convective flow of magnetohydrodynamic hybrid nanofluid past a stretching sheet with velocity and thermal slip conditions", *PLoS One* 16(12), E0260854. DOI: 10.1371/journal.pone.0260854
40. Fagbade, A.I., Falodun, B.O., Omowaye, A.J., (2018). "MHD natural convection flow of viscoelastic fluid over an accelerating permeable surface with thermal radiation and heat source or sink: Spectral Homotopy Analysis Approach", *Ain Shams Engineering Journal*9(4): pp 1029– 1041.
41. Reddy P. Sudarsana, and Chamkha Ali J. (2016). "Soret and Dufour effects on MHD convective flow of Al_2O_3 –water and TiO_2 –water nanofluids past a stretching sheet in porous media with heat generation/absorption", *Advanced Powder Technology* 27: pp 1207–1218.
42. Rashidi, M.M., Mahariq, I., Alhuyi Nazari, M.Oussama Accouche & Muhammad Mubashir Bhatti(2022). "Comprehensive review on exergy analysis of shell and tube heat exchangers". *Journal of Thermal Analysis and Calorimetry*147: pp 12301–12311, <https://doi.org/10.1007/s10973-022-11478-2>.
43. Farooq Umar, Hassan Waqas, Taseer Muhammad, Muhammad Imran, Ali Saleh Alshomrani (2022). "Computation of nonlinear thermal radiation in magnetized nanofluid flow with entropy generation", *Applied Mathematics and Computation* 423(3): 126900.
44. Bhatti, M.M., Bég, O.A., Ellahi, R& Abbas. T. (2022). "Natural Convection Non-Newtonian EMHD Dissipative Flow Through a Microchannel Containing a Non-Darcy Porous Medium: HomotopyPerturbation Method Study". *Qualitative Theory of Dynamical Systems*21:97. <https://doi.org/10.1007/s12346-022-00625-7>.